Towards CYGNUS: A Large Scale, Low Threshold TPC for the Direct Detection of Dark Matter

Warren Lynch

Department of Physics and Astronomy

The University of Sheffield

A thesis submitted in partial fulfilment for the degree of

Doctor of Philosophy

April 6, 2020

For my Grandad.

Acknowledgments

Firstly, I would like to thank my supervisor, Prof. Neil Spooner, for offering me the opportunity to undertake this PhD and for providing guidance and advice over the last three years. I would also like to thank Prof. Ed Daw for keeping me in mind for a PhD position, at Sheffield, a year after my initial interview. Appreciation also goes to Andrew Scarff, Fred Mouton and Anthony Ezeribe, who's help and experience were invaluable towards my progression in all aspects of my PhD. This appreciation extends to the countless PhD students who have worked on DRIFT-IId, and other related projects, in the past. The knowledge obtained from the study of their theses helped guide my work on multiple occasions.

I am grateful to all of the team at Boulby for accommodating the many visits I was privileged to attend during the first year of my PhD. Special thanks goes to Prof. Sean Paling for all of the insightful discussions and help during my visits. Special thanks is also extended to Christopher Toth for imparting his technical expertise on the operation of the DRIFT-IId detector and directly contributing to all of the work I conducted at Boulby.

I would like to express my appreciation to the CYGNUS collaboration for their exchange of knowledge, results and expertise during our multiple meetings and conferences. In particular, thanks goes to Prof. Kentaro Miuchi for hosting my visit at Kobe University and to Tomonori Ikeda and Hirohisa Ishiura for assisting me during my stay.

Thank you to my parents, for allowing their 32 year old son to move back

home to Sheffield so that I could attain my PhD. Without their support and understanding I would not have been able to make this life changing decision. Thank you to my children, Ashlie, Tammy and Callum, for constantly saving my mind from a PhD quagmire and reminding me of the most important thing in life.

My thanks also goes to the friends and colleagues I have made during my time at Sheffield. I have benefitted from their support, help and countless conversations (many of which took place at the University Arms) throughout my studies. Finally, special thanks must be given to an old friend, Craig Yeadon, who, ten years ago, lent me a popular science book on quantum mechanics and relativity.

Abstract

The evidence supporting the existence of a new type of matter, know as dark matter, is both considerable and wide ranging. From this evidence, it is predicted that ∼84% of the matter in the universe is dark. Further to this, multiple theories, that attempt to extend our understanding beyond the incomplete standard model of particle physics, naturally produce dark matter candidate particles. One popular hypothesis states that dark matter is both weakly interacting and massive, leading to the term WIMP (Weakly Interacting Massive Particle). The three methods used to find such a particle are indirect, direct and collider searches.

The focus of this work is the development of a large scale direct detection experiment, capable of reconstructing the direction of a recoiling target nucleus. The detector is envisioned as a Negative Ion Time Projection Chamber (NI-TPC) with a 20 Torr SF_6 target volume. The ultimate goal is to use the discriminatory power of directionality to explore the dark matter parameter space that is subject to a neutrino background. The detector would be either a single 1000 m^3 structure, named CYGNUS-1000, or multiple smaller structures that sum to the same target volume. A first step in this process would be the construction of a 10 m^3 prototype, named CYGNUS-10. The achievable low energy (1-10 keV_{ee}) gamma background rejection of these detectors was studied using simulation and found to be 10^{-4} keV^{-1} yr^{-1} above a 6 keV_{ee} threshold. This result was used, along with a neutron limit of $<$ 1 yr^{-1}, to prove the feasibility of a CYGNUS TPC from a background per-

spective, using a dedicated GEANT4 Monte Carlo simulation. A method to enhance the sensitivity of a future detector, using machine learning (ML), was demonstrated on existing data from DRIFT-IId (Directional Recoil Identification From Tracks). The ML algorithm produced an improved WIMP cross section reach of 32% compared to the standard analysis. The results of this study were used to produce WIMP search reach predictions for a CYGNUS-1000 and CYGNUS-10 TPC, which showed that a 1000 m^3 target volume, of 20 Torr SF_6, could eventually observe a neutrino background with directional sensitivity.

A readout constructed from an MWPC (Multi-Wire Proportional Chamber) and ThGEM (Thick Gaseous Electron Multiplier) amplification stage was found to produce the least background for a CYGNUS TPC. This result led to the construction of an MWPC-ThGEM hybrid prototype using a 10 cm diameter ThGEM and a 30 cm long wire array with sub-mm pitch (the lowest achieved for an MWPC). The chosen array size reflected the scale up requirements of a future detector with large readout areas. For the prototype, 2D track reconstruction in SF_6 gas was demonstrated using alpha tracks and initial gain measurements were performed in CF_4, resulting in gains $\mathcal{O}(10^3)$. A large scale ThGEM device, with an area of 40×40 cm^2, was tested separately from the readout and was shown to produce $\sim$2 orders of magnitude lower gain than it's smaller counterpart, suggesting that the performance of a ThGEM is reduced when scaling the device to larger areas.

A CYGNUS TPC prototype, called CYGNO, is planned for construction at LNGS (Laboratori Nazionali del Gran Sasso). This prototype uses camera based readouts and an atmospheric gas mixture of He and CF_4. The gamma background from the camera was studied here and a TPC design aimed at reducing this was considered. It was found that introducing shielding into the TPC geometry had little effect on the resulting background rate, due to the need for transparent windows, suggesting that other background mitigation methods are required for this readout.

Author's Contributions

Chapter 2 I am a co-author for COSINE-100 and I have contributed towards shift work on this experiment.

Chapter 3 I wrote the simulation code that produced the low energy electron and nuclear recoils in SF_6 and applied the effects of diffusion and readout resolution to the recoil tracks. I wrote the code that picked out the recoil parameters used for the analysis and applied the Decision Tree machine learning algorithm to find the gamma rejection at different detection efficiencies.

Chapter 4 I used the previously written DRIFT-IId code to produce the table of recoil parameters for each recorded event. I then wrote the code that inputs these parameters into the RFC machine learning algorithm.

Chapter 5 The GEANT4 code used to perform the background study was adapted from that used for DRIFT-IId, which was itself heavily developed, by previous PhD student Fred Mouton, for the background study of a 1000 m^3 CYGNUS TPC. I made significant changes to this code to reflect the specific background study conducted in this chapter, which will be published in an upcoming paper.

Chapter 6 I made considerable changes to the GEANT4 code used in Chapter 5 to produce the background study for CYGNUS-10.

Chapter 7 I designed the ThGEM-MWPC readout and made the wire array. I constructed the TPC apparatus used to test the readout. I wrote the code used to analyse the LABVIEW DAQ data.

Chapter 8 I designed the large area ThGEM, with input from my supervisor, colleagues at Sheffield, the CERN MPGD group and Prof. Kentaro. I constructed the circuit used to amplify and shape the ThGEM signal.

Chapter 9 I wrote the GEANT4 code used to produce the CYGNO background study, which was adapted from that used for DRIFT-IId.

Contents

List of Figures

List of Tables

Chapter 1

Introduction to Dark Matter

This chapter provides a general overview of dark matter. Section 1.1 describes an historical account of some of the first observations made that suggested the existence of a new type of matter. The section then outlines the most current observational evidence and estimates of the amount of dark matter in the universe. Section 1.2 provides a theoretical perspective on the possible nature of dark matter particles, consistent with observation.

1.1 Observational Evidence

This section introduces key pieces of evidence in support of the existence of dark matter, since it was fist proposed almost 90 years ago. The evidence is not limited to the few cases presented here, nor is it suggested that every observation discussed is the first of it's kind (unless stated otherwise), rather, the aim of this section is to highlight a few very different methods that all independently predict a yet unobserved type of matter.

1.1.1 The Coma Cluster

One of the first accounts of dark matter comes from Fritz Zwicky's studies of the Coma cluster in 1933 [1]. Zwicky used the virial theorem to calculate the mass of the cluster and compared this to the mass estimated using the cluster's luminosity. To apply the virial theorem the following were assumed: The cluster is in a state of mechanical equilibrium; the galactic motions within the cluster are isotropic; the cluster mass, M, is uniformly distributed; all of the galaxies within the cluster are of the same mass. With these assumptions the theorem was used to equate the cluster's mean kinetic energy, $\langle E_k \rangle$, to it's mean potential energy, $\langle E_p \rangle$ via,

$$\langle E_k \rangle = -\frac{\langle E_p \rangle}{2} \tag{1.1}$$

where,

$$\langle E_k \rangle = \frac{M \langle v^2 \rangle}{2} \tag{1.2}$$

$$\langle E_p \rangle = -\frac{3GM^2}{5R} \tag{1.3}$$

and G is the gravitational constant, R is the cluster's radius and $\langle v^2 \rangle$ is the magnitude of the average square velocity of the cluster's galaxies. With the assumption of isotropy, $\langle v^2 \rangle$ is related to the magnitude of the radial velocity of the galaxies, v_r, by,

$$\left\langle v^2 \right\rangle = 3 \left\langle v_r^2 \right\rangle \tag{1.4}$$

Using the above equations the virial mass of the Coma cluster was calculated as,

$$M = \frac{5R \left\langle v_r^2 \right\rangle}{G} \tag{1.5}$$

Values of v_r were measured, for galaxies within the Coma cluster, from the observed doppler shifts of spectral lines originating from galactic nebulae,

$$v_r = \frac{\Delta\lambda}{\lambda} c \tag{1.6}$$

where λ is the spectral line wavelength and $\Delta\lambda$ is the shift in wavelength. From this a value of $\langle v_r^2 \rangle^{1/2}$, between 1500-2000 km s^{-1}, was obtained. Zwicky calculated that for $\langle v_r^2 \rangle^{1/2} = 1000$ km s^{-1} the Coma cluster mass must be at least 400 times that obtained from luminosity observations alone. Zwicky termed the inferred missing mass, dark matter.

This result led to other mass to light ratio measurements, some of which were summarised in a table produced by M. Schwarzschild in 1954 [2], which is shown in Figure 1.1.

Objects	Distance (in kpc)	Luminosity (in sol. lum.)	Mass (in sol. mass)	Mass/Lum. f
Solar Neighborhood	—	—	—	4
Triangulum Nebula, M33	480	1.4×10^9	5×10^9	4
Large Magellanic Cloud	44	1.2×10^9	2×10^9	2
Andromeda Nebula	460	9×10^9	1.4×10^{11}	16
Globular Cluster, M92	11	1.7×10^5	$<8 \times 10^5$	<5
Elliptical Galaxy, NGC 3115	2100	9×10^8	9×10^{10}	100
Elliptical Galaxy, M32	460	1.1×10^8	2.5×10^{10}	200
Average S in Double Gal.	—	1.3×10^9	7×10^{10}	50
Average E in Double Gal.	—	8×10^8	2.6×10^{11}	300
Average in Coma Cluster	25000	5×10^8	4×10^{11}	800

Figure 1.1: Mass to light (M/L) ratio measurements as of 1954. Table from [2].

Although the measurements shown in the above figure (and that made by Zwicky) were based on the best luminosity estimates available at the time, and were therefore not always accurate, they consistently pointed towards the existence of non-luminous matter. A more modern estimate of the mass to light ratio of the coma cluster, which is given as ∼160 [3], still supports this hypothesis.

1.1.2 Galactic Rotation Curves

Arguably a more dramatic piece of evidence comes from the unexpected observation of flat rotation curves for spiral galaxies.

An object in a circular orbit around a central body experiences a centripetal acceleration of magnitude, v^2/r, where v is the object's speed and r is the distance between the object and the body's centre. This is equal to the magnitude of the gravitational acceleration, GM_r/r^2, experienced by the object due to the presence of the central body, where, M_r is the total mass contained within a spherical volume of radius r. Therefore, v, is given as,

$$v = \sqrt{\frac{GM_r}{r}} \tag{1.7}$$

If the majority of M_r is concentrated at the centre of the system, such as found in the solar system, this results in a Keplerian rotation curve characterised by the relation, $v \propto r^{-1/2}$. As the majority of luminous matter in a typical spiral galaxy is located at it's centre, the same behaviour was expected for galactic rotation curves. However, observations of the Andromeda galaxy made in 1970 [4] showed that v remained ∼constant with increasing r, resulting in a flat rotation curve. Further results published in 1983 [5] reported flat rotation curves from observations of 60 other galaxies. For each galaxy, v was measured from the doppler shift in wavelength (given by Eq. 1.6) of light emitted from clouds of hydrogen and helium. Considering Eq. 1.7, it can be seen that v only remains constant with increasing r if M_r continues to increase with r. This is represented in Figure 1.2, which shows that the flat rotation curve of galaxy NGC 6503 is explained by the addition of a dark matter halo that increases in mass as r increases. The evidence from rotation curves suggests that these halos constitute ∼95% of a galaxies total mass [6].

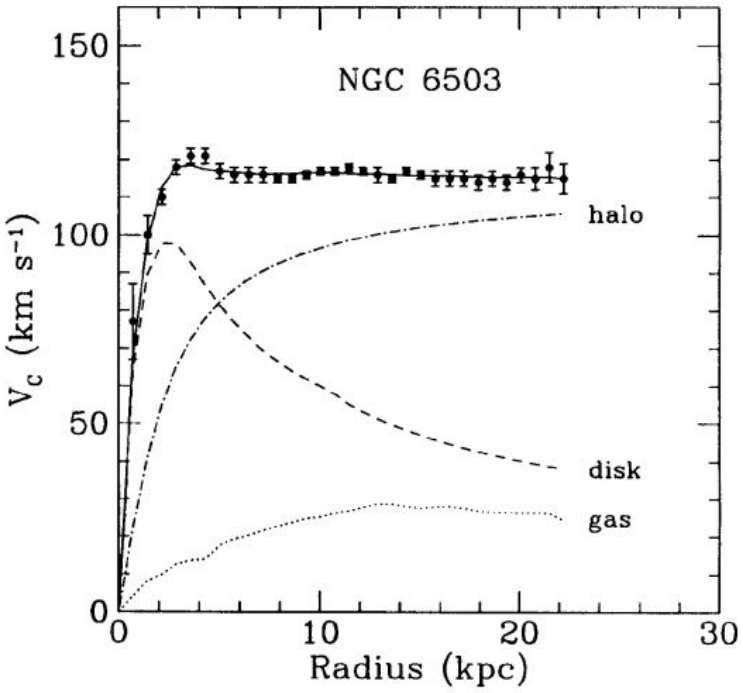

Figure 1.2: An example of a galactic rotation curve for the galaxy NGC 6503 taken from Ref [6]. The disk alone follows a Keplerian profile and the observed flat curve requires the addition of a halo of dark matter surrounding the galaxy.

1.1.3 Gravitational Lensing

Another indication of the presence of dark matter comes from a phenomena predicted by Einstein's theory of general relativity, termed gravitational lensing. The theory states that as mass warps the space-time around it, electromagnetic radiation, traversing nearby, follows the warped path. The first observational evidence of this behaviour was made by Arthur Eddington and Frank Dyson during a total solar eclipse that occurred in 1919 [7]. During the eclipse, the known position of a distant star was seen to change as the light from the star passed near the Sun. This effect was due to the distant star's light being deflected by the Sun's gravitational field.

Gravitational lensing was used in 2006 to show the existence of dark matter within the cluster merger 1E0657-558 [8] or, as it is more famously known, the bullet cluster. Figure 1.3 shows an optical image of the cluster, overlaid with an X-ray image (taken by the Chandra space telescope), shown in pink, and an image of the cluster's mass distribution as inferred using gravitational lensing, shown in blue.

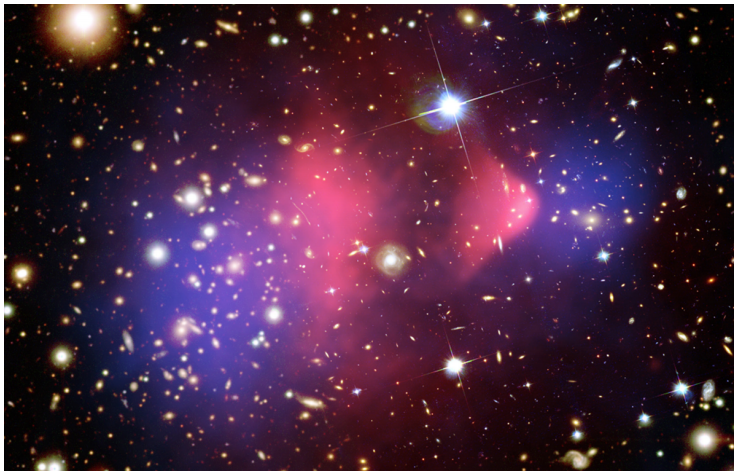

Figure 1.3: Optical image of the cluster merger 1E0657-558 (bullet cluster) overlaid with an X-Ray image (pink) and an image of the cluster's mass distribution (blue), inferred from gravitational lensing. From [9].

In the above figure, the optical image shows the distribution of the stella component (mainly galaxies) within the cluster, which remain mostly undisturbed by the merger. Whilst the X-Ray image shows intracluster plasma experiencing ram pressure during the merger and, therefore, separating away from the stella component. In the absence of dark matter, the cluster's mass distribution would be concentrated around the dominant baryonic mass of the plasma and the blue and pink images on Figure 1.3 would $\sim$ align. Instead, the figure shows that the cluster's mass is mostly concentrated around the non-dominant baryonic component provided by the collisionless stella

material. Therefore, the vast majority of the mass distribution causing the gravitational lensing must be due to the presence of a non-baryonic component, i.e dark matter.

1.1.4 Big Bang Nucleosynthesis

The conclusion from the above sections is that the dominant matter in the Universe is non-luminous. Despite this, it could still be argued that dark matter is somehow composed of baryons, however, consideration of the amount of baryons produced in the early stages of the Universe, during big bang nucleosynthesis (BBN), suggests that this can not be the case.

$\sim$One second after the big bang, at temperatures of around 10^{10} K, the baryonic matter of the Universe (protons and neutrons) began to fuse together and produce deuterium (D). When temperatures reduced to a point at which the photodisintegration of D became statistically less likely, the D survival time was long enough to undergo other fusion processes and create tritium (T), ^{3}He, ^{4}He and a small amount of ^{7}Li. As the temperature reduced further, fusion processes could no longer occur and the number of primordial light elements became constant. The abundance of light elements in the early universe is similar to the same abundance found in remote regions of the cosmos (after taking into account the average amount of elements produced in this region by stella evolution). Figure 1.4 from Ref. [10] shows how spectrographic observations of the light element abundance in these regions (green shaded areas) can be compared to those predicted by the BBN model (blue curves) to give a prediction of the modern day baryonic matter density fraction, given by Eq. 1.8.

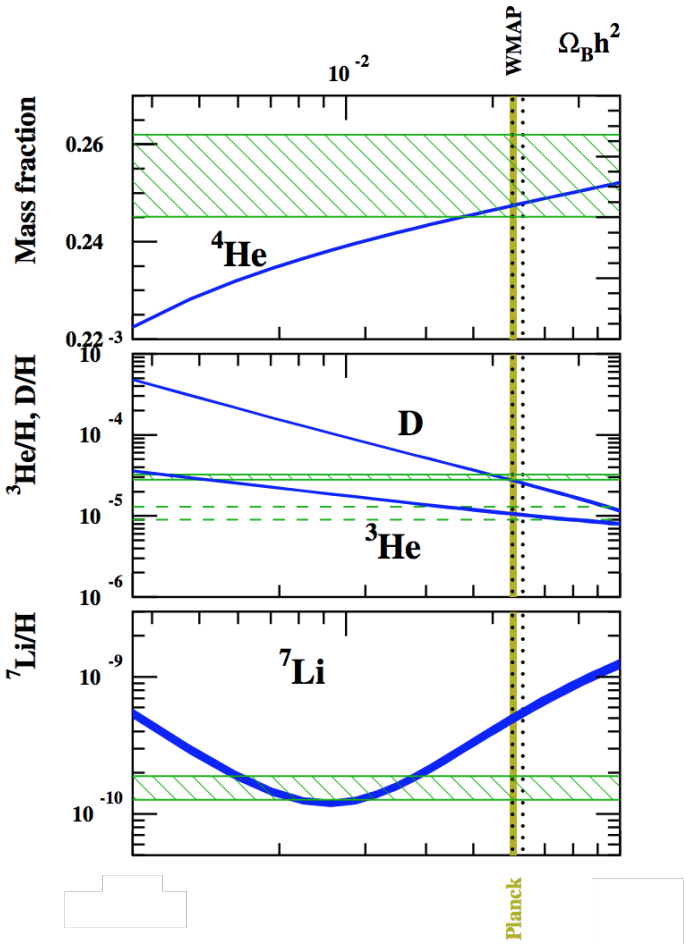

Figure 1.4: Light element abundances as a function of $\Omega_b h^2$, given as baryonic mass fraction (for ^{4}He) and relative to the ^{1}H mass fractions (for D, ^{3}He and ^{7}Li). The green shaded areas are the abundances as measured from spectroscopic observations. The blue curves show how the predicted abundances are expected to change with $\Omega_b h^2$, the thickness of which, represents the prediction uncertainty. The gold and dotted black lines show results from observations of the CMB by Plank [11] and WMAP [12], respectively. Image from [10].

$$\Omega_b = \frac{p_0}{p_{crit}} \tag{1.8}$$

p_0 in Eq. 1.8 is the current baryonic matter density and p_{crit} is the critical density given as,

$$p_{crit} = \frac{3H_0^2}{8\pi G} \tag{1.9}$$

where H_0 is the current Hubble constant and G is Newton's gravitational constant. Ω_b, in Figure 1.4, is multiplied by the normalising constant h, which is given as,

$$h = \frac{H_0}{100\,\mathrm{km\,s^{-1}\,Mpc^{-1}}} \tag{1.10}$$

It can be seen from Figure 1.4 that the observed abundance of D, ^{3}He and ^{4}He fits well with both the BBN prediction and the CMB measurement. The same conclusion can not be made for the ^{7}Li abundance, which is an unresolved question in cosmology known as the lithium problem. However, by only considering elements lighter than ^{7}Li, Figure 1.4 suggests that $\Omega_b h^2 < 0.024$, which for $H_0 = 70$ km s^{-1} Mpc^{-1} gives $\Omega_b < 0.05$. This result indicates that at least 95% of the total density of the Universe must be due to something other than baryonic matter, or, from another perspective, non-visible baryonic matter can not make up all of the missing matter predicted by the other means discussed in this chapter.

1.1.5 Cosmic Microwave Background

Arguably the most compelling evidence for the existence of dark matter comes from observations of the cosmic microwave background (CMB). This isotropic background is produced by photons that uncoupled from matter $\sim 4 \times 10^5$ years after the big bang. During this time, know as the era of recombination, temperatures were low enough for neutral atoms to form. This significantly reduced the amount of electron-photon scattering and allowed the majority of photons to traverse the Universe unimpeded.

The current CMB temperature has been measured as a near uniform 2.7 K [13]. However, small fluctuations in the CMB temperature have been measured, the latest (2018) of which comes from the Plank collaboration [11], and is shown by the temperature power spectrum given in Figure 1.5.

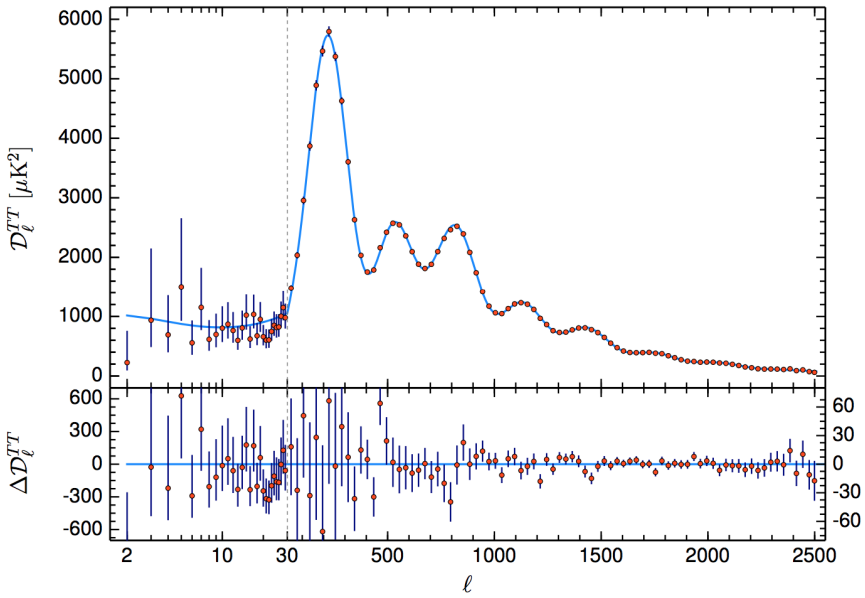

Figure 1.5: Upper panel: CMB temperate angular power spectrum, the x-axis gives the multipole number and the y-axis gives the temperature variation. Bottom panel: The residuals of the fitted line. Image from [11].

The x-axis on the above figure describes the angular separation, θ, between points in the sky, expressed in terms of the multipole number l,

$$l = \frac{180^{\circ}}{\theta} \tag{1.11}$$

The peaks in the data points shown in Figure 1.5 are found to be consistent with theoretical predictions of acoustic oscillations. These oscillations results from over dense regions of space that collapse inward under gravity and then expand back outward due to radiative pressure. The acoustic peaks of the CMB capture a snap shot of this process at the time of recombination. The first peak in Figure 1.5 corresponds to a compression under gravity, the second to a subsequent expansion and the third to another compression. After the first expansion, radiative pressure pushes the majority of baryonic mass away from the over dense regions. This means that the second compression (captured by the third peak in Figure 1.5) is mostly caused by the presence of non-baryonic dark matter, which does not experience radiative pressure. The odd and even numbered peaks, shown in Figure 1.5, correspond to regions of maximum (following a compression) and minimum (following an expansion) density, respectively. The more baryonic matter in the universe the greater the density is during compression, which enhances the odd peaks. By comparing the odd to even peak ratios and the height of the third peak to that predicted by theoretical models of the universe (each containing different amounts of baryonic and dark matter) the baryonic and dark matter densities, given by Eq. 1.12 and Eq. 1.13 respectively, can be obtained.

$$\Omega_b = \frac{\rho_b}{\rho_{crit}} \tag{1.12}$$

$$\Omega_{dm} = \frac{\rho_{dm}}{\rho_{crit}} \tag{1.13}$$

Where ρ_{crit} is the critical density given by Eq. 1.9. Results from the Plank collaboration, give present day estimates of $\Omega_b h^2 = 0.0224 \pm 0.0001$

and $\Omega_{dm}h^2 = 0.120 \pm 0.001$, where h is given by Eq. 1.10 with $H_0 = 67.4 \pm 0.5$ [11]. This result indicates that ∼84% of the total mass in the universe is dark matter.

1.2 Dark Matter Particle Candidates

The previous section explained some of the most prominent observations supporting the existence of dark matter. This section looks at the various theories, proposing a dark matter particle, consistent with these observations. The full extent of theoretically motivated dark matter candidates is not limited to the few cases discussed in this section. Instead, the aim here is to address the current most promising and popular dark matter hypotheses that are consistent with the standard model of cosmology, ΛCDM (Λ Cold Dark Matter) [14]. The model is well supported by the observations discussed in the previous section as well as n-body computer simulations of large scale structure formation in the Universe [15].

1.2.1 Axions

An outstanding question from the theory of QCD is the observed absence of CP (charge-conjugation and parity) violation during strong interactions, to provide a possible solution to this question a new particle, called an axion is required, which also provides a natural candidate for dark matter.

The standard model of particle physics presents no reason why CP should be conserved for the strong force and suggests that it's violation should be apparent from the observation of the neutron's electric dipole moment (nEDM). The nEDM is expected to exist due to the distribution of quarks (one up and two down) within the neutron. The particle, which has a radius of $\sim 1 \times 10^{-18}$ cm and a nuclear charge distribution of $\sim e$, would be expected to have an nEDM of $\sim 1 \times 10^{-18}$ e cm (e = elementary charge). However, to date, an nEDM has not been observed, with the latest result confining it to

$< 3.0 \times 10^{-26}$ e cm (90% CL) [16]. This suggests that either CP is conserved for the strong force or that the amount of violation is extremely small. A possible explanation for this comes from Peccei-Quinn theory [17], which adds a CP-violating term to the QCD Lagrangian, promoting the CP-violation from a constant value to a field that naturally inclines towards zero. The particle associated with excitations of this field was predicted by Weinberg [18] and Wilczek [19] in 1978 and was termed the axion. The Peccei-Quinn theory, therefore, potentially solves both the CP-violation problem and provides a possible explanation to the nature of dark matter.

The axion mass is predicted to be extremely small, on the μeV-meV scale, therefore, the particle is not expected to cause a detectable recoil event. Instead, the axion has a non-zero probability of converting into a photon, which can be detected, in the presence of a magnetic field [20]. This process, known as the Primakoff effect, is shown in Figure 1.6.

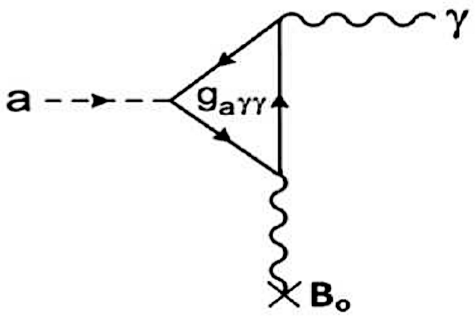

Figure 1.6: The conversion of an axion, a, into a photon, γ, due to the presence of a magnetic field, B. $g_{a\gamma\gamma}$ is the coupling constant for the interaction.

The Axion Dark Matter eXperiment (ADMX) [21] is currently looking for photons produced by the process shown in Figure 1.6. The experiment uses tuning rods to change the frequency of a magnetic field inside a microwave cavity. As the frequency is related to the axion mass, the experiment is able to look for axions of different mass by changing the field's frequency

over time. Figure 1.7 shows the current limits on axion dark matter set by ADMX and other axion experiments (solid lines), along with the predicted limits of future experiments (dashed lines). The results presented in this figure are projected over the axion mass and coupling constant phase space, the diagonal stripes show QCD model predictions for axion dark matter.

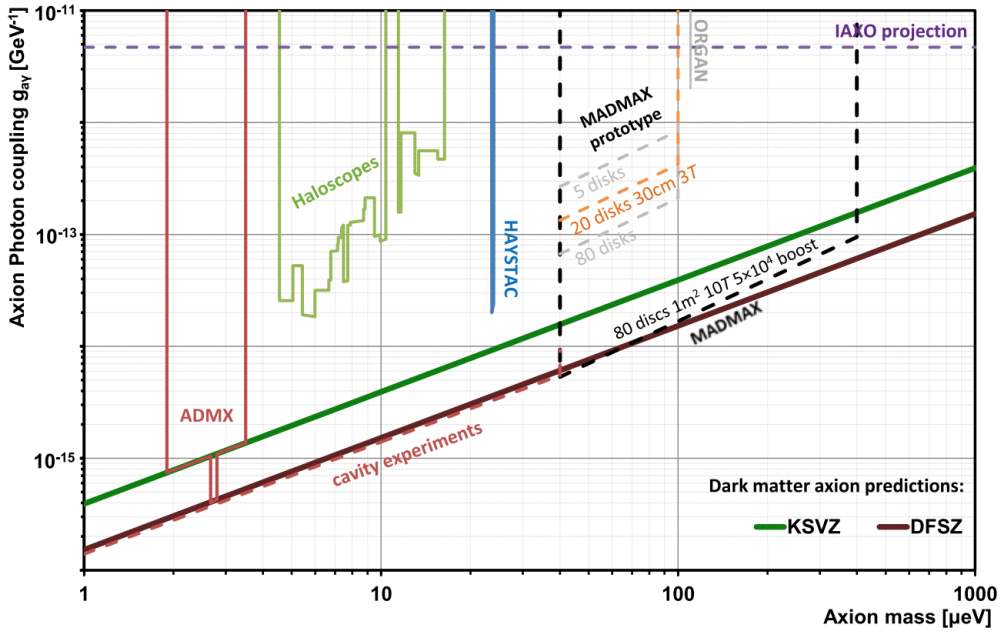

Figure 1.7: Current (solid lines) and predicted (dashed lines) limits on the axion mass and coupling constant for axion dark matter experiments. The two diagonal lines (labelled KSVZ and DFSZ) are predictions from QCD models. Image from [22].

1.2.2 Sterile Neutrinos

There are three neutrino types known to the standard model of particle physics (SM), these are e, μ and τ neutrinos, all of which interact via the weak force and gravity. A fourth type of neutrino is postulated which, unlike the other types, has avoided direct detection by only interacting gravitationally.

Due to it's lack of weak interaction, this fourth type is called sterile and it provides a plausible dark matter candidate.

It has been proven that neutrinos are able to change between the three different types, which is known as neutrino oscillations [23]. This evolution in time indicates that the particle does not travel at the speed of light and as a consequence must have mass. As the vast majority of neutrinos are relativistic, they are not consistent with the cold dark matter predicted by λCDM. However, because most particles within the SM have been shown to exhibit both left and right handed chiral versions, it is predicted that the neutrino should also have a right handed counterpart. The right handed (sterile) neutrino, could be much heavier than the known types and thus provide a candidate for dark matter. As with other right handed particles, the sterile neutrino would not interact weakly and it's presence must be inferred by other means. In October 2018 the mini Booster Neutrino Experiment (MiniBoonNE) combined it's data on neutrino oscillations with that of the Liquid Scintillator Neutrino Experiment (LSND) to show an ν_e and $\overline{\nu}_e$ excess at a 6.1 σ significance level [24]. For a two-neutrino oscillation, it was concluded that the excess would require four different neutrino types, suggesting that sterile neutrinos could have been involved in the oscillation process. Future neutrino detectors, such as the Short-Baseline Neutrino Detector (SBND), will be able to investigate this finding further.

1.2.3 Weakly Interacting Massive Particles

The Weakly Interacting Massive Particle (WIMP) is not necessarily confined to a particular theory, instead, it describes a generic particle that is consistent with λCDM. To fit this model, the WIMP is predicated as being non-relativistic, neutral, massive, stable and weakly interacting. The interaction scale arises from predictions of the dark matter abundance, such that, if the annihilation cross section for a dark matter–anti-dark matter interaction was larger than the weak scale, there would be less dark matter than inferred

from observations [25]. Multiple theories that go beyond the standard model of particle physics (SM) predict the existence of WIMP like particles. Two of the most promising of these theories are discussed here.

Minimal Supersymmetric Standard Model (MSSM)

The Minimal Supersymmetric Standard Model (MSSM) is a version of SUperSYmmetry (SUSY) that predicts the existence of a WIMP particle called the neutralino. SUSY predicts a heavier type of each standard model (SM) particle that are bosons if their SM partners are fermions and visa versa, as shown by Figure 1.8.

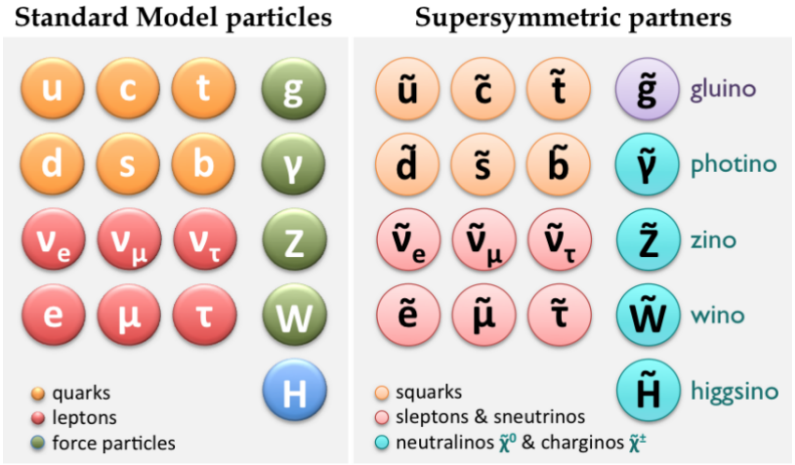

Figure 1.8: The standard model particles and their predicted SUSY partners.

MSSM is the simplest version of SUSY that introduces the least amount of particles required to solve the hierarchy problem associated with the Higgs mass. The problem arises from quantum loop corrections to the boson's mass, which are required due to it's interactions with massive virtual particles such as the W boson [26]. The model produces supersymmetric partners to the SM virtual particles that cancel the quantum corrections and produce a Higgs mass of < 130 GeV c^{-2}. In 2012 the ATLAS detector of the Large Hadron

Collider (LHC) published a finding consistent with a Higgs boson mass of 126.0 $\pm$0.8 GeV c^{-2} [27]. This result is within the bounds predicted by MSSM and, therefore, provides evidence in support of the theory.

MSSM introduces a parity called R-parity, P_R, which is a combination of the baryon (B), lepton (L) and spin (s) quantum numbers and is given as [28],

$$P_R = (-1)^{3B+L+2s} \tag{1.14}$$

Conservation of P_R prevents the lightest supersymmetric particle (LSP) from decaying into SM particles, making the LSP stable. MSSM also predicts that the LSP is a neutralino (see Figure 1.8), making it neutral, and has a mass between 100 GeV c^{-2} - 1 TeV c^2, making it non-relativistic. All of these predictions are consistent with the WIMP criteria outlined at the start of this section. SUSY is not the only symmetrical theory to predict new particles and solve the hierarchy problem. Little Higgs theories also predict additional particles, including less massive versions of the Higgs boson, along with a parity conservation, called T-Parity [29]. Like the neutralino from MSSM, the lightest particle from little Higgs theories is made stable by T-parity conservation and produces a WIMP candidate.

Universal Extra Dimensions Theory

Universal Extra Dimensions (UED) theory predicts the existence of particles, heavier than SM particles, that exist in higher dimensions. The lightest of these is stable and provides a dark matter candidate.

The existence of extra dimensions, beyond the four described by general relativity, was first proposed by Kaluza in 1921 [30]. Kaluza postulated the existence of a fifth dimension that would unify the forces of gravity and electromagnetism (the only known forces at the time). A quantum interpretation

of the theory, now called Kaluza-Klein (KK) theory, was later provided by Klein in 1926 [31], who suggested that motion through a tiny compact circular fifth dimension gives rise to charge quanta. UED is an adaptation of KK that allows for multiple compact extra dimensions, through which, all standard model fields can propagate [32]. UED states that a particle at rest inside an extra dimension appears in four dimensions as a standard model particle (SM). Whilst, a particle with motion inside an extra dimension creates heavier KK-particles in four dimensions, which acquire mass energy due to their higher dimension motions. A KK parity, P_{KK}, (analogous to R-parity in supersymmetry) was introduced to UED [33] and is given as,

$$P_{KK} = (-1)^n \tag{1.15}$$

where n is the KK mode corresponding to the mass of the KK particle. SM particles are predicted by the theory to have, n = 0, so that for SM particles, $P_{KK} = 1$. The conservation of P_{KK} has the consequence that the lightest KK particle (LKP), with n = 1 and P_{KK} = -1, can not decay to a SM particle. Therefore, the LKP is stable and provides a viable WIMP candidate.

1.3 Conclusion

The evidence described in this chapter shows that, since the first discoveries made in the early part of the 20^{th} century, the case for the existence of dark matter has only strengthened. Based on this evidence, it seems indisputable that the vast majority of dark matter is non-baryonic and constitutes most of the mass of the Universe. Although other dark matter candidates exist, the WIMP hypothesis is supported by multiple different theories and, therefore, seems to be the most promising. For this reason, the detection of WIMP dark matter is the main subject of the remainder of this thesis.

Chapter 2

WIMP Dark Matter Detection

There are three different methods employed in the detection of WIMP dark matter particles. The first attempts to create the particles from energetic collisions inside an accelerator, such as the LHC based at the European Organization for Nuclear Research (CERN) in Geneva, Switzerland. The latest search results from the LHC are presented in Section 2.1. The second is to indirectly detect WIMPs from the particles produced as a consequence of dark matter–anti dark matter annihilation or from dark matter decay, results from this method are discussed in Section 2.2. The third is to directly detect a rare baryonic–WIMP interaction. As this method is the main subject of this thesis, an extended review of direct detection results is given in Section 2.3.

2.1 Creation at the LHC

The LHC searches for dark matter with the ATLAS, CMS and LHCb detectors, all of which attempt to create dark matter particles via high energy (up to 13 TeV) proton collisions [34]. As the momentum of the proton beams is in the longitudinal direction, conservation of momentum states that the total transverse momentum is zero both before and after the collision. The

LHC looks for an excess in missing transverse momentum, after the collisions, above that expected from SM particles (neutrinos). This would indicate the presence of new particles, such as dark matter. The LHC also looks for an excess in SM particles, which would appear as a resonance peak above background. This peak could be attributed to either the decay of dark matter mediators, into SM particles, or to the creation of SM particles in conjunction with dark matter. Figure 2.1 shows Feynman diagrams for dark matter produced by a mediating particle (left) and directly from a SM particle collision (right).

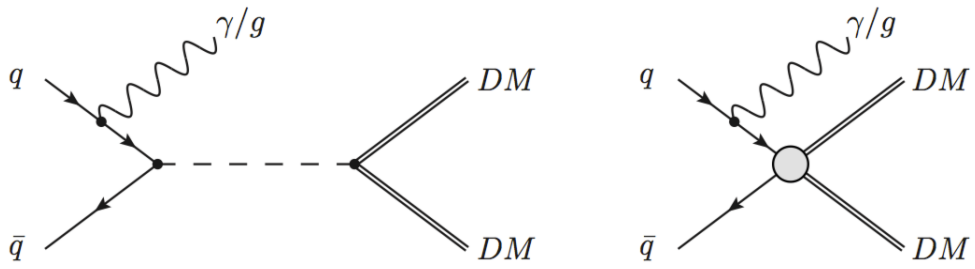

Figure 2.1: Feynman diagrams of dark matter produced by a particle mediating between the SM and non-SM (left) and directly from the collision of SM particles (right). Figure from Ref [35].

The predicted amount of missing transverse energy and SM excess, as well as the type and number of possible mediator particles, depends on the theoretical model under investigation. This enables the LHC to test the predictions of different theoretical models, for which, none have yet resulted in a dark matter discovery [36]. As an example of a model dependent search result, a WIMP mass vs cross section exclusion limit is given in Figure 2.2 for a model in which the dark matter mediator is a Z like boson and the dark matter particle only interacts with leptons. The result shown in this figure is from run 2 of the LHC with the ATLAS detector. For comparison, the figure also includes exclusion curves for some of the world leading direct detection experiments.

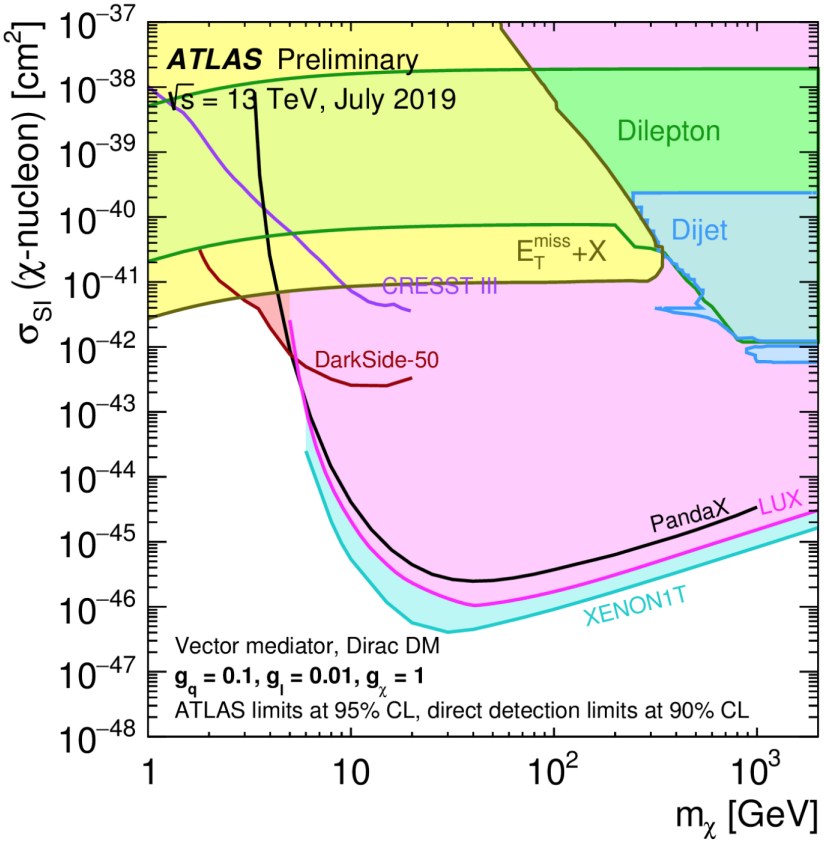

Figure 2.2: Spin-independent exclusion curve result from run 2 of the LHC, using the ATLAS detector, for a dark matter model in which the dark matter particle interacts only with leptons and the mediating particle is a Z like boson. E^T_{miss}+X = events with missing transverse energy and a highly energetic event or "jet" (X) in the transverse direction. Dijet = events with two times X. Dilepton = events with a lepton and anti-lepton pair of the same flavour. Shown for comparison are direct detection results from CRESST III, DarkSide-50, Panda-X, LUX and XENON1T (all of which are discussed in Section 2.3). Figure from [34].

If the LHC were to identify a signal originating from a non-SM particle, it would not be able to establish it as dark matter as the particle's traversal time through the detector would be too short to confirm that it is stable. Instead, a model dependent LHC result would help guide direct and indirect dark

matter search experiments. Although the search, so far, has not revealed a possible WIMP particle, there are still many theoretical models to investigate and the LHC improvements, made for run 3 and run 4, are expected to significantly increase the amount of available data [37].

2.2 Indirect Detection

Dark matter–anti-dark matter annihilation and dark matter decays are, on average, expected to be extremely rare, otherwise the dark matter density would not have been stable enough for large scale structures to form. However, by studying locations across the Universe with a high gravitational field, and therefore a significant dark matter number density, these events could potentially be inferred from an excess in SM background. The main excesses looked for are from high energy γ-rays, neutrinos and charged cosmic rays originating from the Galactic centre, nearby dwarf galaxies, the Sun and the Earth's centre. This allows any experiment capable of detecting these sources to take part in the indirect search for dark matter. For a full review of indirect searches looking for an excess in γ-Ray emissions see Ref. [38], for an excess in neutrinos see Ref. [39] and for an excess in charged cosmic rays see Ref. [40]. The following discusses two possible cases of an observed excess in the γ-ray and cosmic ray backgrounds.

After taking into account the expected γ-ray emissions originating from the Galactic centre, the Fermi Large Area Telescope (Fermi LAT) reported a residual contribution to the γ-ray flux, between 1-100 GeV, which could be evidence of an excess produced by dark-matter annihilation [41]. Although the source of the residual excess is not conclusive, a detailed scrutinisation of the Fermi LAT data, using high-resolution maps, indicated that the residual excess can not be explained by known phenomena and is consistent with WIMP particles, of mass 36-51 MeV c^{-2}, annihilating to $b\bar{b}$ [42]. Figure 2.3 shows a high resolution image of the raw γ-ray flux from the galactic centre

(left) and the residual flux remaining after subtracting the expected background (right).

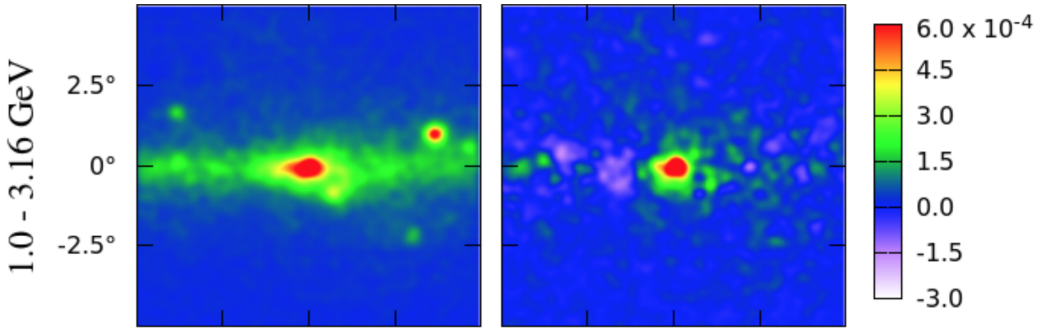

Figure 2.3: High resolution γ-ray images of the Galactic centre. The raw flux is shown on the left and the residual flux is shown on the right, both measured in units of photons cm^{-2} s^{-1} sr^{-1}. Images from [42].

A positron excess from cosmic-rays was discovered by the PAMELA (Payload for Antimatter Matter Exploration and Light-nuclei Astrophysics) detector, which was attached to the Resurs DK1 satellite in Earth orbit. This result can be explained by a dark matter annihilation model in which the product is a new light boson that decays to produce the positron excess [43].

2.3 Direct Detection

Direct detection aims to observe an interaction event between a WIMP and SM particle. As an example, this could occur via a mechanism similar to, or the same as, neutral current exchange. After an event, a WIMP particle would deposit a portion of it's energy to a target nuclei, which would subsequently recoil and produce ionisation, light emission and/or phonon vibrations in the target material. The following describes methods to detect these signals using crystal (Sections 2.3.1 and 2.3.2), noble liquid (Section 2.3.3) and low pressure gas targets. As the latter is the focus of this thesis, an

extended review, of the latest developments towards this method, is given in Section 2.4. Other techniques being employed to directly detect dark matter are described in Section 2.5.

2.3.1 Cryogenic Crystal Detectors

Crystal detectors, maintained at close to zero Kelvin, are extremely sensitive to the minute changes in temperature caused by a particle interaction within the crystal. For semiconducting Ge or Si crystals, the temperature change can be detected by the associated change in resistivity of a connected bolometer. These type of experiments are also able to detect ionisation, caused by a recoil event, using an applied electric field to drift ionised charge onto a collection plate. After shielding the detector from most of the outside radiation, the remaining events can be distinguished as either an electron (background) or nuclear (possible signal) recoil from the ratio of the event's ionisation and phonon signal. The CDMS-II (Cryogenic Dark Matter Search) detector, located at the Soudan Underground Laboratory (SUL), employed these methods to look for low mass WIMPs (< 10 GeV) utilising 19 Ge and 11 Si based crystals, with a total mass of 230 g and 100 g, respectively. In 2013, CDMS-II reported the observation of three signal events within their Si crystals and used a likelihood test to show a 0.19% chance that these were background [44]. However, this result conflicts with the null-findings from the CDMS-II Ge crystals as well as the Ge crystals used in the next generation SuperCDMS detector, located at SUL [45]. The CDMS collaboration are now planning to test the Si result by introducing crystals of the same material into the SuperCDMS detector, which will be moved to the Sudbury Neutrino Observatory (SNOLAB) to provide a greater rock overburden than at SUL and, therefore, increased shielding from the cosmic ray background [46].

Other low energy crystal experiments include: CRESST (Cryogenic Rare Event Search with Superconducting Thermometers) located at Laboratori

Nazionali del Gran Sasso (LNGS), the EDELWEISS (Expérience pour DEtector Les WIMPs En Site Souterrain) experiment located at Modane underground laboratory and CoGeNT (Coherent Germanium Neutrino Technology) located at SUL. CRESST uses $CaWO_4$ crystal targets and CRESST-III is predicted to achieve a recoil threshold of less than 100 eV [47]. EDELWEISS-III, is a next generation dark matter detector using germanium crystals and is predicted to achieve a threshold of a few keV and below [48]. These types of experiments are some of those leading the way with regards to low mass dark matter searches. As a consequence, they are subject to the higher background levels found at lower recoil energies, which can be difficult to model accurately. For example, the CoGeNT experiment originally reported an excess of recoil events below 3 keV, consistent with both the CDMS-II and DAMA/LIBRA results (see Section 2.3.2) [49]. However, closer scrutiny showed that these events were most likely background [50].

2.3.2 Annual Modulation Detectors

In addition to the cryogenic searches described in the previous section, crystal detectors are also being emlpoyed to detect a dark matter annual modulation signal, first predicted in 1985 [51]. As the Sun orbits the Galactic centre it passes through the dark matter halo, which manifests as a 'WIMP wind' in the Earth's frame of reference. During the Earth's orbit, the speed of the WIMP wind modulates as the Earth's velocity component parallel to it first opposes and then aligns with the WIMP wind direction. This process is depicted in Figure 2.4.

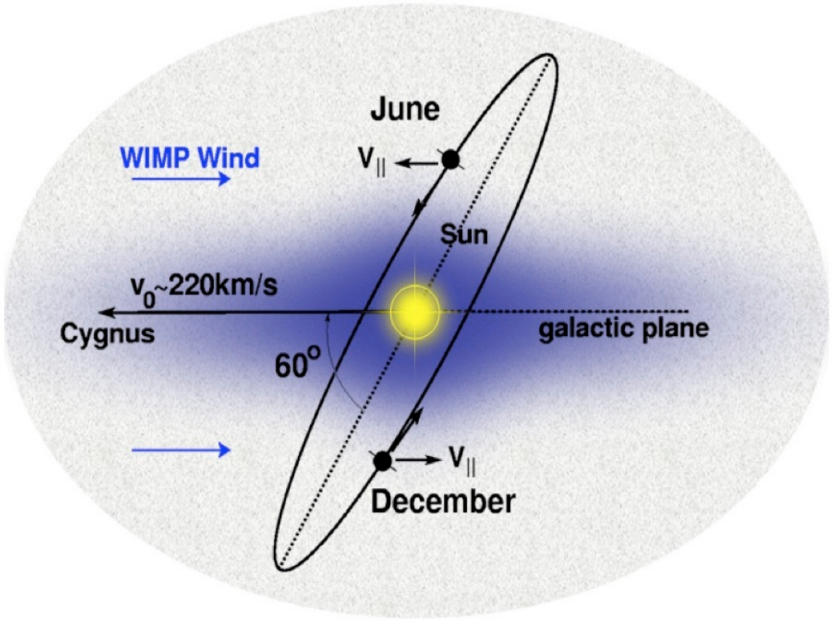

Figure 2.4: The WIMP wind velocity magnitude is higher in June when the Earth's velocity component parallel to the WIMP wind is in the opposite direction and lower in December when the contrary is true. Image accredited to the Sheffield Dark Matter Research Group.

The modulation should be detectable as a corresponding modulation in the recoil energy of a target nuclei. The DAMA/LIBRA experiment uses the light scintillation caused by recoiling nuclei within NaI(Tl) (Thallium doped Sodium Iodine) crystals to look for this signal. The light is collected by Photo-Multiplier Tubes (PMTs) surrounding $\times 25$ 9.7 kg crystals, shielded from outside radiation by a combination of concrete, Cu, Pb, Cd, polyethylene and paraffin shield layers. DAMA/LIBRA reports an annual modulation seen in the 2-6 keV energy region at a 12.9 σ confidence level [52]. The data, shown by Figure 2.5, was collected by the experiment over 2 phases, totalling 14 annual cycles, and is reported to be consistent with the modulation predicted due to the presence of a dark matter halo.

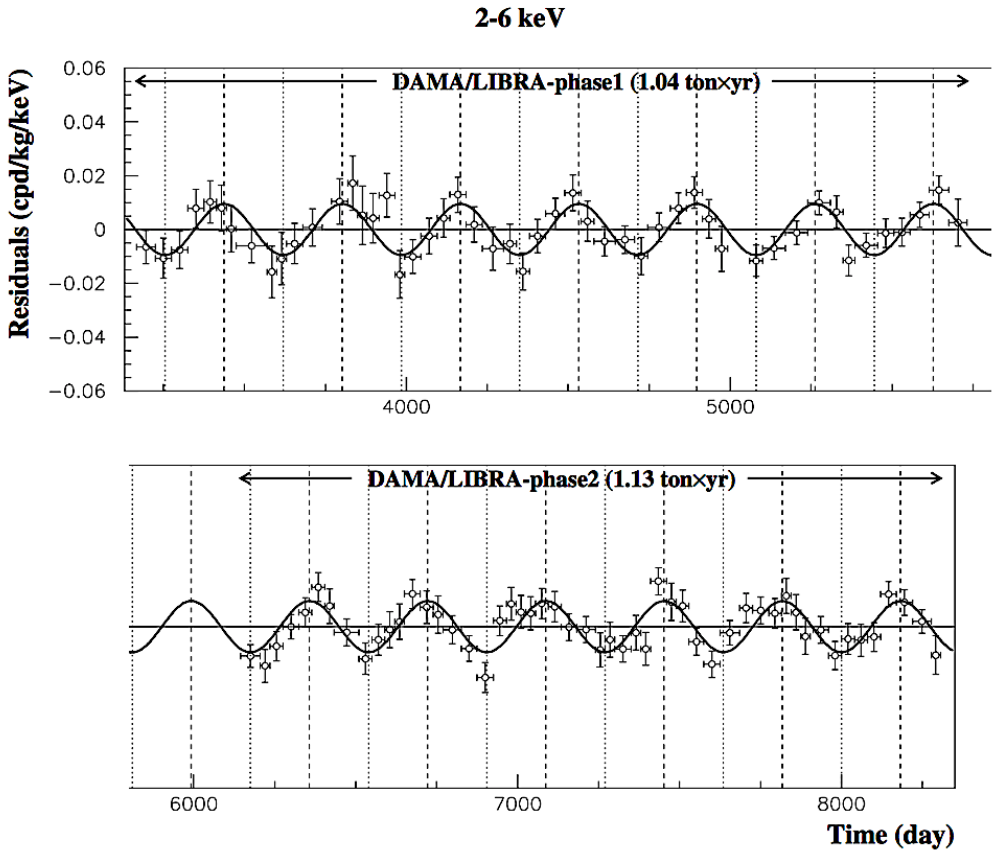

Figure 2.5: The annual modulation observed by phase 1 (top) and phase 2 (bottom) DAMA/LIBRA runs, totalling 14 annual cycles of data taking. The curve is a sinusoidal fit to the data. Figure from [52].

The DAMA/LIBRA result is in contrast to multiple null-findings, reported for the same parameter space, by most of the other experiments described in this chapter. The COSINE-100 detector, located at the Yangyang underground laboratory in South Korea, was established to test the DAMA/LIBRA result by replicating the experiment as closely as possible. The detector measured the light scintillation observed in $\times 8$ NaI(Tl) crystals (totalling 106 kg). After the first 59.5 days of data taking, the COSINE-100 collaboration reported no signal excess above background and were, therefore, able to

disclude spin-independent WIMP nucleon interactions from being the source of the signal observed by DAMA/LIBRA [53]. After a total of 1.7 years of data taking, the COSINE-100 experiment was able to look for the annual modulation reported by DAMA/LIBRA. The results, shown in Figure 2.6, is consistent with both the null-hypothesis (no signal modulation) and the observed DAMA/LIBRA modulation [54].

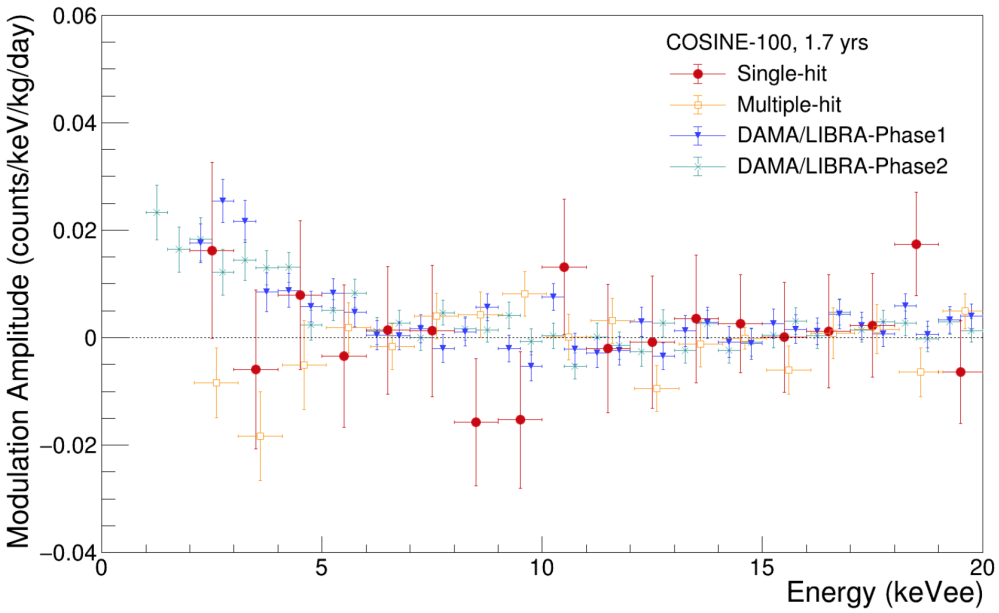

Figure 2.6: Annual modulation as a function of recoil energy for the COSINE-100 result after 1.7 years of data taking. Also shown is the multi-hit results from the COSINE-100 background and the phase 1 and 2 DAMA/LIBRA results. Image from [54].

The COSINE-100 experiment is currently taking data using an improved event selection and plans to reduce the energy threshold to 1 keV. This will allow the experiment to test the DAMA/LIBRA signal to a 3σ significance within the next five years [54].

2.3.3 Noble Liquid Detectors

Direct detection search experiments with noble element targets either use liquid xenon (LXe) or liquid argon (LAr), both of which produce scintillation and ionisation signals. A detailed comparison of the two target types is given by Ref. [55], here, their main advantages are summarised. The benefits of LXe include: it's high atomic mass (131.3, compared to 40 for LAr), which presents a large WIMP target and provides significant self shielding; the lack of radioactive isotopes (for example, LAr includes the radioactive isotope ^{39}Ar); unlike LAr, no wavelength shifters are required to see the scintillation light. The benefits of LAr include: it can be procured straight from the atmosphere, making it much more readily available and, therefore, cheaper to acquire; it allows for better pulse shape discrimination.

Most Noble liquid detectors use a dual-phase process, shown in Figure 2.7, to discriminate between electron recoil backgrounds and nuclear recoils.

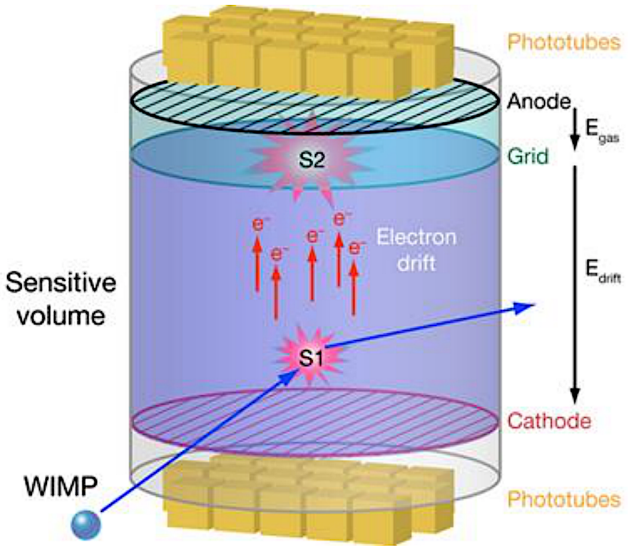

Figure 2.7: Dual phase signal process, used by most noble liquid detectors. S1 occurs in the liquid volume and S2 occurs in the gas phase as a result of drifting ionised electrons. Figure from [56].

The dual-phase process, shown in the above figure, involves the observation of two separate light scintillation signals, the first of which (S1), is due to the primary recoil occurring in the liquid volume. The recoil also ionises electrons, which are drifted by an electric field to a gas phase of the detector where they produce a second light scintillation signal (S2) via the process of electroluminescence. The ratio of S1 and S2 is then used to classify the observation as either background or signal.

Notable experiments that use the dual-phase process in LXe are: the Large Underground Xenon experiment (LUX) located at the Sanford Underground Research Facility (SURF), XENON1T located at LNGS and PandaX-II located at China's Jinping Underground Laboratory (CJPL). All of which are yet to detect a dark matter signal and as a result have set world leading exclusion limits on the WIMP mass and cross section, as reported by Ref. [57] (LUX), [58] (XENON1T) and [59] (PandaX-II). Each experiment also has a planned next generation detector, which will take their target masses beyond the 2 tonnes currently achieved by XENON1T. LUX will join with the ZEPLIN collaboration to build LZ [60], XENON1T will be expanded to XENONnT [58] and the PandaX collaboration are planning to build PandaX-4T [61].

An example dual-phase LAr detector is DarkSide-50, located at LNGS, which also uses pulse shape discrimination to determine signal from background [62]. The Dark Matter Experiment using Argon Pulseshape discrimination (DEAP-3600) uses a combination of pulse shape discrimination and ultra-pure LAr to overcome the ^{39}Ar background without having to use a dual-phase design. The large target mass of DEAP-3600 (3.6 tonnes) meant that it was able to set competative exclusion limits, for spin-independent WIMP interactions in LAr, after just 4.4 days of data taking [63].

2.4 Low Pressure Gas TPCs

As mentioned in Section 2.3.2, there exists a WIMP wind in the Earth's frame of reference due to it's motion around the Galactic centre. The WIMP wind, originating from the constellation of Cygnus, could be detected in a low pressure gas TPC that is able to reconstruct the direction of WIMP induced nuclear recoils. A signal consistent with the WIMP wind would be distinguishable from an isotropic background, and therefore, would provide an unambiguous dark matter detection.

The main subject of this thesis is the direct detection of Spin-Dependant (SD) WIMP dark matter using a gas Time Projection Chamber (TPC). Therefore, the following provides a detailed review of the current progress, in gas TPC technology, towards this goal.

2.4.1 Recoil Axial Signature and Head-Tail Effect

This section describes the components of a recoil track, produced inside a gas TPC, used to derive an incident particle's direction. Reconstruction of the recoiling nuclei gives information regarding the incident particle's orientation with respect to the WIMP wind, which is called the axial directional signature [64]. The vector direction, towards or away from the Cygnus constellation, of the recoiling nucleus can be deduced from the ratio of ionised charge in the first half of the track to that of the second, which is called the head-tail effect (HT) [65]. Nuclear recoils are expected to deposit more ionisation charge at the beginning of the recoil than at the end, producing a positive HT along the direction of motion. Figure 2.8 shows HT measurements, made with the DRIFT-IId (Direction Recoil Information From Tracks) dark matter detector, using neutrons from a ^{252}Cf source to mimic the WIMP wind [65].

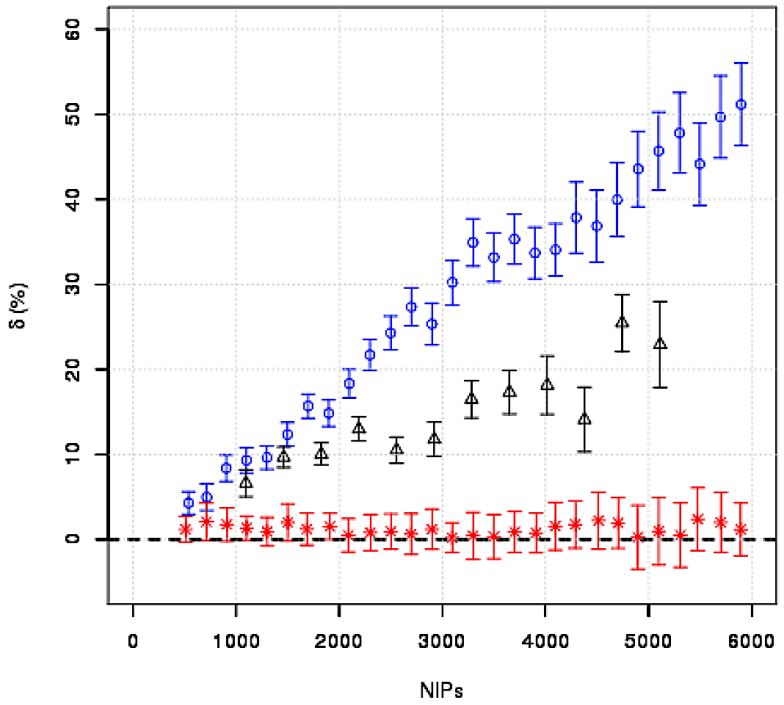

Figure 2.8: HT measured with DRIFT-IId, given as a percentage, δ, (rather than a ratio) and plotted against recoil energy, expressed as Number of Ionised Pairs (NIPs). The blue circles show measurements of nuclear recoils in a gas mixture of CS_2, CF_4 and O_2. The red stars show measurements made in the same gas mixture but for recoils parallel to the readout and the black triangles show measurements of nuclear recoils in pure CS_2 gas. Figure from [65].

The blue and black points in Figure 2.8 show the presence of HT, which is shown to increase in magnitude with recoil energy. The improved HT effect, shown by the blue points in Figure 2.8, is attributed to the addition of lighter fluorine molecules (compared to sulfur), which produce longer recoil tracks and, therefore, a more clearly defined charge distribution [65]. HT is measured in the drift direction so for recoils parallel to the readout no effect is expected, as shown by the red points in Figure 2.8. This can be used to check that the asymmetry is due to HT and not some other influence, such

as the readout electronics, which would be apparent regardless of the recoil's orientation. Ref. [66] used Monte Carlo simulations of recoils, induced within a directional detector, along with null-hypothesis tests of isotropy to establish the number of events required to confirm a signal consistent with the WIMP wind (at a 90% CL). This resulted in a prediction of $\mathcal{O}(10)$ required events with both axial and HT information and an order of magnitude higher number of required events with the absence of HT.

2.4.2 Background from Coherent Neutrino Scattering

As next generation detectors become increasingly sensitive to low mass and low interaction cross sections, coherent neutrino-nucleus scattering (as recently observed by the COHERENT collaboration [67]) will produce an additional background for dark matter searches. This background, from solar, atmospheric and DSNB (Diffuse Supernova Neutrino Background) neutrinos, is shown in Figure 2.9 as a function of mass and cross section. The figure also includes some of the latest results from SD WIMP search experiments. As shown in Figure 2.9, a xenon target is more sensitive to nucleus-neutrino scattering than a fluorine target. This is due to the coherent nature of the interaction, which causes the neutrino-nucleus cross section to scale as A^2, where A is the atomic mass number. For a xenon nucleus, A = 131, whilst for fluorine, A = 19.

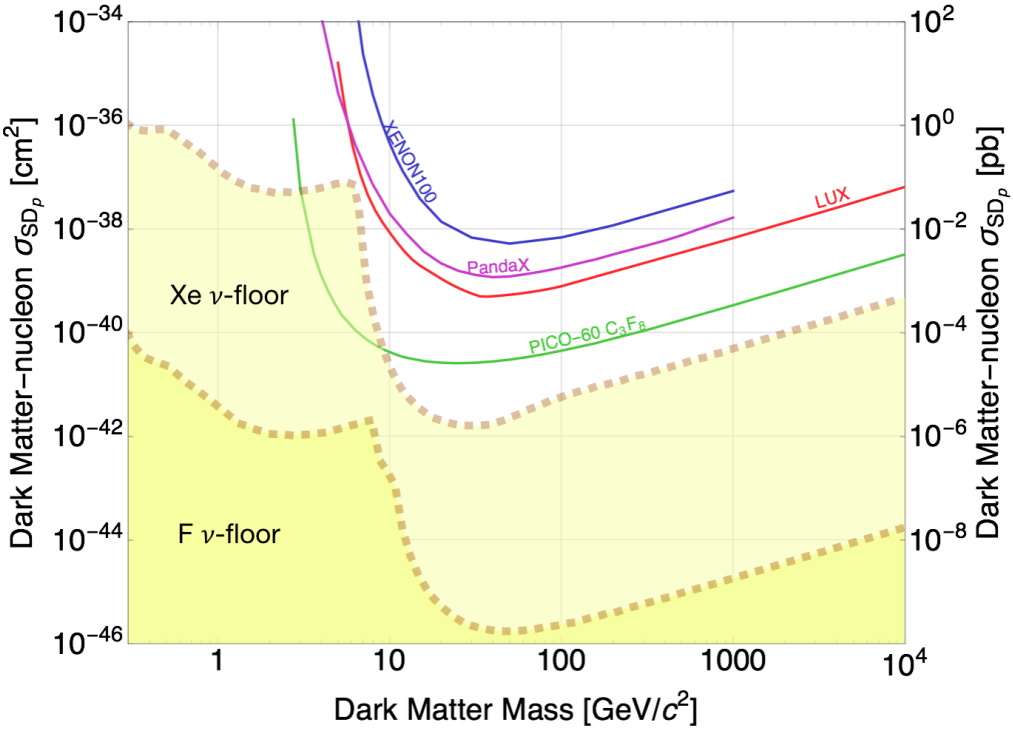

Figure 2.9: WIMP exclusion limits for some of the current SD dark matter detectors, showing the expected neutrino floor for a Xe and F target.

It can be seen from Figure 2.9 that dark matter detectors are starting to push towards a search parameter space with a neutrino background (AKA the neutrino floor). For solar neutrinos, shown by the large bump in the neutrino floor on the left side of Figure 2.9, the background would be non-isotropic and, therefore, distinguishable from that of a WIMP signal inside a directional detector. Figure 2.10 shows the differential event rate distribution across the sky for ^{8}B neutrinos originating from the Sun and for the expected WIMP wind. The figure shows that the two different signals remain separated throughout the year.

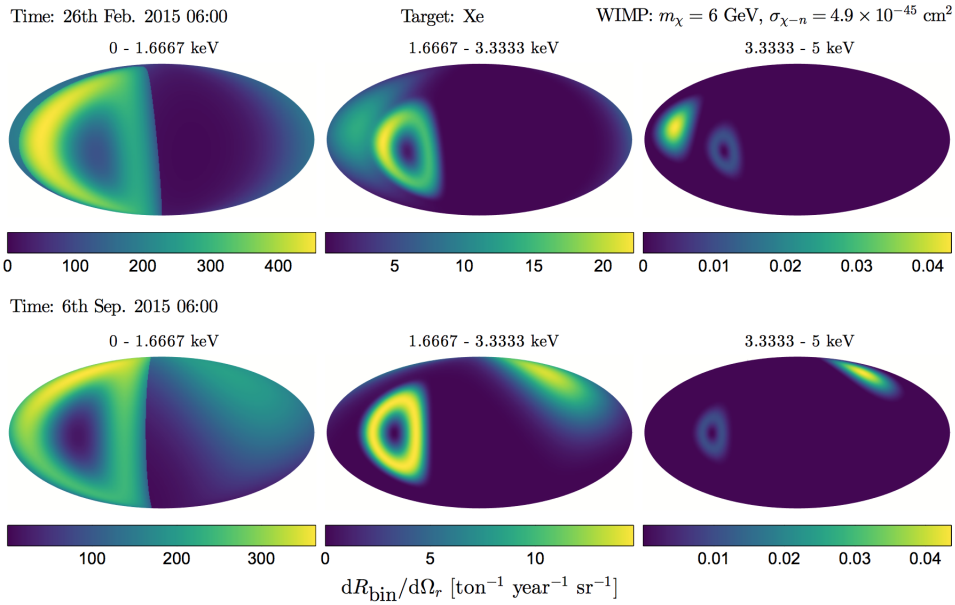

Figure 2.10: Sky map of the expected WIMP wind and solar neutrino (^{8}B) differential event rate. The WIMP contribution is on the left and right of the bottom and top rows, respectively. Figure from [68].

The non-isotropic WIMP wind signal could also potentially be observed above isotropic neutrino backgrounds, such as that caused by the DSNB and atmospheric neutrinos.

2.4.3 Negative Ion TPCs and Fiducialisation

Recent R&D, regarding the ideal gas target for dark matter searches, has shown that the negative ion gas, SF_6, has many of the required properties [69]. These properties are introduced here in the context of DRIFT-IId, which uses a gas mixture of CS_2, CF_4 and O_2. It is then shown that these properties are apparent in SF_6 gas, for which it is argued, makes a more suitable choice for dark matter searches.

A TPCs function is to drift ionised electrons, produced by a recoil event for example, through the gas volume of the detector and on to a signal

collection point. For the DRIFT-IId detector, the positive electron affinity of CS_2 causes ionised electrons to attach to the gas molecule and create negative ions. As the anions are transported by the drift field they diffuse at the thermal limit, an amount of diffusion equivalent to thermal motion. This significantly reducing the amount of diffusion compared to electron drift [70]. The heavier ions also have a slower drift speed, resulting in a detectable difference in the 'time of arrival' between different points of ionisation (for events with a component perpendicular to the readout), which can be used to reconstruct the track in the drift direction. CF_4 gas is included in DRIFT-IId for it's fluorine content, which having a spin value of 1/2, provides a SD target for WIMP interactions [71]. The small amount of oxygen, added to the gas mixture, causes the negative ions to group into separate 'species' of anions with slightly different drift velocities. This causes a delay between the anion species' arrival times at the TPC anode, resulting in a signal with a main peak and three other 'minority' peaks [72]. The difference in anode arrival time, t, between these peaks and the measured drift velocities of the anion species, v, are used to establish the drift distance, z, travelled by the ionised charge [73],

$$z = (t_a - t_b)\frac{v_a v_b}{(v_b - v_a)} \tag{2.1}$$

where a and b are two different peaks. Knowing the z position of the ionisation event, enables DRIFT-IId to achieve fiducialisation in the drift direction [72].

The presence of a minority peak has been proven to exist in SF_6 [69], suggesting that z fiducialisation is possible with this gas. Figure 2.11 shows the main SF_6^- peak and a smaller minority peak, attributed to SF_5^-.

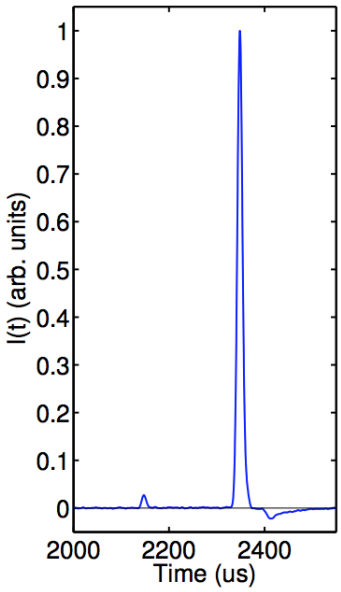

Figure 2.11: The main SF_6^- peak along with a secondary SF_5^- peak, from [69].

The SF_6^- peak also provides anion drift, analogous to CS_2 in the DRIFT-IId gas mixture, allowing for track reconstruction along the drift direction in SF_6 gas. Advantages of using SF_6, over the DRIFT-IId gas mixture, is the higher SD fluorine target available compared to CF_4. The SD target is also increased by not having to use additional (non-SD) gases to provide anion drift and z-fiducialisation. A further advantage is the non-toxicity of SF_6, making it safer and easier to handle than CS_2. The disadvantages of using SF_6 is it's high CO_2 equivalence, making it a significant polutant, and the lower gas gains achieved as a result of the molecule's high electron affinity. The former can be mitigated by cleaning and recirculating the SF_6 gas and the latter can be mitigated using specially designed electron amplification devices, both of these methods are described below.

SF_6 Cleaning and Recirculation

Impurities, such as water oxygen and nitrogen, can accumulate over time within the SF_6 target gas volume. These impurities lower the breakdown voltage of the gas, causing a degradation in gain performance. Cleaning the gas and recirculating it back into the detector would prolong it's usable lifetime and prevent the need to replace the gas volume on a regular basis. After a period of time, at which the gas has become significantly degraded, it can then be captured and disposed of, preventing it's release to atmosphere. R&D towards the cleaning and recirculation of SF_6 has shown that radon impurities, which cause an additional background inside the TPC, can be reduced using 5 Å sieves cooled in dry ice [74], as shown in Figure 2.12.

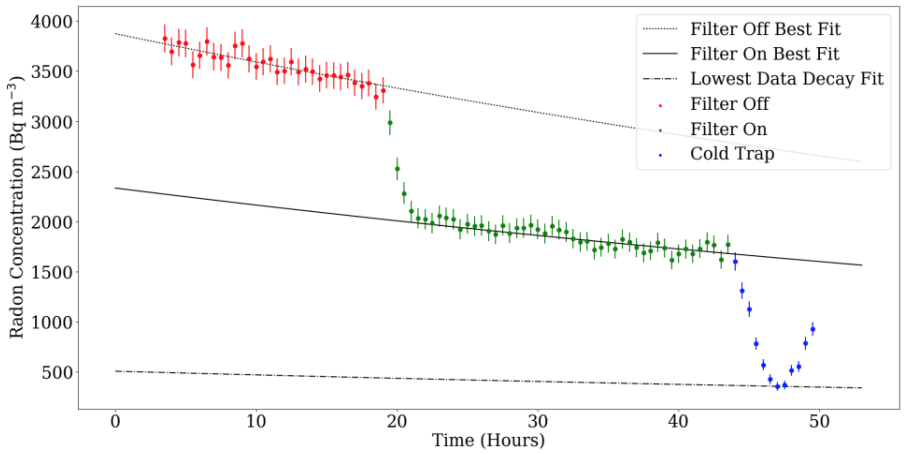

Figure 2.12: The radon reduction achieved by recirculating SF_6 through a 5 Å molecular sieve. Red, green and blue show the radon levels for the sieve off, on and on surrounded by dry ice, respectively. Plot from [74].

The above figure shows a radon reduction factor of ∼2 and ∼8 with the sieve on and with the sieve on and surrounded by dry ice, respectively. The up turn in contamination towards the end of the plot is due to an increase in the dry ice temperature over time. Further R&D efforts are ongoing, using

similar methods, towards the reduction of the other impurities mentioned at the start of this section.

Electron Multiplication with Micro-Pattern Gaseous Detectors

To strip ionised electrons from SF_6^- anions, so they can be collected at the readout, a high electric avalanche field is required before the readout stage. In order to achieve signal amplification in the gas (gain), the avalanche field needs to be high enough to impart the stripped electron with sufficient energy to cause additional ionisation and prevent re-attachment. The high avalanche fields required can be implemented using a type of Micro-Pattern Gaseous Detector (MPGD) called a Gaseous Electron Multiplier (GEM) or a Thick Gaseous Electron Multiplier (ThGEM). Both of these MPGDs are made from three layers: two thin copper layers astride a central insulating layer made from such materials as FR4 or Kapton. GEM's are around 50 μm thick and ThGEMs are usually between 0.4 and 1 mm thick. In both cases the majority of the thickness is due to the insulating layer, with the copper layers being $\sim$5 and $<$ 100 μm thick for GEMs and ThGEMs, respectively. Small holes, of sub-mm diameter, are drilled through the layers in regular intervals. The rigidity of the GEM (or more so, of the ThGEM) allows a high potential difference to be maintained between the copper layers, creating a high avalanche field within the holes. Figure 2.13 shows a microscopic surface image of a ThGEM.

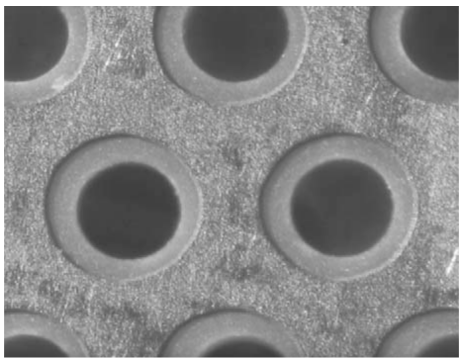

Figure 2.13: A microscopic image of a ThGEM from Ref. [75].

The insulating layer can be seen behind the copper layer, in the above figure, which has been etched away from the hole rim to prevent surface discharges through the holes. Gas gains of $\mathcal{O}(10^3)$ have been observed using a ThGEM in low pressure SF_6, which is high enough to see low energy (5.9 keV) electron recoils from ^{55}Fe X-Rays, as well as the small amplitude signal from the SF_5^- minority peak (see Figure 2.11) [69].

2.4.4 TPC Readout Options

The ideal type of readout for a next generation dark matter TPC has been extensively reviewed [76] [77]. Other than cost, the choice of readout depends on the achievable resolution (both energy and spatial) and radiopurity level. The former helps to increase the signal, whilst the latter helps to decrease the background. The following describes some of the readouts currently under consideration by the CYGNUS collaboration (formed with the goal of producing a large scale gas TPC detector). For each of the readouts discussed, it is presumed that track reconstruction in the drift direction is achievable using a negative ion gas, which, along with the 2D information provided by the readout plane, enables full 3D tracking.

MWPC

The Multi-Wire Proportional Chamber (MWPC) is constructed from wire arrays that collect the ionised charge. The main advantage of an MWPC readout is the low radioactivity produced by the relatively small amount of material used to construct the wires, which are typically between 20-100 μm in diameter. A disadvantage is that the spatial resolution is limited by how closely the wires can be placed together (the pitch). For DRIFT-IId, the avalanche field is produced between the wire arrays. This limits the spatial resolution to 2 mm, as a lower pitch would start to produce electrical discharges between the wires.

As discussed in the previous section, a ThGEM or GEM would be required to produce sufficient electron avalanche in SF_6 gas. For an MWPC with a (Th)GEM avalanche stage, the wire arrays could be held at 0 V, allowing for a reduction in pitch between the wires. This concept has been proven to work in SF_6 gas using an $\sim$4 cm^2 MWPC prototype with a 1 mm pitch and a ThGEM avalanche stage. With this configuration, the prototype was able to achieve a gain $\mathcal{O}(10^3)$ [78]. Figure 2.14 shows an Fe55 spectrum obtained using this MWPC-ThGEM readout in 30 Torr of SF_6. Chapter 7 details the testing of a larger scale (30 cm long) version of this prototype with the wire array maintained at ground potential to allow for a reduced pitch of 600 μm.

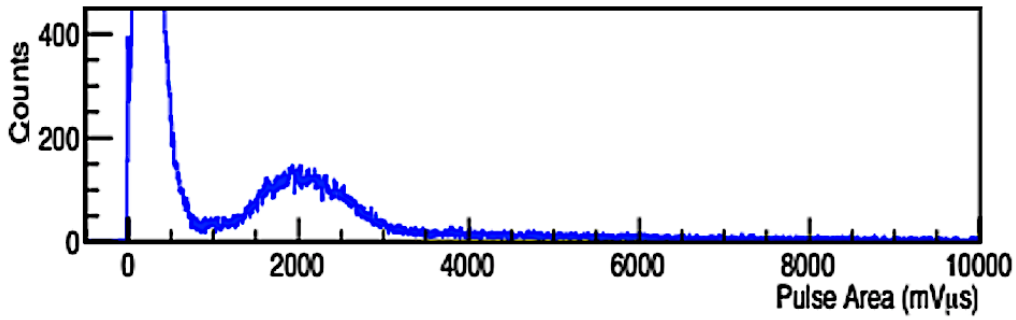

Figure 2.14: Fe55 spectrum obtained using an MWPC prototype with ThGEM avalanche stage in 30 Torr SF_6.

μ-PIC

The micro-pixel chamber (μ-PIC) is a type of MPGD that uses cathode and anode strips to give track information in the 2D plane. Figure 2.15 shows a schematic of the μ-PIC, where the cathode strips can be seen with a regular hole pattern, at the centre of which, are located electrodes that connect to the anode strips at the bottom of the μ-PIC. An avalanche field is created between the cathode and the anode strips, which are separated by a polyimide substrate. This design results in a rigid single piece that can achieve a spatial resolution of 400 μm and would require minimal support structure when scaled to a larger size.

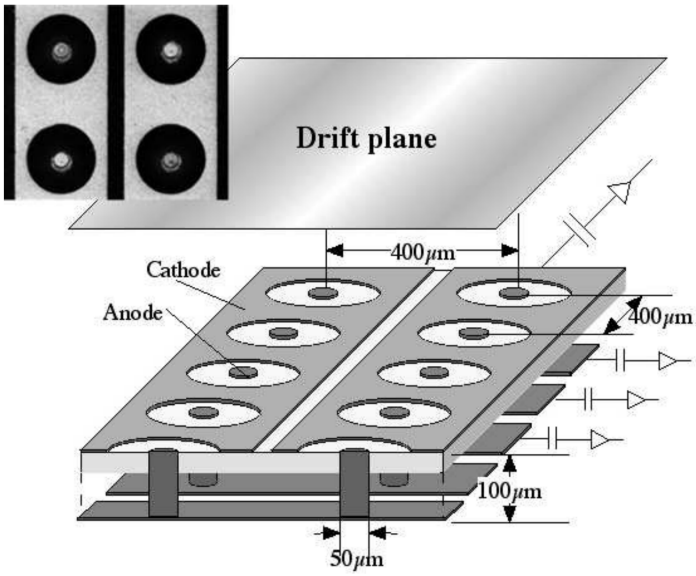

Figure 2.15: μ-PIC Schematic from [79].

The NEWAGE collaboration has reported gains of 1-2$\times 10^3$ in 20 Torr of SF_6 for a 10 $\times$10 cm^2 μ-PIC with a GEM avalanche phase [80]. NEWAGE has also shown the successful operation of a scaled up μ-PIC, with surface area 30.72 $\times$ 30.72 cm^2, in CF_4 gas [81].

Pixel Chip

Pixel readout chips are used to either detect and convert photons into an electric signal or to directly detect ionised charge. Pixel chips that are used for the latter purpose, which are discussed here, are constructed from a semiconducting material, such as silicon, and include an integrated signal amplification stage.

A matrix of pixel chips gives the 2D distribution of ionised charge by the number and location of the chips that collected the charge. Due to the high sampling frequency of pixel chips, the pulse time of arrival can be used to reconstruct track information, in the drift direction, for electron gasses (such as pure CF_4) so that a negative ion gas is not required for this purpose. However, to take advantage of the other benefits associated with negative ion gasses (as discussed earlier in this section), the sampling frequency can be adjusted to allow for the slower anions. This was achieved using 55×55 μm^2 Timepix chips, with a triple GEM avalanche stage, to produce gains $\mathcal{O}(10^3)$ in SF_6 [82].

Track reconstruction using ATLAS FE14B pixels, inside a gas TPC filled with a mixture of He and CO_2, showed that the high positional resolution achievable with pixel chips allows z to be determined from the amount of track diffusion [83], which, as shown by Figure 2.16, is visible from the reconstructed track. This technique offers an alternative to using minority peaks when establishing the z position of ionised charge.

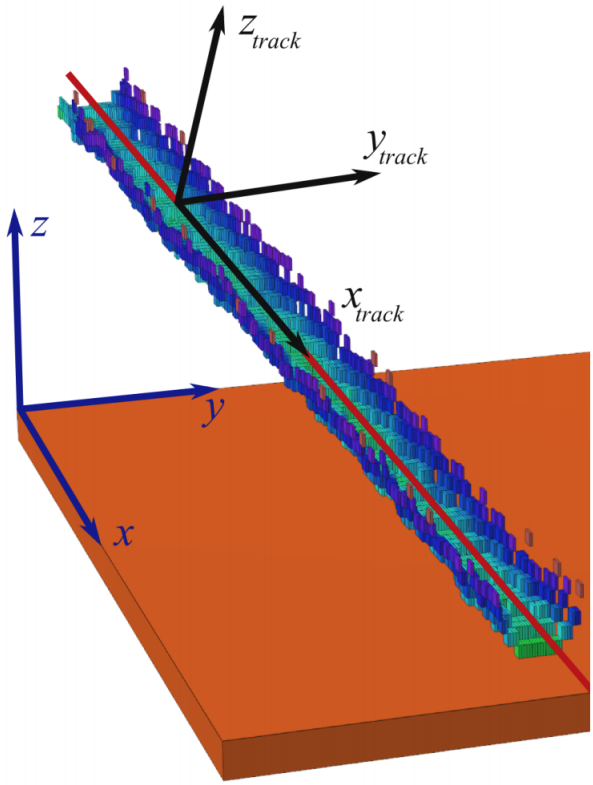

Figure 2.16: Alpha track image from [83]. The track diffusion, which is proportional to the z distance travelled by the ionised charge, can be measured from the width of the z_{track} and y_{track} components.

Micromegas

The Micromesh Gaseous Structure (micromegas) is an MPGD that uses either charge readout strips or pixels connected to collection pads, where the ionised charge is deposited. The micromegas has a fixed micromesh placed above the readout that provides the avalanche field. Figure 2.17 shows a schematic of the micromegas used by the MIMAC collaboration [84], which provides a spatial resolution of $\sim$400 μm.

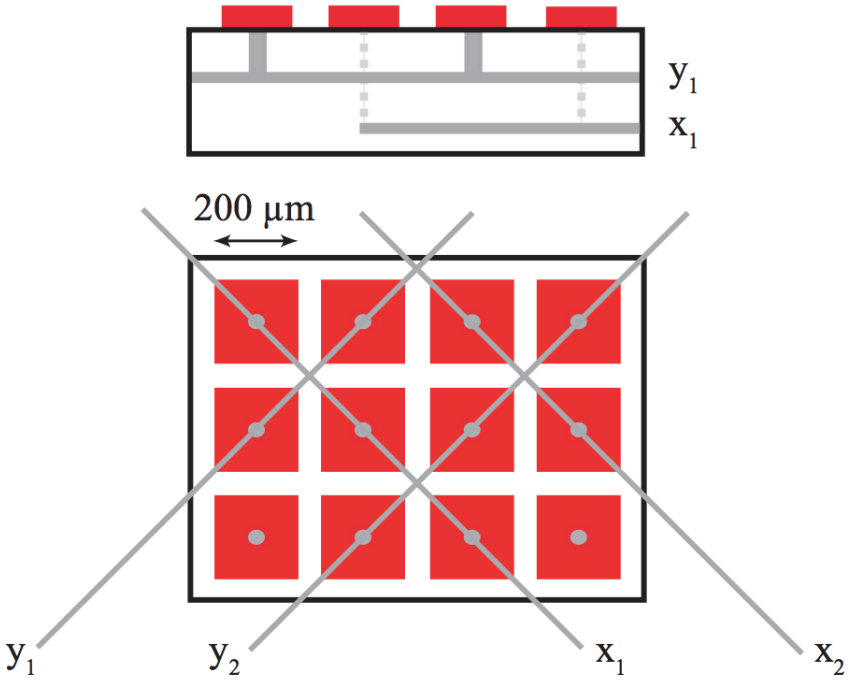

Figure 2.17: Micromegas diagram from [84]. The bottom image shows the micromegas from the top, looking through the mesh and the top image shows the micromegas from the side. The square charge collection pads are shown in red and the readout strips are shown connected to the pads in grey.

The bottom image, in Figure 2.17, shows the readout as viewed from the top, looking down through the mesh onto the collection pads (shown in red), where readout strips can be seen connecting the pads diagonally in the x and y directions. The top image, in this figure, shows the readout from the side, where it can be seen that the strips are separated vertically. The testing of micromegas in low pressure SF_6 is planned for the near future as part of the directional dark matter detection R&D being conducted at Sheffield University.

Cameras

An alternative to collecting ionised charge is to, instead, collect the photons produced by de-excited molecules, excited during the avalanche phase of a detector. Figure 2.18 shows an image, taken with a Charge-Coupled Device (CCD) camera, of an alpha track in 100 Torr CF_4 [85].

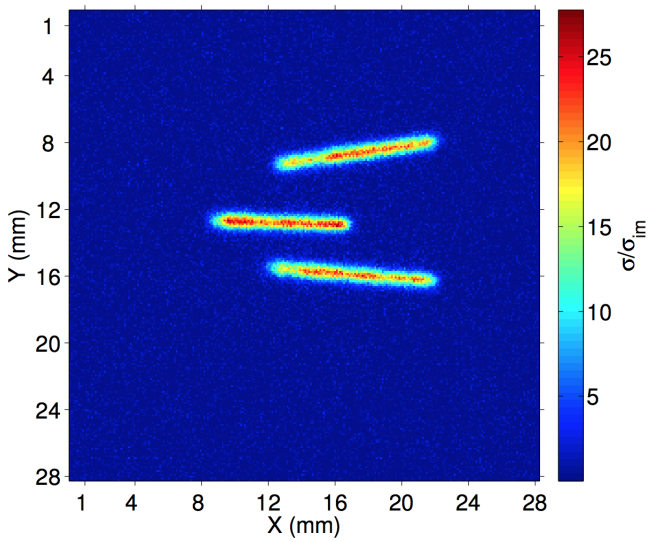

Figure 2.18: CCD camera image of alpha tracks in CF_4, from [85].

The concept of using CCD cameras for the direct detection of dark matter has been proven by the directional detector, DM-TPC (Dark Matter Time Projection Chamber) [86]. DM-TPC used CCD cameras in a CF_4 target volume to produce a SD WIMP limit that reached a cross section of 2.0×10^{-33} cm^2 at a WIMP mass of 115 GeV c^{-2} [87].

The use of Complementary Metal-Oxide Semiconductor (CMOS) cameras, with a triple GEM avalanche stage, for particle tracking has been demonstrated in a gas mixture of He and CF_4 [88]. The light yield in this gas mixture was shown to be 0.2 ph eV^{-1}, such that 1 photon was produced for every 5 electrons ionised in the avalanche fields. The advantages of using a camera based readout include high-resolution tracking and low noise levels,

allowing for low energy thresholds to be achieved (for example, Ref. [88] reports a 2 keV threshold). The disadvantages include the relatively high background levels originating from the camera materials (see Chapter 9) and the low light yield expected from negative-ion gases, although the latter is still to be investigated.

2.5 Other Direct Detection Methods

The direct detection research field has produced many various techniques towards the search for dark matter, most of which have been described in this chapter. This section briefly introduces a few other promising techniques not mentioned thus far.

Reconstructing recoil tracks using nuclear emulsion is being investigated as a possible WIMP detection method [89]. The method looks for silver grains that form around a sub-μm long track trajectory, produced by nuclear recoils within the emulsion.

The TREX-DM (TPC for Rare Event eXperiments Dark Matter) experiment, located at Canfrac Underground Laboratory, takes the opposite approach to the low pressure dark matter searches described in Section 2.4 and uses a high pressure (10 bar) TPC, with micromegas readout, filled with a mixture of Ar and Ne gas [90]. This method sacrifices directionality in favour of a larger target mass.

Spherical Proportional Counters (SPC) are another type of gas TPC used by experiments, such as NEWS-G (New Experiments With Spheres-Gas), to conduct dark matter searches. The cathode of an SPC is provided by the vessel, shown in Figure 2.19 (left), which is held at ground potential, and the anode, shown in Figure 2.19 (right), is provided by a small spherical ball, placed at the centre of the vessel and biased with high voltage via a connecting rod [91].

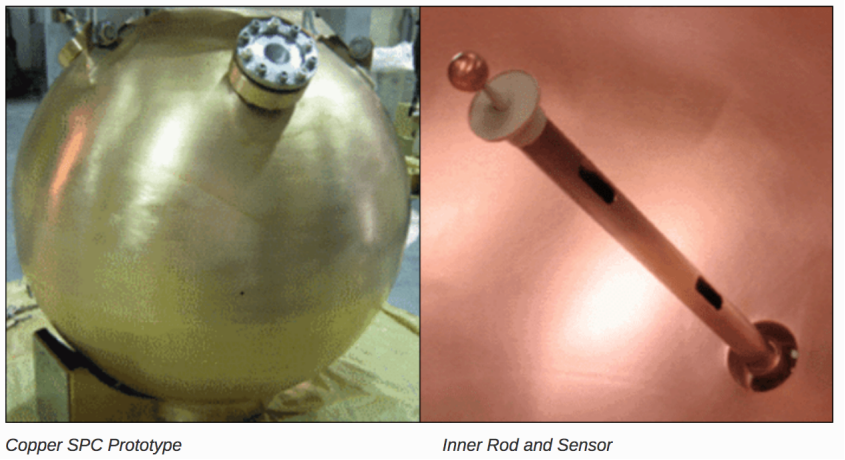

Figure 2.19: NEWS-G prototype detector. Left: The spherical vessel (cathode). Right: The metallic ball (anode) suspended at the end of a connecting rod. Figure from [92].

A spherical geometry provides the most volume per vessel surface area and as a consequence produces a reduced background level, from the vessel, compared to other geometries. Another advantages of this geometry is the low capacitive noise level. These properties enable NEWS-G to achieve a trigger threshold of $\sim$36 eV_{ee} (i.e. a single electron trigger) [93], which is a promising result, in general, for gas TPC dark matter detectors. Similar to the TREX-DM experiment, NEWS-G also uses noble gases at greater than atmosphere pressure ($\sim$3 bar) to search for low mass dark matter candidates [93].

The PICO detectors, located at SNOLAB, are bubble chambers filled with C_3F_8 that detect an ionisation event by the gas bubbles that form around it. The fluorine target enables PICO to set the current world leading (non-directional) SD limit on WIMP dark matter [94].

Chapter 3

Low Energy Gamma Rejection Simulation

The ability of dark matter search experiments to lower their detection threshold is vital, as the search for dark matter pushes towards lower interaction cross sections and WIMP masses. Section 2.4.2 of the previous chapter described how a background from neutrino's will become apparent for next generation detectors. However, a more immediate background at lower thresholds comes from low energy (sub-10 keV) electron recoils produced by the Compton scattering of gammas, which can be difficult to distinguish from nuclear recoils of similar energy. The desired electron recoil rate for a dark matter detector is < 1 yr^{-1}. This can potentially be achieved using low intrinsic background materials and shielding to construct the TPC, which is the subject of Chapters 5 and 6, and by using discrimination techniques during analysis, which is the subject of this chapter. For a dark matter detector capable of directional discrimination (see Section 2.4), features of the recoil track, such as range, can help differentiate between electron and nuclear recoils. In the work presented here, machine learning techniques are used to investigate the level of simulated electron recoils that can be rejected at low energy (1-10 keV) as a function of detection efficiency. The simulated recoils

are also used to investigate the presence of Head-Tail (HT, see Section 2.4.1) over the same energy range.

For the reasons described in Section 2.4.3 of the previous chapter, all simulated recoils were produced in 20 Torr of SF_6 gas, with the exception of the simulation described in Section 3.2, which used recoils generated in CF_4 gas to cross check the simulated quenching factor with measurement. The first section of this chapter describes the recoil simulation procedure and Section 3.3 describes how the effects of spatial resolution and diffusion were added to the simulation. The recoil parameters used for background rejection and the calculation of HT are the subject of Section 3.4 and the recoil analysis procedure is described in Section 3.5. The resulting gamma rejection and HT, before and after diffusion, is given in Section 3.6 for an idealised detector capable of 100 μm resolution and with a 50 cm long drift region. This section also presents results after diffusion for a more realistic detector capable of 600 μm resolution and with the same drift length.

3.1 Recoil Track Simulation

The first essential component of the simulation work described in this chapter is the generation of the ionised electrons produced by electron and nuclear recoil events. The former is described in Section 3.1.1 and the latter in Section 3.1.2.

3.1.1 Nuclear recoils

To generate nuclear recoils, either the GEANT4 (GEometry ANd Tracking) [95] or SRIM (Stopping and Range of Ions in Matter) [96] simulation packages could be used. It was found that the SRIM extension package TRIM allowed for the full recoil cascade to be simulated, which enabled the majority of ionisation to be captured. This was found not to be possible using GEANT4, which only produced the first level of recoils from the primary recoil cascade.

The simulation of nuclear recoils in TRIM was automated via a python script using the pySRIM package [97]. The track information produced by the simulation was output into two separate files. The first, the EXYZ.txt file, included positional information of the track, given in cartesian coordinates, and the electronic and nuclear stopping powers, recorded every time the track lost a few eV in kinetic energy. The second, the COLLISONS.txt file, recorded the energy, particle type and position of nuclear recoils caused by the primary ion as well as the resulting recoil cascades. Each recoil listed in this file with a kinetic energy greater than 200 eV was generated as a separate track in TRIM. The 200 eV threshold was chosen as simulated tracks below this energy were found to rarely produce ionisation. The resulting positional information, in the recoil's EXYZ.txt file, was rotated to reflect the cascade direction and subsequently translated into position along the ion track. The recoil's COLLISONS.txt file was then inspected for further recoil events and the process described above was repeated for those recoils. To increase the track structure detail and to include as much of the ionisation as possible, the process was repeated up to the fourth level or recoils.

The electronic stopping and positional information, included in the EXYZ.txt file for the ion and all simulated recoils, was converted into ionised electron locations using a C++ script. For each step, the script accumulated the energy loss to electronic stopping, E_{stop}, until the value was greater than or equal to the W value of the gas. At this point the size, N, and the centroid positions, X_{cent}, Y_{cent} and Z_{cent} were calculated using Eq. 3.1 and Eq. 3.2 respectively.

$$N = \frac{\sum \mathrm{E}_{stop}}{\mathrm{W}_{value}} \tag{3.1}$$

$$\mathrm{X}_{cent},\ \mathrm{Y}_{cent},\ \mathrm{Z}_{cent} = \frac{\sum(\mathrm{X},\mathrm{Y},\mathrm{Z}\times\mathrm{E}_{stop})}{\sum\mathrm{E}_{stop}} \tag{3.2}$$

Figure 3.1 shows an example of ionised electrons produced by a 50 keV_r fluorine recoil in 20 Torr SF_6.

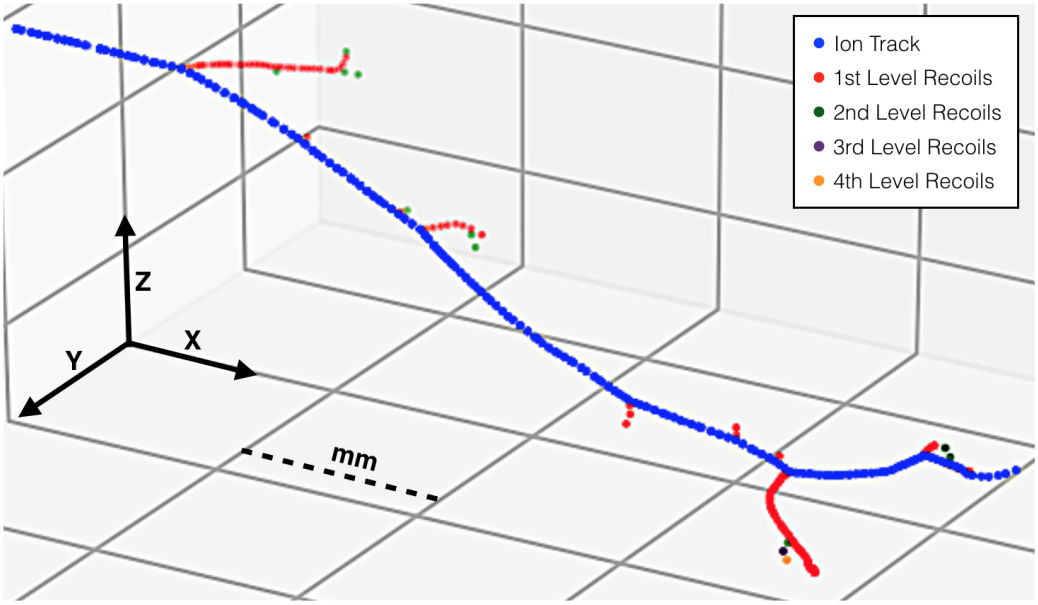

Figure 3.1: Ionised electrons, form the primary, 1st, 2nd, 3rd and 4th level of recoils, for a 50 keV_r fluorine track in 20 Torr of SF_6 gas.

3.1.2 Electron Recoils

As SRIM is specifically designed for the simulation of ions, electron recoils were generated in GEANT4. The fortran based Degrad simulation package [98] was considered but was found not to generate a number of electrons consistent with the measured SF_6 W value of 34±0.4 eV [99]. For GEANT4 simulations, a secondary electron production cut could be fine tuned to produce, on average, the expected amount of electrons. The latest version of

the simulation package was used (version 10.04) with the low energy physics list, G4EmLowEPPhysics, and the photo-absorption and ionisation model, G4PAIModelPhoton. This allowed for the direct generation of secondary electrons ionised by the primary recoil. Figure 3.2 shows the ionisation generated by GEANT4 for a 10 keV electron recoil in 20 Torr SF_6.

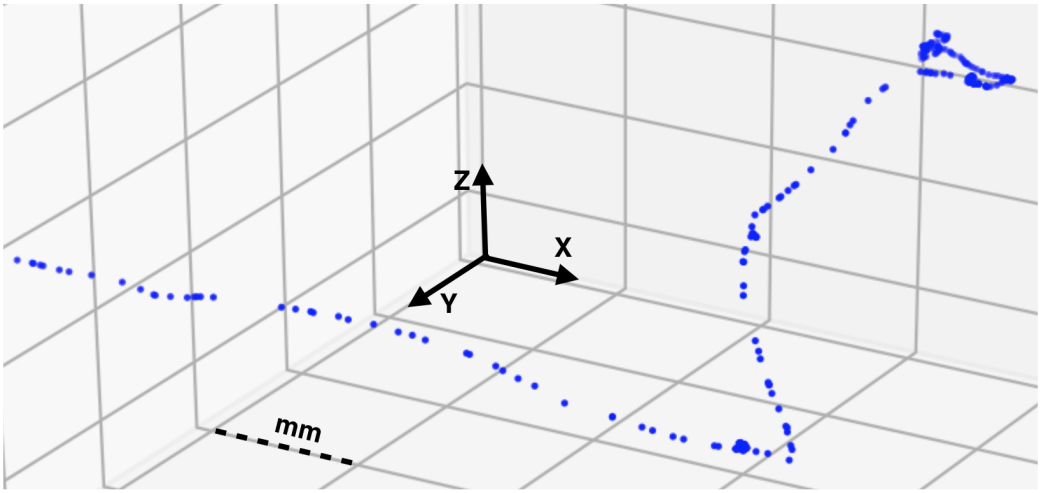

Figure 3.2: Ionisation from a 10 keV electron recoil in 20 Torr SF_6, simulated using GEANT4.

3.2 Simulated Quenching Factor

The quenching factor is the fraction of a nuclear recoil's kinetic energy that is lost to ionisation. It is proportional to the gas composition, pressure and W value as well as the type of recoiling nucleus and it's kinetic energy. Understanding the quenching factor is necessary to convert the observed ionisation into an accurate prediction of the recoil energy.

Due to the lack of reported measurements regarding the quenching factor of SF_6 at low energies, fluorine ions were first simulated in CF_4 at 50 mbar to allow for a direct comparison to the measurements made in Ref. [100]. 100

ions were generated (per recoil energy) for recoil energies between 5 and 50 keV$_r$ and the quenching factor of each recoiling ion was recorded. The mean quenching factor per recoil energy is shown in Figure 3.3.

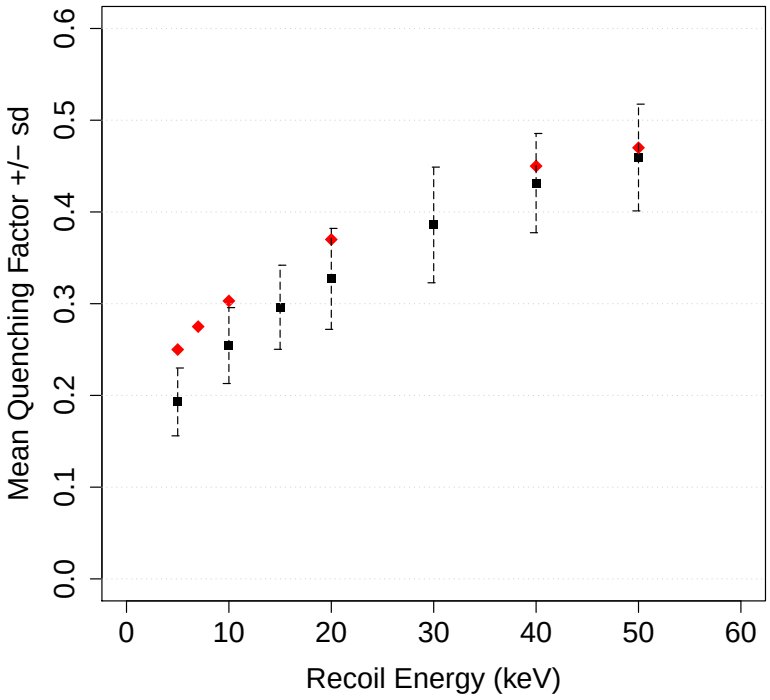

Figure 3.3: Simulated (black squares) and measured (red diamonds) quenching factor for low energy fluorine recoils in 50 mbar CF_4. Measured result taken from Ref. [100].

The result presented in Figure 3.3 shows agreement, within error, with the measurements reported by Ref. [100] for recoil energies at and above 10 keV$_r$. The simulated quenching factor at 5 keV$_r$, shown on this figure, is slightly lower than the measured value, suggesting that the simulation is less accurate at energies of $\sim$2 keV$_{ee}$ and below. After validating the simulation in this way, the same simulation procedure was used to predict the quenching

factor for low energy fluorine and sulfur recoils in 20 Torr SF_6. These are shown by the circular and square data points, respectively, in Figure 3.4.

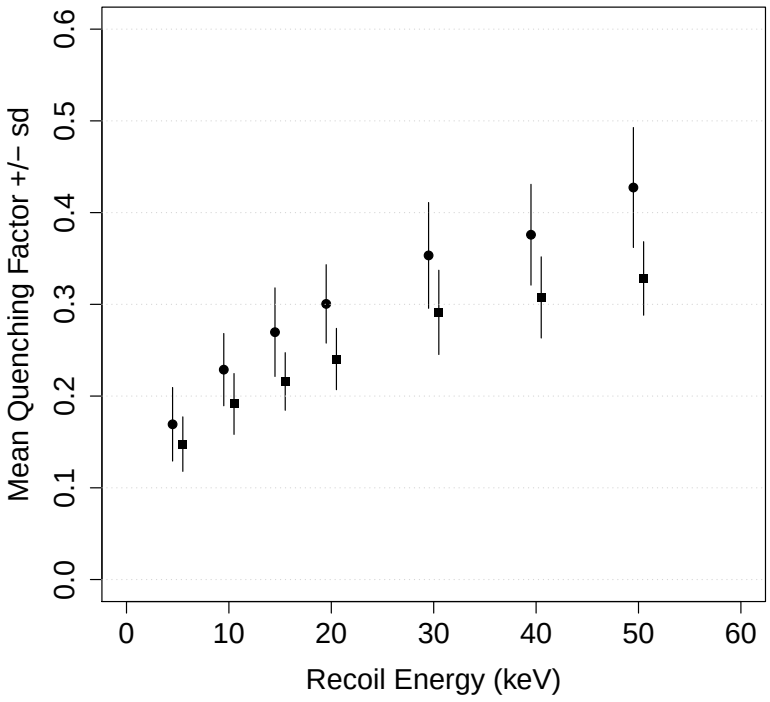

Figure 3.4: Simulated quenching factor for low energy fluorine (circles) and sulfur (squares) recoils in 20 Torr SF_6. The data is slightly offset along the x axis to prevent overlap.

3.3 Diffusion and Spatial Resolution

This section describes the simulation of diffusion and spatial resolution for the recoil tracks described in the first two sections of this chapter. As an example, the simulation is used to show how the raw signal of a 10 keV electron is affected for diffusion lengths of 1, 25 and 50 cm and for spatial resolutions of 10, 20 and 50 μm.

As described in Section 2.4.3 of the previous chapter, for recoils occurring in SF_6 gas, the ionised electrons attach to the electronegative SF_6 molecule and produce the anion, SF_6^-. This then drifts and diffuses within the gas volume. To simulate the attachment process the anions, not the ionised electrons (generated by the procedures described in 3.1.1 and 3.1.2), were simulated at each point of ionisation. The anions were generated inside a 1 m^3 volume of 20 Torr SF_6 gas, using the C++ based simulation tool Garfield [101], and a drift field of 500 V cm^{-1} was implemented in the x direction. The volume size was chosen to provide ample room for the anions to diffuse, over distances of up to 50 cm, without being lost from the simulation. The drift field was chosen to produce a reduced field at which the SF_6^- reduced mobility was known, which was a required input parameter for the simulation. The reduced field, F_0, and reduced mobility, μ_0, were calculated using Eq. 3.3 and Eq. 3.4 respectively, where v_d is the drift velocity, N_0 is the gas number density at 0° C and 760 Torr, E is the the drift field and N is the gas density.

$$\mu_0 = \frac{\nu_d}{F_0 N_0} \qquad (3.3) \qquad\qquad F_0 = \frac{E}{N} \qquad (3.4)$$

F_0 is used as this directly effects the SF_6^- mean energy (which is related to diffusion), such that an increase in N would decrease the anion's mean free path, whilst E is directly proportional to the energy gained by the anion between collisions. The density of an ideal gas at a pressure, P, of 20 Torr and at room temperature, T, is given by Eq. 3.5, where N_A is Avagadro's constant, 6.022×10^{23} mol^{-1} and R is the ideal gas constant, 6.236×10^4 cm^3 Torr K^{-1} mol^{-1}. Inserting Eq. 3.5 into Eq. 3.4 gives the reduced field as a function of E and P for a constant T of 300 K (∼room temperature), as shown by Eq. 3.6.

$$N = \frac{PN_A}{RT} \qquad (3.5) \qquad\qquad F_0 = \frac{ERT}{PN_A} \qquad (3.6)$$

This gives a reduced field, via Eq. 3.6 of ∼78 Td, where 1 Td = 10^{-17} V cm^2. Based on the measurements made by Ref. [69] this results in an SF_6^- anion reduced mobility of 0.540±0.002 cm^2 V^{-1} s^{-1}. This value was imported into Garfield, which then used the information to simulate the drifting of the anion. Ref. [69] also shows that at this reduced field the longitudinal diffusion displays a deviation of ∼20% from the thermal limit. However, thermal diffusion was used as a first approximation to the real diffusion in both the longitudinal, D_L, and transverse, D_T, directions for these simulations. Eq. 3.7 shows the calculation for thermal diffusion, where k_b and q are the Boltzmann constant and the ion charge, respectively, and δs is the step size over which the diffusion was calculated. A δs of 1 μm was chosen as smaller step sizes were found to significantly increase the CPU time. After each δs, Garfield updates the anion position with a diffusion sampled from 3 (2 for each D_T and 1 for D_L) gaussian distributions [102], each given by Eq. 3.7.

$$D_L = D_T = \sqrt{\frac{2k_bT}{qE}}(1 \pm \sqrt{\delta s}) \tag{3.7}$$

To simulate the spatial resolution of different readouts, the x, y and z locations of the anions were binned into a 3 dimensional histogram and the bin size was changed to reflect different resolutions. Figure 3.5 shows a 2 dimensional representation of how the track shape of a 10 keV electron changes with diffusion, increasing from top to bottom, and spatial resolution, increasing from left to right. The figure shows that, as expected, the electron track is less well resolved as both the diffusion increases and the spatial resolution decreases. Despite this, the general shape of the recoil is still

observable on all of the images in Figure 3.5. This indicates that the recoil information required to reject a low energy electron background remains over a range of diffusion lengths and resolutions.

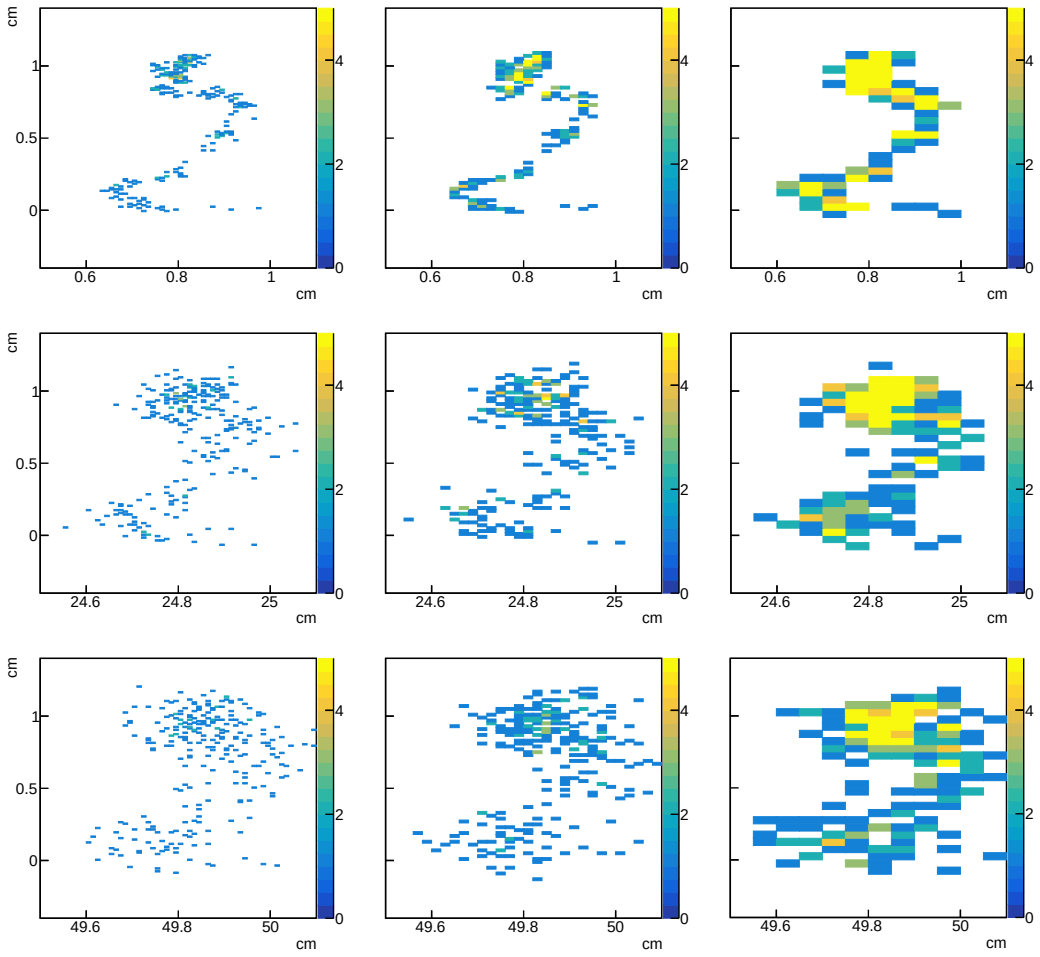

Figure 3.5: The effects of diffusion and spatial resolution on a 10 keV electron track in 20 Torr SF_6. Diffusion lengths of 1, 25 and 50 cm are shown increasing from top to bottom and spatial resolutions of 10, 20 and 50 μm are shown increasing from left to right. The key indicates the electron density per bin.

The next section describes a set of parameters identified from the track profiles of the generated electron and nuclear recoils, after the simulation of diffusion and spatial resolution, that can be used to reject an electron background.

3.4 Discrimination Parameters

With the track simulation established the next step, described here, was the identification of key parameters that maximised the separation between nuclear and electron recoil tracks. The three parameters chosen were range, charge asymmetry and charge density distribution along the track. Range was chosen as, on average, electron recoils produce a lower ionisation density per track length than nuclear recoils and will, therefore, produce longer tracks. In the same vein, the charge density distribution parameter was chosen as this is expected to be more dispersed or 'clumpy' for electrons than for nuclear recoils, which produce a smoother distribution of charge. Finally, the charge asymmetry parameter was chosen as the electron recoil profile is expected to follow a Bragg curve, depositing the majority of charge at the end of the track and creating a large asymmetry. Although nuclear recoils deposit most of their energy as ionisation at the beginning of the track, the asymmetry is expected to be less. These features can be recognised from a visual inspection of the electron and nuclear recoils, of similar energy, shown in Figure 3.6.

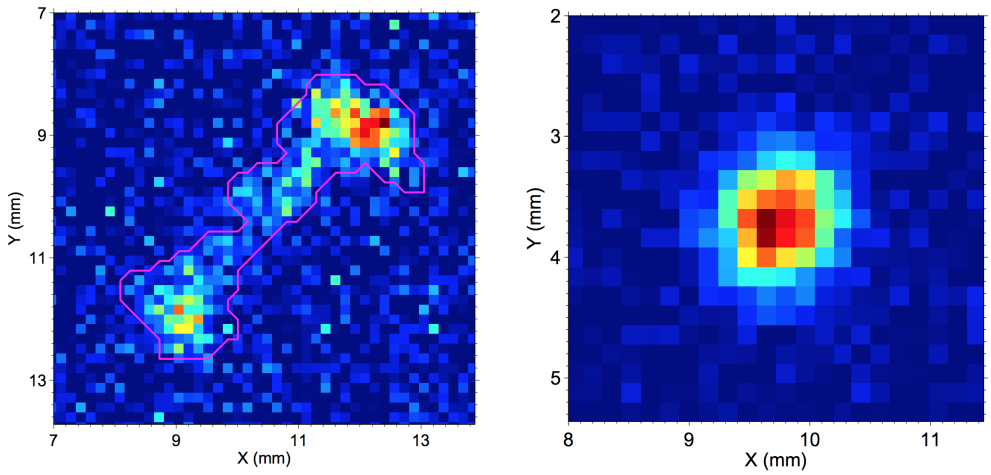

Figure 3.6: Left: 24 keV electron recoil. Right: 28 keV_{ee} nuclear recoil. Taken, in 100 Torr CF_4, using CCD camera imaging [85].

Although the above figure shows recoils in CF_4 gas, the track profiles are expected to be very similar in SF_6.

To calculate the parameters a Singular Value Decomposition (SVD) algorithm was used to create a line of best fit to the 3D distribution of ionised electrons. The SVD algorithm factorises the matrix of 3D electron positions, $\mathbf{P}$, into three separate matrices:

$$\mathbf{P}_{m\times n} = \mathbf{U}_{m\times m} \cdot \mathbf{\Sigma}_{m\times n} \cdot \mathbf{V}^T_{n\times n} \tag{3.8}$$

where $\mathbf{U}$ and $\mathbf{V}$ are unitary matrices and $\mathbf{\Sigma}$ is a diagonal matrix of non-zero, real numbers. The m rows of the $\mathbf{P}$ matrix lists the electrons and the n columns gives their position in cartesian coordinates. The three matrices, $\mathbf{U}$, $\mathbf{\Sigma}$ and $\mathbf{V}^T$ represent a rotation a scaling and a rotation, respectively. The first row of the transpose of $\mathbf{V}$, $\mathbf{v}_0$, gives the bases vector for a least squares line of best fit to the positional data. An example fit is shown in Figure 3.7 for an 11 keV_{ee} fluorine recoil in 20 Torr SF_6.

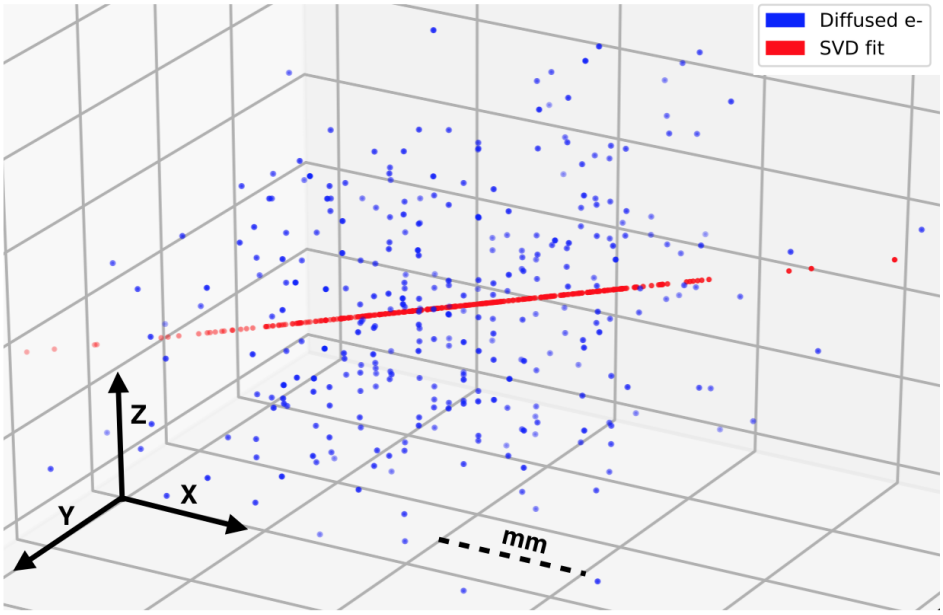

Figure 3.7: The blue points are ionised electrons from an 11 keV_{ee} fluorine recoil in 20 Torr SF_6, after 25 cm diffusion and with a 100 μm resolution. The red points are the electron positions projected onto a line of best fit.

The blue points, in the above figure, are the ionised electron positions, after 25 cm diffusion, binned to reflect 100 μm spatial resolution. The projection of the electron locations onto the fitted line (the red points in Figure 3.7) were calculated as,

$$\mathbf{v_0}(\mathbf{p}_m \cdot \mathbf{v}_0) \ , \ \mathbf{P} = [\mathbf{p}_0, ..., \mathbf{p}_m] \in \mathbb{R}^{m \times n} \tag{3.9}$$

and the range parameter was calculated from the line of best fit as,

$$\mathbf{max}\ \{\mathbf{p}_m \cdot \mathbf{v}_0\} - \mathbf{min}\ \{\mathbf{p}_m \cdot \mathbf{v}_0\} \tag{3.10}$$

The charge asymmetry parameter, λ, was measured in the positive x-

direction, $v_{0,x}$, as the ratio of charge in the first half of the fitted line to that of the second half, with the half way point defined as,

$$\frac{\mathbf{max}\ \{\mathbf{p}_m \cdot \mathbf{v}_0\} + \mathbf{min}\ \{\mathbf{p}_m \cdot \mathbf{v}_0\}}{2} \mathrm{v}_{0,x} \tag{3.11}$$

Nuclear recoils were generated in the positive x-direction to simulate the expected WIMP wind in the lab frame of reference (see Section 2.4 of the previous chapter), whilst the electron recoils were generated isotropically. For each simulated recoil type (electron, fluorine and sulfur) of a certain energy, the number of λ >1 was recorded as λ_{HT} and the HT value was derived as,

$$\mathrm{HT} = \frac{\lambda_{\mathrm{HT}}}{N} \pm \sqrt{\frac{\mathrm{HT}(1-\mathrm{HT})}{N}} \tag{3.12}$$

where N is the number of recoils simulated. The statistical error in the above equation is boolean in nature as each recoil has a value of λ that is either less than or greater than 1. For the directed nuclear recoils, the majority are expected to have a λ greater than 1 and, therefore, Eq. 3.12 is expected to give HT $>$ 0.5. This should then distinguish the nuclear recoils from the isotropic electron background, which is expected to show no statistical λ bias and, therefore, Eq. 3.12 is expected to give HT $\simeq$ 0.5.

The charge density variation along the track was measured as the standard deviation from the mean electron density along the fitted line. Figure 3.8 shows this for a 7 keV$_{ee}$ fluorine recoil in 20 Torr SF_6, which has a charge density variation of 5.15 electrons per 100 μm bin or 5.15×10^{-2} q $\mu\mathrm{m}^{-1}$, where q is the electron charge.

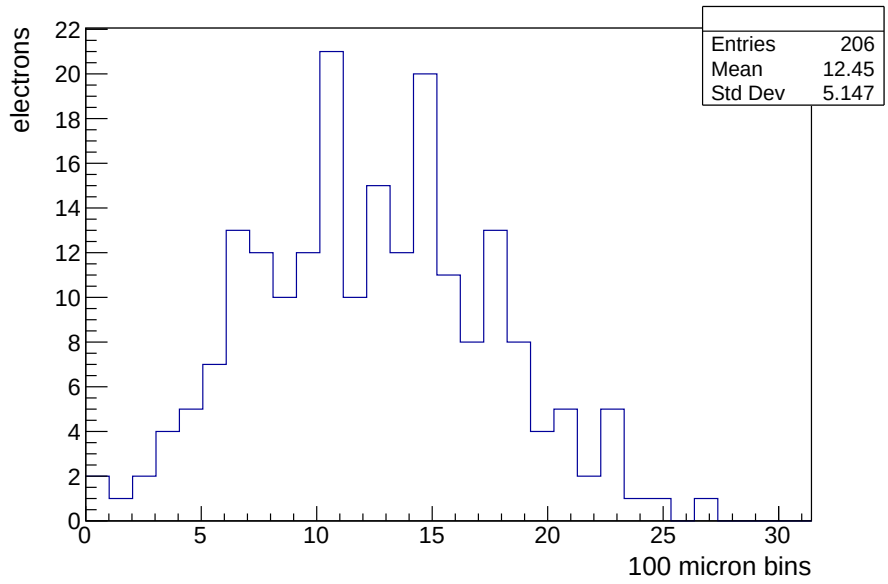

Figure 3.8: Electron density distribution, for 100 μm resolution, over the length of the best fit line for a 7 keV$_{ee}$ fluorine recoil in 20 Torr of SF_6. The charge density variation parameter is the 'Std Dev' value given in the stats box (top right).

A strong correlation is expected between the range and charge variation parameters as longer tracks are more likely to have a greater spread in electron density. However, the charge density parameter includes information about the track structure that is used to help distinguish between nuclear and electron recoils of similar range. Figure 3.9 shows where fluorine, sulfur and electron recoils of 6$\pm$0.5 keV$_{ee}$ are positioned within a parameter space made up of the three parameters discussed. The recoil data in this figure is based on 25 cm diffusion and 100 μm resolution.

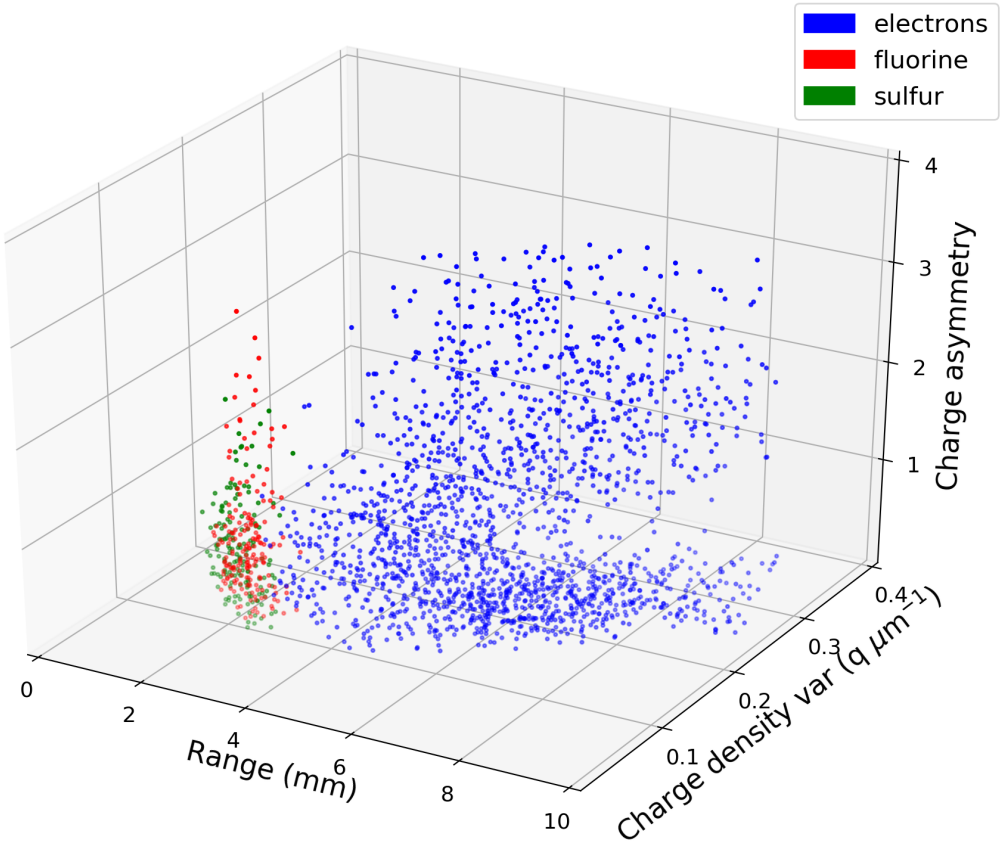

Figure 3.9: Parameter space made up of the parameters: range, charge asymmetry and charge density variation. For a spatial resolution of 100 μm and after 25 cm diffusion. Fluorine, sulfur and electron recoils of 6 $\pm$0.5 keV$_{ee}$ in 20 Torr SF_6 are shown as red, green and blue points respectively.

The above figure clearly shows the discrimination potential of the three parameters discussed in this section. It can be seen, from this figure, that the most effective separators between electron (blue) and nuclear (red and green) recoils are the fitted range and, the closely correlated, charge density variation parameters. The charge asymmetry parameter is not as effective, however, it does still provide some added discrimination at higher values. The recoil data plotted in Figure 3.9 is for an energy of 6 $\pm$0.5 keV$_{ee}$, which was chosen as an average for the 1-10 keV$_{ee}$ energy range. For example, the

same plot for 10 keV_{ee} energies would show even greater separation between the electron and nuclear recoils and the opposite is true for energies < 6 keV_{ee}. In the next section a new type of analysis, for gas TPCs, is introduced that can maximise the discrimination potential visible in Figure 3.9.

3.5 Decision Tree Analysis

It can be seen from Figure 3.9 that, on the main, there exists good separation between nuclear and electron recoils. However, the figure also shows some cross over between the two recoil types, where the separation between them, if it exists, is less easy to recognise by eye. Therefore, a Decision Tree (DT) algorithm, from the python module scikit-learn [103], was used to help develop the best possible parameter cuts, for the recoil data, that maximises the electron rejection at different recoil detection efficiencies. The usual function of a DT is to train a signal selection algorithm on a given data set and number of parameters, which can then be tested on a separate set of data (this is the basis of the analysis performed in Chapter 4 for DRIFT-IId). However, for the analysis described in this section, the DT is instead used to estimate the background rejection capabilities, for recoil energies between 1 and 10 keV_{ee}, at different detection efficiencies. The following describes the process used to achieve this.

The DT analysis choses cuts, based on the three parameters discussed in Section 3.4, that optimises the separation between signal (nuclear recoils) and background (electron recoils). The level of the analysis can be set such that a level one analysis performs just a single cut on the data and produces two data sets, a level two analysis performs a further cut on the data and produces four data sets and so on. If the data is fully separated as either pure background or pure signal no further cuts are performed. Figure 3.10 shows a level three DT analysis performed on the recoil data shown in Figure 3.9.

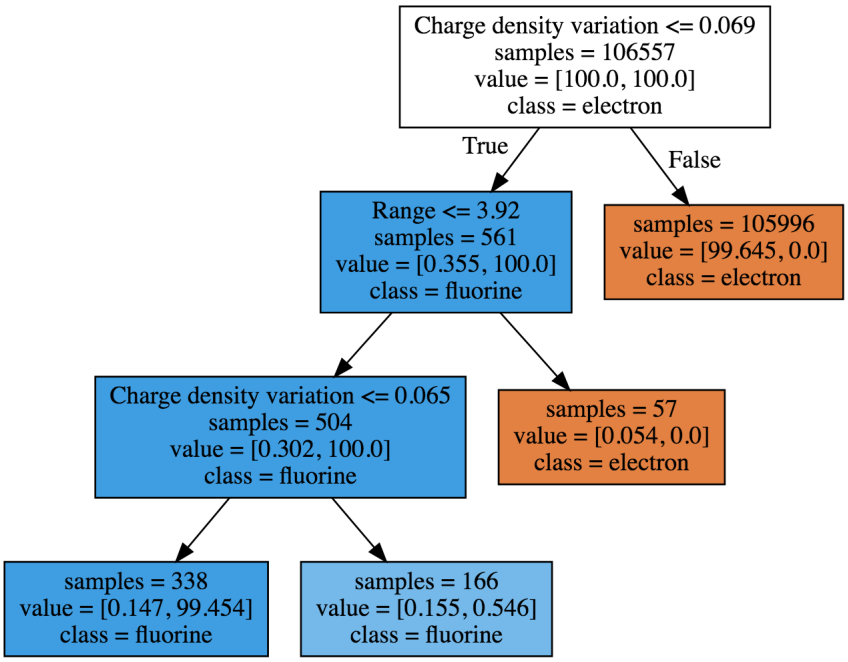

Figure 3.10: Level three DT analysis performed on a recoil sample made up of 6±0.5 keV_{ee} electron and fluorine recoils. For each box, the left and right side of the row labelled "value" gives the percentage (units not shown) of electron and fluorine recoils, respectively, remaining after each cut.

The data in the above figure is made up of $\sim 10^5$ electron and ~200 fluorine recoils. Each box on the figure represents an array of recoil parameters and lists the following: the parameter being used to separate the data (top row); the number of recoils in the box (second row); the percentage of electron (left) and nuclear recoils (right) in the box; the majority classification (last row). It can be seen from Figure 3.10 that a cut in charge density variation of < 0.069 q μm^{-1} rejects $\sim$ 99.6% of the electron background whilst keeping 100% of the fluorine recoils. Following the signal path, shown in dark blue on Figure 3.10, shows that the electron rejection can be increased to $\sim$ 99.9% by introducing a range cut of $<$ 3.92 mm and reducing the charge density variation cut down to $<$ 0.065 q μm^{-1}. However, this also has the effect of reducing the fluorine recoil detection efficiency from 100% to $\sim$ 99.5 %.

DTs with an increasing level of cuts will increase the electron rejection even further but will also start to further reduce the signal detection efficiency. By studying DTs with up to 20 levels, the electron rejection at different detection efficiencies was investigated for recoil energies at and below 10 keV_{ee}. In each case the electron recoil is either rejected or not, which results in a boolean distribution. Therefore, the error on the rejection factor was computed in the same way as the error in HT (see Eq. 3.12).

A DT also gives information on the significance of each parameter used to help separate the data. The most significant parameter used in the analysis shown in Figure 3.10 was the charge density variation, as a cut on this parameter rejects most of the background. Figure 3.11 shows the parameter significance after the initial cut, for 12 more levels of cuts, which allowed the background rejection to be studied down to 10% detection efficiency. It can been seen from the figure that all parameters have a significant affect on background reduction, with the range parameter being the most important in this case. The significance of each parameter varies with the amount of cut levels chosen, however, on average there exists a contribution from all three parameters.

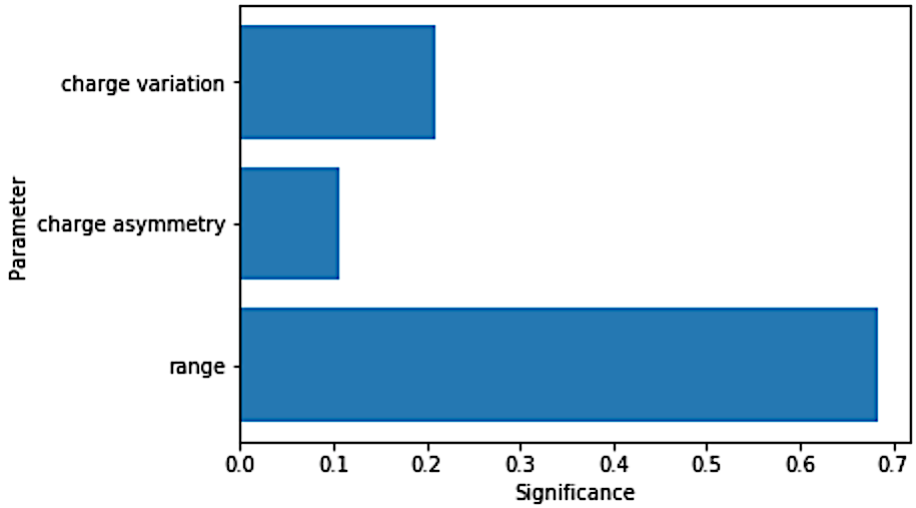

Figure 3.11: The significance of each parameter in separating nuclear recoil data from electron recoil background, given after the initial cut (which removed the majority of background).

3.6 Resulting HT and Gamma Rejection

All of the following results are based on a gas TPC with a target volume of 20 Torr SF_6 at room temperature and with a drift field of 500 V cm^{-1}. For each energy between 1 and 10 keV_{ee}, approximately 10^5 gamma induced electron recoils, 200 fluorine and 200 sulfur recoils were simulated.

Figure 3.12 shows the measured HT for the simulated fluorine, sulfur and electron recoils between 1-10 keV_{ee}, for a resolution of 100 μm. The diamond (square) points on this figure show the effect before (after) diffusion. The figure shows significant HT before diffusion, at all energies, for both fluorine and sulfur recoils and no clear HT after an averaged 25 cm diffusion, with the exception of 10 keV_{ee} fluorine recoils. As expected the electron HT is consistently 0.5 (within error) at all energies, before and after diffusion, correctly identifying the background's isotropic distribution.

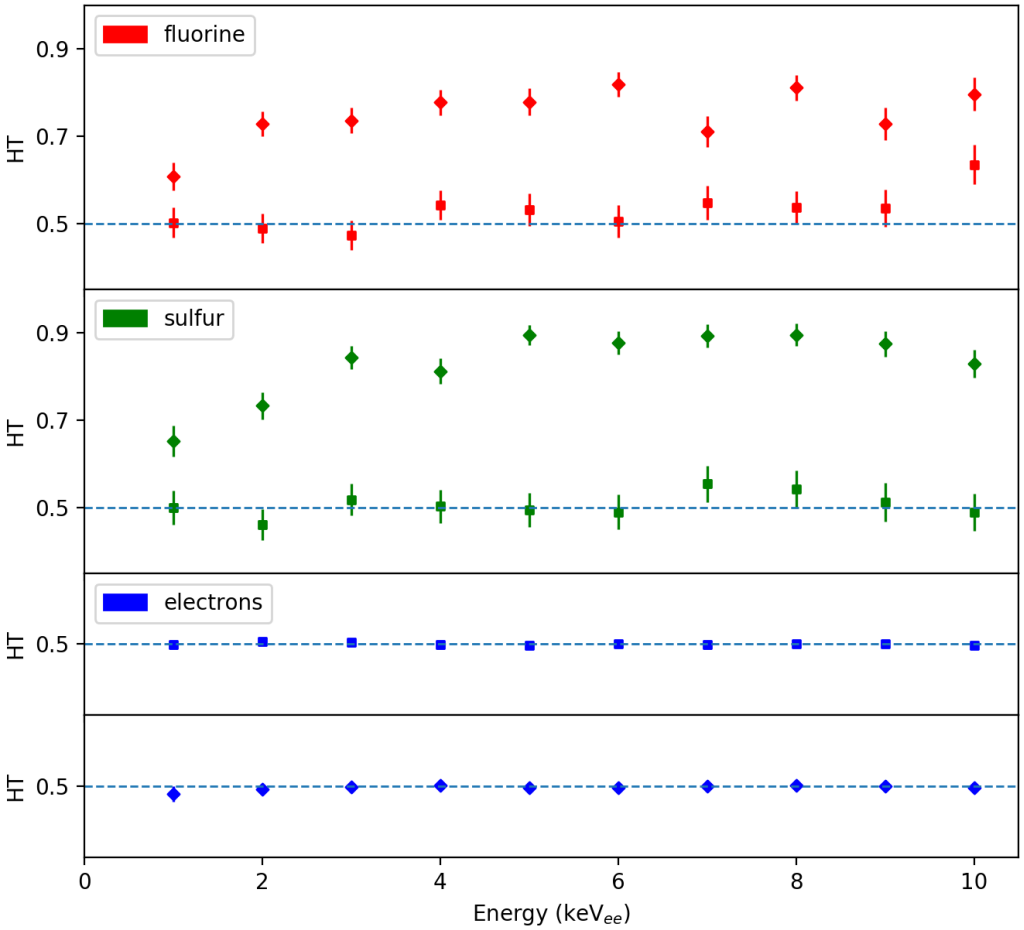

Figure 3.12: Low energy HT measured before (diamond points) and after (square points) diffusion in 20 Torr SF_6 for fluorine, sulfur and electron recoils in the energy range 1-10 ± 0.5 keV$_{ee}$. The simulation was conducted at 100 μm resolution and a 50 cm drift region was simulated by diffusing all tracks over an averaged 25 cm.

The results of Figure 3.12 suggests that HT could be used to look for a WIMP signal at low energy and low diffusion, by identifying anisotropy within the recoil data. However, the result also suggests that the affect reduces with diffusion. The exact relation between the magnitude of the observed HT and the amount of diffusion can not be inferred from these results, and as such, should be a focus of future work. That said, the preliminary result presented here, suggests that HT would be more obvious for recoils occurring closer to the readout.

For energies greater than 6 keV_{ee} all of the electrons were rejected at high signal detection efficiencies, as shown by Table 3.1 for 100 μm resolution and 25 cm diffusion. This amount of diffusion was chosen as the mean amount experienced by recoils distributed uniformly within a 50 cm drift region, which is based on the DRIFT-IId drift length (see Chapter 4).

Table 3.1: Detection efficiencies at which all, $\sim 10^5$, electrons were rejected, for fluorine (top row) and sulfur (bottom row) recoil energies above 6 keV_{ee}.

Energy (keV_{ee})	7	8	9	10	
Efficiency (%)	69	75	75	100	Fluorine
	93	99	100	100	Sulfur

As the electron recoils were either rejected or not, the result was boolean in nature and the gamma rejection error was calculated in the same way as the HT error (see Eq. 3.12). This meant that the high gamma rejection factor of 10^{-5}, associated with the results given by Table 3.1, produced an error of $\pm 10^{-5}$. For this reason, a sample size of 10^5 caused gamma rejection factors better than 10^{-4} to be unreliable. This error could be reduced by increasing the background sample size, from 10^5 to 10^6, however, the CPU time required to achieve this would also increase ten fold. Therefore, lines were instead fitted to data points representing lower rejection factors and used to make predictions of the detector efficiency at higher rejection factors.

The gamma rejection factor at detection efficiencies between 20 and 100%, for fluorine and sulfur recoils with energies between 1 and 5 ± 0.5 keV$_{ee}$, are shown on the left and right of Figure 3.13 respectively.

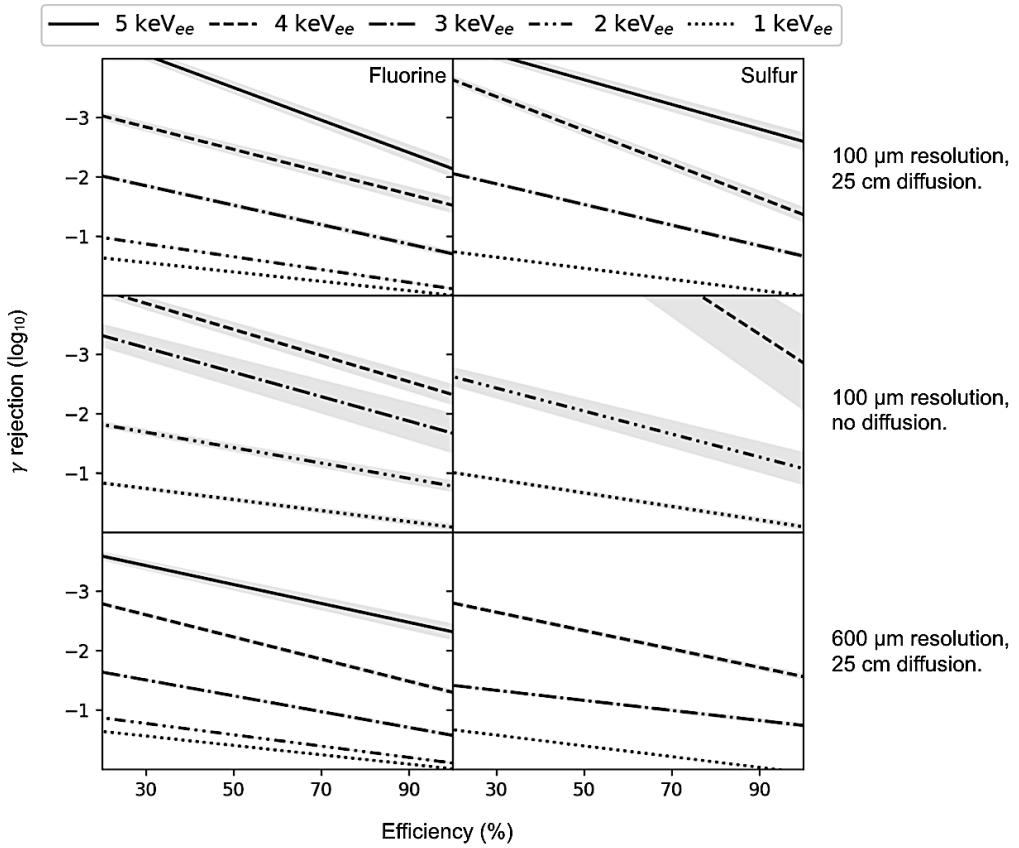

Figure 3.13: Gamma rejection at detector efficiencies of 20-100% for fluorine (left) and sulfur (right) recoils in 20 Torr SF_6, for recoil energies of 1-5 ± 0.5 keV$_{ee}$. Top row: 25 cm diffusion, 100 μm resolution, middle row: no diffusion, 100 μm resolution, bottom row: 25 cm diffusion, 600 μm resolution. The shaded region shows one sigma deviation from the fitted lines.

The top, middle and bottom rows of Figure 3.13 show, respectively, the rejection factor at 25 cm diffusion and 100 μm resolution, no diffusion and

100 μm resolution and 25 cm diffusion and 600 μm resolution. The latter represents a more realistic spatial resolution and matches that used by the prototype readout discussed in Chapter 7. The lines on the figure are linear least square fits to the rejection factor data points and the fits were weighted using the relative boolean error of each rejection factor. To ensure a reliable fit, data points with relative errors greater than one half of the point value were not used and a fit was only attempted if at least 5 data points were present. Gamma rejection at detector efficiencies of less than 20% showed deviation from a linear profile, therefore, no fit was attempted below this efficiency. The shaded regions around the fitted lines represent one sigma deviations.

Figure 3.14 shows the gamma rejection between 1 and 10 keV$_{ee}$, extrapolated from Figure 3.13 for a 50% detection efficiency. The top, middle and bottom rows of Figure 3.14 show, respectively, results for 25 cm diffusion and 100 μm resolution, no diffusion and 100 μm resolution, and 25 cm diffusion and 600 μm resolution. The first column of the figure shows results for fluorine recoils and the second column for sulfur recoils. The error bars, shown in blue on the figure, were used to perform linear weighted orthogonal distance regression fits to the data, which are shown by the solid lines. The error in gamma rejection comes from the one sigma error of the fitted lines in Figure 3.13 and the error in energy was $\pm$0.5 keV$_{ee}$. The dotted lines in Figure 3.14 represent predictions where no data was available. The shaded regions on the figure show one one sigma deviation from the fitted lines.

Figure 3.14 shows a wide range in gamma rejection capabilities at low energy, for example the top row shows a rejection factor of $\sim 10^{-8}$, within error, at 10 keV$_{ee}$, for both fluorine and sulfur recoils, and a steep decline towards < 0.1 at 1 keV$_{ee}$. The figure also shows a significant reduction in the gamma rejection after diffusion, for example at 6 keV$_{ee}$ the rejection factor reduces by $\sim$2 and $\sim$4 orders of magnitude for fluorine and sulfur recoils respectively, at the same (100 μm) resolution. Comparing the gamma

rejection at different resolutions (after 25 cm diffusion), Figure 3.14 shows a less severe reduction, with ∼similar results at both resolutions below 8 keV_{ee} and ∼one order of magnitude better results for 100 μm resolution above this energy.

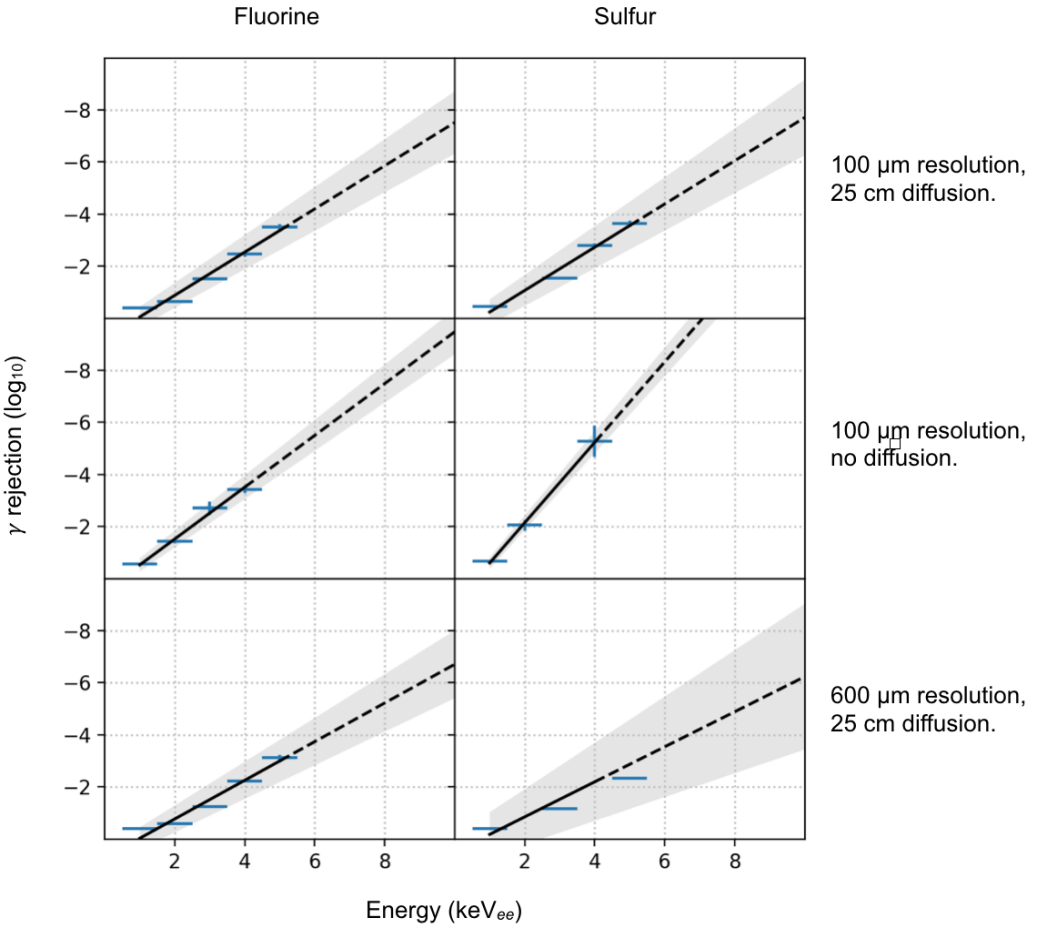

Figure 3.14: Gamma rejection at 50% detection efficiency for fluorine and sulfur recoils with energies between 1-10 keV_{ee}, given for different diffusion lengths and spatial resolutions. The blue points with error bars were extrapolated from the data shown in Figure 3.13 and the solid line is a fit to these points. The dotted lines are predictions of the rejection factors. The shaded region shows 1 σ deviation from the fitted lines.

The results presented in Figure 3.14 show the first (to the authors knowledge) serious attempt at a low energy (sub-10 keV$_{ee}$) analysis for a gas TPC. The diffusion is shown as either off (zero drift) or on (averaged 25 cm drift), of course in reality, diffusion is not on or off but a continues function of the drift distance. Therefore, the approximate gamma rejection at low diffusion lengths (>0cm and <25 cm) can be estimated from these results. For example, for an averaged 10 cm diffusion length, the rejection would be approximately half way between that found at the minimum, 0 cm, and maximum, 25 cm, diffusion limits. This would correspond to an ∼1 (for fluorine) and ∼2 (for sulfur) orders of magnitude better rejection after 10 cm diffusion, compared to the rejection found after 25 cm diffusion.

The high rejection factors, found in this section, indicate that a significant gamma background could be tolerated for a large next generation gas TPC. These backgrounds are studied and compared to the gamma rejection results found here, for a 1000 m^3 and 10 m^3 gas TPC in Chapters 5 and Chapter 6, respectively.

The results of this chapter could be improved by using real, rather than simulated, recoil events. It is therefore an R&D priority to test prototype readouts in SF_6 gas and obtain real recoil data. The construction and operation of such a prototype is discussed in Chapter 7.

3.7 Conclusion

This chapter detailed the first attempts made to investigate the gamma rejection of a low pressure gas TPC, at sub-10 keV$_{ee}$ energies, using simulated recoils. The nuclear and electron recoils were generated using SRIM and GEANT4, respectively, for a 20 Torr SF_6 gas target. Spatial resolution and diffusion were implemented into the simulation, the latter was achieved using GARFIELD to simulate a drift field of 500 V cm^{-1}. It was shown how a decision tree analysis could be used to find parameter cuts that maximise

the gamma rejection at different detection efficiencies. The gamma rejection at 600 μm spatial resolution, after 25 cm diffusion, and at 100 μm spatial resolution, before and after 25 cm diffusion, was investigated (25 cm was chosen to represent the mean diffusion experienced by events occurring uniformly within a 50 cm drift region). Three recoil parameters were used for the gamma rejection analysis, these were range, charge asymmetry and charge density variation.

From the charge asymmetry parameter it was possible to look for a HT affect that could be used to distinguish an anisotropic signal over an isotropic background. The affect was found to be a function of track diffusion, being more obvious at no diffusion and almost non-existent after 25 cm diffusion, for recoil energies between 1 and 10 keV$_{ee}$. This suggests that HT could be used to look for an anisotropic WIMP signal at low energy for recoil tracks experiencing low diffusion.

For both fluorine and sulfur recoils, the simulated gamma rejection was found to be higher before diffusion. This would indicate that the ability to reject gammas varies with drift length, with shorter drift lengths giving better rejection factors, as expected. Although the results of this chapter can be used to approximate the gamma rejection for different diffusion lengths, the simulation could be used in future to find a more accurate relation between gamma rejection and diffusion. The variation in gamma rejection between 100 and 600 μm readout resolutions was only found to be significant at and above 8 keV$_{ee}$. Below this energy, a readout with 6 times less spatial resolution, than an idealised 100 μm, was found to give similar results after 25 cm diffusion. This suggests that the readout resolution has less impact on the achievable gamma rejection after the charge has been spread out, due to diffusion, over a relatively large readout area (compared to the area covered by the initial ionisation event). The small variation in gamma rejection performance, with resolution, was one of the main motivations behind the construction of a 600 μm pitch MWPC prototype, which is discussed in

Chapter 7.

The results of this chapter could be improved with the simulation of a greater number of background events. This would reduce the significant error attributed to large gamma rejection factors, improving the gamma rejection predictions at higher energies (6-10 keV_{ee}). The identification of more recoil parameters would also help to further distinguish signal from background and improve the resulting background rejection. The decision tree analysis, used in this chapter, is an example of a machine learning algorithm. Instead of being used to investigate the possible gamma rejection at different detector efficiencies, a similar analysis could be trained and tested on a large (real or simulated) data set and the resulting analysis model could be used to directly search for a WIMP event from future data. The next section provides an example of this using data from the DRIFT-IId detector.

Chapter 4

Improved DRIFT-IId Detector Efficiency using Machine Learning

A next generation large scale gas TPC, such as those introduced in the next two chapters, will require a high detection efficiency in order to exploit the maximum amount of target mass at it's disposal. The previous chapter used a machine learning algorithm, called a decision tree (DT), to explore the gamma rejection capability of a future low pressure gas TPC, sensitive to low energy recoils (sub-10 keV_{ee}). This chapter describes how a similar algorithm can be used to maximise the detection efficiency of such a TPC. Data provided by the DRIFT-IId experiment, introduced in Section 2.4.3 of Chapter 2, provides a means to investigate this, whilst also potentially improving the detectors existing sensitivity.

DRIFT-IId is a 1 m^3 low pressure Negative Ion Time Projection Chamber (NI-TPC), located at the Boulby Underground Laboratory, designed to directly detect WIMP dark matter particles and to ultimately identify the WIMP wind originating from the Cygnus constellation (see Section 2.4 of Chapter 2). This is potentially achieved by studying the directional information of recoils caused by WIMP-nuclei interactions within the detector's target gas volume. This chapter describes a new type of data analysis that

uses a machine learning algorithm called Random Forest Classifier (RFC) to increase the DRIFT-IId detector efficiency. Section 4.1 describes the configuration and operation mode of the detector, Section 4.2 gives a theoretical calculation of the expected WIMP interaction rate within the target gas volume and Section 4.3 describes the new analysis procedure. The results of the latter two sections are used to produce an improved SD WIMP exclusion limit for DRIFT-IId, presented in Section 4.4, which corresponds to an increase in sensitivity of $\sim$30%. This result will have a greater impact on the search potential of a next generation detector, which will have a significantly larger target volume than DRIFT-IId.

4.1 The DRIFT-IId Detector

The DRIFT-IId detector, shown in Figure 4.1, consists of two MWPCs (this readout was introduced in Section 2.4.4 of Chapter 2) placed 50 cm away from, and to the left and right of, a central cathode. The cathode provides a high voltage of -31.9 kV, which is reduced in uniform steps towards each MWPC. This is achieved using a field cage consisting of 31 stainless steel rings, mounted onto an acrylic frame, that surround the target volume of gas. The first and last rings of the field cage are connected to the cathode and MWPC, respectively, using 33 MΩ resistors and each intermediate ring is connected to it's adjacent counterpart by the same method. The field cage maintains a uniform drift field between the cathode and MWPCs of 580 V cm^{-1}, over 50 cm, which inhibits the lateral displacement of ionised charge as it drifts towards the readout.

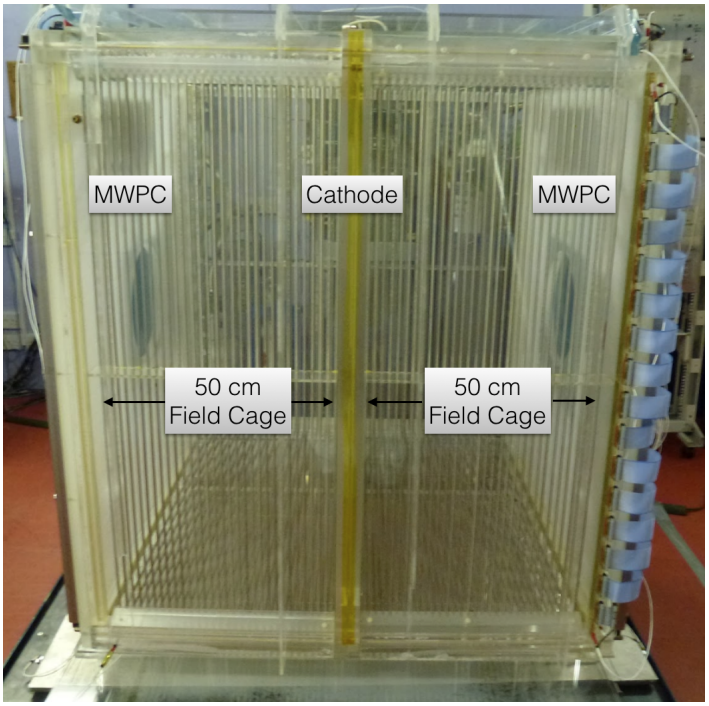

Figure 4.1: DRIFT-IId NI-TPC. Each MWPC, left and right, is separated from a central cathode via a 50 cm field cage.

Each MWPC is comprised of three separate arrays of 552 stainless steel wires with 2 mm pitch. The three arrays make up an anode of 20 μm thick wires, and two grids, placed orthogonal to the anode, of 100 μm thick wires, as shown by the schematic in Figure 4.2. The separation between the grid and anode wires is 1 cm, within this region an avalanche field is produced by setting the grid wires to -2884 V and maintaining the anode wires at ground potential. The avalanched signal is collected on 448 of the anode wires, which in turn, induces a response on the same number of inner grid wires (see Figure 4.2). 52 wires, situated on both sides of each grid, provide a veto region around the array that is used to exclude events entering the fiducial volume from the outside. 41 wires, on both sides of the anode, provide the same veto for this array. 11 anode wires, situated before the veto on both sides, are stepped down in voltage to prevent electrical break down

at the extremities of this array. The anode and inner most grid provide track information in the x and y directions, respectively. For these arrays, every 8th signal wire is grouped in order to minimise the amount of processing electronics. The grouping size was chosen as neutron calibrations showed that no recoil, within the energy region of interest (<200 keV_r), trigger 8 or more wires. Each group of signal and veto wires is processed by a Cremat-110 pre-amplifier and Cremat-200 shaper, with 4 μs shaping time, before being recorded by the DRIFT-IId Data AQuisition system (DAQ).

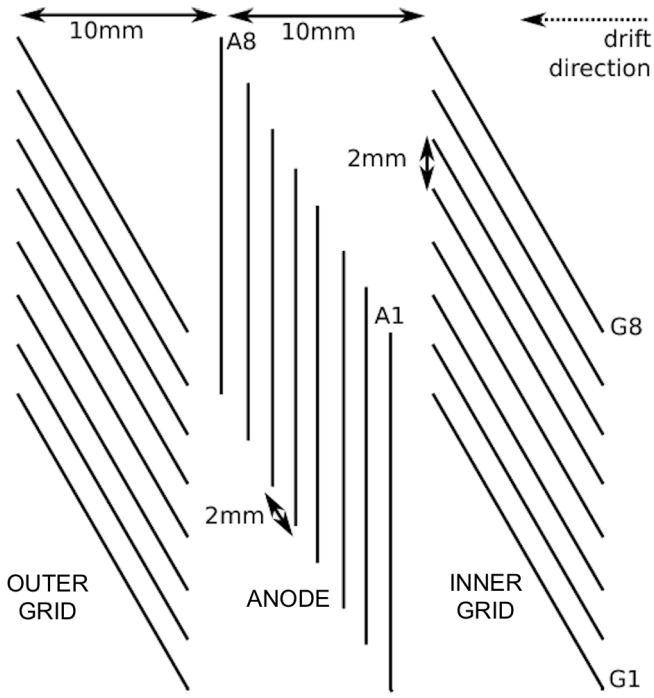

Figure 4.2: A schematic showing part of one of the two MWPCs used by DRIFT-IId. Made from three arrays of 552 stainless steel wires of 100 μm (grid) and 20 μm (anode) diameter. The wire pitch of each array is 2 mm and the separation between the arrays is 1 cm.

The DRIFT-IId detector is placed inside a 7 mm thick steel vacuum vessel [104]. The vessel is surrounded by polypropylene pellets, which provide

shielding from neutrons produced during the radioactive decay of isotopes found within the surrounding rock walls. Gamma shielding is not used as DRIFT-IId, instead, uses a combination of signal threshold and short shaping time to prevent the low ionisation density of Compton scattered electrons from triggering a response. This allows for a gamma rejection of 1.98×10^{-7} with a threshold of $\sim$18 keV$_{ee}$ [105]. The vacuum vessel allows the detector to operate at a pressure of 41 Torr, utilising a gas mixture of CS_2, CF_4 and O at a pressure of 30, 10 and 1 Torr, respectively. As described in Section 2.4 of Chapter 2, the gas mixture provides negative ion drift, a spin-dependant (SD) target and fiducialisation in the drift direction, due to the presence of minority peaks. The latter, combined with the planar information from the MWPC readout, allows the location of an event to be determined in 3D. Figure 4.3 shows the main ionisation peak, produced by a recoil event inside the DRIFT-IId gas volume, along with two smaller minority peaks.

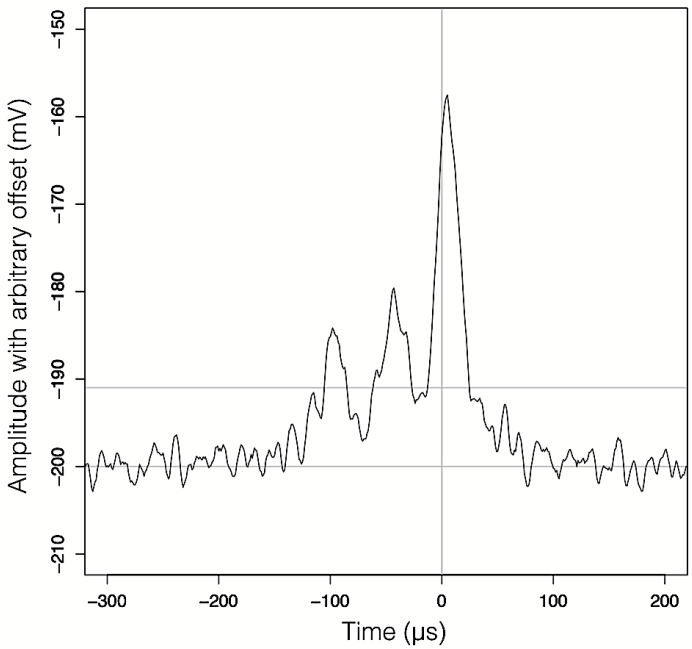

Figure 4.3: Neutron event showing the main peak and two minority peaks.

Knowing the drift distance travelled by an event, enables background events occurring at the cathode and MWPC to be vetoed. This is especially important for cathode events produced by the decay of Radon Progeny Recoils (RPR). RPRs are produced when ^{222}Rn gas, caused by isotope decay within surrounding materials, mixes with the target gas volume and decays to produce the cation, ^{218}Po. The cation drifts toward the cathode, where it can become trapped within the cathode material and decays to produce ^{214}Po and ^{210}Po nuclei, which can then recoil in the gas volume near to the cathode plane. Most of these events can be tagged and removed with the identification of an accompanying alpha particle, which is produced during the decay process. Figure 4.4 shows an example RPR with coincident alpha event, which can be clearly identified by the multiple wire hits caused by it's long ionisation trail. If the alpha particle becomes trapped within the cathode material, however, it is not detected and the RPR recoil can mimic a WIMP signal. This is mostly avoided with the implementation of a thin film aluminised-mylar cathode of 0.9 μm thick, which prevents the majority of alphas from becoming trapped [106]. The remaining RPRs are vetoed by cutting all events that occur within 2 cm of the central cathode.

The ability to veto background in three dimensions ensures that the target volume of gas is fully fiducialised. This along with the external neutron shielding and gamma rejection, allows for the elimination of all background above a certain threshold, and hence, enables the DRIFT-IId detector to run background free. This allowed the DRIFT collaboration to set limits on the possible mass and cross section of WIMP dark matter [105], which remain the most stringent for a detector with directional sensitivity. Section 4.3 looks to improve on these results using a new data analysis technique based on machine learning.

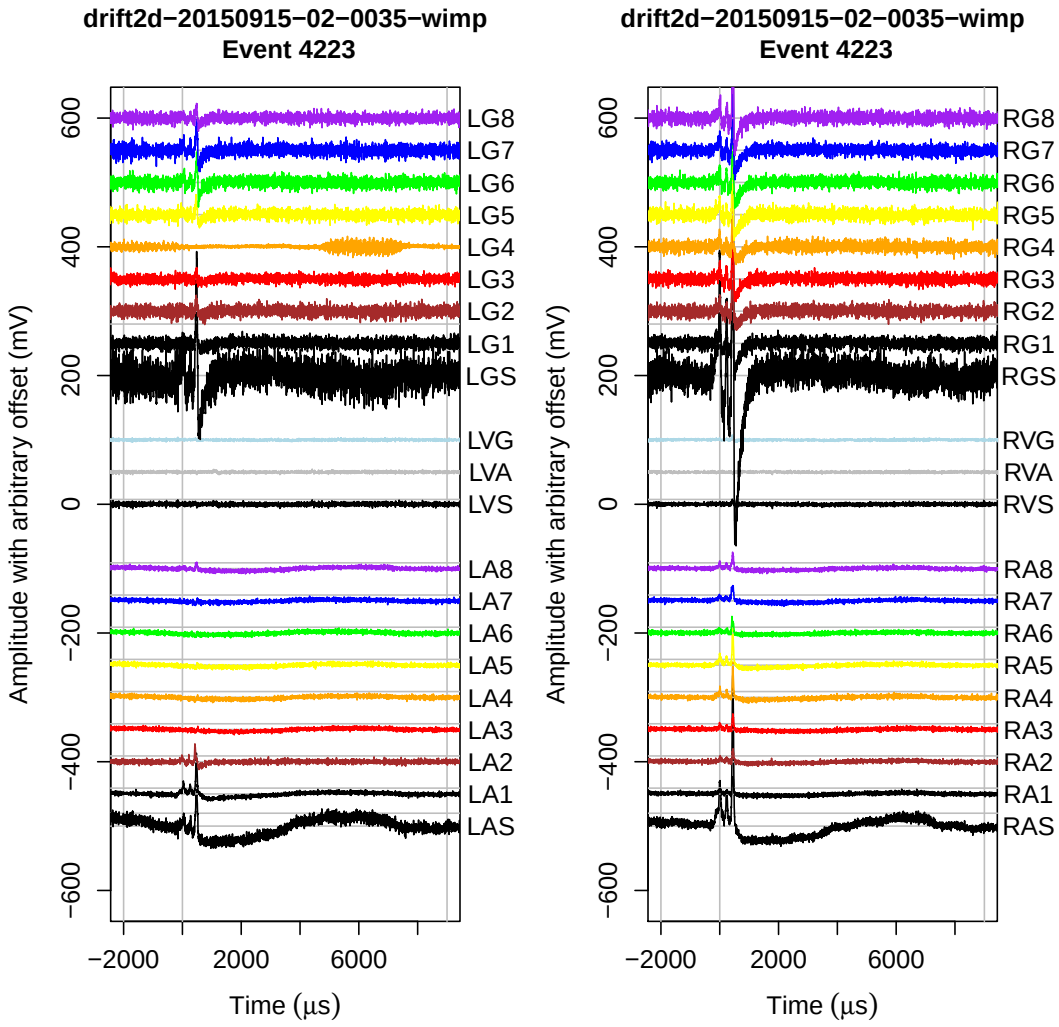

Figure 4.4: RPR recoil event originating from the cathode and triggering on the left MWPC anode wire groups 1 and 2 (LA1, LA2), and some of the grid wires, with associated alpha particle triggering on all of the anode and grid wire groups of the right MWPC (RA, GA). The index notation from 1 to 8 signifies the wire group. The wires labelled V are veto wire groups and S stands for the summed result of all triggered wires.

4.2 Event Rate

This section details the derivation used to predict the rate of SD WIMP interactions, occurring within the DRIFT-IId target volume, as a function of WIMP mass and cross section. The derivation assumes a spherical, isothermal, galactic halo of non-relativistic WIMP dark matter as predicted by ΛCDM. Although DRIFT-IId does contain spin independent targets, the main target is the spin dependent (SD) fluorine found in CF_4 gas. Fluorine's dependency on spin is due to it possessing an odd number of protons (9), which gives the element the same spin as the proton: $\frac{1}{2}$. The following section and the analysis performed in Section 4.3 focuses exclusively on a SD search for WIMP dark matter using a fluorine target.

4.2.1 Basic Rate

This section develops a basic rate equation from first principles by assuming a constant WIMP wind velocity magnitude, v_0, and by invoking a classical hard sphere approximation for nuclei interactions.

For a WIMP particle traversing, at speed v_0, through a cubic volume of gas with side length L, the expected rate of elastic interactions between the particle and fluorine nuclei is,

$$\frac{N_0 v_0 \sigma_{WN}}{L^3} \tag{4.1}$$

where σ_{WN} is the WIMP-nuclei cross section and N_0 the number of fluorine nuclei. The latter is given as,

$$\frac{N_A(mol^{-1}) \times M_{total}(kg)}{17.85 \times 10^{-3}(kg\, mol^{-1})} \tag{4.2}$$

where the denominator is the molar mass of fluorine, M_{total} is the total

mass of fluorine in the detector and N_A is Avogadro's constant.

Predictions of the local dark matter density vary, Ref [107] suggests that it could be 3.9×10^5 GeV c^{-2} m^{-3}. However, to compare the results of this chapter to previous DRIFT-IId results [105], the same standardised local dark matter density, ρ_W, of 3.0×10^5 GeV c^{-2} m^{-3} is used. With this density, a volume of size L^3 (measured in m^3) contains a number of dark matter particles, of mass M_W, given by,

$$\frac{L^3\rho_W}{M_W} \tag{4.3}$$

The expected rate of interactions from this number of WIMPs is given as the product of the expected rate from a single WIMP (Eq. 4.1) with Eq. 4.3,

$$R_0 = \frac{N_0\rho_W v_0\sigma_{WN}}{M_W} \tag{4.4}$$

DRIFT-IId is used to search for WIMP-nucleon interactions within the gas volume via the recoil's they produce, which have an energy,

$$E_R = \frac{\mu^2 v_0^2}{M_F}(1-\cos\theta) \tag{4.5}$$

Here M_F is the fluorine mass in GeV c^{-2}, θ is the scattering angle and μ is the reduced mass of the WIMP-nucleus system in the interaction centre of mass frame,

$$\mu = \frac{M_F M_W}{M_F + M_W} \tag{4.6}$$

The maximum possible recoil energy, which occurs at $\theta = \pi$, is

$$E_R^{max} = \frac{2\mu^2 v_0^2}{M_F} \tag{4.7}$$

Assuming that the scattering angle is random and uniform, the normalised probability of a recoil of energy E_R occurring, $p(E_R)$, must be constant for all recoil energies and is given, therefore, as the reciprocal of E_R^{max},

$$p(E_R) = \frac{M_F}{2\mu^2 v_0^2} \tag{4.8}$$

Factoring this probability into Eq. 4.4 gives the differential rate,

$$\frac{\mathrm{d}R}{\mathrm{d}E_R} = R_0 p(E_R) = \frac{N_0 M_F \rho_W \sigma_{WN}}{2M_W \mu^2 v_0} \tag{4.9}$$

4.2.2 Velocity Distribution

In this section, the singular value given for the dark matter velocity magnitude, v_0, is replaced by a more realistic Maxwell-Boltzmann velocity distribution of the form,

$$f(v) = e^{-\frac{v^2}{v_0^2}} \tag{4.10}$$

Substituting v_0 in Eq. 4.9 with v (a value between the minimum and maximum possible velocity magnitude) and then multiplying by the velocity distribution described by Eq. 4.10 and integrating gives,

$$\frac{\mathrm{d}R}{\mathrm{d}E_R} = \frac{R_0 p(E_R)}{2\pi v_0^2} \int \frac{f(v)}{v}\, \mathrm{d}^3 v \tag{4.11}$$

where $2\pi v_0^2$ is a normalising constant that returns unity for a 4π velocity distribution with integration limits of 0 and infinity. More accurate integration limits would be v_E (the magnitude of the Earth's velocity relative to the dark matter distribution) and v_{esc} (the magnitude of the galactic escape velocity). Ref [108] shows that integrating Eq. 4.11 between these limits gives,

$$\frac{\mathrm{d}R(v_E, v_{esc})}{\mathrm{d}E_R} = R_0 p(E_R) k \times \left[\frac{\pi^{1/2}}{4} \frac{v_0}{v_E} \left(\mathrm{erf}\left(\frac{v_{min} + v_E}{v_0} \right) - \mathrm{erf}\left(\frac{v_{min} - v_E}{v_0} \right) \right) - \exp\left(\frac{-v_{esc}^2}{v_0^2} \right) \right] \tag{4.12}$$

Here, v_{min} is the minimum velocity required to produce a recoil of energy E_R, given by $(p(E_R)E_R)^{1/2} v_0$, and k is a scaling factor that accounts for the change in integral upper limit from infinity to v_{esc}. The value of k is close to unity, given as 0.9965 [108].

4.2.3 Cross Section

The classical approach used, in the previous section, to calculate the WIMP interaction rate is only valid where the target nucleus de Broglie wavelength, $\lambda = 2\pi\hbar/q$ (where q is the momentum of the recoiling nucleus), is far greater than it's size. For the majority of fluorine recoils, the momenta produces a λ not much greater than the size of the nucleus and the classical approximation becomes less accurate. This leads to a form factor correction, $F(qr_n/\hbar)$, to the interaction cross section, where r_n is the radius of the target nucleus.

Dividing by $\hbar$ (from here on $\hbar = 1$) makes the form factor a dimensionless number that can be used to scale the cross section such that,

$$\sigma_{WN} = F(qr_n)^2 \sigma_0 \tag{4.13}$$

where σ_0 is the cross section at the limit of zero momentum transfer. For SD interactions the form factor can be approximated as [108],

$$F(qr_n)^2 = \begin{cases} [\sin(qr_n)/qr_n]^2 & (qr_n < 2.55,\ qr_n > 4.5) \\ 0.047 & (2.55 \leq qr_n \geq 4.5) \end{cases} \tag{4.14}$$

For a fluorine target, $r_n \approx 1.0$ fm $\times 19^{1/3} = 2.7$ fm and q can be converted to E_R via, $0.5 \times q^2 \times M_F^{-1}$. The form factor remains dimensionless by dividing through by $\hbar c$. This allows the form factor to be plotted as a function of E_R for fluorine, as shown by Figure 4.5.

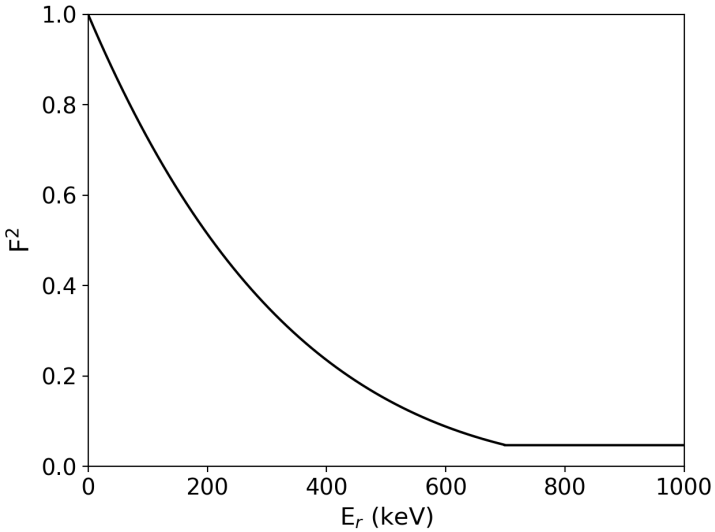

Figure 4.5: Form factor correction as a function of recoil energy for fluorine.

The above figure shows that the form factor reaches a constant value of 0.047 at a recoil energy of ∼700 keV, this corresponds to the point at which qr_n, in Eq. 4.15, is greater than 2.55.

The DRIFT-IId detector has an upper threshold on it's fiducial volume of 6000 NIPs (Negative Ion Pairs), for fluorine nuclei this corresponds to a recoil energy threshold of around 200 keV and, therefore, a maximum qr_n of ∼0.18. For this reason, the form factor correction to the WIMP-nucleus cross section, for SD searches conducted with the DRIFT-IId detector, is given as,

$$F(E_R r_n)^2 = \frac{\sin^2(E_R r_n)}{(E_R r_n)^2} \tag{4.15}$$

In order to compare WIMP search results between different detectors using different SD targets, the WIMP-proton cross section (at the limit of zero momentum), σ_{Wp}, is used in place of σ_0. A relation between the two is given by [109],

$$\sigma_0 = \sigma_{Wp} \frac{C^p_{WN}}{C_{Wp}} \frac{\mu^2}{\mu_p^2} \tag{4.16}$$

where, μ_p and μ are the WIMP-proton and WIMP-nucleon reduced masses in the centre of mass frame, C_{Wp} is a dimensionless correction to the cross section for a WIMP-proton scatter and C^p_{WN} is the correction factor applied due the proton contribution to the WIMP-nucleon cross section. Substituting the above two equations into Eq. 4.13 gives,

$$\sigma_{WN} = \frac{\sin^2(E_R r_n)}{(E_R r_n)^2} \sigma_{Wp} \frac{C^p_{WN}}{C_{Wp}} \frac{\mu^2}{\mu_p^2} \tag{4.17}$$

4.2.4 Differential Rate Equation

Scaling Eq. 4.9 by Eq. 4.15 (the form factor) and replacing σ_{WN} with Eq. 4.17, gives,

$$\frac{\mathrm{d}R}{\mathrm{d}E_R} = R_0(\sigma_{Wp})p(\mu_p) = \frac{\sin^2(E_R r_n)}{(E_R r_n)^2}\frac{C^p_{WN}}{C_{Wp}}\frac{N_0 M_F \rho_W \sigma_{Wp}}{2M_W \mu_p^2 v_0} \tag{4.18}$$

This then provieds a final expression for the differential event rate equation,

$$\frac{\mathrm{d}R(v_E, v_{esc})}{\mathrm{d}E_R} = R_0(\sigma_{Wp})p(\mu_p)k$$
$$\times \left[\frac{\pi^{1/2}}{4}\frac{v_0}{v_E}\left(\mathrm{erf}\left(\frac{v_{min}+v_E}{v_0}\right) - \mathrm{erf}\left(\frac{v_{min}-v_E}{v_0}\right)\right) - \exp\left(\frac{-v^2_{esc}}{v_0^2}\right)\right] \tag{4.19}$$

where, R_0 is now a function of σ_{Wp}, not σ_0, and p is a function of μ_p, not μ. Table 4.1 summarises the other parameters that make up the rate equations.

Table 4.1: Parameters, either predicted or measured, that make up the rate equation, other than the WIMP mass or cross section which are unknown.

Parameter	Value	Units	Ref
ρ_W	0.3	GeV c^{-2} cm^{-3}	[110]
v_0	230	km s^{-1}	[111]
v_E	260	km s^{-1}	[108]
v_{esc}	600	km s^{-1}	[112]
C^p_{WN}/C_{Wp}	0.91	-	[109]
k	0.9965	-	[108]

Figure 4.6 shows a plot of Eq. 4.19 for $M_F = 0.024$ kg (the DRIFT-IId fiducialised fluorine mass, see Section 4.3.2), $M_W = 100$ GeV c^{-2} and $\sigma_{Wp} = 0.1$ pb.

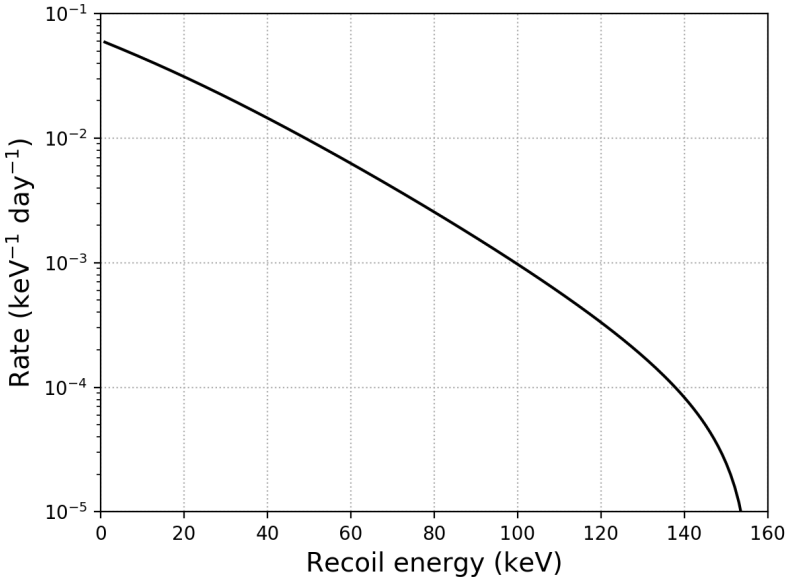

Figure 4.6: An example of the expected SD WIMP recoil rate, as a function of recoil energy, inside the DRIFT-IId detector, for 100 GeV c^{-2} WIMPs with a 0.1 pb cross section.

The downturn at higher energies, seen in the above figure, is due to the $\sin^2$ function included in Eq. 4.15.

A remaining scaling factor for the differential rate equation is the DRIFT-IId detector efficiency. The next section describes an analysis that improves the current efficiency, resulting in an increased sensitivity to the detectable rate, and therefore, to a larger range of WIMP masses and cross sections.

4.3 Data Analysis

The latest published DRIFT-IId dark matter exclusion limits are given by Ref. [105], since this result, there has been an additional ∼100 days of run time. An updated limit, including this run time, is given by Ref. [113]. This section describes efforts to improve the efficiency of the DRIFT-IId analysis, used previously, by employing a machine learning algorithm similar to that described in Chapter 3.

4.3.1 Data Selection and Calibration

Machine learning works by training and testing an algorithm on data that is known to be, in this case, either signal or background. For the signal data, DRIFT-IId was exposed to a ^{252}Cf source, placed 10 cm above, and at the centre of, the TPC vessel. The source produced neutrons at a rate of $2.8 \pm 0.2 \times 10^3$ s^{-1} [105], a portion of which entered the fiducial volume and caused nuclear recoils that mimicked a WIMP signal. A total 0.9 days of neutron exposure was used to train and test the algorithm on signal recognition. For the background data, 100 days of previously analysed WIMP search data [113] was used, along with gammas produced during 3 days of exposure to $\times 3$ ^{60}Co sources, placed on top of the vessel. For the WIMP search, 55 days of previously analysed data was used in order to compare the results to the published ∼55 days [105]. Table 4.2 gives the list of files (as stored on the HEP file cluster at the University of Sheffield) containing the recoil data discussed and gives their usage as either background, signal or WIMP search.

Table 4.2: DRIFT-II data files used for the analysis.

Start	End	Usage	Days
drift2d-20141204-03-wimp	drift2d-20150701-02-wimp	Background	99.99
drift2d-20150223-03-co60	drift2d-20150224-01-co60	Background	2.98
drift2d-20151002-01-neut	drift2d-20150619-01-neut	Signal	0.90
drift2d-20150709-02-wimp	drift2d20151002-02-wimp	WIMP search	55.24

The avalanche field between the grid and anode arrays of the MWPCs (see Section 4.1) causes multiplication of each ionised electron, captured within the field, by a factor of ∼1000 [114]. The electronics used by DRIFT then amplifies this signal further. The total signal amplification is known as the gain of the detector and it helps to provide a better signal to background ratio. However, the original NIPs (Number of Ionised Pairs) caused by a recoil event is lost. In order to regain this information the detector needs to be calibrated using a source that produces recoils of a known energy. All of the data used in this section was calibrated by regularly exposing the fiducial volume to two ^{55}Fe sources, located behind each MWPC. The sources were placed behind an automated shutter that opened every six hours for approximately three minutes. During this exposure the 15 mV hardware threshold was lowered to enable 5.9 keV electron recoils, caused by the photoabsorbtion of ^{55}Fe X-rays, to be recorded. This produced a signal of known energy that was used, along with the gas mixture W value (25.2±0.6 eV [115]) and the recorded pulse heights, to calibrate the gain of each MWPC, enabling the deposited recoil energy to be reconstructed.

4.3.2 Recoil Discrimination Parameters

After some initial waveform processing, involving the removal of high and low frequency noise (originating, respectively, from the cathode and mains supply), any event passing a hardware threshold of 15 mV was recorded by the DAQ. This section describes the parameters, derived from the recorded

waveforms, used to remove background events from the data.

The first parameter cuts used were boolean in nature, such that, any events producing a 'true' response to the following were identified as background and removed:

1) Triggered 8 or more wires. An event that causes 8 wires to trigger has an ionisation trail of at least 16 mm in length and is, therefore, most likely an alpha event.

2) Triggered both MWPCs simultaneously. A WIMP interaction is extremely unlikely to occur on both sides of the detector at the same time.

3) Produced non-contigouos wire hits. A recoiling nucleus is expected to produce an uninterrupted trail of ionisation.

4) Originated within 11 cm of the MWPCs. For these events, the drift time is too short for the minority carries to separate out and produce clear peaks (see Section 4.1 and Figure 4.3). Therefore, the positional reconstruction along the drift direction can not be trusted.

5) Occurred within 2 cm of the cathode. These events have most likely originated from the cathode, as described in Section 4.1.

6) Produced more than 6000 NIPs. This corresponds to a recoil energy greater than 200 keV, which can only be produced by a WIMP with a velocity magnitude exceeding the escape velocity of the Galaxy, see Section 4.2.2.

The effect of cut 4 and 5, along with the veto region around the MWPCs (see Section 4.1), is to create a DRIFT-IId fiducial volume, V, of,

$$2 \times 0.8\,\mathrm{m}^2 \times (0.48 - 0.11)\,\mathrm{m} = 0.59\,\mathrm{m}^3 \tag{4.20}$$

where, the reduction in area from 1 m^2 to 0.8 m^2 is due to the presence of the veto and guard wires. For a CF_4 pressure, P, of 10 Torr at a room temperature, T, of 300 K, the total fiducialised SD mass of DRIFT-IId is,

$$\frac{PM_{CF_4}V}{R_{gas}T} = 24.1g \tag{4.21}$$

where R_{gas} is the gas constant given as 0.062 m^3 Torr K^{-1} mol^{-1} and M_{CF_4} is the total molar mass of fluorine contained within a CF_4 molecule, given as, 4×19 g mol^{-1} = 76 g mol^{-1}.

The next stage of cut parameters were based on continuous values, such as the anode wire hit parameter, which, after the 8 wire cut, has a value of between 1 and 7. The continuous parameters used for the analysis are listed in Table 4.3.

Table 4.3: The continuous parameters used to remove background from the DRIFT-IId data.

Anode hits	The number of anode wires hit.
Risetime	The duration between 10% and 90% of the maximum pulse height recorded on the anode wires.
Peak Ratio	The ratio of the minority peaks to that of the main peak (see Figure 4.3).
Grid NIPs	The response induced on the grid wires, converted to NIPs.
Grid/anode	The ratio of Grid NIPs with the NIPs detected on the anode wires.

Figure 4.7 shows probability density histograms for the parameters listed in Table 4.3 for signal (red) and background (blue) events. It can be seen from this figure that, for each parameter shown, at least some separation exists between signal and background events. Other parameters were investigated but did not show enough clear separation between the two types of events.

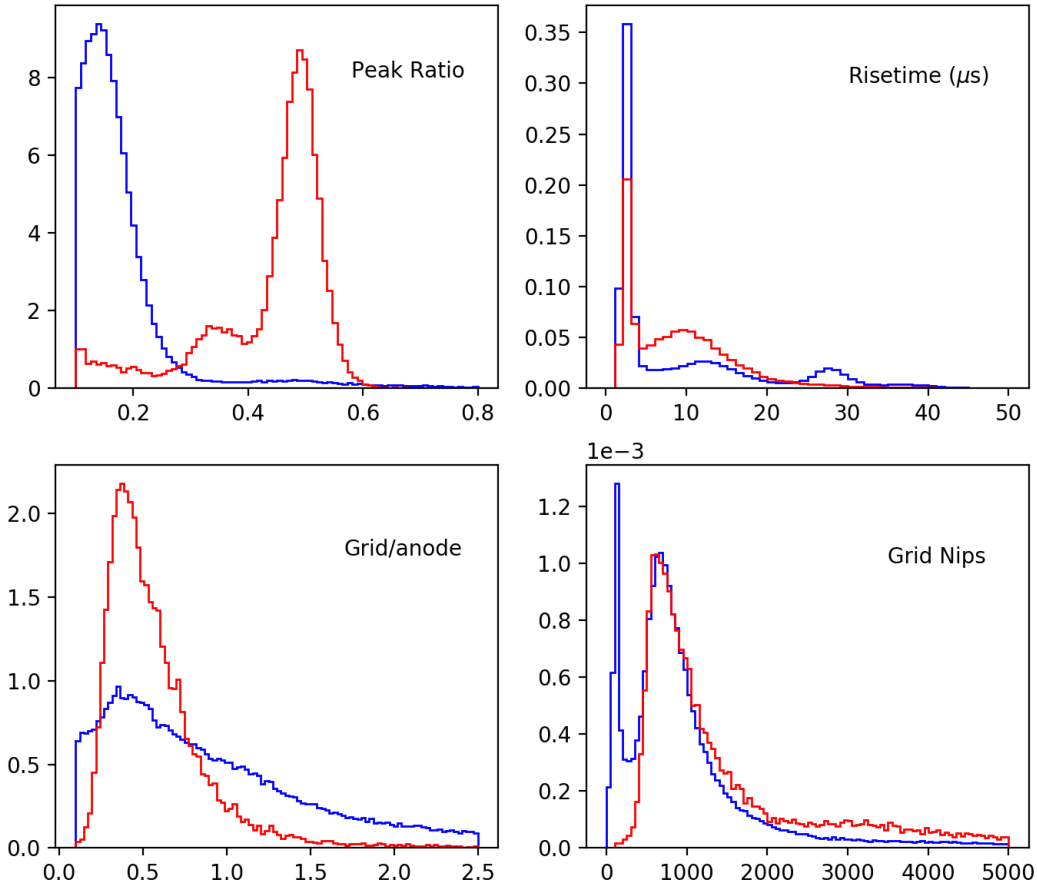

Figure 4.7: Probability density histograms for the parameters listed in Table 4.3 for background (blue) and signal (red) events. The x-axis gives the parameter value and the y-axis gives the probability in arbitrary units.

The standard way of producing cuts, for the parameters listed in Table

4.3, would be to investigate the best cut positions from the type of histograms shown in Figure 4.7. For the new analysis described in the next section, the boolean cuts were applied to the recoil data first (reducing the background by 27%) and the remaining recoil parameter data were used to produce a more complex background rejection model based on machine learning.

4.3.3 Analysis Algorithm

A python machine learning algorithm, called a Random Forest Classifier (RFC) [103], was used to produce a new type of DRIFT-IId analysis. The algorithm is based on the DT method for finding the best parameter cut positions that maximise signal to background separation. This method was used in Section 3.5 of Chapter 3 to study the low energy background rejection capability of a simulated next generation detector. Figure 3.10 of Section 3.5 shows how a decision tree separates data based on the best parameter cut locations. An RFC algorithm produces multiple DTs using the signal and background recoil parameter data described in the previous section. It then computes an averaged result from all of the trees to provide a better overall background rejection, compared to that of a single tree. The accuracy of the analysis can be optimised by setting the depth and number of DTs. The depth selects the DT level used by the analysis, which was described in Section 3.5 of Chapter 3. Selecting a depth too small would limit the decision tree's ability to separate signal from background, whilst selecting a depth too large would overfit the data during training and produce a less accurate result when tested. Increasing the number of trees used by the RFC creates a more accurate averaged result. However, this also increases the CPU time involved and, at some point, a larger number of trees either no longer improves the result or provides such a small improvement that the trade-off in CPU time is not beneficial.

The total 103 background and 0.9 signal days, listed in Section 4.3.1, were split such that 80% was used to train the analysis and 20% was used to

test the resulting analysis model. The data selection was stratified so that the same ratio of background to signal events was maintained for both the training and testing data sets. After training, the RFC returned a probability score, for each event, between 0 (most likely background) and 1 (most likely signal). A confidence cut with a value between 0 and 1, was then found that removes all of the background from the training data. The percentage of remaining signal events, after the confidence cut was applied, gave the analysis cut efficiency. The accuracy of the analysis model produced by the RFC was then checked using the test data set. If the model incorrectly identified a large percentage of the test data background events as signal, then it was not an accurate model. Conversely, if all background events from the test data were correctly rejected but the analysis efficiency was significantly reduced, compared to the training analysis efficiency, then the RFC model was overfitted to the training data. By fine tuning the depth and number of decision trees, used by the analysis, the most accurate and efficient model was achieved. This was found to occur for a DT depth and number of 12 and 1000, respectively, with a confidence cut of 0.982. This model still incorrectly identified 2 events (from the test set) as signal, which were later rejected by eye.

The 2 events are shown to the left and centre in Figure 4.8 and can be compared to an example signal event, from a neutron recoil, shown to the right in this figure. The waveform profile of the centre image, obviously does not compare to that of a nuclear recoil of similar energy and distance from the readout, shown on the right. The second event, shown to the left in Figure 4.8, was about half the energy of the other event and was slightly more ambiguous, and therefore, less straight forward to reject. However, comparison of the anode sum line of this event, labelled LAS (Left Anode Sum) on the figure, and that of the nuclear recoil event, labelled RAS (Right Anode Sum), revealed a clear profile difference between them that was used to reject the non-recoil event.

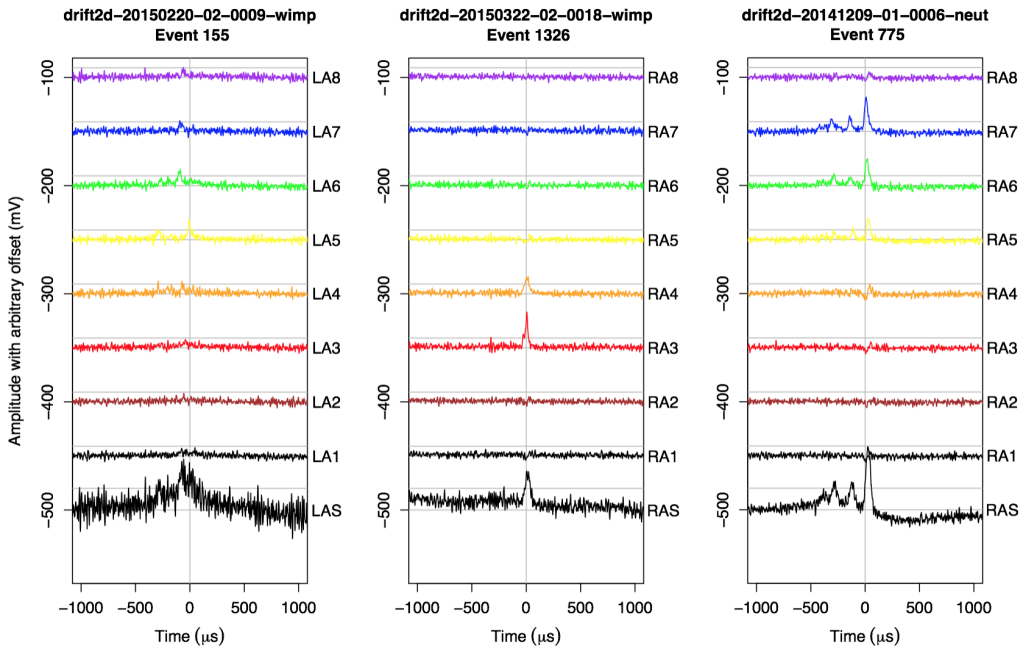

Figure 4.8: The left and centre images show the waveforms of the 2 events that passed the RFC testing. The right image shows the waveform of a nuclear recoil with the same z position (∼35 cm) as the 2 events and the same energy (∼4000 NIPs) as the event shown in the centre image.

4.3.4 Improved Detector Efficiency

The cut efficiency of the model produced by the RFC analysis was converted into a detector efficiency by comparing the amount of signal identified by the model to that predicted by simulation. The simulated GEANT4 results used to study the detector efficiency are those used by Ref [105] for the same purpose. The simulation produced 0.9 billion neutrons, originating from the ^{252}Cf source position described in Section 4.3.1. To reduce the CPU time, the simulation was run at 25 times the actual gas pressure, which was possible as the probability of multiple scattering was found to be negligible (via simulation) at this higher pressure. For each simulated neutron event, that produced a recoil inside the DRIFT-IId gas volume, the resulting recoil

type, energy and distance from the readout, d, were recorded. The recoil energy was converted to NIPs using known conversion rates that take into account the quenching factor per recoil energy and the W value of the gas. The conversion rates, up to 100 keV$_r$, are shown in Table 4.4.

Table 4.4: NIPs conversion rates for neutron events simulated inside the DRIFT-IId detector. C =carbon, F = fluorine, S = sulfur. Values from [105].

keV$_r$	C NIPs	F NIPs	S NIPs
10	164	140	115
20	395	332	259
30	659	552	416
40	946	792	588
50	1243	1055	773
60	1559	1326	966
70	1877	1616	1167
80	2205	1911	1370
90	2547	2223	1575
100	2886	2528	1788

The DRIFT-IId fiducial volume was binned into energy and d, using a bin width of 250 NIPs and 2 cm, respectively. For each bin, the ratio between signal correctly identified by the RFC analysis and signal predicted by the simulation was evaluated. The result is shown as a false colour heat map in Figure 4.9 (left), where white represents 100% efficiency and red represents no efficiency. This can be compared to the efficiency map achieved using the standard DRIFT-IId analysis [105], shown to the right in this figure, which uses the same false colour scale.

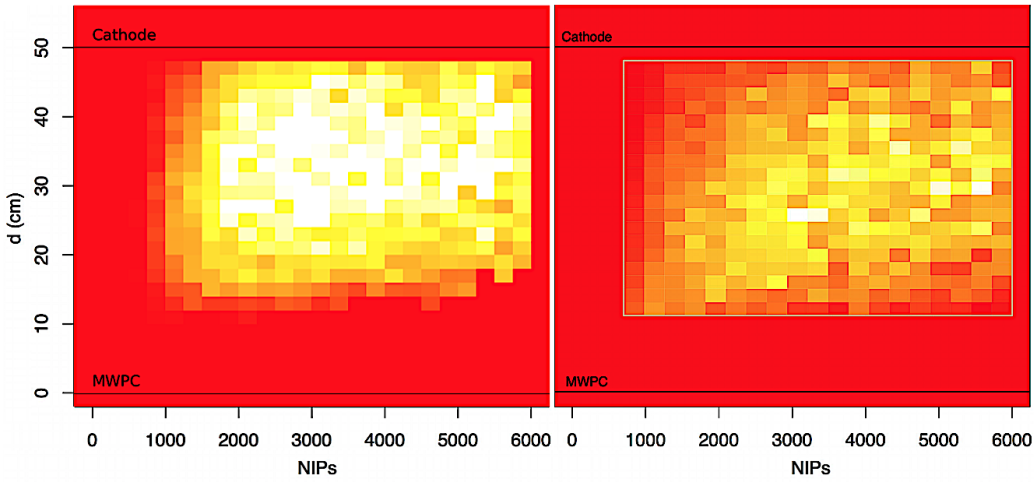

Figure 4.9: Efficiency maps for the RFC analysis (left) and the standard analysis (right). White = 100%, red = 0%. The image on the right was taken from [105].

It is clear, from a comparison of the two images in the above figure, that the RFC analysis model improves the detector efficiency. For the standard analysis, Figure 4.9 (right) shows a reduction in efficiency at high NIPs values and low d, and at high d values and low NIPs. The former is due to high energy events producing a large main peak, which causes the peak ratio parameter cut to remove the majority of these events. The latter is due to the larger amount of diffusion, experienced by charge drifting from high d, which dampens the signal amplitude and pushes either the main peak or the minority peaks below threshold. These effects are still apparent in Figure 4.9 (left) for the RFC analysis, however, the reduction in efficiency is much less. This is a result of the DT analysis method, which does not remove events that fail a parameter cut but instead treats the data as a separate group of recoils that can be subject to further analysis. Therefore, a signal event that fails one parameter cut can still be identified as signal, by a DT, if it passes further data reduction stages. Figure 4.10 shows the detection efficiency averaged over each of the NIPs bins shown in Figure 4.9 (left). The

y error, in this figure, is given as $\sqrt{\text{detected}}/\text{predicted}$ and the error in x is the energy bin width (250 NIPs).

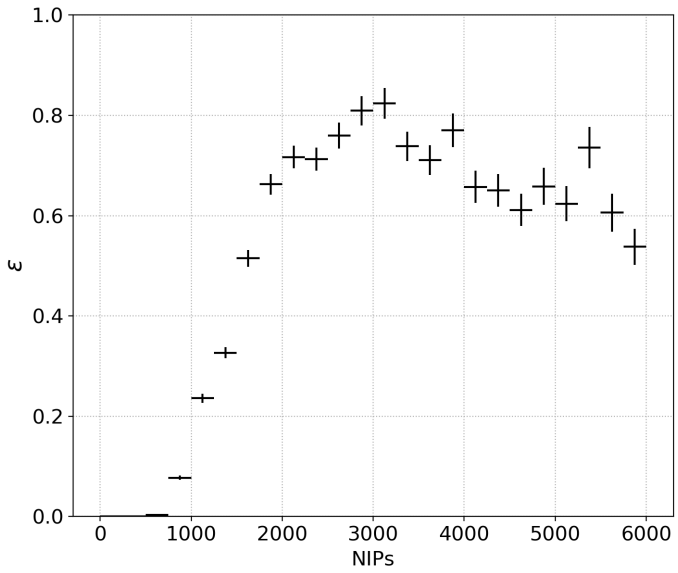

Figure 4.10: The detector efficiency, as a function of NIPs for the RFC analysis.

As expected, the above figure shows a drop off in efficiency at lower and higher NIPs values. This is due to, respectively, the loss of minority peak information at low energy and the large main peaks that can occur at higher energies, as previously explained.

4.4 Improved Limit Curve Result

The RFC analysis model, described in Section 4.3.3, was applied to 55 days of WIMP search data. After which, it was found that 2 events remained within the fiducial volume. As with the 2 events remaining after the RFC testing (see Section 4.3.3), examination of these events by eye, revealed that neither

response was consistent with the expected signal profile of a nuclear recoil. The two events in question, shown to the left and centre of Figure 4.11, were very similar in appearance, z position and energy. However, neither event resembles the nuclear recoil, with similar z and energy, shown to the right of Figure 4.11.

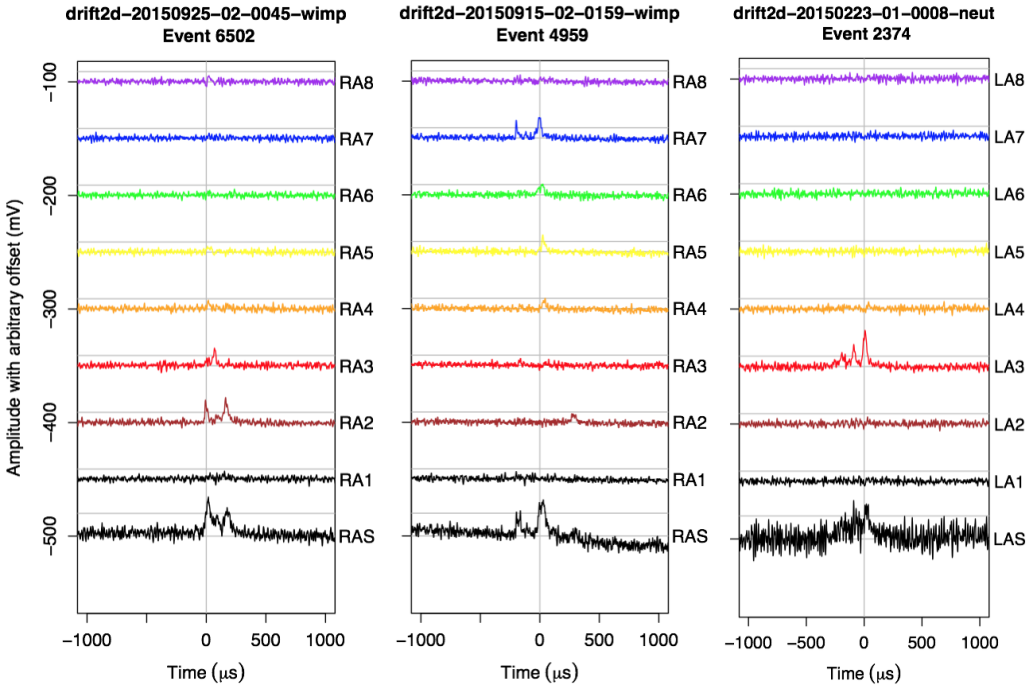

Figure 4.11: The left and centre images show waveforms of the two events left over after the RFC WIMP search analysis. Both events have a NIPs value of ∼1500 and a z position of ∼20 cm. For comparison, the right image shows the waveform of a nuclear recoil with 1400 NIPs and a z position of 22 cm.

The left and centre images on the above figure do include multiple peaks, as expected for a gas with minority carriers (see Section 2.4.3 of Chapter 2). However, the profile of these peaks does not follow that expected of a nuclear recoil (shown by the image on the right of the above figure), on this basis, the events were rejected. As well as being used to perform WIMP search

analysis, a machine learning algorithm could be employed, in future work, to examine the waveforms of events and produce a more accurate minority peak ratio parameter (this parameter was described in Section 4.3.2). This would then improve the ability of the RFC analysis to reject events similar to those shown in Figure 4.11 (left and centre).

After the analysis the data shown in Figure 4.10 was used to scale the WIMP rate (per WIMP mass and cross section) to give a detectable rate and produce a new DRIFT-IId dark matter exclusion limit. To achieve this the differential rate given by Eq. 4.19 was integrated over the interval E_1 and E_2, which are the lower and upper edges of the energy bins used to study the detector efficiency. The solution is not a simple or short expression so for the sake of brevity the following are defined,

$$\begin{aligned}
\exp_+(E_2,E_1) &= \exp\left(-\sqrt{p(E_R)E_2}+\frac{v_E}{v_0}\right)^2-\exp\left(-\sqrt{p(E_R)E_1}+\frac{v_E}{v_0}\right)^2\\
\exp_-(E_2,E_1) &= \exp\left(-\sqrt{p(E_R)E_2}-\frac{v_E}{v_0}\right)^2-\exp\left(-\sqrt{p(E_R)E_1}-\frac{v_E}{v_0}\right)^2\\
\mathrm{erf}_+(E_2,E_1) &= \mathrm{erf}\left(\sqrt{p(E_R)E_2}+\frac{v_E}{v_0}\right)-\mathrm{erf}\left(\sqrt{p(E_R)E_1}+\frac{v_E}{v_0}\right)\\
\mathrm{erf}_-(E_2,E_1) &= \mathrm{erf}\left(\sqrt{p(E_R)E_2}-\frac{v_E}{v_0}\right)-\mathrm{erf}\left(\sqrt{p(E_R)E_1}-\frac{v_E}{v_0}\right)
\end{aligned} \tag{4.22}$$

where, v_0 and v_E are defined in Section 4.2.1 and Section 4.2.2 respectively and their values are given in Table 4.1. $p(E_R)$ is defined by Eq. 4.8. The function arguments differ from those given in Eq. 4.19 as v_{min} has been converted to E_R. With the above expressions the solution to the rate equation for the finite energy region E_1 and E_2 is,

$$R(E_1,E_2)=\varepsilon(E_R)\frac{F(E_1r_n)+F(E_2r_n)}{2}\frac{C^p_{WN}}{C_{Wp}}\frac{R_0(\sigma_{Wp})}{E_0(\mu_p)}\frac{k_0}{k_1}\left[\frac{\sqrt{\pi}}{4}\frac{v_0}{v_E}\times\right.$$
$$\left(\sqrt{\frac{(E_2-E_1)E_0}{\pi}}(\exp_+(E_2,E_1)-\exp_-(E_2,E_1))-\frac{E_0v_E}{\sqrt{\pi}v_0}(\exp_+(E_2,E_1)+\exp_-(E_2,E_1))+\right.$$
$$(E_2-E_1)(\mathrm{erf}_+(E_2,E_1)-\mathrm{erf}_-(E_2,E_1))+E_0(\frac{v_E}{v_0})^2(\mathrm{erf}_-(E_2,E_1)-\mathrm{erf}_+(E_2,E_1))+$$
$$\left.\left.\frac{E_0}{2}(\mathrm{erf}_-(E_2,E_1)-\mathrm{erf}_+(E_2,E_1))\right)-(E_2-E1)e^{\left(-\frac{v_{esc}}{v_0}\right)^2}\right] \tag{4.23}$$

where, $\varepsilon(E_R)$ is the detector efficiency between E_1 and E_2, as given in Figure 4.10 of the previous section, and $\frac{F(E_1r_n)+F(E_2r_n)}{2}$ is the mean form factor (see Eq. 4.15 of Section 4.2.3) between E_1 and E_2.

For a particular M_W, the lowest σ_{Wp} that could be excluded, at 90% confidence, was that which produced 2.3 events (based on poisson statistics). For each integer M_W between 10 and 10^4 GeV c^{-2} this σ_{Wp} was found as,

$$\sigma_{Wp}=2.3\left(\sum_{E_{min}}^{E_{max}}\frac{R(E_1,E_2)M_{total}t_{total}}{\sigma_{Wp}}\right)^{-1} \tag{4.24}$$

where M_{total} and t_{total} are the total mass of the detector and the total exposure time, respectively. This results in the RFC exclusion curve shown by the blue solid line in Figure 4.12, where all M_W and σ_{Wp} above the curve are excluded by DRIFT-IId (at a 90% CL). The current limit, published by Ref [105], derived using the standard analysis is shown by the red dashed line in this figure.

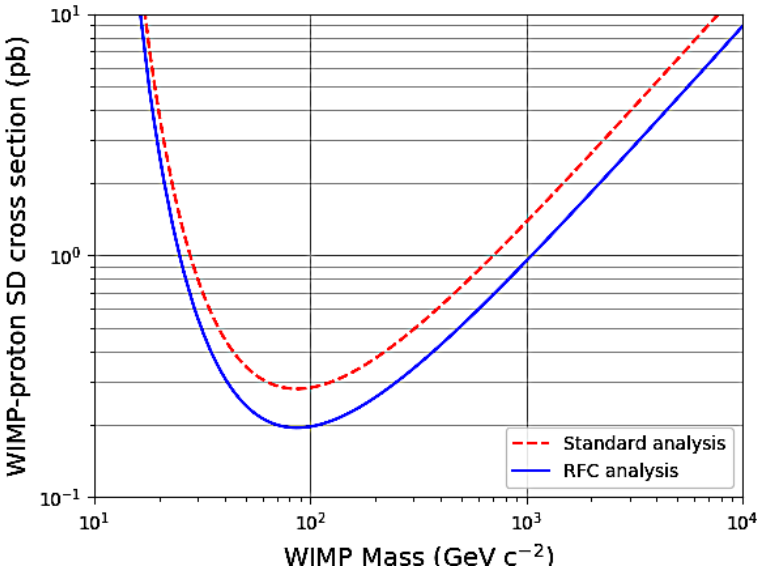

Figure 4.12: DRIFT-IId SD WIMP exclusion limits for the RFC analysis (blue solid line) and the standard analysis (red dashed line).

The lowest σ_{Wp} for the RFC analysis was 0.19 pb, which occurred at a M_W of 87 GeV c^{-2}. The improvement in efficiency at low energy ($<$ ~2000 NIPs) increased the detector's sensitivity to lower M_W. This can be seen in Figure 4.12, where the curve is shifted further to the left, compared to the standard analysis curve which has it's lowest point at a σ_{Wp} of 0.28 pb and a M_W of 100 GeV c^{-2}. This result corresponds to a 32% increase in cross-section reach with the new analysis.

4.5 Conclusion

The new RFC analysis, described in this chapter, improved the efficiency achieved by the standard analysis and as a result was able to exclude more of the SD WIMP search parameter space for the same mass and exposure time. Testing of the analysis algorithm revealed that two events remained from a total of ~21,000 background events, included in the test set, giving

a background rejection of 99.9998%. However, having to reject a few events by eye means that the analysis is not completely blind and will need some improvement in future. Part of this improvement will occur naturally as the RFC accuracy increases with the amount of training data available to it. The resulting 90% limit exclusion curve, from the RFC analysis, reaches a cross section of 0.195 pb at 100 GeV c^{-2} and 0.192 pb at 87 GeV c^{-2}. The difference in exclusion limits between the standard and RFC analysis is equivalent to an increase in sensitive target mass of almost one third. The readout spatial resolution of the DRIFT-IId MWPC is 2 mm, a next generation detector with improved resolution would consequently have a better signal to noise ratio, and therefore, a better background rejection than DRIFT-IId. This would increase the efficiency of a future detector beyond the results presented in this chapter. To this end, a prototype MWPC with 600 μm resolution was created, which is described in Chapter 7. The importance of detection efficiency is most notable when considering the running costs, of a large scale gas TPC, as a function of detector performance. For example, a 100% efficient (idealised) detector would take half the time to reach a particular WIMP search parameter space, compared to the same detector running at 50% efficiency, and therefore, would incur half the running costs in doing so. In conclusion, the increase in efficiency produced using machine learning based data analyses, will have a significant impact on the performance and total running cost of large mass next generation gas TPCs, such as those proposed in the following sections.

Chapter 5

CYGNUS-1000 TPC Background Study

The next goal for directional technology is to probe the WIMP parameter space below the neutrino floor. As described in Section 2.4.2 of Chapter 2, the unique ability to identify a recoil's direction could allow for a neutrino background rejection. To achieve this a directional detector would require a volume $\mathcal{O}(10^3)$ m^3, whether as a single unit or multiple units distributed across different underground sites. This chapter details work towards the first key step in determining the feasibility of a such an experiment, namely a detailed assessment of the backgrounds. This is achieved through the study of an example concept, termed CYGNUS-1000, comprising a 1000 m^3 monolithic detector filled with 20 Torr SF_6 gas, located at the Boulby Underground Laboratory. The gas was chosen for the reasons discussed in Section 2.4.3 of Chapter 2. Boulby was chosen due to the familiarity of the background levels and environment at this site. However, results could be extrapolated to other potential sites such as the Laboratori Nazionali del Gran Sasso (LNGS) for example.

GEANT4 [95] was used to model the geometry of the detector, as described in Section 5.1, and simulate the neutron and gamma backgrounds,

using the procedures described in Section 5.2. A separate procedure was used to simulate the rock background, which is described in Section 5.3. The strategy here was to work inwards from the rock walls, then the vessel and then finally the internal components. The background due to the rock wall and vessel material is discussed in Section 5.4 and the background due to the internal TPC components is discussed in Section 5.5. Other sources of background, originating from cosmic ray interactions and radon gas contamination, are discussed in Section 5.6. Finally, the potential search reach of CYGNUS-1000 is presented in Section 5.7.

Neutrons are of particular concern for dark matter detection as they can cause recoils within a target volume that mimic a WIMP signal, therefore, the goal here is to limit the neutron background to less than one per year within the recoil energy region of interest: 1 to 200 keV$_r$. This would mean that if a nuclear recoil event was observed within one year of running, the statistical analysis described by Feldman and Cousins [116] could be used to establish the event as signal at a 90% C.L. Using the same analysis, if the expected background rate was, instead, $\geq$one per year then this event would still be consistent with background. For this reason, a detector with a limit of less than one neutron event per year has a greater discovery potential and allows for the most stringent dark matter discovery limits to be established. Chapter 3.6 shows that it may become possible to discriminate up to 10^4 gamma induced electron recoils per year per keV, at and below a recoil energy of 10 keV, therefore, this was the goal for the gamma rejection study presented in this work. For the background study, the external, vessel and internal components were treated individually and the limits were applied separately in each case. The results can then be used to guide future studies that investigate the cumulative sum of background from a more specific TPC design, as is done in the following chapter.

A previous background simulation study, of a large scale gas TPC for dark matter detection, was conducted by Ref. [117]. However, this study

focused on higher pressure CS_2 gas (not low pressure SF_6 as is done here). Also, this study provides a more comprehensive review of the backgrounds from multiple readout and vessel material options and includes both neutron and gamma contributions. Further to this, the scale of detector considered here is much larger than considered in Ref. [117].

5.1 Vessel and TPC Geometry

The CYGNUS-1000 vessel was simulated as a cube of side length 10 m, located underground at Boulby. A simplified model was used for the simulations in which the vessel walls and gamma shielding were regarded as a single structure, referred to throughout this chapter as the 'vessel material'. The results can then be used in future, to help guide a more detailed design with the vessel and gamma shielding separated. The structural support required for the TPC vessel was not simulated directly, instead, results from the vessel background simulations, conducted for different thicknesses of steel and titanium, can be extrapolated to provide a background estimate for an averaged thickness of support structure. Figure 5.1 shows a GEANT4 generated image of the CYGNUS-1000 vessel located inside a rock cavern and surrounded by a neutron shield made of water (which is discussed in Section 5.4.1). A back-to-back configuration was envisioned for the TPC with a 50 cm drift region between the central cathode and each readout, an example of this configuration is shown by Figure 5.2. For a 10 m length, this resulted in 10 cathodes and 20 readouts with respective total areas of 1000 and 2000 m^2. Although a 50 cm drift distance was used here, the results can be extrapolated to study the background for other drift distances.

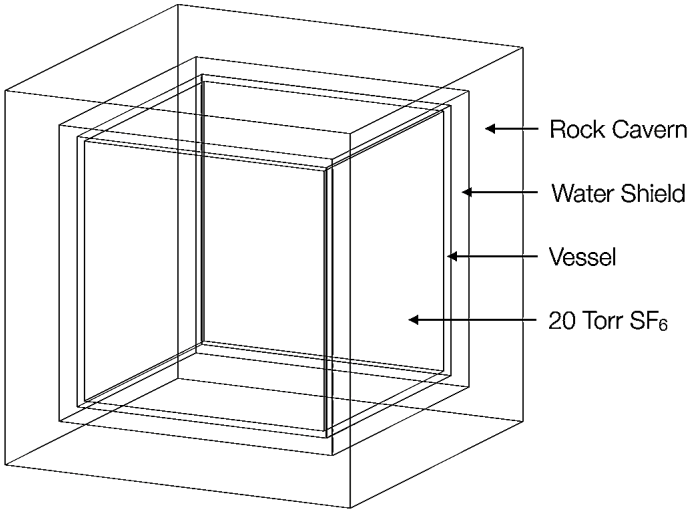

Figure 5.1: GEANT4 generated image of the CYGNUS-1000 vessel with surrounding water shield.

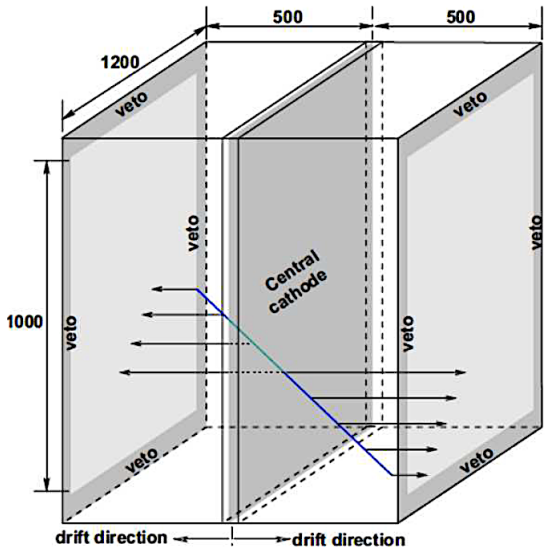

Figure 5.2: Example of a readout-cathode-readout, back-to-back configuration, taken from [118].

5.2 Simulation Procedure

The background studies were conducted using the highest radiopurity levels, for the materials, reported in the literature. These were sourced mainly from other dark matter search experiments, for instance, the steel and titanium values come from the LZ technical design report [119]. The material's ^{238}U, ^{232}Th and ^{40}K activities are listed in Table 5.1 and the rock salt activities used for Boulby are listed in Table 5.2.

Table 5.1: Materials used for the background simulations and their radiopurity levels given in mBq kg^{-1}.

Material	$^{238}_{92}$U	$^{232}_{90}$Th	$^{40}_{19}$K	Ref
Steel	0.27	0.49	0.40	[119]
Titanium	<0.09	0.23	< 0.54	[119]
Copper	< 0.012	< 0.0041	0.061	[120]
Acrylic	0.029	0.039	2.1	[121]
Silicon	< 12.35	< 4.07	< 6.81	[122]
Aluminium	< 0.52	1.94	< 6	[123]
Polyimide	< 36.79	< 27.52	< 410	[124] [125]
Kapton	< 98.77	< 36.59	58.82	[122]

Table 5.2: Salt rock activities in mBq kg^{-1} for Boulby.

$^{238}_{92}$U	$^{232}_{90}$Th	$^{40}_{19}$K	Ref
864	508	3.5×10^4	[122]

Table 5.1 shows that some up the reported radiopurity levels are upper limits. For this work, these limits are used as the actual measured value and results are discussed with this taken into account. Activities from other

isotopes are sometimes reported in the literature but the three most common were selected here to enable a direct comparison between the different materials. A ^{235}U radioactivity level of 0.0072 times the ^{238}U activity, based on the ^{238}U/^{235}U abundance ratio, was included for all neutron simulations.

Neutron production rates, due to spontaneous fission and (α,n) reactions, were obtained using Sources4C [126] for the materials listed in Table 5.1 and for the salt rock found at Boulby. These spectra were then input into the GEANT4 simulation, which produced the neutrons within the simulated material. The amount of neutron recoils observed within the gas volume during the simulation, R_n, could then be converted into a recoil rate per year, f_n, via,

$$f_n = \frac{R_n P_{tot} V_{tot} \lambda}{N_n} \tag{5.1}$$

Where, P_{tot} is the total neutron production rate from Sources4C, in units of m^{-3} yr^{-1} (mBq/kg)$^{-1}$, V_{tot} is the total material volume in m^3, N_n is the number of neutrons simulated and λ is the material activity in mBq kg^{-1}.

The gamma background was produced by homogeneously populating the material with the ^{238}U, ^{232}Th and ^{40}K isotopes. GEANT4 then automatically follows the full decay chain of each isotope, assuming secular equilibrium, and produces the associated gammas. A portion of the gammas enter the target gas volume where they Compton scatter and cause an electron recoil background. For each isotope, the amount of decays simulated, N_{decays}, the mass of the material under consideration, M, and the number of recorded electron recoils, R_{el}, were used to calculate the expected recoil rate per year, f_{el}, via,

$$f_{el} = \frac{R_{el} M \lambda}{N_{decays}} \tag{5.2}$$

5.3 Rock Background Flux

The simulation of a large rock cavern along with the transportation of background events through the rock can be extremely CPU intensive. Further to this, a large proportion of the simulated background may not emerge from the rock surface, resulting in a significant waste of CPU time. Instead of running such a simulation for each rock background study, the simulation was conducted once and the neutron and gamma flux at the rock surface was recorded. This flux was then used in subsequent simulations to create the background directly at the rock surface and the resulting recoil rate within the TPC gas volume, f, was calculated as,

$$f = \frac{RF_{tot}A_{surf}}{N} \tag{5.3}$$

where, R is the number of recoils detected, A_{surf} is the total surface area of the simulated rock cavern, F_{tot} is the total background flux (neutron or gamma) and N is the number of background events simulated.

5.3.1 Neutron Flux

To simulate the rock surface neutron flux, a Source4C spectrum, of the neutron production rate per energy in salt, was used by the GEANT4 simulation to populate a 5 m thick wall of salt rock with neutrons. Figure 5.3 shows the spectrum, which was calculated using the activities listed in Table 5.2 and a rock salt density of 2170 kg m^{-3} [127]. The starting depth of simulated neutrons that reached the rock surface was recorded and the flux was calculated using Eq 5.1, with R_n replaced by the number of neutrons reaching the surface. The rock neutron spectrum was produced using the correct activities so λ in Eq. 5.1 was set to unity. The resulting flux was divided by the rock surface area and is shown as a function of rock depth in Figure 5.4.

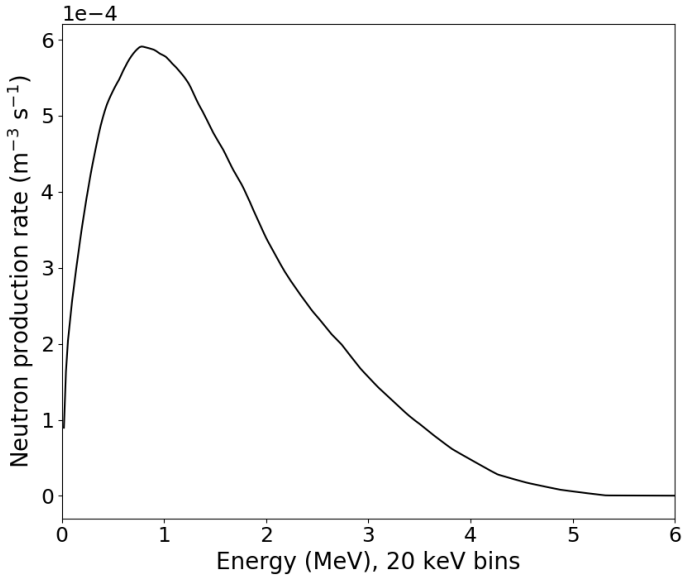

Figure 5.3: Neutron production rate per energy for Boulby salt rock, calculated using Sources4C.

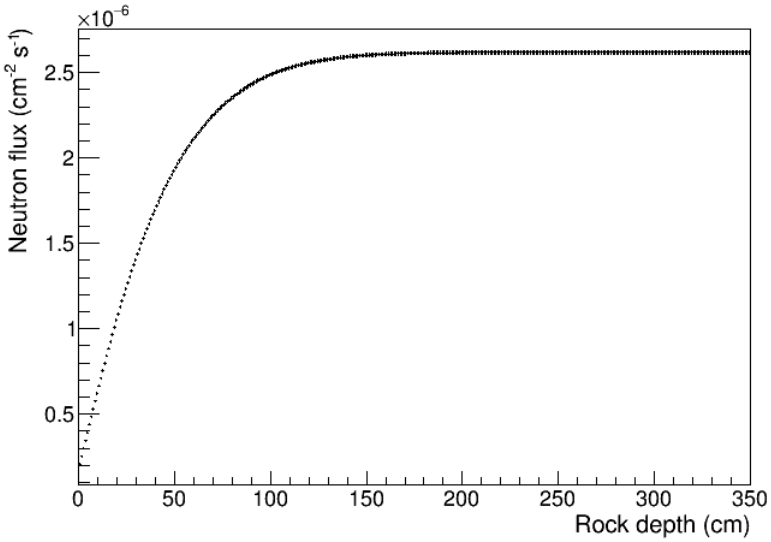

Figure 5.4: Total neutron flux at the rock surface as a function of rock depth.

It can be seen from Figure 5.4 that the flux saturates at around 1.5 m, therefore, the simulated 5 m of rock was more than adequate to capture the majority of the neutron flux at the rock surface. The flux between 0.01 and 3 MeV was found to be 2.1×10^{-6} cm^{-2} s^{-1}, in good agreement with previous simulations of the rock neutron flux at Boulby [128]. The total flux over all possible neutron energies, F_{tot}, was found to be 2.62×10^{-6} cm^{-2} s^{-1}. The flux per neutron energy (for 10 keV bins) at the rock surface is shown by Figure 5.5.

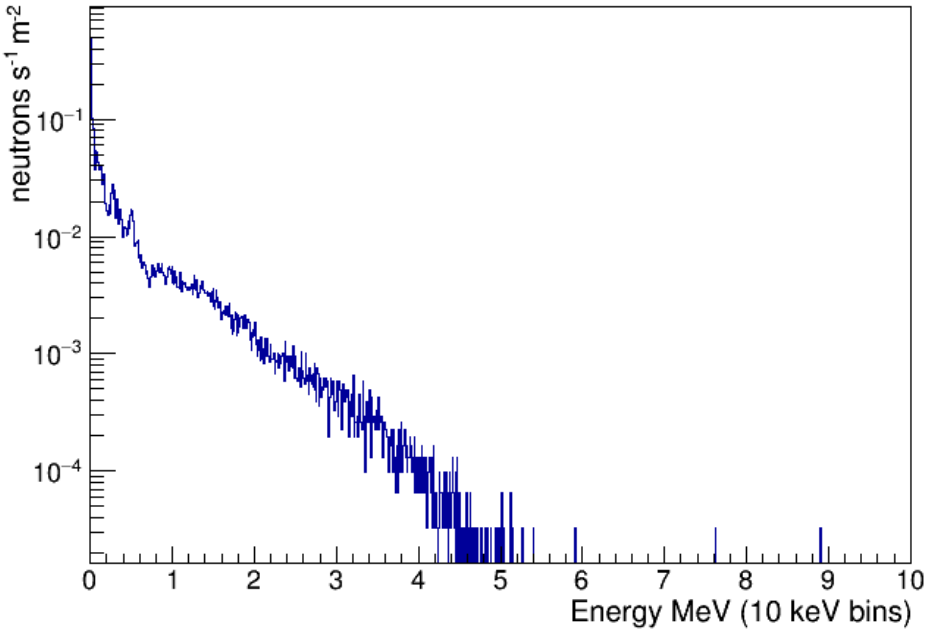

Figure 5.5: Rock surface neutron energy spectrum.

Figure 5.5 shows a contribution from thermal neutrons below 1 MeV and a peak due to fast neutrons at 1 MeV that decays exponentially, as expected. The spectrum was used as input into GEANT4 for the generation of neutrons at the rock surface.

5.3.2 Gamma Flux

To produce the rock surface gamma flux, a 50 cm thick rock wall was simulated and populated with ^{238}U, ^{232}Th and ^{40}K isotopes. The gammas, produced via the decay of these isotopes, which emitted from the rock surface had their originating depth recorded. The total gamma flux at the surface was calculated using the values given by Table 5.2 and Eq. 5.2, with R_{el} replaced by the number of gammas contributing to the flux. The result was then divided by the rock wall surface area and is plotted as a function of rock depth in Figure 5.6, where it can be seen that the flux saturates at around 40 cm.

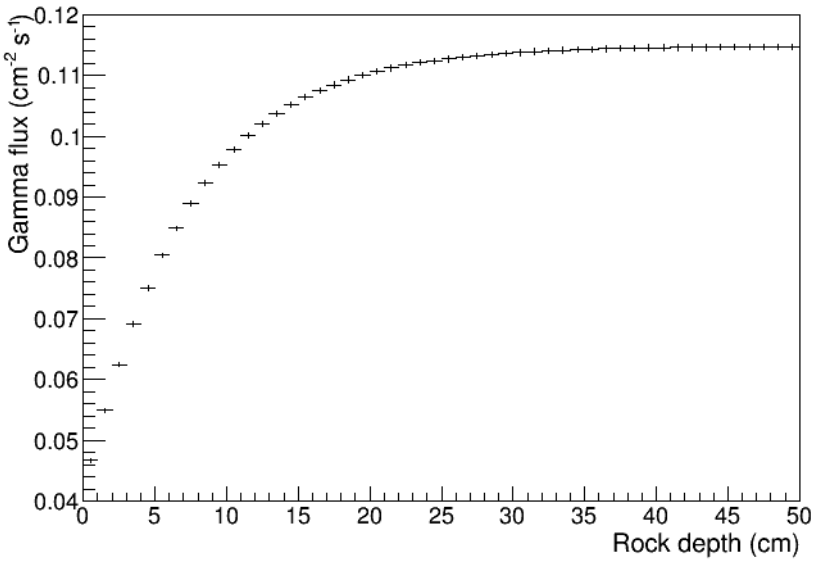

Figure 5.6: Gamma flux at the rock surface as a function of rock depth.

The total gamma flux, F_{tot}, was found to be 0.115 cm^{-2} s^{-1} in close agreement with the surface gamma flux measured, just outside of the Boulby laboratory entrance, in Ref. [129]. The flux per energy (in 10 keV bins) used to create the gamma background at the rock surface is shown in Figure 5.7, where prominent lines from each isotope decay chain are labeled.

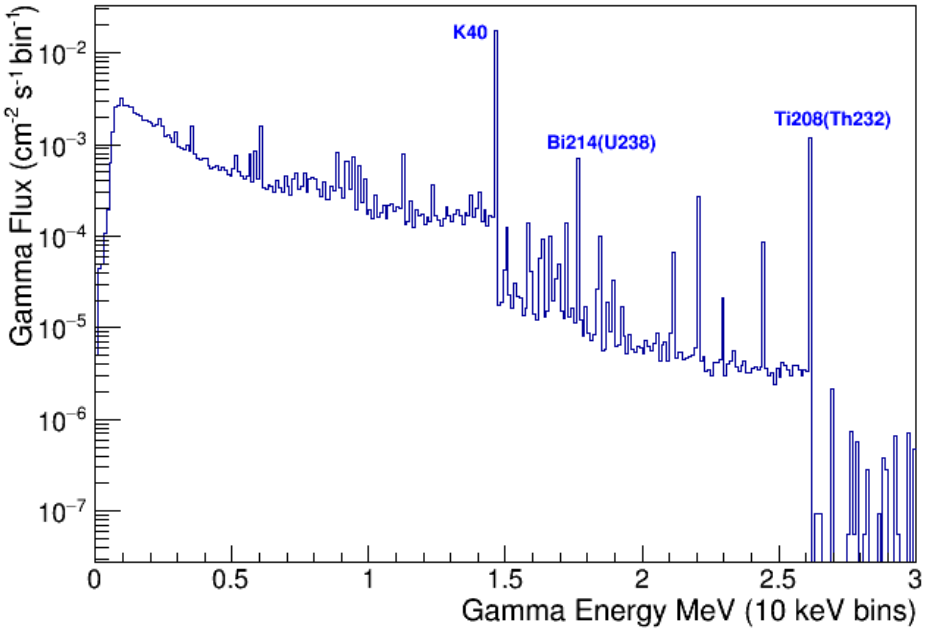

Figure 5.7: Rock surface gamma energy spectrum.

5.4 Rock and Vessel Backgrounds

This section describes the neutron and gamma background originating from the rock cavern and vessel material. The neutron background is investigated first and is discussed in the following two subsections. The gamma background originating from the vessel material and surrounding rock can not be studied separataly, as an increase in vessel thickness would provide shielding from the rock background but would also increase the vessel background. Therefore, the two background sources are discussed together in Section 5.4.3. For the vessel material, steel, titanium, copper and acrylic were investigated at a thickness of 5, 10, 20 and 30 cm, using the radiopurity levels listed in Table 5.1.

5.4.1 Rock Neutron Background

Water was selected as the shielding material for neutrons due to it's high hydrogen content. The shielding was simulated surrounding the central 1000 m^3 gas volume and the energy spectrum shown in Figure 5.5 was used to create the neutrons at the rock surface. 1.5 m of rock was simulated to allow for the back scattering of neutrons. The recoil rate within the TPC gas volume, due to rock neutrons, was calculated using Eq. 5.3 for water shield thicknesses between 10 and 50 cm. The background rate per water shield thickness data points were used to fit the solid line in Figure 5.8, which was then used to predict the rate for larger water shields, shown by the dashed line in Figure 5.8.

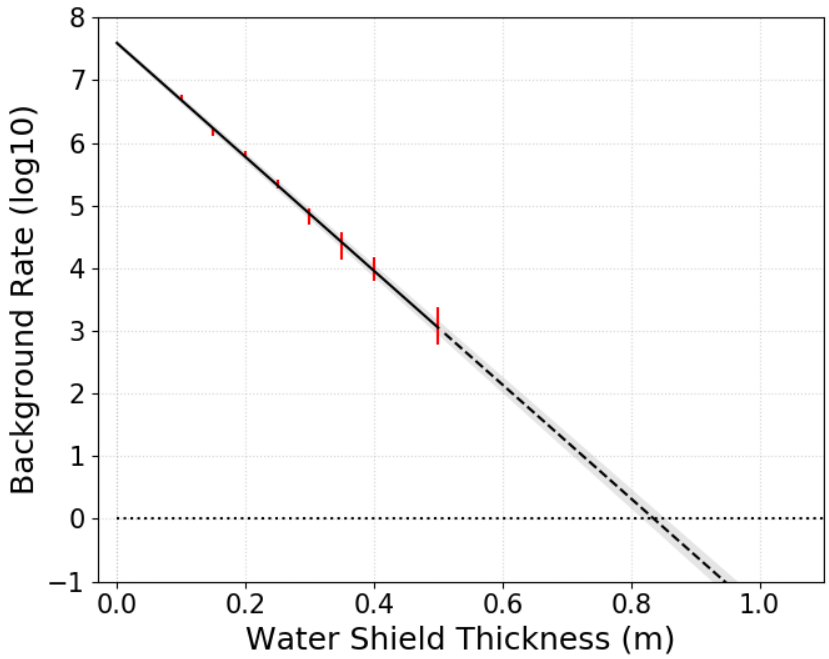

Figure 5.8: Predicted water shielding for a rock neutron recoil rate below 1 yr^{-1}, indicated by the horizontal line at y=0. Red data points (with error bars) = the simulation results. Solid line = fit to the data points. Dashed line = extrapolation to larger water shields. Grey band = 1 σ error.

Figure 5.8 shows that a water shield of ∼85 cm thick would be required to reduce the neutron background below limit. The figure also shows that with the addition of around 10 cm more water shielding, the rock neutron background could be reduced down to $<< 1$ yr^{-1}. The CPU time required to produce enough recoil statistics in the target volume, for a 50 cm thick water shield, totalled ∼2 weeks. The simulation at 50 cm was conducted at 40 Torr, twice the normal pressure, in order to increase the number of observed events. It was checked, using 10 cm of shielding, that the simulation with increased pressure returned the same result as that conducted at 20 Torr, after taking into account the factor of two difference. The pressure could not be increased further however, as it was found that the relation between pressure and recoil statistics became non-linear above 40 Torr. Even with the increased pressure and large CPU time only 4 events where observed. This result suggested that a huge CPU time would be required, to observe a similar number of events, for simulations conducted with a water shield greater than 50 cm thick. For this reason, water shielding greater than 50 cm was not simulated, instead, results from thinner water shields were extrapolated to estimate the neutron background, as shown by the dashed line in Figure 5.8.

The background from water was not included here due to the extremely low activities reported: 10^{-4} ppb for both ^{238}U and ^{232}Th [122]. It is also assumed that the neutron background, from the water, would be reduced to a negligible level by the material's self shielding properties. For these reasons, further consideration of this background source was left for future work.

5.4.2 TPC Vessel Neutron Background

The vacuum vessel, being the TPC component with by far the largest mass, has the potential to dominate the neutron background. Here, the neutron recoil rate within the TPC gas volume, due to the vessel neutron background, is described, for the materials and thicknesses outlined at the start of this section. For each material, the neutron energy spectrum produced by Sources4C

was used to populate the GEANT4 simulated vessel with neutrons. The resulting recoil rates were then calculated using Eq. 5.1 and are summarised in Table 5.3. The checkmarks in this table indicate radiopurity levels that produce a recoil rate within limit (< 1 per year). If the rate was found to be above limit, the activity levels that could be tolerated were estimated and are included in the same table, along with the reduction factor this implies.

Table 5.3: Neutron recoils per year for different vessel materials of different thickness and the ^{238}U and ^{232}Th levels required for < 1 recoil per year. Checkmarks indicate an acceptable radiopurity level.

Material	Thickness (cm)	Recoils (yr^{-1})	U limit (mBq kg^{-1})	Th limit (mBq kg^{-1})	U reduction factor	Th reduction factor
Steel	5	21±4	0.016	0.019	17	26
	10	50±9	5.5×10^{-3}	9.4×10^{-3}	49	52
	20	177±25	1.8×10^{-3}	2.3×10^{-3}	150	213
	30	242±36	1.5×10^{-3}	1.5×10^{-3}	180	327
Titanium	5	$< 11\pm3$	0.013	0.015	7	15
	10	$< 45\pm8$	4.2×10^{-3}	3.2×10^{-3}	21	72
	20	$< 88\pm15$	2.9×10^{-3}	1.5×10^{-3}	31	153
	30	$< 200\pm28$	1.2×10^{-3}	6.9×10^{-4}	75	333
Copper	5	$< 0.39\pm0.07$	✓	✓	-	-
	10	$< 1.0\pm0.16$	✓	✓	-	-
	20	$< 2.0\pm0.3$	5.6×10^{-3}	✓	2	-
	30	$< 2.6\pm0.4$	4.1×10^{-3}	✓	3	-
Acrylic	5	0.11±0.01	✓	✓	-	-
	10	0.17±0.02	✓	✓	-	-
	20	0.21±0.04	✓	✓	-	-
	30	0.17±0.04	✓	✓	-	-

The above table shows that an acrylic vessel produces a neutron recoil rate within limit for all simulated thicknesses, however, as will be shown in the next section, this material does not provide sufficient shielding from the rock gamma background. The next best material, with regards to a low neutron background, is shown by Table 5.3 to be copper. A copper vessel

of $\leq$ 10 cm thick would produce a neutron background within limit. The same could also be true for a 20 cm (30 cm) thick copper vessel if the actual ^{238}U activity of this material is approximately a factor of two (three) less than the given upper limit value. For the same reasons, the ^{238}U activity in titanium could also be within the required limit, however, this is less likely than with copper as the reduction factor, in this case, is much more severe. Even if this were true for titanium, the ^{232}Th activity would still require further reduction. For a steel vessel further purification would be needed to reduce the neutron background from this material at all thicknesses.

5.4.3 Rock and Vessel Gamma Background

The same vessel materials studied in the previous section are studied here with regards to their gamma background. As the vessel material provides shielding against rock gammas, this background is also investigated for each material. The electron recoil rate within the TPC gas volume due to the vessel and rock gamma backgrounds were calculated using Eq. 5.2 and Eq. 5.3 respectively. For the rock, gammas were produced at the surface using the energy spectrum shown in Figure 5.7. For the vessel, the gammas were produced by populating the material, in GEANT4, with the unstable isotopes: ^{238}U, ^{232}Th and ^{40}K. For the reasons presented at the beginning of this chapter, the gamma induced electron background was considered for the recoil energy range, 1-10 keV, and a limit of 10^4 yr^{-1} keV^{-1} was imposed.

The electron recoil rates are shown in Table 5.4 for gammas originating from the rock and from the vessel. The table also shows the total recoil rate from the sum of both background sources. For vessel materials that produce a gamma background within limit, a checkmark was used to indicate an acceptable radiopurity. Failing this, the material radioactivity levels were scaled down until a recoil rate within limit was achieved. This resulted in upper limits for the material isotope activities, which are given by the final three columns of Table 5.4.

Table 5.4: Rock and vessel gamma background for different vessel materials of different thickness. Checkmarks indicate an acceptable radiopurity level. For vessel backgrounds above limit a prediction of the acceptable radiopurity level is provided.

Material	Width (cm)	Rock γ recoils (keV^{-1} yr^{-1})	Vessel γ recoils (keV^{-1} yr^{-1})	Total γ recoils (keV^{-1} yr^{-1})	^{238}U limit (mBq kg^{-1})	^{232}Th Limit (mBq kg^{-1})	^{40}K Limit (mBq kg^{-1})
Steel	5	$3.8\pm0.3\times10^{6}$	$6.6\pm0.6\times10^{5}$	$4.4\pm0.4\times10^{6}$	0.003	0.0045	0.08
	10	$6.0\pm1.0\times10^{5}$	$7.2\pm0.9\times10^{5}$	$1.32\pm0.19\times10^{6}$	0.003	0.004	0.06
	20	$2.1\pm0.6\times10^{4}$	$7.3\pm1.4\times10^{5}$	$7.5\pm1.5\times10^{5}$	0.0027	0.0042	0.075
	30	$4.6\pm3.0\times10^{3}$	$6.3\pm1.5\times10^{5}$	$6.3\pm1.5\times10^{5}$	0.003	0.0053	0.053
Titanium	5	$1.0\pm0.2\times10^{7}$	$< 2.9\pm0.2\times10^{5}$	$< 1.0\pm0.2\times10^{7}$	0.003	0.0046	0.06
	10	$3.8\pm0.9\times10^{6}$	$<4.13\pm0.36\times10^{5}$	$< 4.2\pm0.9\times10^{6}$	0.0022	0.0031	0.05
	20	$6.6\pm1.1\times10^{5}$	$< 4.17\pm0.53\times10^{5}$	$1.08\pm0.16\times10^{6}$	0.002	0.0035	0.041
	30	$< 4.8\pm3.1\times10^{4}$	$< 5.11\pm0.71\times10^{5}$	$< 5.6\pm1.0\times10^{5}$	0.0017	0.0027	0.041
Copper	5	$2.3\pm0.2\times10^{6}$	$< 1.57\pm0.17\times10^{4}$	$2.3\pm0.2\times10^{6}$	0.0057	✓	✓
	10	$4.0\pm0.9\times10^{5}$	$< 1.60\pm0.24\times10^{4}$	$4.1\pm0.9\times10^{5}$	0.0058	✓	✓
	20	$9.5\pm4.0\times10^{3}$	$< 1.58\pm0.33\times10^{4}$	$< 2.53\pm0.73\times10^{4}$	0.0056	✓	✓
	30	$5.1\pm3.3\times10^{2}$	$< 1.58\pm0.43\times10^{4}$	$< 1.6\pm0.5\times10^{4}$	0.0053	✓	✓
Acrylic	5	$2.5\pm0.3\times10^{8}$	$3.44\pm0.32\times10^{5}$	$2.5\pm0.3\times10^{8}$	0.0002	0.0017	0.037
	10	$1.90\pm0.19\times10^{8}$	$5.97\pm0.57\times10^{5}$	$1.90\pm0.19\times10^{8}$	5.7×10^{-4}	9.3×10^{-4}	0.024
	20	$9.7\pm1.4\times10^{7}$	$1.14\pm0.12\times10^{6}$	$9.8\pm1.4\times10^{7}$	3.4×10^{-4}	5.4×10^{-4}	0.011
	30	$4.1\pm0.9\times10^{7}$	$1.12\pm0.14\times10^{6}$	$4.2\pm0.9\times10^{7}$	3.2×10^{-4}	4.9×10^{-4}	0.013

It can be inferred from the above table that if the actual ^{238}U activity in copper is a factor of $\sim$2 less than it's upper limit, then all thicknesses of copper would produce a tolerable gamma background. This is a consequence of the self shielding properties of copper, which causes the material's gamma surface flux to saturate at low thickness (< 5 cm). The table shows that acrylic is far less effective as gamma shielding, compared to the other options, which is expected due to it's lower density. Table 5.4 also shows that for a tolerable gamma background level, from steel and titanium, a radioactivity reduction $\mathcal{O}$(10-100) is required for each isotope.

5.5 Internal TPC Background

This section discusses the internal TPC background produced by the different readout options introduced in Section 5.5.1 and from the main background contribution from the cathode and field cage, discussed in the same section. The resulting neutron and gamma backgrounds, recorded in the TPC gas volume, originating from these components are presented in Section 5.5.2.

5.5.1 TPC Components Investigated

Various TPC readout options, such as those described in Section 2.4.4 of Chapter 2, are currently being considered by the CYGNUS collaboration [77], with consideration given to the readout performance, cost and background. As the work presented here is exclusively in terms of background, only readouts with the most radiopure materials were considered. These were the Micro Pixel Chamber (μ-PIC), pixel chip and MWPC. Other readouts, which are still viable from a non-background perspective, were not included here due to their higher radioactivity levels, these are briefly mentioned in Section 5.5.3. The background from a camera readout is presented as a separate piece of work towards a specific CYGNUS protoype, which is discussed in Chapter 9. The background from a Gaseous Electron Multiplier, GEM, and thick GEM, ThGEM, amplification stage were also investigated. The following gives a short description of the amplification stages and readouts, chosen for this work, from a background perspective. A more general description of their configuration and applicability to dark matter searches is given in Section 2.4.3 and Section 2.4.4 of Chapter 2, respectively.

The μ-PIC readout as used by NEWAGE [124] is composed of a double-sided circuit board separated by a 1 mm-thick polyimide substrate. The substrate produces the majority of background for this readout and is, therefore, the focus of this study with regards to the μ-PIC background.

A readout based on the ATLAS FE-I4 pixel chip [130] is silicon based

with metal and dielectric layers. Copper and aluminium make up the bulk of the metal layers, which also include small amounts of other metals such as tantalum, chromium and titanium. For the pixel chip background study a simplified model, made from a 400 μm thick block of 98% silicon, 1% copper and 1% aluminium by mass, was simulated.

An MWPC readout has two main sources of background: the wires and the acrylic frame supporting the wires. For this readout, 50 μm thick wire was simulated and the background results were scaled to a total MWPC steel wire mass estimate of 1.94 kg. This is based on an estimated 1.94 g of steel wire that make up the two MWPCs in the 1 m^3 DRIFT-IId TPC. For the acrylic frame, a 1 cm thick frame with a 2 cm thick border was simulated. It is envisioned that each frame would hold a 1 m^2 wire array.

A typical GEM has a 50 μm thick Kapton layer coated with a thin ($\sim$5 μm) copper layer on either side. Only the Kapton was simulated as it is the main mass contributor and has a relatively high background compared to copper, as shown by Table 5.1.

In order to achieve high gas gains of $\sim$10's to 100's of thousand, the stacking of GEMs is required such as in Ref. [85]. This, of course, would double or even triple the background due to Kapton. An alternative approach is to use a ThGEM, which has a thicker insulating layer. ThGEMs are usually between 0.4 and 1 mm thick, 1 mm was chosen for these simulations as, at this thickness, the insulating layer can be made of low background acrylic [131]. The copper layers of a ThGEM are thicker than that of an ordinary GEM, therefore, 0.1 mm of copper was simulated on either side of the acrylic.

For each readout and amplification stage a 1 m^2 sheet of material was simulated at the appropriate thickness and positioned centrally inside the TPC gas volume. For the MWPC readout a single frame and a single wire, 1 m in length, was simulated. The resulting recoil rates, due to the material background, were scaled to reflect the rate expected from the total 2000 m^2 readout area. Table 5.5 lists the readout and amplification options investi-

gated, along with the average material thickness that was simulated and the total mass for 2000 m^2.

Table 5.5: The simulated readouts, materials, thickness and total mass.

Readout	Material	Thickness (mm)	Total mass (tons)
ThGEM	Acrylic	1.0	2.36
	Copper	0.1	3.6
μ-PIC	Polyimide	1.0	2.84
GEM	Kapton	0.05	0.0142
MWPC	Steel	0.05	1.94×10^{-3}
	Acrylic	10×20	0.236
Pixel Chip	Silicon	0.4	1.86
	Copper	3.9×10^{-3}	0.07
	Aluminium	4.5×10^{3}	0.024

A large scale TPC readout would require structural support and this would most likely be made of acrylic. The design of this, and the background contribution, is not explored here, as the purpose of this section is to compare the readout component base materials directly. The inclusion of a large scale support structure would, however, further increase the background inside the vessel for all readouts and the exact amount of support required would depend on the readout. For example, the forces and torques exerted by the wire tension of an MWPC means that this readout would require a more rigid support structure than that of other readouts. The basic acrylic frame investigated in this section, for the MWPC, is used to hold the wires in position and not to provide structural support. For the same reasons, the background contribution from readout electronics is not studied here. However, it is expected that in general this can be reduced by, where possible, placing shielding around the electronics or locating the bulk of the electronics outside of the vessel.

For the cathode and field cage components, the alumina found inside the resistors that make up the partition chain along the field cage (used to define

the drift field between the cathode and readout) provides the highest source of background. Therefore, the resistor chain is the focus of this study with regards to the field cage and cathode backgrounds. The total amount of resistors required for a 10 m long CYGNUS TPC would be ∼10 times the 66 resistors required for the 1 m long DRIFT-IId field cage [104], totalling 660 resistors. TREX-DM report radiopurity levels of 0.4±0.2 and $<$ 0.023 mBq/pc for ^{238}U and ^{232}Th, respectively [132], for their field cage SM5D resistors. These resistors have dimensions 6.4 × 3.2 × 0.55 mm [133]. A block of alumina with these dimensions was simulated at the centre of the TPC gas volume and the resulting background rates were scaled to reflect the full amount of resistors required.

5.5.2 Neutron and Gamma Background

Using the procedure described in Section 5.2 and the radioactivity levels listed in Table 5.1, the neutron and gamma background rates within the CYGNUS-1000 gas volume were calculated for each TPC component discussed in the previous section. As was done in Section 5.4, upper bounds on the isotope activites were provided for recoil rates above limit. The results are listed in Table 5.6 and Table 5.7 for the neutron and gamma backgrounds, respectively.

Table 5.6 shows that an MWPC readout with ThGEM amplification would produce a recoil rate, from neutrons, within limit. This is only the case as the ThGEM is made of low background acrylic. For the GEM, which is constructed from Kapton, the neutron background is ∼one order of magnitude higher than the acceptable limit. The radioactivity levels used for the silicon material, found inside the pixel chip readout, were upper limits. Therefore, the neutron background from this readout could still be $<$ 1 yr^{-1} if the actual ^{238}U and ^{232}Th activity of silicon is ∼40 and ∼10 times lower, respectively, than the upper limit values. As with silicon, the radioactivity levels of the polyimide material, found in the μ-PIC readout, were also upper

limits. However, in this case the ^{238}U and ^{232}Th activities would have to be ∼200 and ∼70 times lower than the upper limit values, respectively, in order to produce a neutron recoil background of < 1 yr^{-1}. The result regarding the field cage resistors, given by Table 5.6, shows that this main background source, from the field cage and cathode configuration, is within the neutron recoil rate limit.

Table 5.6: Neutron recoils yr^{-1} for different readout materials and estimated ^{238}U and ^{232}Th radiopurity for < 1 yr^{-1}. Checkmarks indicate an acceptable radiopurity level.

Readout	Material	Neutron recoils (yr^{-1})	U/Th limit (mBq kg^{-1})
ThGEM	Acrylic	0.122±0.002	✓
	Copper	2.4±1.6×10^{-3}	✓
μ-PIC	Polyimide	<160±16	0.185/0.20
GEM	Kapton	< 9±1	13.6/18.7
MWPC	Steel	4±0.5×10^{-4}	✓
	Acrylic	0.048±0.004	✓
Pixel Chip	Silicon	25±3	0.31/0.40
	Copper	2.9±0.3×10^{-4}	✓
	Aluminium	0.29±0.03	✓
Resistors	Ceramic	< 0.35±0.23	✓

Table 5.7 below shows that the ThGEM amplification stage and MWPC readout gamma background is only just above the 10^4 limit. In both cases the ^{40}K radioactivity of acrylic needs to reduced by a factor of ∼4 and ∼2, for the ThGEM and MWPC frame, respectively. The MWPC background could also be reduced by minimising the amount of material used to construct the readout frame. Both the pixel chip and μ-PIC readouts were found to be above the gamma rejection limit by ∼1 and ∼4 orders of magnitude, respectively. As mentioned previously, the pixel chip silicon material and

the μ-PIC polyimide material radioactivities are upper limits, therefore, the actual gamma background could be much lower and even within the required limit. This is more likely for the pixel chip readout which, as mentioned, is only 1 order of magnitude above the tolerable gamma background rate. The high levels of ^{40}K found within Kapton (as shown in Table 5.1) causes the gamma background from this readout to be above limit, making it difficult to justify it's use over that of a ThGEM. The GEM result also emphasises the need to produce ThGEM's from acrylic, as described in Section 5.5.1, rather than Kapton. The total gamma background from the field cage resistors, shown in Table 5.7, was found to be above limit and a reduction in the ^{238}U activity of $\sim \frac{1}{4}$ would be required in this case. An alternative method here, could be to construct the field cage with around 4 times less resistors.

Table 5.7: Gamma recoil rates for different TPC component materials and the ^{238}U, ^{232}Th, and ^{40}K limits to achieve 10^4 recoils keV^{-1} yr^{-1}. Checkmarks indicate an acceptable radiopurity level.

Readout	Material	γ recoils (keV^{-1} yr^{-1})	U limit (mBq kg^{-1})	Th limit (mBq kg^{-1})	K limit (mBq kg^{-1})
ThGEM	Acrylic	$3.3\pm0.7\times10^4$	✓	✓	0.54
	Copper	$< 1.5\pm0.3\times10^3$	✓	✓	✓
μ-PIC	Polyimide	$< 1.3\pm0.2\times10^7$	0.12	0.09	0.12
GEM	Kapton	$1.57\pm0.02\times10^5$	✓	✓	3.65
MWPC	Steel	1.8 ± 0.3	✓	✓	✓
	Acrylic	$2.4\pm0.1\times10^4$	✓	✓	0.88
Pixel chip	Silicon	$< 2.55\pm0.19\times10^5$	0.26	0.29	0.46
	Copper	$< 24\pm2$	✓	✓	✓
	Aluminium	$< 937\pm77$	✓	✓	✓
Resistors	Ceramic	$2.5\pm1.3\times10^4$	0.13	✓	✓

5.5.3 Other readouts

Available readout systems are by no means limited to the cases studied here. For example the micro-RWELL [134], which combines a GEM-like structure and printed circuit board readout, was not considered here due to the high background rates quoted for printed circuit boards: 380 ppb ^{238}U, 1100 ppb ^{232}Th, 310 ppm ^{40}K [122]. Similarly, a micromegas readout was not considered due to the high potential background: $<$ 119.3 ppb ^{238}U, 41.4 ppb ^{232}Th, and $<$ 54.9 ppm ^{40}K [135]. To determine if either of these technologies would be a viable option for CYGNUS, further R&D efforts to improve the material radiopurity are required.

As with the pixel chip readouts, it could be argued that optical technology, such as the CMOS cameras used by the LEMON project [88], provides the highest resolution imaging. However, to reduce the background from the camera electronics the CMOS cameras would have to be located outside of the vessel, with transparent windows between the cameras and the gas volume to act as shielding. To achieve this, a whole rethinking of the vessel design, particularly to include transparent windows of low activity, would be required. The backgrounds relevant to this special case are discussed separately in Chapter 9.

5.6 Additional Background Sources

This section describes the additional background found within the TPC gas volume due to cosmic ray interactions and internally produced radon gas. These are discussed in turn by Sections 5.6.1 and 5.6.2.

5.6.1 Cosmic Ray Background

Muons

High energy muons, created by cosmic ray showers, can penetrate the Earth's surface and enter either the TPC gas volume or the immediate environment surrounding the TPC. Cosmic ray muons that produce spallation neutrons, therefore, constitute an additional neutron background. A previous Monte Carlo study, regarding the muon induced background for a CYGNUS-1000 TPC of 50 Torr SF_6 gas [113], found that no neutron events were observed from 200 million simulated muons. This led to an upper limit result on the muon induced neutron background, at Boulby, of less than 3 yr^{-1} at a 90% CL. As the gas pressure used for this study is only 20 Torr the same upper limit applies. This result suggests that the actual neutron background, from cosmic ray muons, could be above limit. However, it is feasible to reject this background by detecting the coincidence muon using plastic scintillators or by detecting the ionisation produced by muons that enter the fiducial volume.

Cosmogenic Activation

When materials are present at the surface they are subject to a much higher flux of cosmic rays then they would be if situated underground. If TPC materials spend a significant time above ground, cosmic ray interactions can generate different long-lived isotopes within them. These isotopes can then produce an additional source of background once the materials are transported underground and used in the TPC construction. For a large mass TPC such as CYGNUS-1000, cosmogenic activation has an increased influence on the ultimate background rate. The activity of a cosmogenically activated isotope is expressed as [136],

$$A = R[1 - e^{-\lambda t_{\text{exp}}}]e^{-\lambda t_{\text{cool}}}\,, \tag{5.4}$$

where R is the production rate, λ is the decay constant, t_{exp} is the time the material spent exposed to the cosmic ray flux and t_{cool} is the 'cooling off' time the material spent underground.

Activation can occur in all materials, but we use copper here as an example. Cosmic ray interactions with copper at sea level can produce multiple unstable isotopes, the longest lived of these is ^{60}Co which originates from ^{59}Co contamination and has a half-life of 5.26 years. Measurement of the ^{60}Co activity in copper were performed by Ref. [137] after a relatively long $t_{\text{exp}} = 345$ days compared to a much shorter $t_{\text{cool}} = 14.8$ days. The activity was found to be $340\pm^{82}_{68}$ μBq kg^{-1}. The upper end of this measurement, results in an estimated upper limit for the rate of gamma-induced electron recoils, for a 5 cm thick copper vessel, of $< 9.8\pm0.6\times10^{4}$ keV^{-1} yr^{-1} in the 1–10 keV energy region. This rate is ∼6 times larger than the upper limit recoil rate due to ^{238}U, ^{232}Th, and ^{40}K radioactivity in the same thickness of copper (see Section 5.4.3). Since the measurement and simulation of the cosmogenic activation in copper show good agreement [137], a future detailed study of cosmogenics in CYGNUS-1000 could use the same simulation tool, ACTIVIA [138], to predict the minimum amount of time a material should spend both above ground and cooling off underground, in order to limit activation.

For SF_6, the longest-lived isotope of fluorine, ^{18}F (with a half-life of 109.77 minutes), is too short-lived to produce a lasting background contribution. Nearly all isotopes of sulfur have half-lives on the scale of seconds to minutes with the exception of ^{35}S, which has a half-life of 87.5 days. ACTIVIA was used to simulate 90 days of surface time, during which the SF_6 gas was exposed to cosmic rays sampled from an energy spectrum ranging between 10-10000 MeV. After this, a 180 day cooling off period underground was assumed, during which time the gas was not exposed to the cosmic ray flux. This resulted in a ^{35}S production rate of $R = 0.021$ kg^{-1} day^{-1}, giving a decay rate of 2.61 mBq/kg. The 1000 m^3 TPC, filled with SF_6 at 20 Torr, holds ∼160 kg of gas, of which ∼35 kg is sulfur, therefore, the total decay

rate for the detector is 91.35 mBq. To estimate the background due to this isotope decay, 10^5 ^{35}S decays were simulated, using GEANT4, at the centre of the TPC gas volume. Only three gamma induced electron recoil events, between $1-10$ keV, were observed during the simulation time, which totalled $\sim$12.5 days. This resulted in an estimated background rate of 90 ± 50 yr^{-1}, too small to be a significant electron recoil background.

In general, the amount of cosmogenic activation can be reduced by limiting t_{exp} and extending t_{cool}. In addition, the amount of time the material spends as air-shipment, and therefore, subject to a higher cosmic ray flux, should be limited. It may also be possible to electroform the material underground at the construction site.

5.6.2 Radon Gas

The rejection of Radon Progeny Recoils, RPRs, has been achieved by the DRIFT-IId collaboration. A discussion on this type of background and the mitigation methods used by DRIFT-IId is given by Section 4.1. The same methods as those described in the aforementioned section, such as using an ultra thin cathode material and fiducialisation, could be used by CYGNUS-1000 to mitigate the radon induced background. Section 2.4.3 of Chapter 2 describes how fiducialisation is possible in SF_6 gas.

5.7 CYGNUS-1000 Search Reach

Eq. 4.23 and Eq. 4.24 of Chapter 4 were used here to calculate the potential search reach of CYGNUS-1000 (at a 90% CL). An exposure of 1 and 10 years was considered for an idealised 1 keV$_{ee}$ threshold with 100% detection efficiency and for a 6 keV$_{ee}$ threshold with 50% detection efficiency. The latter, more realistic configuration, was based on the results of Chapter 3, which indicated a feasible gamma rejection of 10^{-4} at 50% efficiency, for energies of 6 keV$_{ee}$ and above, for a TPC with a 50 cm long drift region.

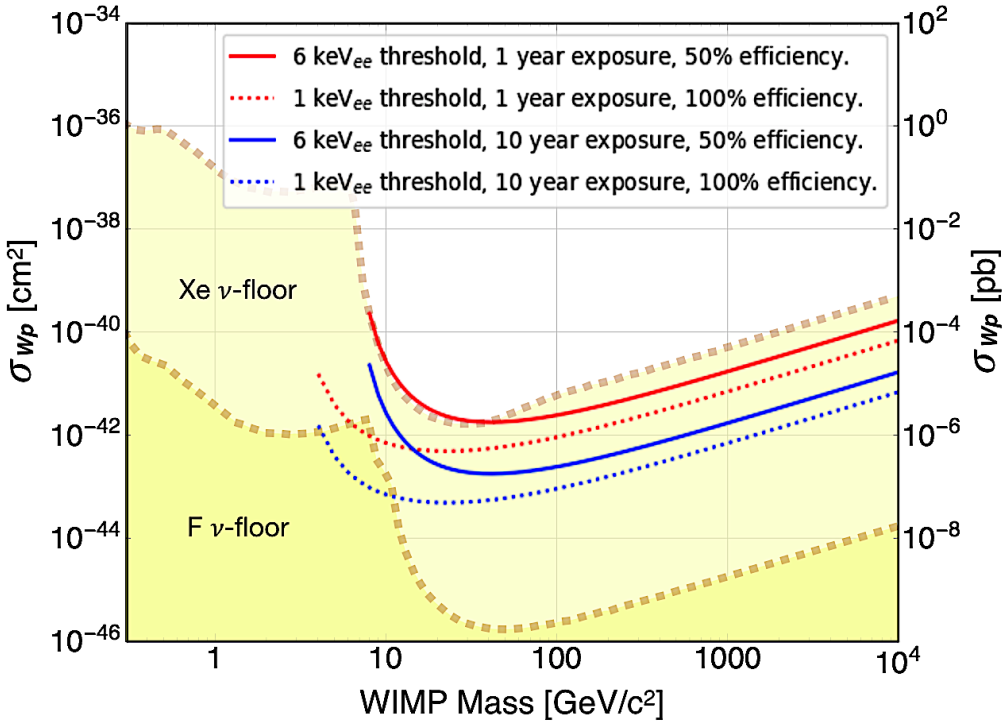

Figure 5.9: CYGNUS-1000 search reach after 1 (red) and 10 (blue) year exposures, for a 6 keV$_{ee}$ threshold and 50% detection efficiency (solid line) and for a 1 keV$_{ee}$ threshold and 100% detection efficiency (dotted line).

The above figure shows that for all thresholds, exposures and efficiencies considered, the CYGNUS-1000 TPC would easily reach into the neutrino background parameter space of a Xe based detector. The figure shows that for a 1 keV$_{ee}$ threshold and 100% detection efficiency, the fluorine target of the CYGNUS-1000 TPC would become sensitive to the neutrino floor after just one year of running. For a 6 keV$_{ee}$ threshold and 50% detection efficiency, it would take more than 10 years of running to start observing a neutrino background.

5.8 Conclusion

This chapter described a Monte Carlo investigation of the neutron and gamma background found within the prospective CYGNUS-1000 TPC. The TPC was simulated with a 1000 m^3 volume of SF_6 gas at a pressure of 20 Torr. The study focused on the background produced by the TPC vessel, shielding, internal TPC components and the salt rock found at the Boulby underground laboratory. Consideration is also given towards the background produced by cosmic ray interactions and internally produced radon gas. For the neutron and gamma backgrounds, respective limits of <1 yr^{-1} and $<10^4$ keV^{-1} yr^{-1} were established with the aim of finding TPC components within limit or, failing that, to estimate the radiopurity level required to achieve this. The chosen gamma limit was based on the the results reported in Chapter 3.

It was found that 85 cm (95 cm) of water shielding would reduce the neutron background to <1 ($<<1$) yr^{-1}. To shield against rock gammas, a 30 cm copper vessel would be sufficient. However, the actual ^{238}U activity of copper would have to be $\sim$half that of the upper limit used in this study, in order to keep the total gamma background, from the rock cavern and vessel, within limit. This would also cause the vessel neutron background to be within limit. Future screening efforts are required to better understand the actual copper radioactivity and confirm these conclusions. A vessel constructed of 30 cm copper would most likely require a steel or titanium support structure. If this structure were to average 5 cm in thickness, the total neutron and gamma backgrounds would be increased above limit. The support structure would, therefore, have to be $<$ 5 cm thick on average and even in this case, the material used (either steel or titanium) may need further purification. The support structure could also be embedded within the copper to allow the vessel to provide some shielding from this additional background source.

A back-to-back configuration with a 50 cm separation between each readout and cathode was adopted for the TPC, resulting in a total readout area of 20×100 m^2. The readout closest to achieving a background within limit was

the MWPC with ThGEM amplification stage. The latter, constructed using a low background acrylic insulating layer. This configuration meets the required neutron background limit, however, the gamma rejection capabilities at low energy would need improvement in order to accommodate this background or alternative materials of lower radioactivity would be required. For most of the other readouts, further screening is needed and ultimately R&D efforts towards their redesign and construction may be required to produce background rates within limit. The background could also be reduced by increasing the drift distance between cathode and readout, thus decreasing the number of readouts required. However, this would increase the diffusion for events with longer drift durations, which would have an impact on the achievable electron discrimination.

Considering other background sources, that due to radon gas can be mitigated using known methods, currently employed by the DRIFT-IId TPC, such as fully fiducialising the gas volume and using ultra thin material to construct each cathode. For cosmic ray backgrounds, the low rate of muon induced nuclear recoils can be mitigated using coincidence tagging of the events and the amount of cosmogenic activation can be reduced by limiting the exposure time of materials at the surface and allowing for the required cooling off period underground.

The search reach of a CYGNUS-1000 TPC would extend further into the SD parameter space, than a similar mass Xe based detector, without having to reject a neutrino background. For a 6 keV_{ee} threshold and 50% detection efficiency the TPC would not become sensitive to the neutrino floor, even after 10 years of exposure. However, the results at 1 keV_{ee} threshold and 100% detector efficiency indicate that future R&D, along the lines of that discussed in Chapters 3 and 4 with regards to threshold lowering and detector efficiency, respectively, is required to realise the full search potential of the CYGNUS-1000 TPC.

As mentioned at the start of this chapter, the CYGNUS-1000 concept

may not be realised as a single large scale structure, instead, the target volume could be shared between multiple smaller detectors. The next section describes such a detector, with a 10 m^3 volume, and builds on the results of this chapter to produce a similar background study but for a more detailed and specific TPC design.

Chapter 6

CYGNUS-10 TPC Background Study

The results from Chapter 5 indicate the potential feasibility of a large scale directional detector of order 1000 m^3. However, it is recognised that a staged approach in detector development will be needed to reach this goal. A reasonable first step, that goes beyond the current 1 m^3 volume demonstrated by DRIFT-IId, is considered to be a moderate scale-up to 10 m^3. The scaled-up TPC, termed CYGNUS-10, would also include the technology developments discussed in Section 2.4 of Chapter 2, such as SF_6 operations and the use of ThGEM avalanche devices. This chapter presents work towards the realisation of a full conceptual design for CYGNUS-10, with a focus on the expected radioactive background. The recoil rate limits and energy regions described in Chapter 5, of < 1 yr^{-1} between 1-200 keV_r and $< 10^4$ keV_{ee}^{-1} yr^{-1} between 1-10 keV_{ee}, were used in this work, for the neutron and electron background respectively.

6.1 Laboratory Geometry and TPC Design

Boulby's Large Experimental Cavern (LEC), shown in Figure 6.1, was chosen as the location for the TPC. The LEC, which is 30 m long, 7 m wide and 6 m tall [139], was specifically designed to house a large scale gas TPC such as CYGNUS-10. For instance, the LEC is orientated to maximise the directional signal expected from the WIMP wind (see Section 2.4.1 of Chapter 2).

Figure 6.1: Layout of the Boulby Underground Laboratory. The LEC is the large corridor in the top left of this figure. Figure from [140].

In the previous chapter, a simple cube design was chosen for CYGNUS-1000 as it was envisioned that a more complex geometry, for such a large TPC, would cause construction issues. The basic cube design would also be the most cost effective for a large scale TPC, as the shielding could be provided in the form of ready made blocks. For the smaller CYGNUS-10 TPC, however, these issues are less significant and other geometries could be considered. Therefore, in this case, it was decided that the vessel should be cylindrical. This geometry provides natural support from the atmospheric pressure exerted on the vessel walls during low pressure operations and, as a result, allows the vessel walls to be constructed from steel of just 13 mm thick

[141], minimising the associated background from this material. A cylindrical geometry also allows the two end pieces of the vessel to be built as single large flanges, something that would not be feasible at the scale of CYGNUS-1000. The flange dimensions could not exceed the maximum possible for the transportation of a single structure into Boulby mine so the radius of these pieces were set at 1.1 m. The TPC and LEC area were simulated in GEANT4 and the former is shown centrally located within the latter by the GEANT4 generated image shown in Figure 6.2.

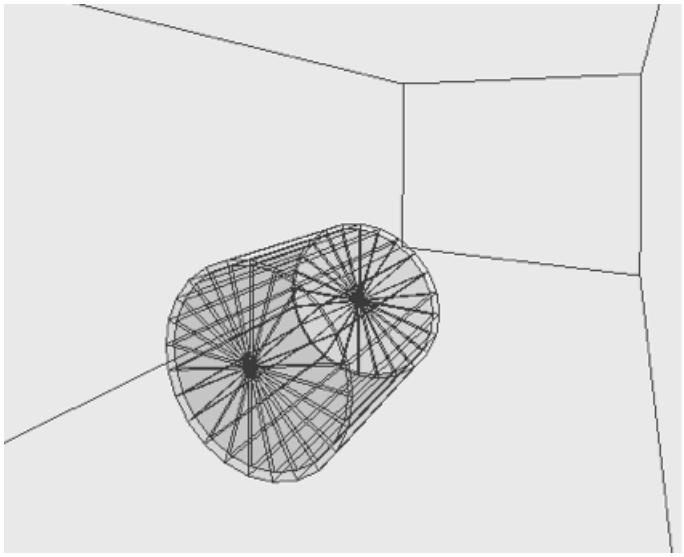

Figure 6.2: GEANT4 generated image of the CYGNUS-10 vessel, located at the the centre of the LEC area.

The same back-to-back, readout-cathode-readout, configuration used for the CYGNUS-1000 design (see Section 5.1 of the previous chapter) was envisioned here for the CYGNUS-10 TPC. However, unlike CYGNUS-1000 the exact design of this for CYGNUS-10 depends on the internal shielding requirements (see Section 6.3), which affects the length of the vessel (as the radius is fixed at 1.1 m). For this reason, further discussion on the internal TPC components and geometry is left until Section 6.4.1.

6.2 Rock Neutron Background

The same procedure used in Section 5.4.1 (previous chapter) was followed in this work to find the amount of water shielding required to produce a recoil rate, due to rock neutrons, within limit. The simulated LEC has a total surface area of 864 m^2, for a rock neutron surface flux of 2.62 m^{-2} s^{-1} (see Section 5.3.1, previous chapter), this gives a total neutron flux, F_{lec}, of approximately 2260 s^{-1}. To estimate the size of water shielding required, a cylindrical volume of water was simulated, surrounding the vessel, for thicknesses of between 0 and 35 cm, increasing in 5 cm increments per simulation. The resulting recoil events observed in the gas volume, R_n, due to rock neutrons, was recorded after each simulation and the recoil rate per year, f_n, was calculated as,

$$f_n = \frac{R_n \times F_{lec}}{N} \tag{6.1}$$

where N is the number of neutrons simulated. The recoil rate as a function of water shield thickness is shown in Figure 6.3. The figure shows an exponential fit to the data, which was used to predict the water thickness for a recoil rate of <1 and < 0.1 yr^{-1}. It can be seen, from this figure, that 38±2 cm of shielding would reduce the neutron recoil rate to < 1 yr^{-1} and the rate can be reduced further to < 0.1 yr^{-1} for a water shield thickness of 46±2 cm. The latter was rounded to 50 cm and this thickness of water shielding was included in the remaining simulations.

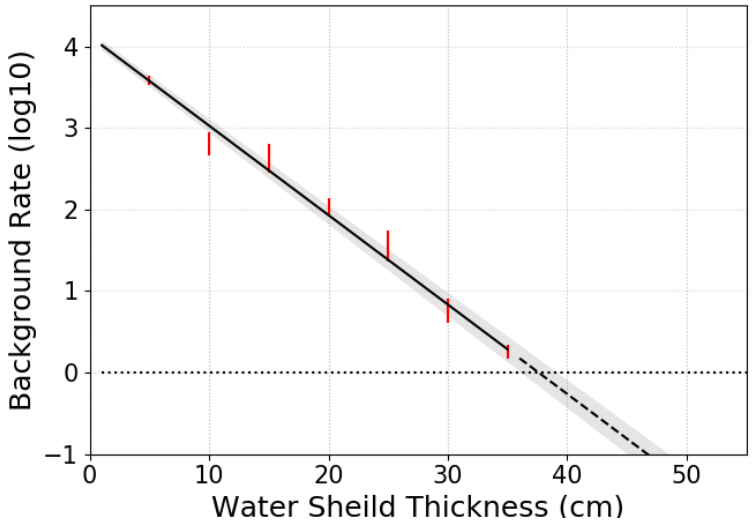

Figure 6.3: Recoil rate within the gas volume, due to rock neutrons, as a function of water shield thickness. Solid line = exponential fit to the data, dashed line = fit extrapolated to larger water shield thicknesses, grey band = 1 σ error, dotted line = recoil rate of < 1 yr^{-1}.

The extrapolation used in Figure 6.3 was required for the same CPU time considerations described in Section 5.4.1 of the previous chapter. The simulated rate with a 30 cm (35 cm) water shield was conducted at an increased pressure of $\times 10$ ($\times 100$) in order to generate enough statistics to allow for a rate prediction. The pressure increase was possible as long as the probability of neutron double scattering remained negligible. This was checked, using 10 cm of water shielding, for which, the simulation returned the same results (after applying the appropriate reduction factor) at all pressures considered.

6.3 Rock Gamma and Vessel Background

This section describes a simulation study of the electron recoil rate, found within the TPC gas volume, due to the Compton scattering of rock and vessel

gammas. The simulation was conducted using the procedures described in Section 5.2 (for vessel gammas) and Section 5.3 (for rock gammas) of the previous chapter. The rate due to vessel gammas was calculated using Eq. 5.2 and the radioactivity levels for steel, listed in Table 5.1. The contamination due to ^{60}Co, which is introduced to steel through industrial processors, was also included with a measured activity level of 1.6 mBq kg^{-1} [119]. Eq 5.3 was used to calculate the rate due to rock gammas.

Results from Section 5.4.3 showed that copper was the most effective gamma shielding material and also produced the lowest intrinsic gamma background. Therefore, to reduce the electron recoil rate, due to gammas produced by the steel vessel, copper shielding was placed on the inside of the vessel walls. This internal shield was simulated at thicknesses of between 1 and 5 cm, in 1 cm increments. As the radius of the cylindrical vessel could not be increased (see Section 6.1) the length of the vessel was instead increased, along with the water shield, in order to maintain a 10 m^3 TPC gas volume. Figure 6.4 shows the resulting recoil rates for no shield and for a shield thickness of 2 and 5 cm.

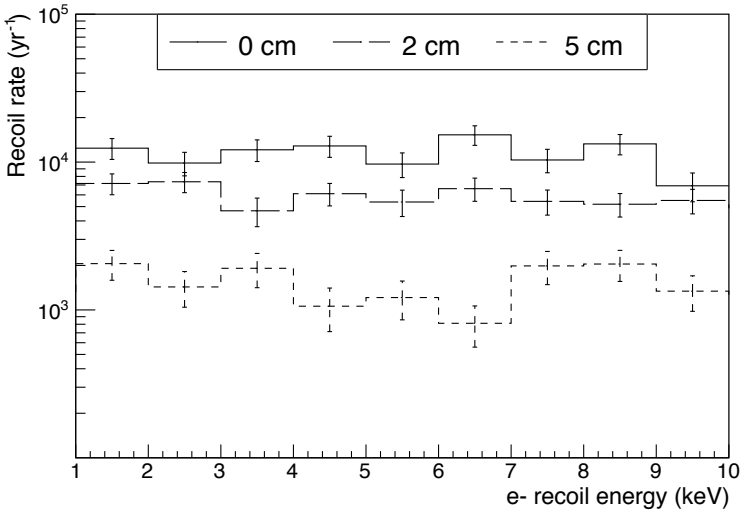

Figure 6.4: Electron recoil rates, per keV, from CYGNUS-10 vessel gammas for a 0, 2 and 5 cm thick internal shield.

An observable feature of the data, shown in the above figure, is the flatness of the rate at all energies. This is a consequence of the recoils being produced by Compton scattering, which (for the energy range being considered here) creates a continuum of recoil energies with no bias towards a particular energy (i.e a flat recoil spectrum). Figure 6.4 shows that an internal copper shield of 5 cm is enough to produce a background well within limit, giving an average electron recoil rate, due to vessel gammas, of $1.5\pm0.4\times10^3$ keV^{-1} yr^{-1}. The electron recoil rate due to gammas produced in the copper shield was also studied and found to be < 500 keV^{-1} yr^{-1}.

As well as shielding against the vessel gamma background, the internal copper shield also helps reduce the rock gamma background. However, a simulation of the latter, with the internal copper shielding in place, was still found to produce a rate of $\sim3\times10^5$ keV^{-1} yr^{-1} on average (for the region 1-10 keV), which is well above the upper limit. Thus, further copper shielding, placed externally to the steel vessel, is required. This external shielding was simulated around the outside of the cylindrical vessel walls, with a different thickness for each simulation run. Ten billion gammas were then produced at the rock surface of the LEC for each run, using the procedure described in Section 5.3. It was found that 10 cm of external copper shielding was enough to reduce the rock gamma recoil rate within limit, producing an average of $1.6\pm0.7\times10^3$ recoils keV^{-1} yr^{-1} (1-10 keV). The gamma background due to the external copper shield was also investigated, using the radioactivity level for copper listed in Table 5.1 and was found to be < 100 keV^{-1} yr^{-1} (1-10 keV). This very low rate is most likely due to the gammas produce in the external shield having to pass through the internal shielding.

Table 6.1 summarises the TPC shielding required to produce an average gamma recoil rate within limit. As the simulations included the water shielding, described in Section 6.2, this is also included in Table 6.1.

Table 6.1: TPC shielding geometry required to produce an average gamma recoil rate within limit for an energy range of 1-10 keV.

Internal shield (cm)	External shield (cm)	Water shield (cm)	Recoil rate (keV^{-1} yr^{-1})
5	10	50	$3.1 \pm 1.1 \times 10^3$

The total neutron background, from the geometry listed in Table 6.1, was also investigated using the procedure described in Section 5.2 and Eq. 5.1 (previous chapter). This was found to be 0.017 ± 0.007 yr^{-1}, well within the 1 yr^{-1} limit.

6.4 Internal TPC Background

In the previous chapter, results from Section 5.5 showed that the readout closest to achieving the neutron (<1 yr^{-1}) and gamma ($<10^4$ keV^{-1} yr^{-1}) background limits was the MWPC with ThGEM amplification stage. This section investigates the background rates due to this readout configuration for the CYGNUS-10 prototype. The background from a 1 mm thick cylindrical acrylic frame is also investigated. The purpose of which is to provide a support structure for the readouts and field cage, as well as providing electrical insulation between the TPC voltages and internal shield. The background due to the same field cage resistors described in Section 5.5 of the previous chapter, is also investigated here for the CYGNUS-10 field cage.

6.4.1 Internal TPC Geometry

As mentioned in Section 6.1, the steel vessel radius can not exceed 1.1 m. For a 13 mm thick vessel with a 5 cm internal copper shield (see Table 6.1) this gives a maximum target gas volume radius of 1.037 m. Therefore, to

maintain a 10 m^3 volume of gas, the steel vessel length was simulated as 3.08 m. These dimensions are summarised in Table 6.2.

Table 6.2: TPC vessel, internal shield and target gas dimensions for a 10 m^3 target volume.

	Radius (mm)	Length (mm)
Vessel	1100	3080
Int. shield	1087	3054
Target gas	1037	2954

For a back-to-back readout design, the target gas length shown in Table 6.2 allows for a drift distance of ∼70 cm for a TPC consisting of two cathodes and four readouts. This configuration is shown by Figure 6.5, where the structures outlined in red and blue are the cathodes and readouts, respectively. A 2 cm clearance gap was maintained between each structure (readout and cathode) and the internal shield, this reduced the total target gas volume from 10 m^3 to ∼9.5 m^3. However, this is a practical requirement that allows for support structure and other TPC infrastructure such as HV access and cables.

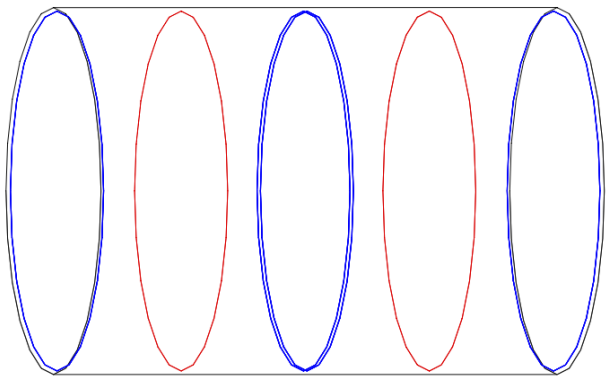

Figure 6.5: CYGNUS-10 TPC back-to-back geometry. Red = cathode, blue = readout.

A drift distance of 70 cm is 20 cm longer than that envisioned for CYGNUS-1000 and that used by DRIFT-IId (see Section 4.1 of Chapter 4). However, improvements in detector efficiency at high drift lengths, as shown in Section 4.3.4 of Chapter 4 for the DRIFT-IId TPC, suggest that it is possible to operate with longer drift regions. This design gives a total cathode and readout area of approximately 6.8 and 13.6 m^2, respectively. The results of this study can be extrapolated to other possible drift distances, for example a drift distance of 35 cm would incur ∼twice the readout background.

6.4.2 Gamma and Neutron Backgrounds

The structures considered for the CYGNUS-10 internal TPC background study are listed in Table 6.3 along with the simulated materials, dimensions and total mass.

Table 6.3: The internal TPC structures simulated along with their dimensions, material composition and total mass.

Structure	Material	Dimensions	Total Mass (kg)
Frame	Acrylic	1 mm thick hollow cylinder, radius 1017 mm, length 2914 mm	22
ThGEM	Acrylic	×4, radius 1017 mm, 1 mm thick	15.3
ThGEM	Copper	×8, radius 1017 mm, 0.1 mm thick	23.3
MWPC	Steel	×8 arrays, radius 1017mm, 0.1 mm thick	10.2
Resistors	Alumina	×200, 6.4 mm, 3.2 mm, 0.55 mm	$\sim 9^{-3}$

The 8 arrays, listed in the above table for the 4 MWPC readouts, are due to each of these readouts being constructed from two orthogonal wire arrays.

At 1 mm thick, the ThGEMs can be made of acrylic [131], which has a higher radiopurity than the Kapton usually used for this purpose. Copper, 0.1 mm thick, was also simulated on either side of each ThGEM. The wires, constituting the MWPC arrays, were envisioned as 0.1 mm thick with a 0.1

mm gap between each wire. This is an idealised MWPC configuration, however, more practical designs, with less spatial resolution (greater gap between wires), would produce less background. Therefore, the idealised model considered here, is the worse case scenario from a background perspective. To simulate the MWPCs, one long wire was positioned centrally inside the TPC gas volume and the resulting background was scaled to reflect the total from all 8 wire arrays. The simulated resistors were the same SM5D models [133] considered for CYGNUS-1000 (see Section 5.5.1 of the previous chapter). For the ∼3 m long CYGNUS-10 TPC, at least 200 of these would be required, based on the 66 resistors used for the 1 m long DRIFT-IId field cage [104]. To study the background from these resistors, a single resistor was simulated at the centre of the TPC gas volume and the resulting recoil rate was scaled to reflect the total background from 200 resistors.

After each simulation run, the background from the TPC material was calculated using the procedure described in Section 5.2 (previous chapter) and the activities listed in Table 5.1. The neutron and gamma background recoil rates were calculated using Eq 5.1 and Eq 5.2, respectively. Table 6.4 shows the neutron background for each of the materials and Figure 6.6 shows the gamma background for the same materials, the total recoil rate is given by the solid black line in this figure.

Table 6.4: CYGNUS-10 internal neutron background.

Structure	Material	Recoil Rate (yr^{-1})
Frame	Acrylic	$1.6 \pm 0.4 \times 10^{-3}$
ThGEM	Acrylic	$1.3 \pm 0.3 \times 10^{-3}$
ThGEM	Copper	$2.6 \pm 0.7 \times 10^{-6}$
Wires	Steel	$1.1 \pm 0.2 \times 10^{-4}$
Resistors	Alumina	$1.2 \pm 0.6 \times 10^{-5}$
Total	Internal TPC	$\sim 3 \pm 1 \times 10^{-3}$

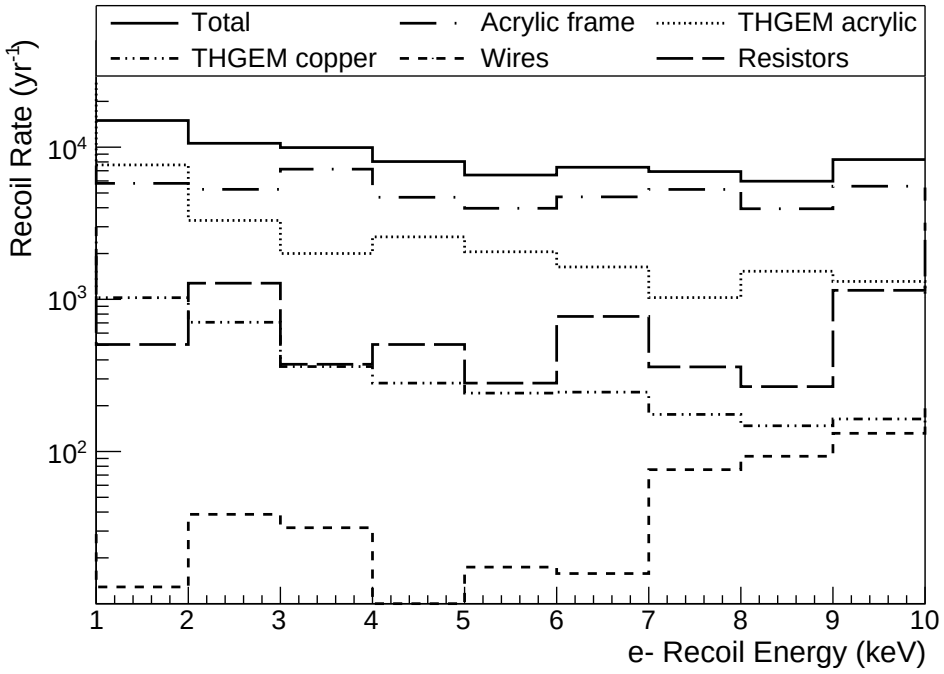

Figure 6.6: The internal TPC electron recoil background, between 1 and 10 keV, originating from gammas produced within the structural materials listed in Table 6.3. The total rate is shown by the solid black line.

Table 6.4 shows that the total neutron background, from the internal TPC components, is well within the imposed limit of 1 yr^{-1}. The above figure shows that the gamma background is just within the 10^4 keV^{-1} yr^{-1} limit above 3 keV and is only just above this limit at lower energies.

6.5 Total Background

The total electron background (yr^{-1} keV^{-1}), from the Compton scattering of gammas, was given as the sum of the internal, vessel and rock background contributions and is shown in Figure 6.7. The vessel and internal backgrounds are also shown separately in this figure and the contribution from rock gammas was included as an added 1.6×10^3 yr^{-1} keV^{-1}, which is the

average value (between 1-10 keV) given by Section 6.3. It can be seen from Figure 6.7 that the total gamma background is just within limit ($< 10^4$ keV^{-1} yr^{-1}) above 4 keV and is just above limit at lower energies.

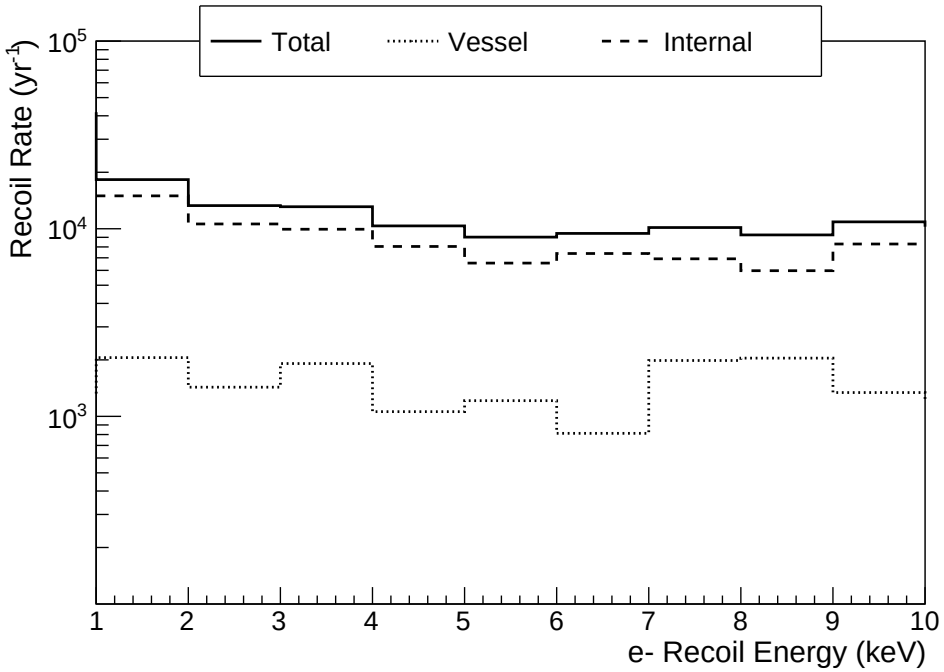

Figure 6.7: Total gamma-electron recoil background for CYGNUS-10 and the contribution from the steel vessel and internal TPC components. The rock gamma background is included as an averaged amount per keV.

The neutron background, from both the internal components and vessel, was found to be $\sim$0.02 yr^{-1} and the same background from the surrounding rock did not exceed 0.1 yr^{-1}. Therefore, the total neutron recoil rate within the target gas volume was well within the 1 yr^{-1} limit.

6.6 CYNGUS-10 Search Reach.

Results from Section 3.6 of Chapter 3 indicate that 10^4 electron recoils could be rejected per year per keV at and above a threshold of around 6 keV_{ee}. Using Eq. 4.23 and Eq. 4.24 of Chapter 4, a projected limit curve (at 90% CL) was calculated for an idealised CYGNUS-10 TPC with a 1 keV_{ee} threshold and 100% detection efficiency and for a more realistic CYGNUS-10 TPC with a 6 keV_{ee} threshold and 50% detection efficiency. The idealised case envisions future improvements in background discrimination that would allow for a 10^4 keV^{-1} yr^{-1} gamma rejection at and above 1 keV. The limit curves were calculated for a one year and ten year exposure and are shown in Figure 6.8.

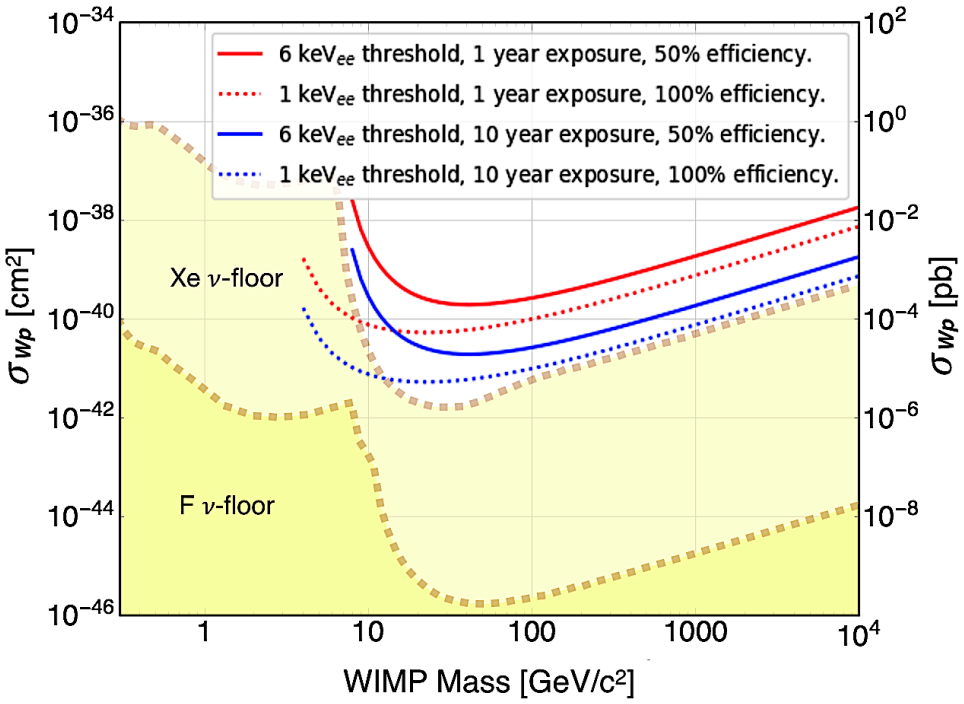

Figure 6.8: CYGNUS-10 search reach after 1 year (red) and 10 year (blue) exposures, for 6keV_{ee} threshold and 50% detection efficiency (solid line) and for a 1 keV_{ee} threshold and 100% detection efficiency (dotted line).

The results presented in Figure 6.8 suggest that a CYGNUS-10 TPC, with a threshold lower than 6 keV$_{ee}$, would be able to perform a background free search of a parameter space that, for a SD WIMP search experiment using a Xe target, would otherwise be susceptible to a neutrino background. However, it can be inferred from the same figure that the fluorine target mass of the TPC would not become sensitive to the neutrino background, even after 10 years of exposure, for any threshold or efficiency. This result would suggest that the CYGNUS-10 TPC should be considered as a prototype for the larger CYGNUS-1000 TPC and/or as the first of many modules that will collectively sum to a mass the same as, or even greater than, that achieved by a monolithic 1000 m^3 detector.

6.7 Conclusion

This chapter described the simulated background found within a CYGNUS-1000 prototype TPC, located at Boulby, named CYGNUS-10. The background from neutron recoils, between 1-200 keV$_r$, and gamma induced electron recoils, between 1-10 keV, was studied for a target gas volume of 20 Torr SF_6. The recoil rate, within the gas volume, due to neutrons and gammas originating from the rock cavern, vessel, shielding and internal TPC components was investigated. A limit on the neutron and gamma recoil rates of <1 yr^{-1} and $<10^4$ keV^{-1} yr^{-1}, respectively, was imposed.

It was found that for a CYGNUS-10 cylindrical vessel design, a 50 cm thick water shield and a 15 cm thick copper shield (10 cm external and 5 cm internal), reduced the neutron and gamma background contributions, from the rock, vessel and copper shielding, to within limit. The TPC was envisioned with a back-to-back (readout-cathode-readout) configuration with 70 cm drift regions. The internal TPC components investigated included: 4 ThGEM's (used for signal amplification), 8 MWPC wire arrays (used to readout the signal in 2D), a 1 mm acrylic frame (used for structural support

and voltage insulation) and 200 resistors (used to configure the field cage). With these additional background sources, the total neutron background was found to be $<<1$ yr^{-1}, while the total gamma background was found to be within limit for recoil energies >4 keV. Below this energy, the gamma background was found to be only just above limit (between 1-2$\times10^4$ keV^{-1} yr^{-1}). The CYGNUS-10 TPC would also be subject to the additional backgrounds discussed in Section 5.5.3, of the previous chapter, for the CYGNUS-1000 TPC, however, the same mitigation methods discussed in that section could also be used for CYGNUS-10.

WIMP exclusion limits were predicted for a realistic CYGNUS-10 TPC with a 6 keV$_{ee}$ threshold and 50% detection efficiency (based on results from Section 3.6 of Chapter 3), as well as for an idealised version that could achieve a 1 keV$_{ee}$ threshold and 100% detection efficiency. The resulting limit curves showed that the CYGNUS-10 TPC could explore a parameter space that would prove difficult for a Xe based detector (due to the higher neutrino floor for a Xe target). However, a larger scale TPC or multiple 10 m^3 TPCs would be required to extend the sensitivity into the neutrino floor for a fluorine based target.

The background study presented in this, and the previous, chapter suggest that the best readout option, from a background perspective, would be an MWPC with ThGEM avalanche phase. The testing of a prototype version of this readout is the subject of the next chapter.

Chapter 7

CYGNUS-10 Readout Prototype ThGEM-MWPC Hybrid

The study described in the previous two chapters revealed that the main concern, from a background perspective, for a large scale TPC such as CYGNUS-1000 or CYGNUS-10 comes form the internal TPC components. In particular, the choice of readout was found to significantly impact the background rate. For this reason, an important step for the CYGNUS collaboration is to find a low background readout that does not compromise on other important aspects, such as low energy threshold, high positional resolution and 3D track reconstruction. As described in the previous chapters, most readouts (such as pixel chip or μ-PIC for example) do not currently meet the required radiopurity levels, at least in the case of CYGNUS-1000. The most promising readout, in terms of low background, is the MWPC. However, the magnitude of the avalanche field, induced between the wire arrays of an MWPC, is limited to the amount of tension that the wires can withstand before breaking. This means that, for the reasons given in Section 2.4.3 of Chapter 2, it is not feasible to solely operate an MWPC readout in SF_6. Instead, by combining the readout with a ThGEM, the avalanche field can be induced through the ThGEM rather than between wire arrays, which can then be dedicated to

the accumulation of the avalanched signal. This hybrid design also allows for the combination of high ThGEM gains with low noise wires to potentially produce a significant signal to noise ratio. Further to this, not having to apply voltage to the wires allows the wire pitch to be reduced (compared to the 2 mm pitch of the DRIFT-IId MWPCs). The design, setup and testing of a 600 μm pitch wire array with ThGEM avalanche stage is the subject of this chapter.

For CYGNUS-10, and eventually CYGNUS-1000, large readouts will be required to cover the scaled-up areas. A typical readout would be between 30×30 cm^2 and 1×1 m^2. The prototype introduced in this chapter is at the lower end of this scale, utilising a 30 cm wire array. The next chapter describes the study of a similar size ThGEM but for the work presented here, a more commonly sized ThGEM of 10 cm diameter was used, as the performance of this device is well understood and, therefore, allows for a direct test of the wire array. Only 16 30 cm long wires, placed along a single axis of the readout plane (x-axis), were required for these initial tests, the goal of which were: to show MWPC wire operations at sub-mm pitch; establish the readout gain; to demonstrate tracking for a readout with a size relevant to a future large scale TPC. The work presented here, builds on previous results that show the successful operation of a 4 cm^2 ThGEM-MWPC hybrid, with 1 mm pitch, in low pressure SF_6 gas [78].

The design and setup of the prototype is covered in detail by Section 7.1 and the testing, including gain measurements and track reconstruction, is covered in Sections 7.2 and 7.3, respectively.

7.1 Readout Design and TPC Configuration

The ThGEM was constructed at the European Organization for Nuclear Research (CERN) using the parameters listed in Table 7.1.

Table 7.1: ThGEM parameters in mm.

Diameter	Width	Hole diameter	Hole pitch	Etched rim
100	0.4	0.4	0.6	0.04

The MWPC was constructed as a single array of 16 100 μm steel wires, with a 600 μm pitch. Resulting in the highest spatial resolution achieved for an MWPC wire array (known to the author), which as described in Section 3.3 of Chapter 3, is important for low energy background rejection. A 1 mm gap was maintained between the ThGEM and the wires and the readout was mounted onto a printed circuit board (PCB), designed using the PCB software package EAGLE (Easily Applicable Graphical Layout Editor) [142] and constructed by Quick Circuits UK [143]. The readout is shown, mounted onto the board, in Figure 7.1.

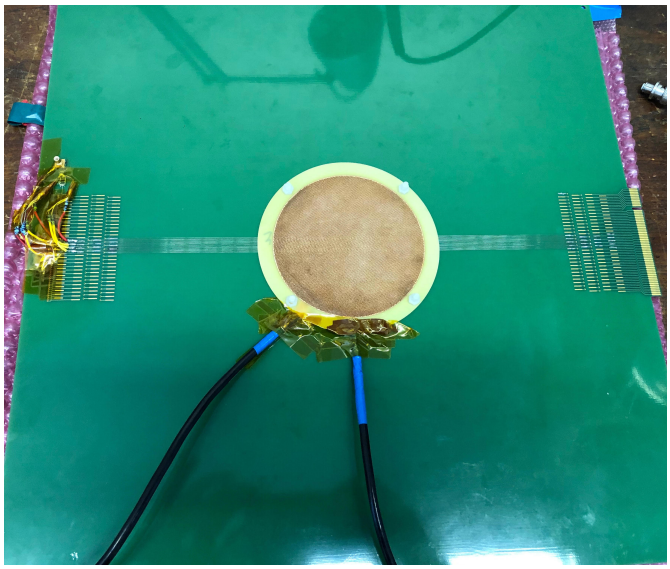

Figure 7.1: ThGEM-MWPC hybrid readout. The two SHV cables attached to the ThGEM were for voltage supply. The wires were grounded via 1 MΩ resistors (shown on the left of the figure).

Figure 7.2 below, shows the design schematic, created in EAGLE, of the PCB wire connection pads and card edge connector (shown on the right in Figure 7.1). The latter was used to connect the wires to SMC (SubMiniature version C) cables, which then transferred the signal to the processing electronics.

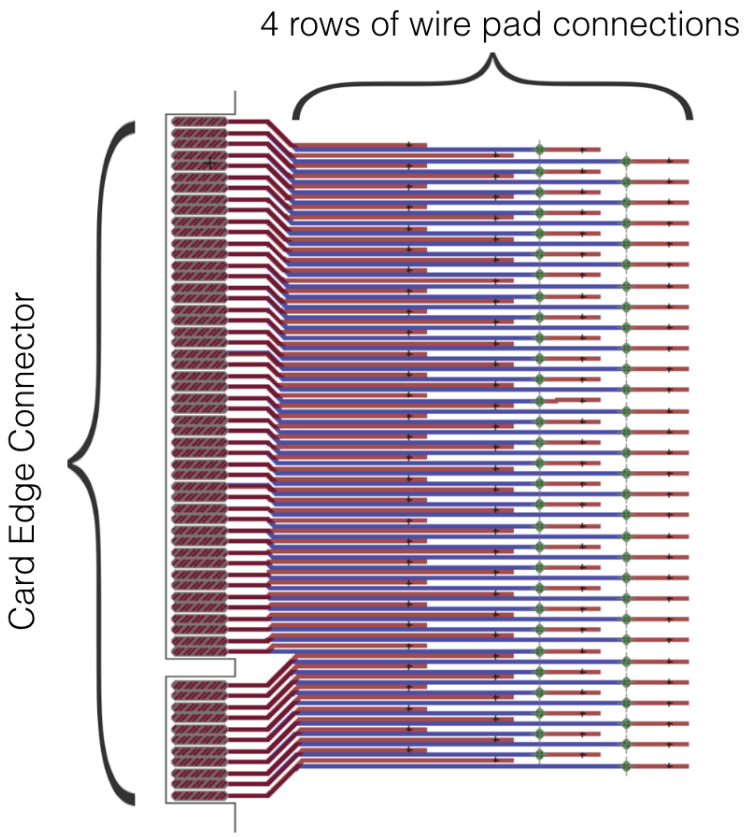

Figure 7.2: A design schematic, created using EAGLE, showing the wire connection pads (denoted by the black crosses) and card edge connector of the ThGEM-MWPC PCB.

The wire connection pads, shown in the above figure, were horizontally separated into four rows, to prevent any overlap between them. The blue and red lines on the figure show the electrical connections between the wire pads

and the card edge connector. The blue lines are on the top of the board and the red lines are underneath. The green dots show via points that connect the top of the board to the bottom. The electrical connections were separated onto either side of the board to ensure sufficient spacing between them. The 100 μm wires, constituting the array, were held in place by tension weights and then soldered, by eye, onto the centre of each wire connection pad. An error of $\pm$150 μm was estimated for the wire positions.

The readout was separated from a copper plate cathode by a 9 cm field cage, the cathode and field cage are shown in Figure 7.3.

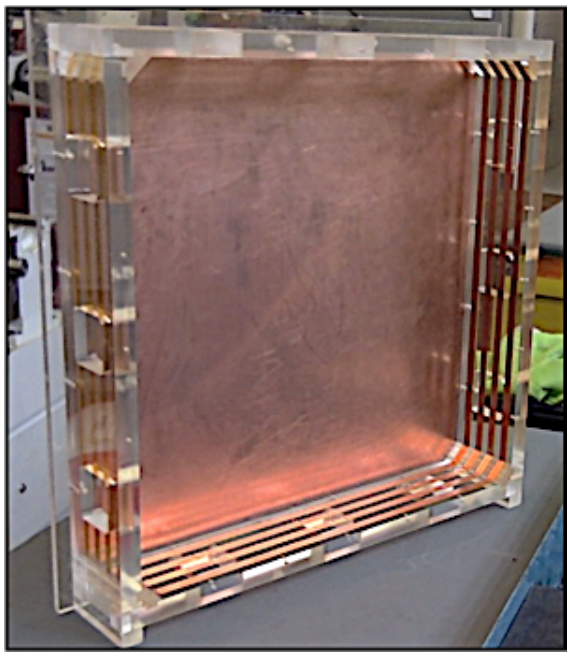

Figure 7.3: Field cage and cathode used to create the drift field for the ThGEM-MWPC hybrid readout.

The field cage was constructed out of acrylic and the field rings were made of 1 cm thick copper tape. The cathode and each ring was consecutively connected together using 33 MΩ resistors and the final ring was connected

to ground via a 100 MΩ resistor. The full readout, field cage and cathode configuration is shown in Figure 7.4.

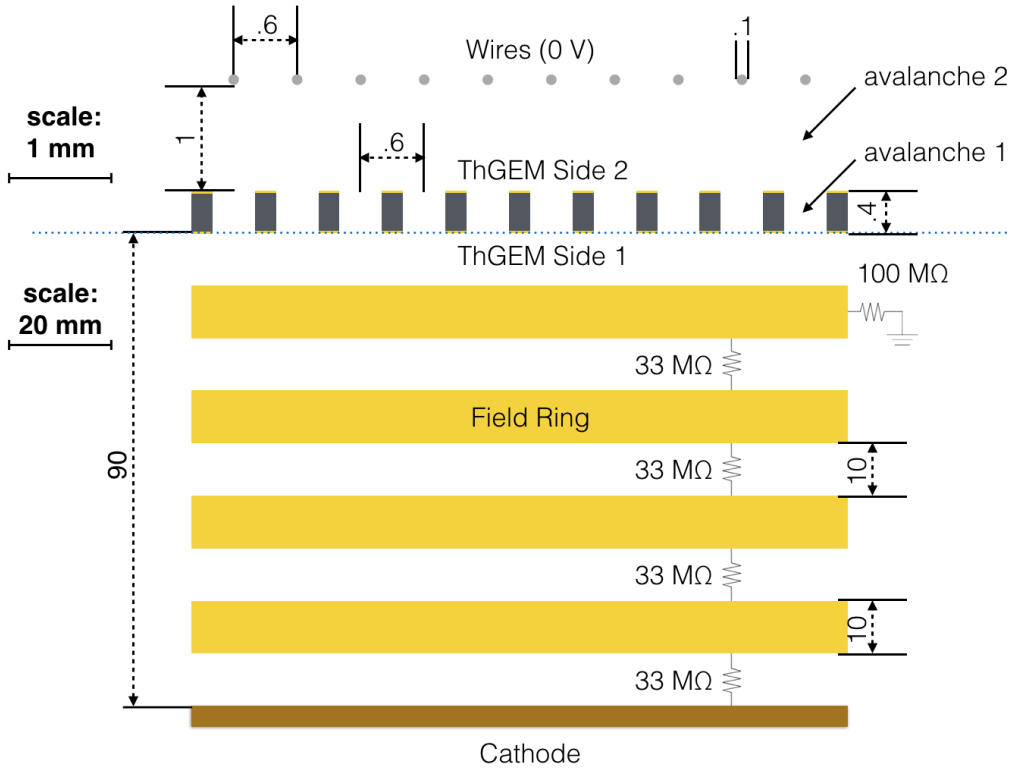

Figure 7.4: ThGEM-MWPC readout, cathode and field cage configuration shown to scale. The blue dotted line, between the readout and field cage, denotes a change in scale. There are two avalanche fields present in the configuration, one within the ThGEM and one between the ThGEM and wires, labelled avalanche 1 and 2 respectively.

As side 1 of the ThGEM (see above figure) was at negative potential for all voltage setups, the field cage resistor configuration ensured that the drift field was always in the correct direction and was stepped down uniformly towards the ThGEM potential. The configuration shown in Figure 7.4 includes two avalanche fields, one between either side of the ThGEM and one between the ThGEM and wire array (labelled 1 and 2, respectively, on the figure).

Each wire was individually grounded via a 1 MΩ resistor, shown on the left of Figure 7.1. The resistors ensured that signal collected on the wires was not sent to ground and that each wire was separated from the others. The wire signal was collected at the opposite side of the board to the resistors using a card-edge connector, where it was then sent to a Cremat-110 pre-amplifier [144] and Cremant 200 4 μs shaper [145] for digitisation, amplification and pulse shaping. The signal was then received by a 16 channel National Instruments Labview Data Acquisition System (DAQ) where it was recorded as digital waveforms. The TPC (made up of the ThGEM, MWPC, cathode, field cage and electronics) was placed inside a 2 cm thick steel vacuum vessel. Figure 7.5 shows the full TPC setup inside the vessel, with the ThGEM and MWPC wires attached to the PCB and then mounted onto the field cage.

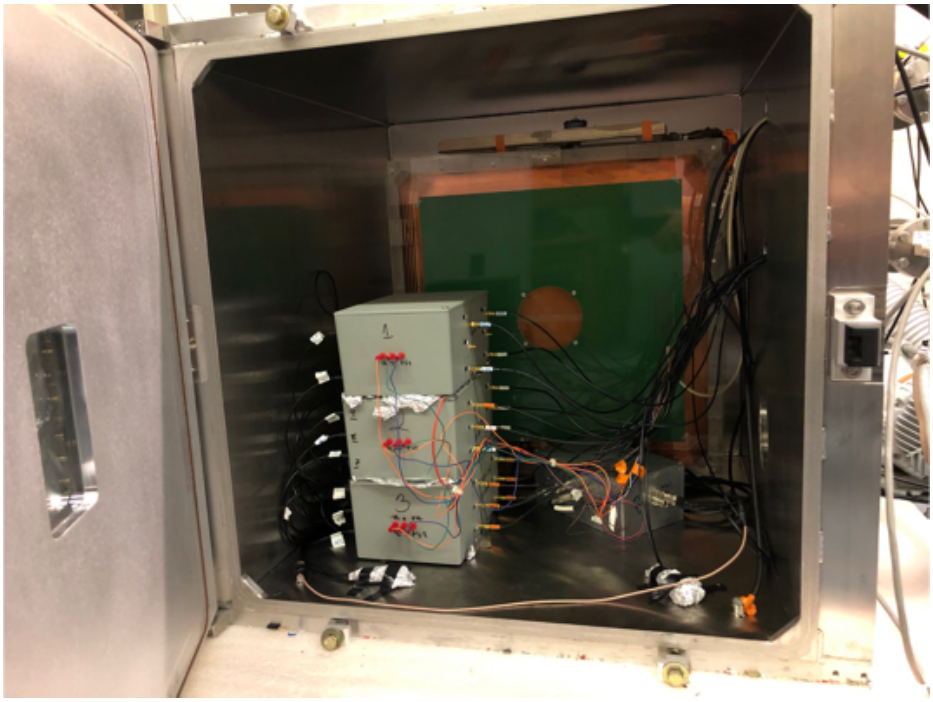

Figure 7.5: The prototype TPC setup inside the steel vacuum vessel.

The three grey boxes, in the above figure, contain the MWPC pre-amplifiers and shapers and the silver box on the floor of the vessel contains the same electronics for the ThGEM, allowing the ThGEM response to be studied independently of the MWPC.

7.1.1 Electric Field Configuration

For the gain measurements described in Section 7.2, the gain due to avalanche 1 was studied independently of that due to avalanche 2 (see Figure 7.2). This was done to study the separate contributions, to the total gain, from the two avalanche fields. The signal was collected on either side 2 of the ThGEM (see Figure 7.2) or on the wires, depending on wether the gain contribution from avalanche 1 or avalanche 2, respectively, was being studied. Table 7.2 shows an example of the voltage configuration used for signal collection on side 2 of the ThGEM and on the wires. The table also lists the corresponding drift, avalanche 1 and avalanche 2 fields.

Table 7.2: Voltage configuration examples for signal collection on the wires and on the ThGEM. As shown in Figure 7.2, side 1 is the ThGEM side facing the cathode and side 2 is the ThGEM side facing the wires.

Signal Collection	Cathode (V)	Side 1 (V)	Side 2 (V)	Wires (V)	Drift field (V cm^{-1})	Avalanche 1 (V cm^{-1})	Avalanche 2 (V cm^{-1})
Wires	-3400	-880	-200	0	280	17000	2000
ThGEM	-3200	-680	+200	0	280	17000	0

To study the electric field line configuration for signal collection on the ThGEM and on the wires, Ansys Mechanical v14.5 [146] was used to create field maps from the TPC geometry and different field configurations listed in Table 7.2. The maps were imported into Garfield [101] and 100 electrons were simulated above the ThGEM with a uniform spatial distribution. Diffusion was turned off in the simulation so that the field lines could be observed

directly from the electron drift paths. These are shown in Figure 7.6 for electrons entering one of the ThGEM holes and being collected on side 2 of the ThGEM (left) and on one of the wires (right).

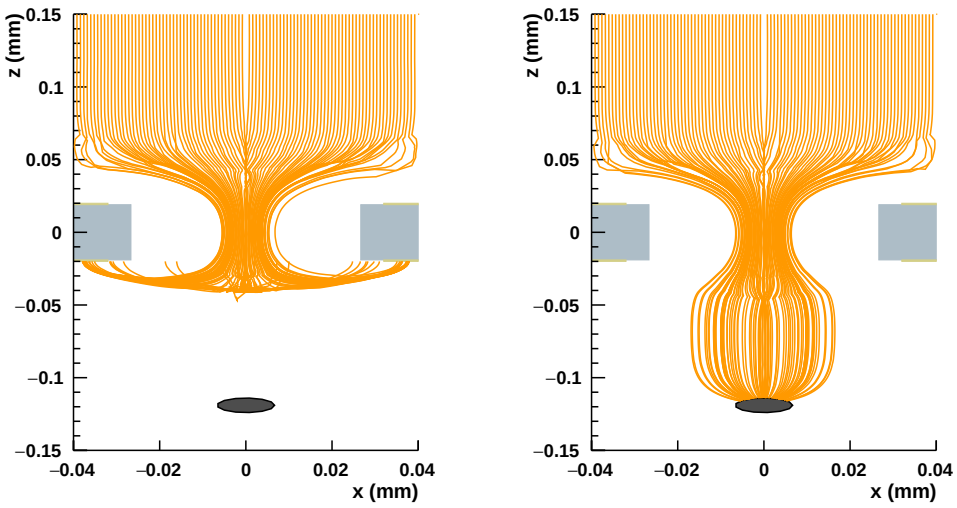

Figure 7.6: Electron drift paths (with no diffusion), generated in Garfield, for the two voltage configurations listed in Table 7.2. Signal collection on the ThGEM and on the wires is shown on the left and right, respectively.

The above figure shows, that as expected, the field lines terminate on the ThGEM or on the wire depending on the chosen field configuration.

7.2 Gas Gain Measurements

Gain is produced when ionised electrons enter a high electric field region, such as the avalanche fields shown in Figure 7.4, causing the electron to accelerate and produce further impact ionisation. The ionised electrons cause further ionisation and their number grows exponentially, as expressed by Eq 7.1 [147] below,

$$n(d) = n_0 \mathrm{e}^{\alpha d} \tag{7.1}$$

where α is the first Townsend coefficient, $n(d)$ is the number of electrons leaving an avalanche region of length d and n_0 is the initial number of electrons (the primary ionisation). The gain is then given as $n(d)/n_0$.

The ultimate goal for the ThGEM-MWPC hybrid readout is to prove gains $\mathcal{O}(10^3)$ are possible in 20 Torr SF_6, as achieved by Ref. [69] using similar ThGEM readouts. However, for these initial tests, CF_4 gas was selected due to the higher gains achievable with electron drift (as opposed to negative ion drift, where attachment processes can reduce the electron signal). A stable gas pressure of 50 Torr was chosen to limit the number of electrical breakdown events that could occur during the initial testing phase.

7.2.1 Calibration of the Signal Electronics

As well as the signal amplification produced by the avalanche fields (gain), further amplification was also produced by the pre-amplifier and shaping electronics, which enabled small signal responses to be visible on the recorded waveform. To prevent this extra amplification from being associated with gain, the electronics were calibrated. This was achieved using an Ortec Model 480 Pulser [148] to generate pulses with voltage amplitude, V. The pulses were converted into a charge, q, by passing them through a capacitor with capacitance, C, to give, $q = VC$. This charge was then passed through the pre-amplifier and shaping electronics and the resulting signal amplitude was recorded. By varying the amplitude of the pulses, produced by the pulser, a linear relation between input charge and output signal amplitude was found, which could then be used to convert any signal into a charge reading. Such a relation is shown in Figure 7.7 for the ThGEM electronics.

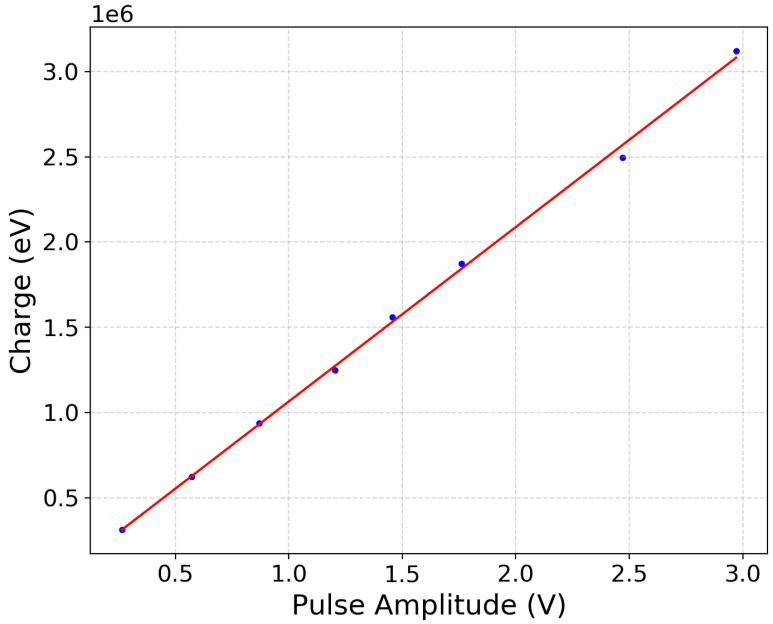

Figure 7.7: Linear relation between charge and signal pulse height, found from calibrating the ThGEM electrons.

7.2.2 ^{55}Fe Measurements

As the avalanche field through the ThGEM (avalanche 1) was expected to provide the majority of the electron multiplication, the change in ThGEM and wire gain with variation in this field was studied, whilst the drift and avalanche 2 fields were kept constant. To produce a known amount of ionisation charge inside the TPC gas volume, an ^{55}Fe source was placed within the drift region, close to the readout, as shown in Figure 7.8. ^{55}Fe decays via electron capture to produce ^{55}Mn and a 5.9 keV X-Ray. The latter is subsequently photo-absorbed by a CF_4 molecule, resulting in the emission of a 5.9 keV electron. As the electron recoils in the gas, it's energy is deposited as ionisation. CF_4 has a W value of 34.2 eV [149] and, therefore, the recoil produces a known ionisation of 5900 eV / 34.2 eV = 172 q, where q is the

elementary charge.

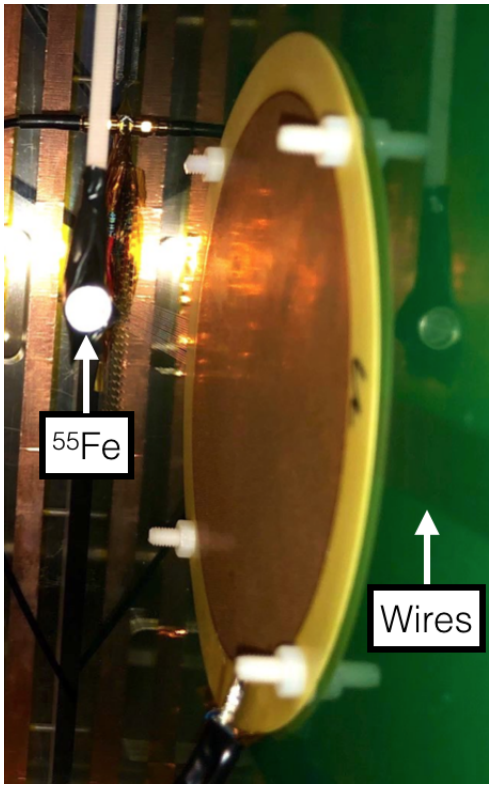

Figure 7.8: ^{55}Fe source positioned close to the readout.

To study the gain, the known ionisation charge was compared to the mean avalanche charge, collected on both the ThGEM and the wires, for avalanche 1 fields of between 16500 and 18000 V cm^{-1}, increasing by 250 V cm^{-1} increments (all other fields where kept at the constant values listed in Table 7.2). The mean charge, for each avalanche 1 field, was calculated from a gaussian fit to a spectrum of signal amplitude responses, recorded during an ^{55}Fe exposure. An example of such a spectrum, produced using a Multi-Channel Analyser (MCA), is shown in Figure 7.9 for signal collection on the ThGEM. Comparison of the signal spectrum (blue) and background spectrum (red), in this figure, was used to confirm that the ThGEM was

detecting the source.

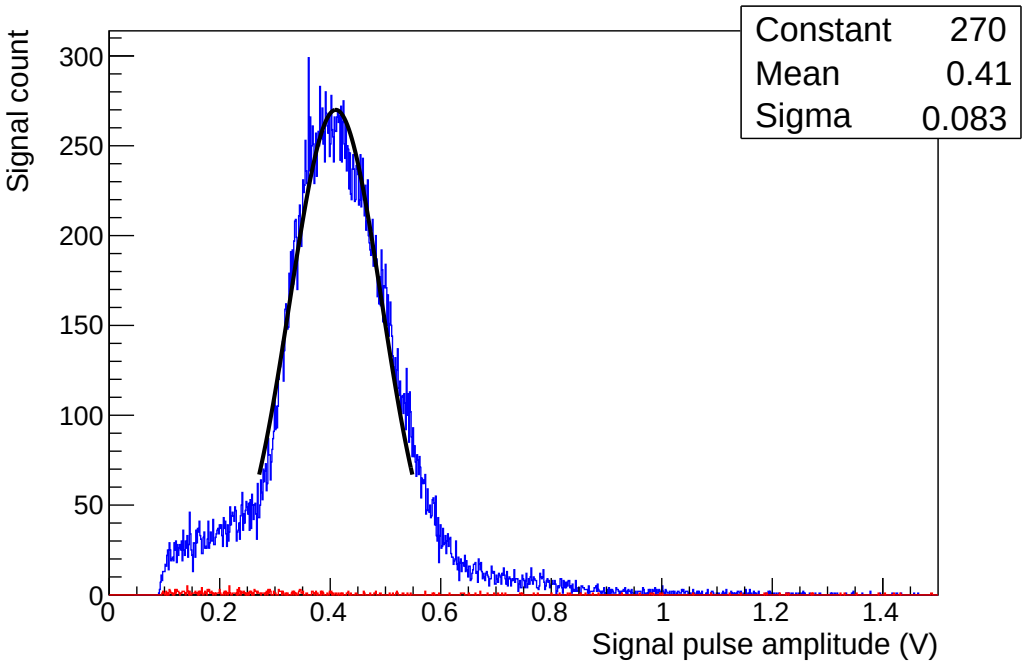

Figure 7.9: Blue: Spectrum of signal collected on the ThGEM during an ^{55}Fe exposure with an avalanche 1 field of 17500 V cm^{-1}. Red: Background spectrum taken with the same field configuration and duration (100 s) used for the ^{55}Fe exposure but with the source removed. Black: Fitted gaussian. The MCA default binning is 8192 bins over a 12 V range.

A clear peak can be seen in the above figure, to which, a gaussian curve was fitted (shown in black). This was used to derive the mean signal amplitude, which is related to the gain, and the FWHM (Full Width at Half Maximum), which is related to the energy resolution. The high signal to background ratio, shown in Figure 7.9, was achieved by locating the preamplifiers inside the vessel and as close to the MWPC as possible. This helped to minimise the noise induced on the SMC cables, which transported the raw signal to the preamplifiers.

The same spectrum is shown in Figure 7.10 for signal collection on the

wires during a 10 minute ^{55}Fe exposure, from which, the presence of signal above background can be observed. An increased exposure time was required for the wires (compared to that of the ThGEM), as the total signal collection area was much smaller.

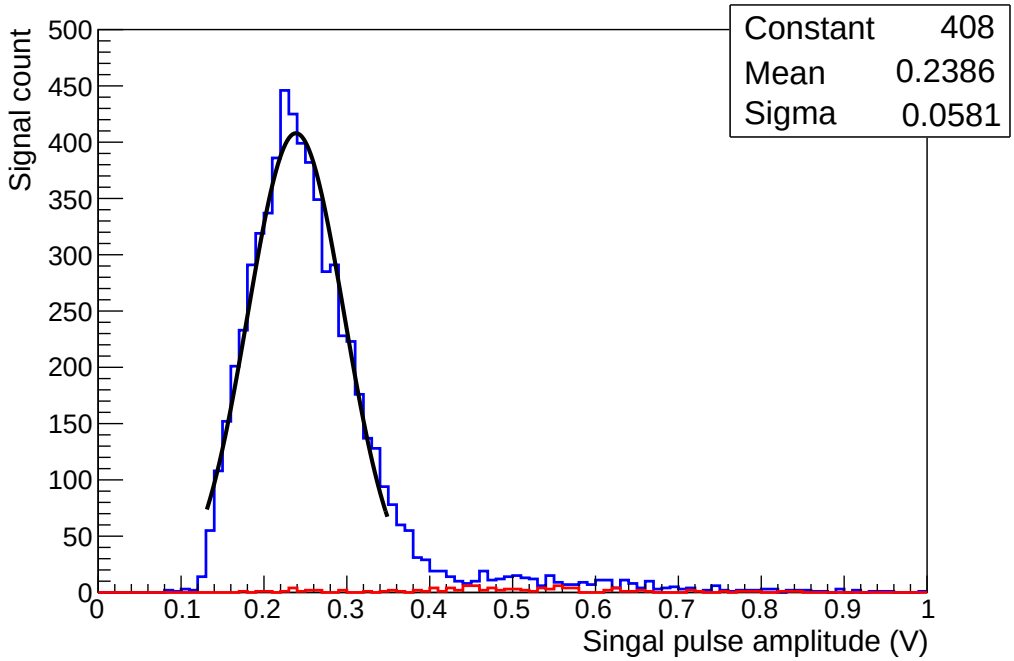

Figure 7.10: Blue: Signal spectrum for signal collected on the wires during an ^{55}Fe exposure with an avalanche 1 field of 17250 V cm^{-1}. Red: Background spectrum taken with the same field configuration and duration (10 minutes) used for the ^{55}Fe exposure but with the source removed. Black: Fitted gaussian. The bin width used for the spectra is 10 mV.

During the ^{55}Fe exposures, the wire signal was seen to extend across up to five separate wires, an example of this is shown in Figure 7.11. Due to the multi-wire responses, the amplitude of each wire was summed to give a total amplitude, which is the data presented in Figure 7.10. This meant that, for some of the time, only part of the full signal was being recorded and the total amplitude was, therefore, slightly lowered. This caused the peak shown in

Figure 7.10 to be slightly skewed to the left.

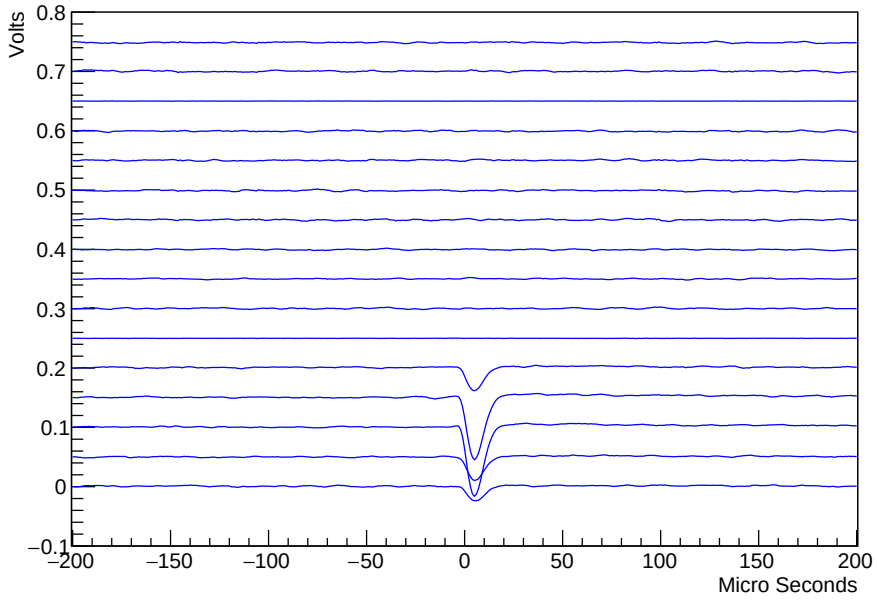

Figure 7.11: ^{55}Fe signal, in 50 Torr of CF_4, showing response across five wires.

The lack of response seen at low voltage amplitudes, for both ^{55}Fe spectra shown in Figures 7.9 and 7.10, was due to the threshold position, which was set to remove low amplitude noise and to minimise the data collection dead time. Although both peak positions are similar for both the ThGEM and wire spectra, this is not an indication of similar gain, mainly because the binning is different for each spectra but also because the ThGEM and wire electronics were calibrated independently.

7.2.3 Results and Discussion

The gain variation with avalanche 1 field is shown in Figure 7.12 for signal collection on the wires, where the error is given as the standard deviation

of the fitted gaussian curves. Also included in this figure are two gain measurements made for signal collection on the ThGEM (the red points), which show a gain of 79±28 and 104±40 for avalanche 1 fields of 17500 and 18000 V cm^{-1}, respectively. The field between the ThGEM and wires (the avalanche 2 field) contributes an additional gain factor of ∼15.

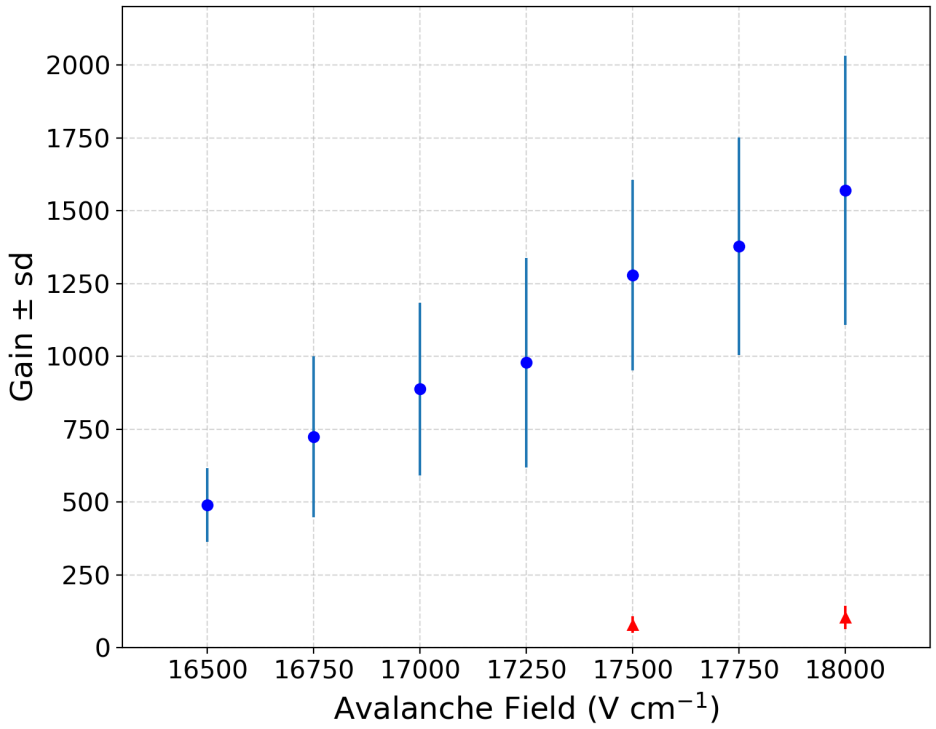

Figure 7.12: ThGEM-MWPC hybrid readout gain (blue), for avalanche 1 fields between 16500 and 18000 V cm^{-1}. The remaining fields are set at the constant values listed in Table 7.2. Shown in red are two ThGEM gain measurements.

The mean FWHM resolution of the ThGEM and MWPC was measured from the data in Figure 7.12 and found to be 74% and 73%, respectively. The lack of significant change in energy resolution, between the ThGEM and the MWPC, indicates that the resolution is determined by the avalanche field

through the ThGEM.

These results demonstrate that the ThGEM-MWPC hybrid concept works well in CF_4 gas at a 30 cm scale and with a sub-mm pitch. However, previous ThGEM gain studies, conducted using the same type of ThGEM (without MWPC) as used in this work, have proven to produce gas gains, in 50 Torr CF_4, of $\sim\times100$ that reported in this study [150]. The observed reduction in gain was most likely due to a degradation in ThGEM performance caused by damage incurred from the handling and operation of the device over time (the ThGEM used in this study was at least four years old). In particular, this involves damage inflicted on the ThGEM holes due to a build up of small discharge events. This could also result in a variation in avalanche fields between each ThGEM hole and, therefore, negatively effect the energy resolution. For these reasons, it was not possible to observe ^{55}Fe signal, with this readout, in SF_6 gas. However, as described in Section 2.4.4 of Chapter 2 a measurement made in 20 Torr SF_6, using an earlier ThGEM-MWPC readout prototype, reports a gain $\mathcal{O}(10^3)$ [78]. Figure 2.14, of the aforementioned section, shows an ^{55}Fe spectrum taken with this prototype, which has an $\sim$4 cm^2 readout area and 1 mm wire pitch. This result provides a proof of concept for the operation of a ThGEM-MWPC hybrid readout in SF_6 gas, indicating that, with improvement (i.e. a new ThGEM device) the same result would be possible for the larger prototype discussed in this chapter.

7.3 Alpha Track Reconstruction

Although low energy ^{55}Fe X-Rays were not observed in SF_6 gas, the tracking of particles in this gas, using the 30 cm long, sub-mm wire array, remains a key goal of this work. This section describes the reconstruction of higher energy (compared to ^{55}Fe) alpha tracks with the ThGEM-MWPC hybrid readout and details the process used to measure the SF_6^- reduced mobility.

The SF_6 pressure was optimised to give the clearest signal response, which

occurred at a pressure of 15 Torr. The alphas where produced, with an energy of 5.5 MeV, using an ^{241}Am source, which was initially positioned behind a shutter device placed on top of the field cage (the shutter can be seen in position in Figure 7.5). By closing the shutter the TPC was shielded from the emitted alphas and no signal response was observed, which confirmed that the response observed with the shutter open was due to the source.

With this confirmation, the next step was to investigate the presence of signal delay across the wires, which was required to both reconstruct the alpha tracks in 2D and to measure the SF_6^- reduced mobility. The delay is a result of drifting SF_6^- ions (as described in Section 2.4.3 of Chapter 2) that are produced by a recoil with a vector component normal to the readout plane. An example of signal delay, detected using the ThGEM-MWPC hybrid prototype, for an ^{241}Am alpha, is given in Figure 7.13.

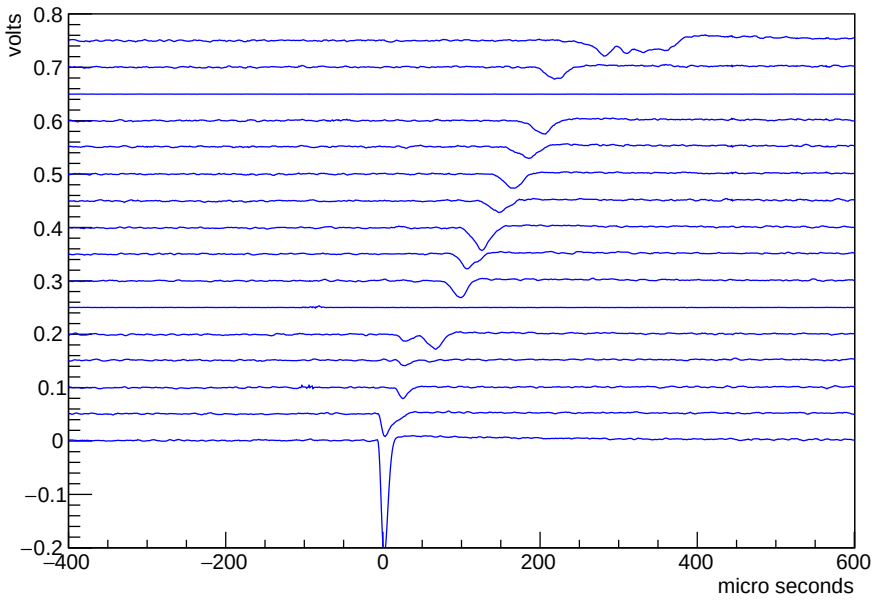

Figure 7.13: Alpha track in 15 Torr of SF_6, showing signal delay between each wire. The two wires showing no response were purposely disconnected due to a high noise level observed on those wire.

The delay in signal response, seen for some of the alpha events, was used to study the ion drift speed, v_d. From this, the reduced mobility, μ_0, could be derived for a drift field, E, of 300 V cm^{-1} and for 15 Torr of SF_6 gas. By combining Eq. 3.3 and Eq. 3.4, from Chapter 3, μ_0 can be expressed as,

$$\mu_0 = \frac{v_d N}{E N_0} \tag{7.2}$$

where N_0 is the SF_6 gas density at 0 °C and 760 Torr and N is the gas density at room temperature and 15 Torr.

For alpha events showing signal delay, the duration between the first and last signal response, t, and the separation (along the drift direction) between the corresponding ionisation, L, could be used to calculate the drift velocity via, $v_d = L/t$. Figure 7.14 shows the source position used to induce signal delay across the wires. The geometry shown in this figure results in the maximum value of L, L_{MAX}, occurring when an emitted alpha particle crosses the intersection point marked by the red circle in the figure.

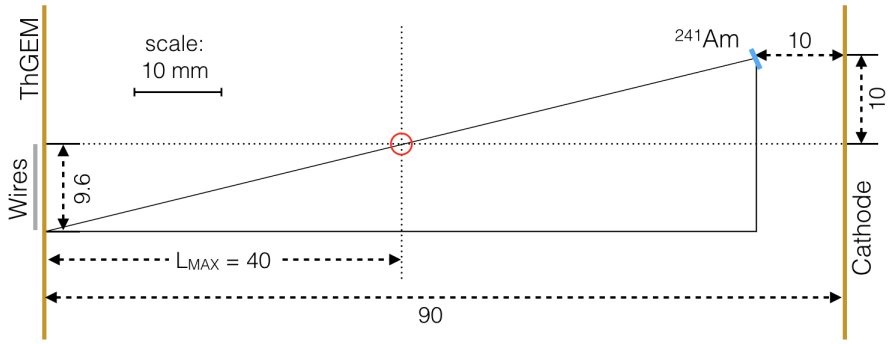

Figure 7.14: The source position used to induce signal delay across the wires. The ^{241}Am source is shown by the blue rectangle. The red circle shows the intercept point, between an emitted alpha and the first wire, when $L = L_{MAX}$.

As the source emits alpha particles isotropically, the average L, $\overline{L}$, can be approximated as the middle value between L_{MIN}, corresponding to no delay, and L_{MAX}, which is shown in Figure 7.14 to be 4 cm. This gives $\overline{L}$ $\sim$2 cm, which along with the mean t, $\bar{t}$, gives the average drift velocity, $\overline{v}_d = \overline{L}/\bar{t}$. To calculate $\bar{t}$, only alpha recoils that produced a signal above 10 mV on at least 10 wires were selected. Alpha events with t greater than 400 μs were found to contain either multiple events or a significant noise element, therefore, these events, as well as those with no signal delay, were cut from the data. The alpha selection process reduced the data from 486 to 65 events, for which $\bar{t} = 301 \pm 45$ μs, giving, $\overline{v}_d = 67 \pm 9$ m s^{-1}. Inputting the latter into Eq. 7.2 (in place of v_d) gives, $\mu_0 = 0.48 \pm 0.06$ V^{-1} cm^2 s^{-1}. This agrees, within error, with the reduced mobility value of 0.540 ± 0.002 V^{-1} cm^2 s^{-1}, which was extrapolated from measurements made by Ref. [69] for the same reduced field (E/N).

Figure 7.15 shows the 2D distribution of ionisation for three different alpha recoils in 15 Torr SF_6, demonstrating track reconstruction with sub-mm resolution using the large area ThGEM-MWPC hybrid readout. The signal response on each wire was converted to the ionisation charge shown in this figure using the procedure described in Section 7.2.1, along with an SF_6 W value of 34 eV [99]. The drift distance (z) of the ionisation, shown in Figure 7.15, was reconstructed as, $z = \overline{v}_d t$. The figure shows ionisation from only a part of each full alpha track as the particle is not fully contained within the drift volume. Despite this, an increase in ionisation can be seen towards the end of the observable recoils, which is associated with the start of the alpha particle's Bragg peak.

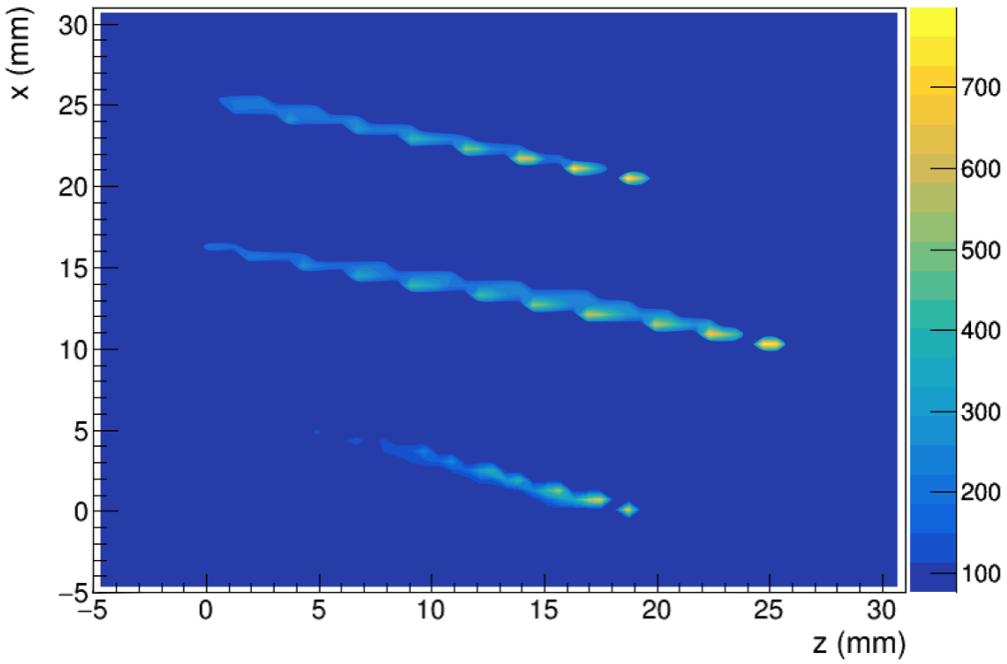

Figure 7.15: Contour plot of alpha ionisation in 15 Torr SF_6. The key gives the electron density.

7.4 Conclusion

This chapter described the performance of a CYGNUS-10 prototype, constructed from an MWPC readout with a ThGEM amplification stage. The ThGEM used was 10 cm in diameter with a 600 μm hole pitch. The wires constituting the MWPC were 100 μm thick with 600 μm spacing, resulting in the highest spatial resolution achieved by an MWPC (known to the author). Gain measurements taken in 50 Torr CF_4 were found to be unexpectedly low, being in the region of $\sim 10^2$ rather than the $\sim 10^4$ gains reported in the literature. The low gain was most likely due to degradation in the ThGEM performance with time due to an accumilation of damage. Despite this, observation of signal collection on the wires, from low energy ^{55}Fe X-Rays, proved that the ThGEM-MWPC hybrid readout does work at large scales

(30 cm) and with sub-mm pitch. The low gain measured in CF_4 meant that it would be unlikely to observe the X-Rays in SF_6 gas, however, this was achieved for a smaller preceding prototype readout of a similar design, which suggests that, with improvements the same result could be achieved for the larger prototype described in this chapter. Although gain measurements in SF_6 were not attempted in this work, track reconstruction of alpha events was shown in 15 Torr of SF_6. Using the alpha track data, the negative ion reduced mobility was investigated and found to be 0.48 ± 0.06 V^{-1} cm^2 s^{-1}, in agreement with measurements found in the literature. The results presented in this chapter suggest that a ThGEM-MWPC readout is a viable option for a large scale TPC such as CYGNUS-10 or CYGNUS-1000. The next stage of prototype tests, for this type of readout, should look to include a second wire array, in the y-direction, to enable full 3D tracking and should include a new or cleaned/repaired ThGEM device to allow for gain measurements in SF_6.

Chapter 8

Testing of a Large Area ThGEM

The work presented in the previous chapter showed the successful operation of a high resolution MWPC-ThGEM readout, with a wire array of appropriate length for a future large scale CYGNUS TPC. The ThGEM used for this readout prototype was 10 cm in diameter. Whilst it would be feasible to tile this size of ThGEM to cover large readout areas, it would be preferable, and cheaper, to construct these devices on a similar scale to that of the readout (between 30×30 cm^2 and 1×1 m^2). This is true, not only for the MWPC-ThGEM prototype discussed in the previous chapter, but for any type of potential CYGNUS TPC readout, which will all require a stable avalanche phase. This chapter reports a study, along these lines, of a large area ThGEM, conducted in collaboration with the CERN MPDG group. The work was also a collaborative effort with Kobe University, where the study took place, with the ultimate aim of comparing multiple large scale readout options inside a single CYGNUS prototype TPC, called CYGNUS-KM (CYGNUS-Kamioka).

For this chapter, the ThGEM design and experimental setup is discussed in Section 8.1 and the measurement technique and calibration is discussed in Section 8.2. Section 8.3 then describes a simulation procedure used to predict the ThGEM performance and this is compared to the gain measurement

result presented in Section 8.4.

8.1 Large Area ThGEM Design and Setup

The ThGEM was constructed at the European Organization for Nuclear Research (CERN), with the parameters listed in Table 8.1.

Table 8.1: Large Area ThGEM parameters.

Size (mm^2)	Signal Area (mm^2)	Hole Pitch (mm)	Hole Diameter (mm)	Hole Rim (mm)	Thickness (mm)
400×400	354×354	1.2	0.4	0.04	0.4

A previous large area ThGEM study, conducted in collaboration with the Atomic Weapons Establishment (AWE) [150], revealed issues that the new design, for the ThGEM presented in this chapter, aimed to alleviate. These design features, which where implemented after discussion with the CERN MPDG group, are described in the following.

The ThGEM copper surface, on the side where voltage was to be applied, was segmented, as shown by Figure 8.1, to help localise the damage inflicted by electrical discharge. The voltage was applied to each segment via surface mounted 1 MΩ resistors, which reduced the current flow to the ThGEM during the application of voltage and prevented current surges, occurring at a segment, from reaching the attached electronics or other parts of the ThGEM. Figure 8.1 shows a veto strip surrounding the segments, which was included in the design to exclude external events entering the TPC gas volume. However, the veto was not tested as part of the work presented in this chapter as the focus here was the electron amplification performance only. Figure 8.2 shows a scaled drawing of three ThGEM holes, with the hole pitch, diameter and etched rim dimensions given in Table 8.1.

Figure 8.1: Large area ThGEM produced at CERN. The segmented side is shown with the surrounding veto ring. The surface mounted resistors can be seen connected to the segmented pads.

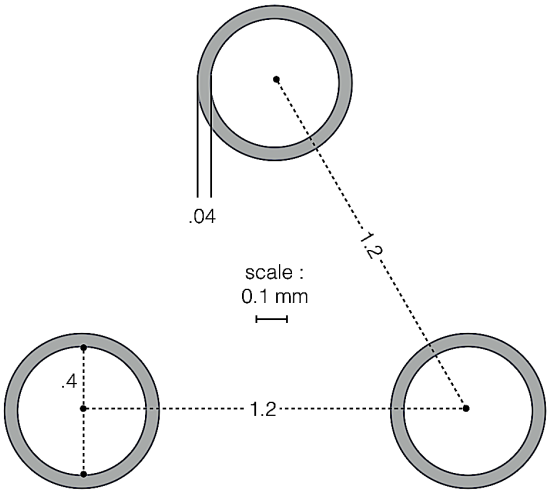

Figure 8.2: To scale diagram of three ThGEM holes, showing the hole diameter, pitch and etched rim.

The ThGEM was designed to fit the CYGNUS-KM vessel, which is located at Kobe University. The vessel design, shown in Figure 8.3 (top), allows for the fitting of 18 different readouts, which can then be directly compared using the same TPC setup (gas composition, voltage arrangement, drift distance etc.). Readouts of $\sim$30$\times$30 cm^2 can be fitted to the opposite side of the vessel flanges shown in Figure 8.3 (bottom, left).

Figure 8.3: Top: Design drawing of the CYGNUS-KM vessel. Bottom: Front of the CYGNUS-KM vessel, located at Kobe University, showing the multiple door flanges (left) and prototype testing vessel that replicates a single door flange (right).

At the time of these tests, CYGNUS-KM was still under construction at Kobe University. Therefore, the tests were conducted inside a smaller prototype vessel, shown in Figure 8.3 (bottom, right). This vessel was made to exactly mimic a single flange of the larger CYGNUS-KM vessel but with a shortened drift distance of 5 cm, compared to the 50 cm provided by CYGNUS-KM.

The ThGEM was supported 11 cm away from the vessel door flange using acrylic rods, which positioned it 5 cm away from a thin film Mylar cathode installed inside the vessel. Figure 8.4 (top left) shows the ThGEM connected to the supporting rods and attached to the vessel door flange. The bottom left of this figure shows the cathode, through which, the ThGEM can be seen on the opposite side. The image on the right in Figure 8.4 shows a sketch of the ThGEM and cathode configuration inside the vessel, as well as the two feedthroughs used to pass the high voltage (HV) supply to the ThGEM and cathode and to pass signal to the electronics. No field cage was used for these tests as the ratio of readout area to drift distance was sufficient to assume that all of the ionised charge, contained within the drift volume, remained contained as it drifted towards the readout. Further to this, as these tests were only concerned with the ThGEM gain performance, no track reconstruction was required and, therefore, charge displacement, due to diffusion, was not a concern.

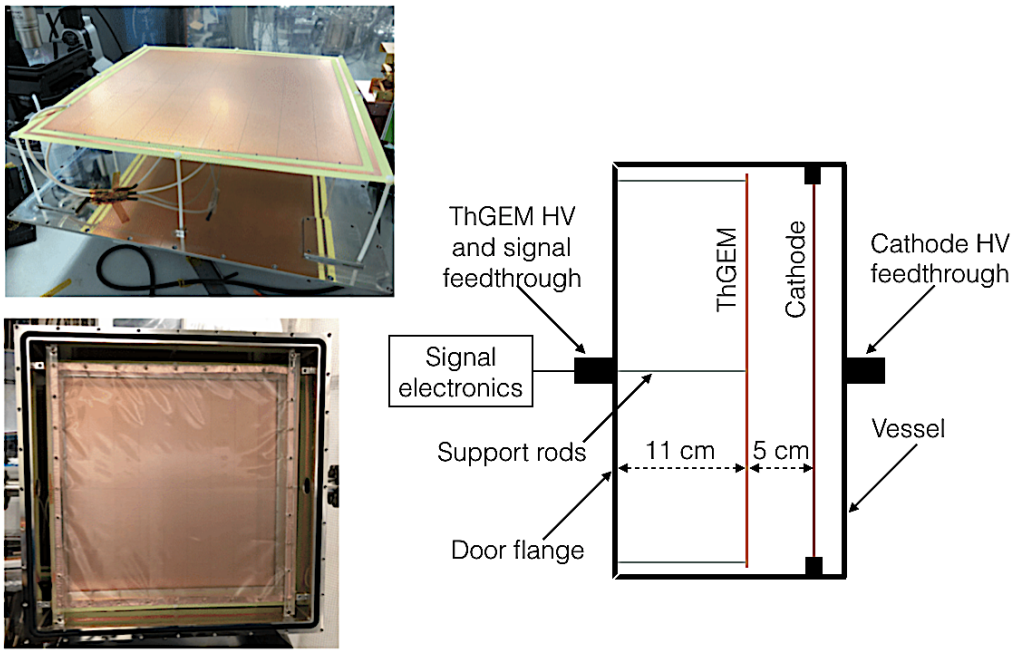

Figure 8.4: Top left: CERN ThGEM installed onto the test vessel door flange. Bottom left: Thin film Mylar cathode installed inside the test vessel. Right: Sketch (not to scale) of the ThGEM and cathode configuration inside the CYGNUS-KM prototype vessel.

The signal processing electronics, shown in Figure 8.5 (top), included a Cremat-111 preamplifier [151], an AD8011 amplifier [152] and an RC circuit, which was used to shape the signal by implementing a 47 μs decay time. The schematic at the bottom of this figure shows the circuit design of the electronics. In order to record spectra using a Multi-Channel Analyser (MCA), the signal had to be inverted from negative to positive using a fan in-out device. This device had a 50 Ω impedance, which effectively halved the signal amplification provided by the electronics. This was taking into account during the calibration of the electronics, which is described in the next section.

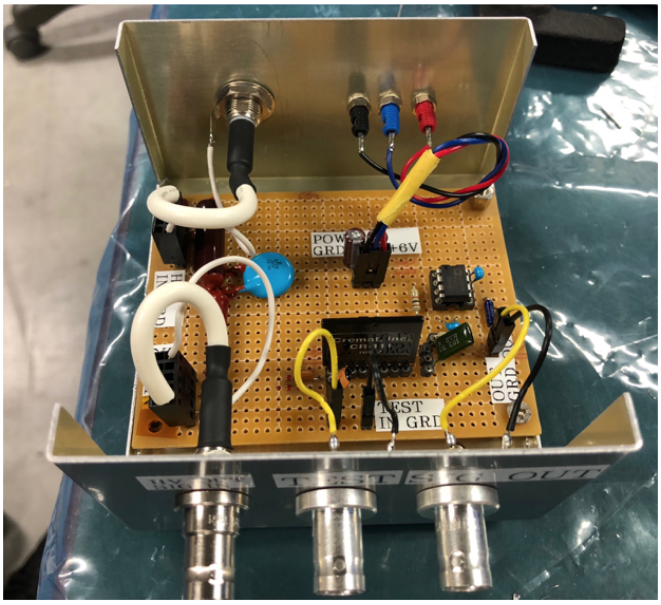

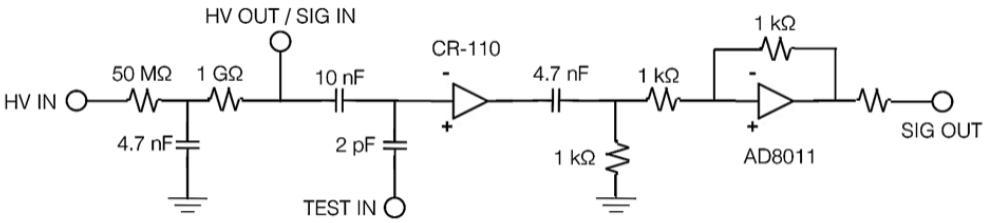

Figure 8.5: Top: signal processing electronics used for the ThGEM tests conducted at Kobe. The CR-111 preamplifier and AD8011 amplifier chips can be seen attached to the board. Bottom: circuit diagram of the electronics.

8.2 Measurement Procedure and Calibration

The eventual goal is to test large area ThGEMs in SF_6 gas. However, as was done for the ThGEM-MWPC readout in Chapter 7, CF_4 gas was chosen for the tests described in this chapter so that electrons could be drifted and higher gains could be achieved. Initial gain measurements were attempted using an ^{55}Fe source but no clear signal was observed, therefore, all further

tests were conducted using an ^{241}Am source, which produces a larger signal from the emission of 5.5 MeV alphas. SRIM [96] calculations of 5.5 MeV alphas in CF_4 showed that the particle's range was no greater than 26 cm at a gas pressure of 50 Torr, as shown in Figure 8.6.

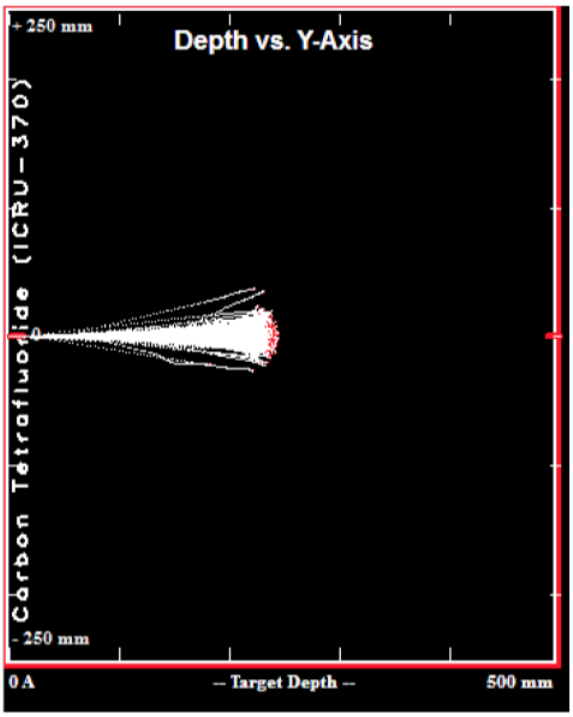

Figure 8.6: SRIM range calculation for 5.5 MeV alphas traversing 50 Torr of CF_4 gas. The alpha track range does not exceed 26 cm.

The maximum alpha range of 26 cm, shown in the above figure, did not exceed the length of the ThGEM readout area (see Table 8.1). A further SRIM calculation showed that, on average, 99.7% of the alpha particle's energy was converted directly into ionisation, shown by the red area in Figure 8.7.

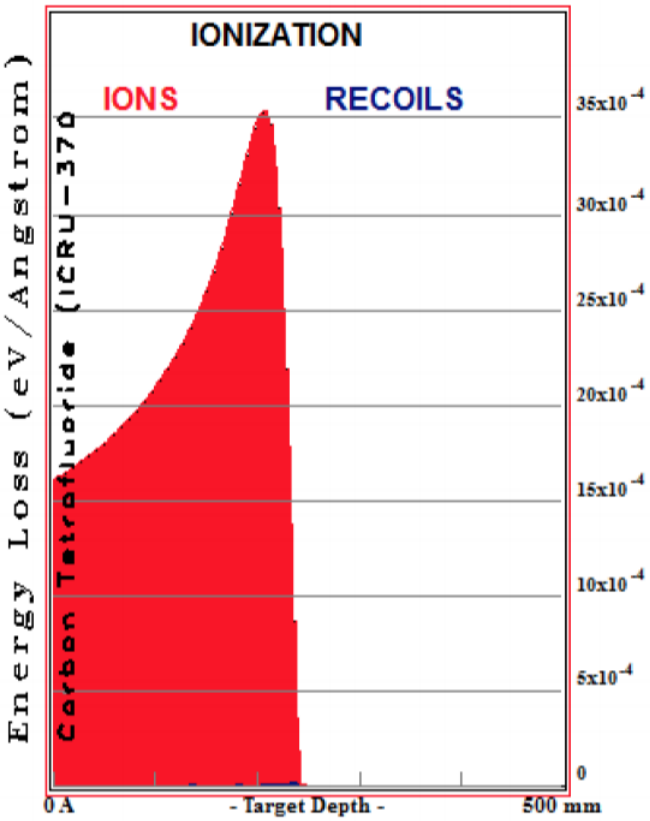

Figure 8.7: SRIM calculation of the energy loss to ionisation (red) and recoils (blue) for 5.5 MeV alphas in 50 Torr CF_4 gas.

These SRIM calculations indicated that by using a pressure of 50 Torr and by collimating the source to emit alphas parallel to the ThGEM, it could be assumed that the alpha tracks were fully contained within the drift region and deposited 5.5 MeV in ionisation.

The ^{241}Am alpha source was placed inside the vessel, just above the ThGEM and in-between the ThGEM and cathode. Example signal pulses induced by the alphas, taken using an oscilloscope connected to the signal electronics, are shown in Figure 8.8.

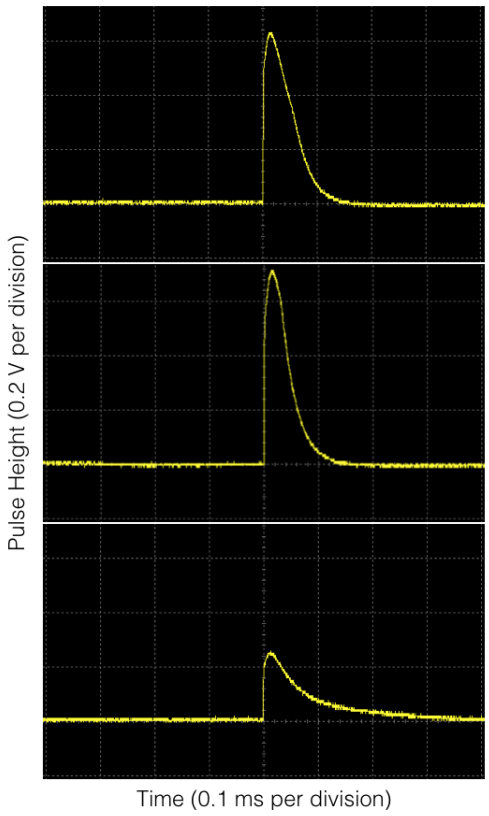

Figure 8.8: Three signal pulses induced by alpha ionisation in 50 Torr CF_4, recorded using an oscilloscope, for a 300 V cm^{-1} drift field and for a ThGEM voltage difference of 660 V.

MCA spectra of the alpha signal amplitudes were recorded for a drift field of 300 V cm^{-1} and for ThGEM voltage differences of between 560 and 660 V, increasing in 10 V intervals. The lowest voltage difference corresponded to the avalanche field at which signal was first observed and the highest corresponded to the field just below the point at which breakdown was observed.

A low pass filter was used when applying the ThGEM voltage to reduce high frequency noise originating from the voltage supply. For each MCA spectrum a gaussian function was fitted and the mean and sigma values were used to estimate the signal peak position and error. An example spectrum, for a voltage difference of 600 V, is shown in Figure 8.9. The fitted gaussian can be seen as the red curve in this figure and background noise can be seen decaying exponential as the MCA channel number increases.

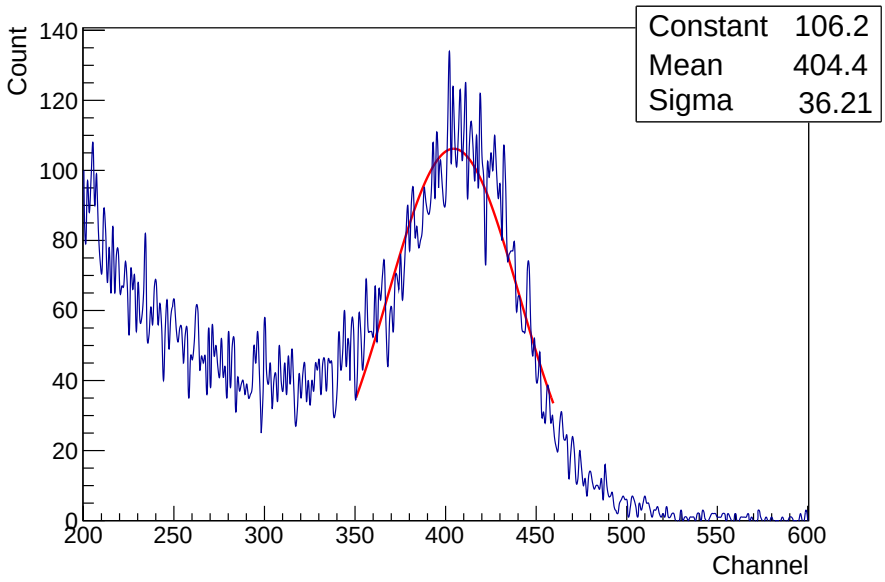

Figure 8.9: MCA alpha spectrum. The channel number corresponds to the signal amplitude and the count shows the number of signal responses within a certain amplitude bin. The fitted gaussian is shown in red.

Each MCA channel number, shown in the above figure, was associated with a signal amplitude. This was converted to a charge value by calibrating the electronics using the same procedure described in Section 7.2.1 of Chapter 7. The gain was then calculated as the ratio of this charge value (which was produced after the avalanche stage) to that of the initial charge deposited by the alpha track, which was given as 5.5×10^6 eV / 34.2 eV = 1.6×10^5 q, where

q is the elementary charge and 34.2 eV is the gas W value [149]. The gain measurement result is presented in Section 8.4, where it is compared to the predictions made using the simulation procedure described in the following section.

8.3 Large Area ThGEM simulation

This section describes the simulation procedure used to predict the expected ThGEM gain for the drift and avalanche fields mentioned in the previous section. The detector geometry and fields, used in the simulation, were modelled using ANSYS Mechanical v14.5 [146] and are described in Section 8.3.1. The ANSYS field maps were then imported into Garfield [101], which was used to simulate the transportation of electrons through the detector geometry and field configuration in 50 Torr of CF_4 gas. It is known that electrons landing on the dielectric layer of a ThGEM effect the avalanche field over time, the simulation of this effect, using a similar procedure to that described by Ref. [153], is detailed in Section 8.3.2. The gain simulation process is then described in Section 8.3.3.

8.3.1 Detector Geometry and Fields

The ThGEM geometry was modelled in ANSYS using the parameters listed in Table 8.1. As the electric field was identical at each ThGEM hole it was only necessary to model a single hole and the surrounding surface closest to it. Further to this, only a quarter of the geometry was required as Garfield could mirror the imported maps over the x and y axis and produce the full electric field configuration. Figure 8.10 shows the ThGEM hole geometry, created in ANSYS, after a quarter has been mirrored over each axis.

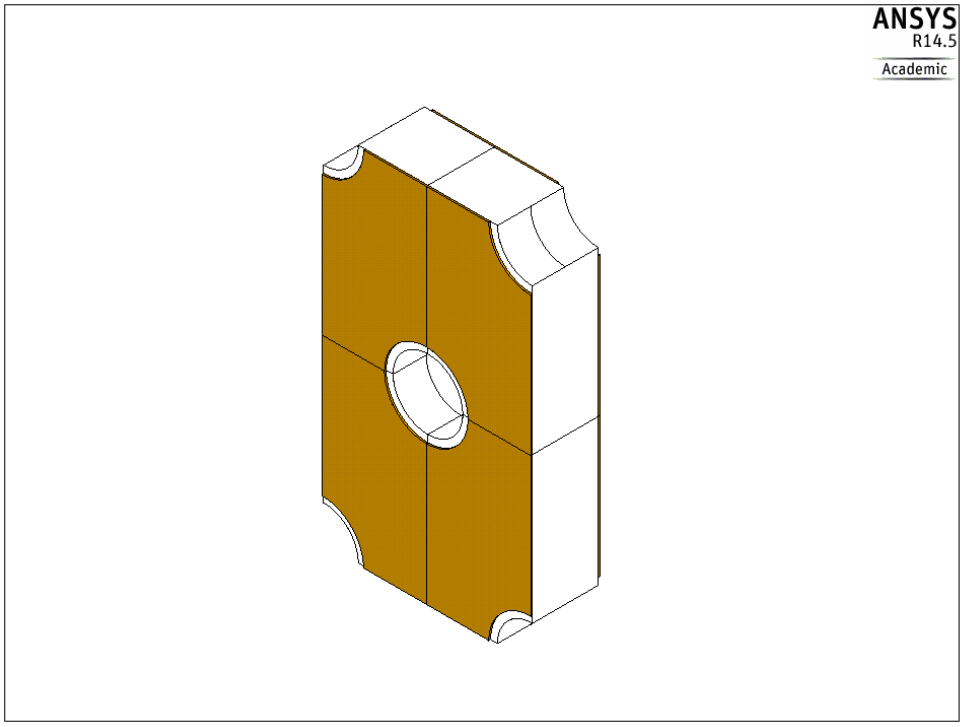

Figure 8.10: ThGEM geometry modelled using ANSYS. It can been seen that mirroring a quarter of the geometry over the x and y axis produces a single ThGEM hole.

The gold and white areas in the above figure represent the copper and the dielectric material, respectively. The materials were defined in ANSYS by their relative permittivity, which for copper was infinite, for the dielectric it was 4.8 [154] and for the gas a value of 1 was used. For copper, the material's resistivity was also defined as zero. Figure 8.11 shows an example of the calculated equipotential lines, through the ThGEM geometry shown in Figure 8.10, for a 700 V difference between the ThGEM copper surfaces.

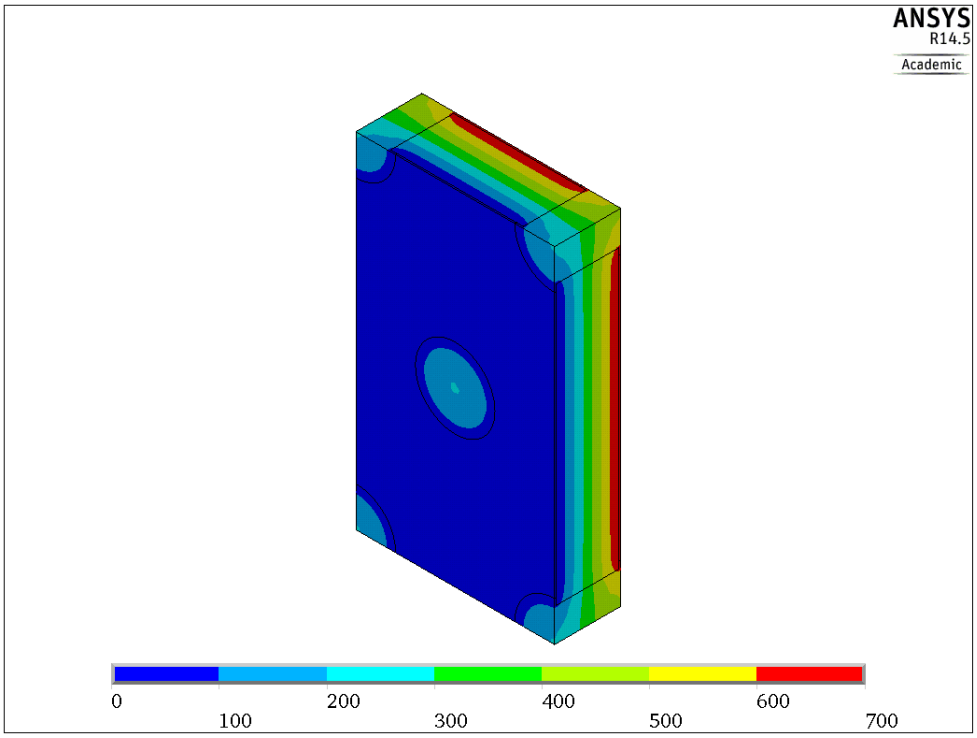

Figure 8.11: Equipotential lines through the ThGEM geometry, calculated in ANSYS, for a 700 V difference between the ThGEM copper surfaces.

The drift field was modelled, using ANSYS, as a 1 cm long gas region, located before the ThGEM, with an electric field of 300 V cm^{-1}. A gas induction region of 1 mm was included, located behind the readout side of the ThGEM, to allow for the transportation of electrons after the avalanche stage. The equipotential lines of the drift, avalanche and induction fields are all shown together, for a quarter of the ThGEM geometry, in Figure 8.12. The field map shown in this figure was that imported into Garfield, which then reflected the geometry over the x and y axis to produce the full field configuration, as previously mentioned.

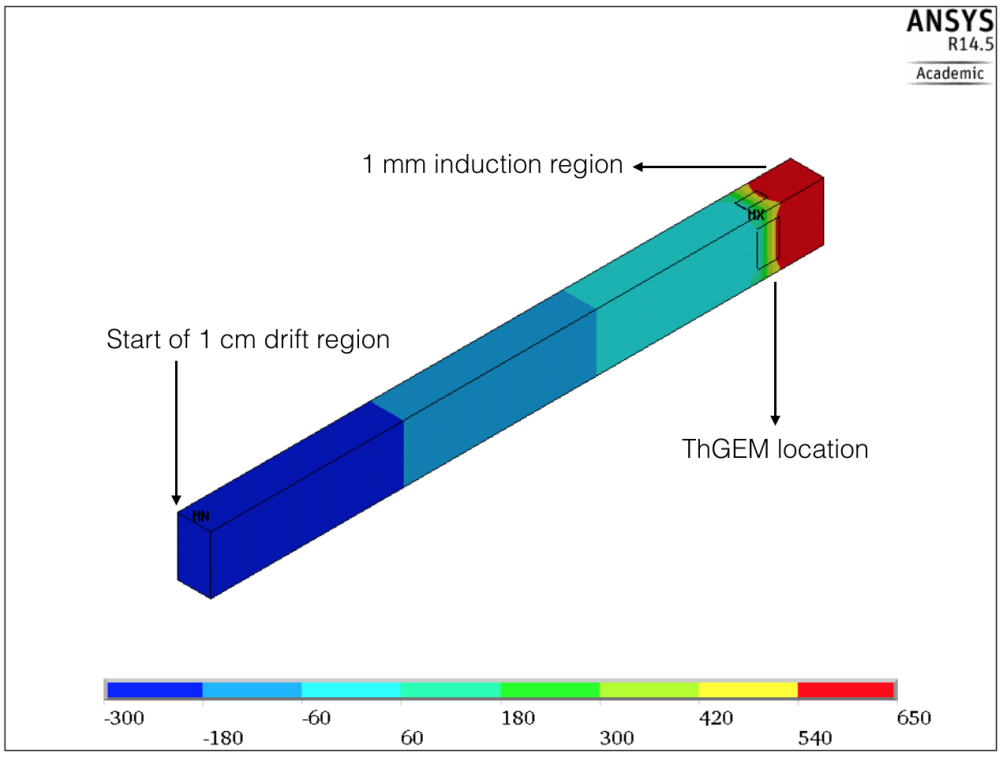

Figure 8.12: One quarter of the full field configuration, modelled in ANSYS and imported into Garfield, shown as equipotential lines. The side of the ThGEM facing the drift region is set at 0 V and the opposite side at 650 V. The 1 cm drift region, located before the ThGEM, is set at 300 V cm^{-1} and a 1 mm induction region is included behind the ThGEM to allow for electron transportation after the avalanche stage.

8.3.2 ThGEM charge up

To accurately simulate electron avalanche through the ThGEM, the charge up effect of the insulating glass-epoxy material (found in-between the copper layers) must first be simulated. The charge up is caused by electrons and ions, produced during an avalanche, attaching to the material's dielectric surface. The resulting accumulation of charge causes an electric field that opposes the avalanche field and ultimately reduces the gain of the ThGEM

down to a constant value, at which point no further significant amount of electrons or ions attach to the material. To investigate the distribution of the accumulated charge, the insulating layer of the ThGEM geometry was split into ten equal layers in ANSYS, as shown by Figure 8.13.

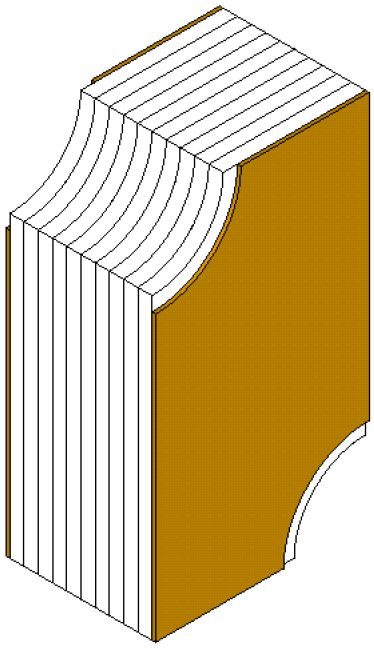

Figure 8.13: A quarter segment of the ANSYS ThGEM geometry, showing the insulating layer split into 10 equal parts.

In order to include the charge accumulation due to ions, argon gas was simulated (rather than CF_4) as Garfield includes the mobility tables for the transportation of cations in this gas (which is not the case for CF_4). The argon pressure was set to 110.15 Torr, to match the gas density found at 50 Torr CF_4, which is the gas and pressure used for the measurements described in Section 8.2. The charge up process of the ThGEM insulating layer is related to the material permittivity (as discussed above) and the gas density, which affects the avalanche process. Therefore, by keeping the latter con-

stant, it was assumed that changing the gas composition had no significant effect on the charge up process being investigated.

During the simulations the drift field, modelled with ANSYS, was kept at a constant 300 V cm^{-1} and the ThGEM potential difference was maintained at 500 V. One hundred electrons were then generated, in Garfield, above the ThGEM hole and allowed to avalanche through it. The end point locations of the electrons and ions, produced by the avalanche, were recorded and if the particle's location was found to coincide with one of the insulating layers, the particle's charge was added to that layer in ANSYS. New field maps, including the additional charges, were then produced and the simulation was repeated with the new maps. The entire process was automated by a C++ script and repeated until the ThGEM gain, which is defined here as the mean amount of electrons (per repetition) that left the ThGEM hole and landed on the copper surface, reached a constant value. For each repetition, the gain was recorded and is shown as a function of repetition number in Figure 8.14.

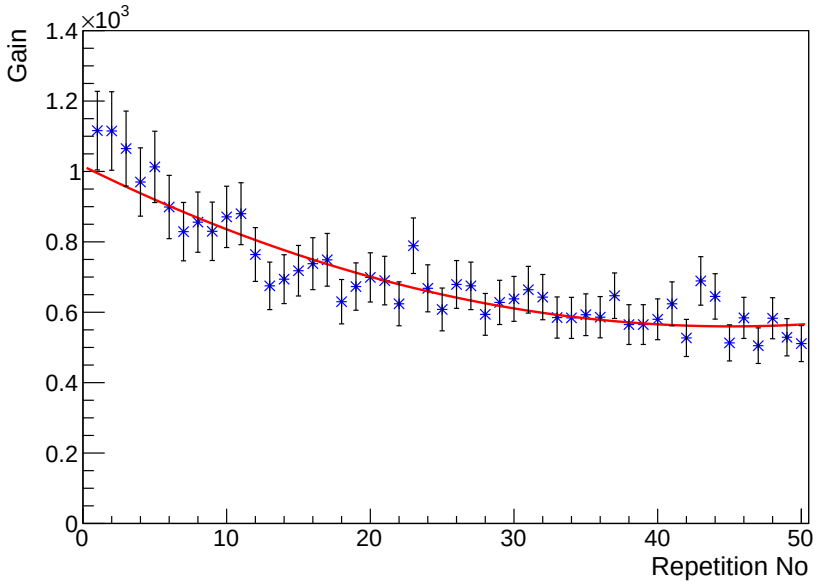

Figure 8.14: Decrease in gain due to the charge up of the ThGEM's dielectric material. The red line is a second degree polynomial fit to the data.

The error bars in the above figure were calculated as the mean gain multiplied by $n^{-1/2}$, where n is the number of electron avalanches simulated per repetition (100). The fitted line, in Figure 8.14, shows that the gain is approximately constant after around 40 repetitions, at which point it has been reduced to around half the value measured after one repetition.

The ThGEM charge up effect was included, for the remaining simulations discussed in this chapter, by applying the charge accumulation found after 50 repetitions to each field map generated in ANSYS. Figure 8.15 shows the avalanche field through the ThGEM hole, generated using Garfield, before any charge accumulation and after the material is fully charged.

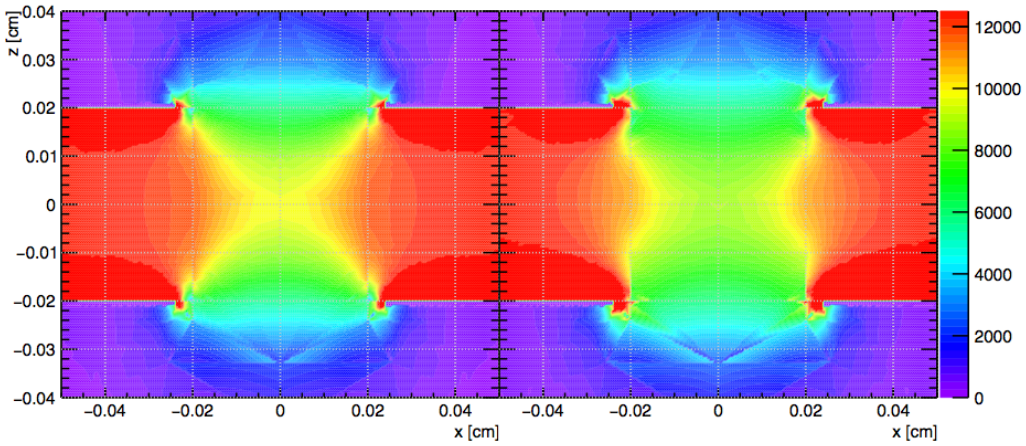

Figure 8.15: ThGEM field before (left) and after (right) charge accumulation on the insulating material, in V cm^{-1}.

The above figure shows that the electric field is reduced, at the centre of the hole, after the dielectric material is fully charged. This result indicates that the avalanche process of the ThGEM is also reduced when taking into account the accumulation of charge on the ThGEM's insulating material, resulting in the gain reduction shown in Figure 8.14.

8.3.3 Gain simulation

ANSYS field maps were produced within the ThGEM operating range of 560 to 660 V (see Section 8.2), in steps of 10 V. The charge up effect (reported in the previous section) was also included for each field map. After importing the field maps into Garfield, electrons were simulated at random positions between 0.1 and 1 cm above the ThGEM and within the diamond shaped area shown in Figure 8.16.

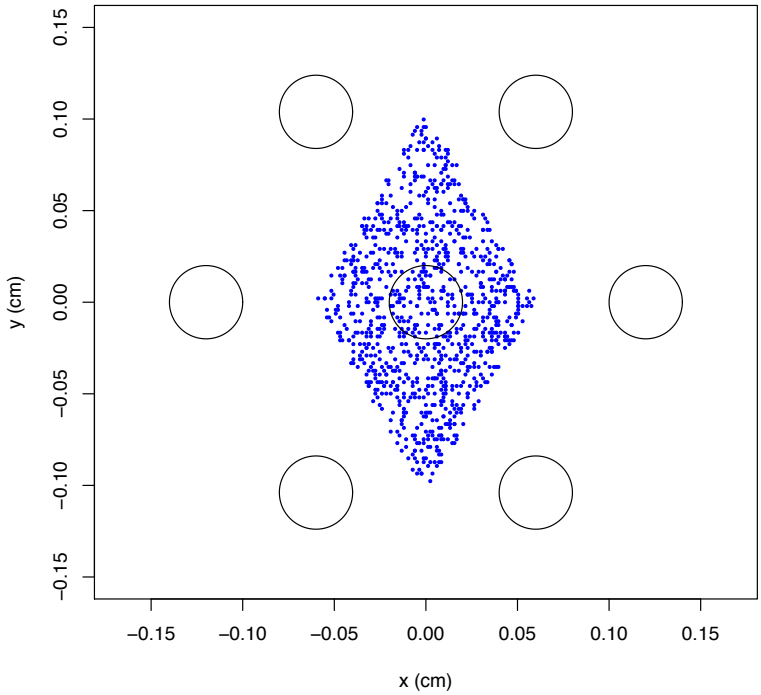

Figure 8.16: Electrons (blue points) located above the ThGEM within a diamond shaped area that is subject to field lines converging towards the ThGEM hole.

Electrons located outside of the area, depicted in the above figure, were not subject to field lines that converged towards the hole geometry, modelled in ANSYS, being used to conduct the gain measurements.

One hundred electrons were simulated per voltage step and the resulting mean gain per step is shown in Figure 8.17.

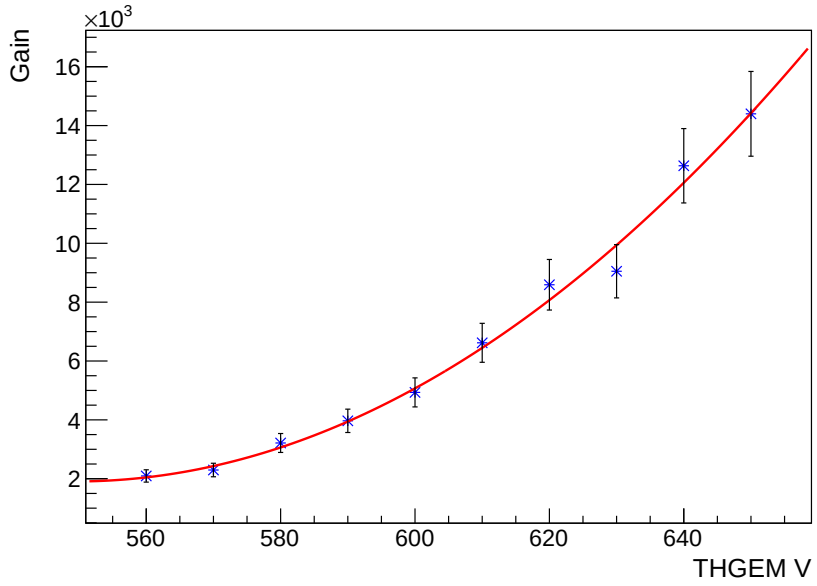

Figure 8.17: Simulated gain per ThGEM voltage difference, with fitted exponential curve shown in red.

This result was used to predict the expected ThGEM performance, the measurements of which, are given in the next section. Without simulating the charge-up effect, the result shown in Figure 8.14 of the previous section, indicates that the performance would have been over-estimated by a factor of $\sim$2.

8.4 Gas Gain Measurements

The ThGEM gain results, measured using the calibration and procedure described in Section 8.2 and the setup described in Section 8.1, are shown in Figure 8.18. Section 8.3.2 showed, via simulation, that the charge up effect of the ThGEM's insulating glass-epoxy material causes the avalanche field to

decrease. Therefore, it is not straightforward to directly translate the voltage difference between each copper surface of the ThGEM to the avalanche field existing within the ThGEM holes. For this reason, the results shown in Figure 8.18 are presented as voltage differences of between 560 and 660 V, the operating range of the ThGEM (as described in Section 8.2).

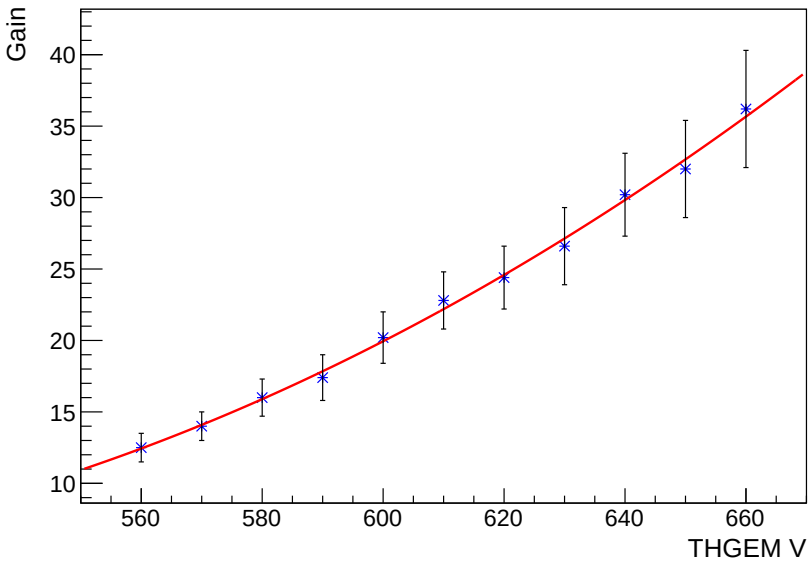

Figure 8.18: Measured gain per ThGEM voltage difference, with fitted exponential curve shown in red.

Comparing the result shown in the above figure with that predicted by simulation (see Figure 8.17), shows a predicted gain of between 150 and 400 times higher than actually measured. This suggests that factors, other than the charge up of the ThGEM's insulating layer, are negatively influencing the gain performance. One of these factors could be the damage incurred to the ThGEM during it's handling, as described for the smaller area device in Section 7.2.3 of Chapter 7. However, this is less likely for the large area device studied here, mainly because the ThGEM is much newer but also because of the design features, described in Section 8.1, that were implemented to

prevent damage. Despite this, in some respects, damage is also increasingly likely for a larger device, simply because it includes more holes than a smaller ThGEM and just a few damaged holes can effect the overall performance. For example, the maximum avalanche that can be achieved through the ThGEM is limited to the strength of the field that can be applied through the holes without causing breakdown, which for damaged holes will occur at lower avalanche fields. Despite the design improvements made, over the AWE produced ThGEM (see Section 8.1), the gain results presented in this chapter are consistent with the AWE ThGEM study conducted by Ref. [150]. This would suggest that the reduced gain is not just a consequence of damage or of the charge up effect studied in this chapter but could, instead, be an issue inherent to the scaling-up of these devices.

8.5 Conclusion

This chapter described the performance of a large scale ThGEM, produced at CERN, during tests conducted at Kobe University. Simulation was used to show how the avalanche field through the ThGEM is expected to decrease due to the charge up affect of the ThGEM's insulating material. By taking this effect into account, a simulated gain curve was produced for the ThGEM over a range of voltage differences. The measured results were found to be significantly lower, by a factor of $\sim$400 at the highest voltage difference, than those predicted by the simulation. Further to this, Ref [150] also describes a gain study, conducted by the author in collaboration with the Atomic Weapons Establishment (AWE), using a similar large area ThGEM produced by the UK company Quick Circuits. The results reported for this ThGEM, are consistent with those presented in this chapter and, therefore, suggest that the performance of smaller area ThGEMs (which have been shown to produce gains $\mathcal{O}(10^4)$ for the same gas and pressure [150]) does not translate in a straight forward manner to similar but larger area devices. Additional

R&D, possibly involving ThGEMs with different parameters, is required to further understand why this is the case and ultimately the tiling of smaller area ThGEMs may be required for a CYGNUS-10 or CYGNUS-1000 TPC.

Chapter 9

Camera Background Study for CYGNO Prototype

It was mentioned in Section 5.5.3 of Chapter 5 that a TPC designed to operate a camera based readout would differ to that of other TPC designs not involving cameras. This chapter describes a Monte Carlo background study of a camera based CYGNUS prototype, named CYGNO, which is planned for construction at Laboratori Nazionali del Gran Sasso (LNGS). A camera based readout offers high resolution track reconstruction, compared to an MWPC or μ-PIC readout for example, which could potentially allow for an improved background rejection at low energy (sub-10 keV_{ee}). However, the intrinsic background from the camera, particularly at low energy, is assumed to be higher than found from other readouts due to the increased amount of electronics involved. The focus of this study, was to use GEANT4 simulations to investigate the gamma background rate, found within the CYGNO gas volume, originating from a CYGNO camera. The TPC geometry and gas setup is discussed in Section 9.1. The gamma background is quantified by a material screening process described in Section 9.2. As part of this work, a shielding design was introduced with the aim of reducing the gamma background, the simulation and results of which, is discussed in Section 9.3.

9.1 CYGNO TPC Design

The TPC, shown in Figure 9.1, is envisioned as a 1 m^3 target gas volume located inside a 2 cm thick aluminium vessel. The TPC has a back-to-back configuration constituting a central cathode with two stacks of three GEM's on either side. The GEM's provide an avalanche region where ionised signal is amplified and photons are produced via molecular and atomic de-excitation. The photons are then recorded by $\times 18$ CMOS cameras surrounding the gas volume. Figure 9.1 shows the CYGNO vessel design and camera locations as seen from the top of the TPC and from one side.

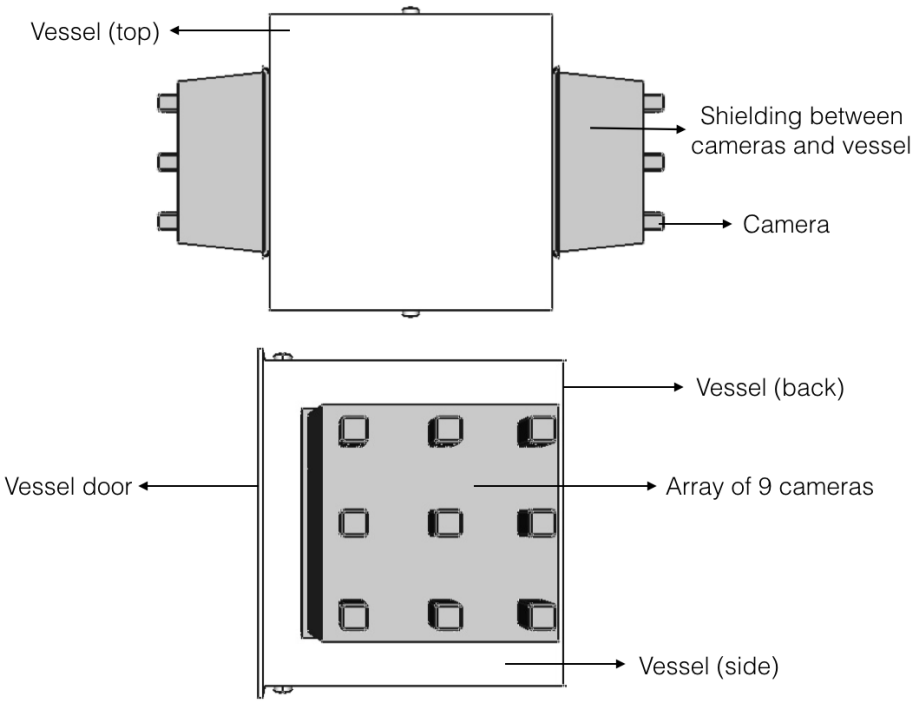

Figure 9.1: CYGNO design from the top of the vessel (top) and from one side (bottom). 6 of the 18 camera locations can be seen from the top of the vessel. The structures, labelled as shielding, between the cameras and the vessel are used to prevent light contamination from entering the vessel. From the side, the configuration of 9 of the total 18 cameras can be seen.

The prototype builds on previous R&D conducted with the LEMON detector [88] and uses the same gas mixture of He and CF_4 but at a ratio of 70/30 (at atmospheric pressure), rather than 60/40. This ratio was selected as it reduces the gas density, compared to the latter, and therefore, reduces the amount of electrons available for the Compton scattering of the gamma background.

9.2 CMOS Camera radio-assay

High Purity Germanium detectors (HPGe), located at LNGS, were used to perform a radioassay of one of the Hamamatsu ORCA-flash 4.0 cameras [155] (including the camera objective) selected for CYGNO. The GeMPI (Germanium-Max Plank Institute) and GePaolo (Germanium-Paola) detectors were used, respectively, to assay the camera over a live time of 83383 s and the objective over a live time of 504104 s. The results of the radioassay are listed in Table 9.1, where the uncertainties are given at a 68% CL.

Table 9.1: Radioassay results for the CYGNO camera and objective in units of Bq pc^{-1}.

Isotope	Camera	Objective	Total
^{238}U	7±2	0.9±0.3	7.9±2.3
^{235}U	0.4±0.1	0.031±0.008	0.431±0.108
^{232}Th	2.1±0.2	0.077±0.009	2.177±1.009
^{226}Ra	1.8±0.1	0.41±0.02	2.21±0.12
^{138}La	0	0.52±0.04	0.52±0.04
^{137}Cs	0.09±0.03	< 0.0057	< 0.0957±0.03
^{60}Co	< 0.012	< 0.01	< 0.022
^{40}K	1.9±0.3	11±1	12.9±1.3

Secular equilibrium was found to be broken for the ^{238}U decay chain at

the point of ^{226}Ra. Therefore, the decay chain at, and after, this point is given by the ^{226}Ra activity listed in Table 9.1. Two separate measurements, made at different points along the ^{232}Th decay chain, suggest that secular equilibrium is maintained in this instance.

9.3 CMOS Camera Background Simulation

This section describes the use of simulation to predict the gamma background rate, within the CYGNO target gas volume, due to one of the cameras. To shield against the camera background, a dividing wall of 4 cm thick copper was simulated between the camera and the gas volume, with the camera located behind a 2 cm thick silica window. The window diameter was 4 cm to accommodate the camera's maximum aperture. A drawing of the geometry, which was simulated using GEANT4, is given in Figure 9.2.

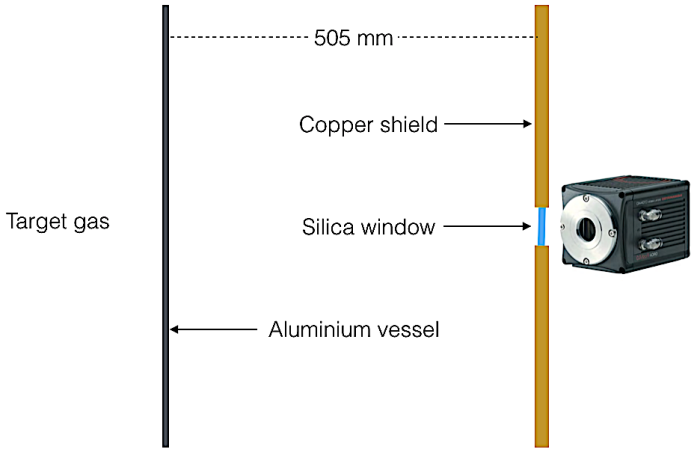

Figure 9.2: Drawing of the GEANT4 geometry, including the aluminium vessel, copper shielding and silica window. Camera image from Ref. [155].

The distance between the copper shielding and the vessel, shown in the above figure, is to accommodate the camera shielding shown in Figure 9.1. The camera was simulated as a point source located just behind the window,

in the position denoted by the camera image in Figure 9.2. One million decays (or decay chains, where relevant) were simulated, for each isotope listed in Table 9.1, at this position. The resulting gamma induced electron recoil rate (per year), f, within the target volume of gas, for a given energy was calculated as,

$$f = \frac{\lambda R}{N} \tag{9.1}$$

where R is the number of recoils observed within a certain energy bin, λ is the isotope radioactivity from Table 9.1 and N is the number of decays simulated. Figure 9.3 shows the resulting gamma recoil rates for a camera with no shielding wall in place, for a camera with the shielding in place and for the same as the latter but with a 2 cm silica window included.

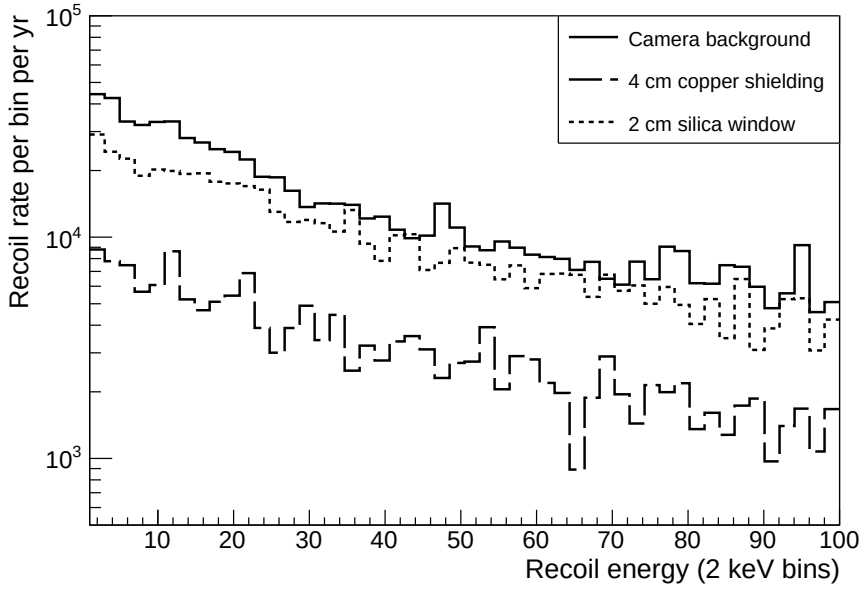

Figure 9.3: Gamma recoil rates, between 1 and 100 keV, for a single camera with no shielding, a 4 cm thick copper shield and a 4 cm thick copper shield with a 2 cm thick silica window.

Simulating the shielding with no window shows that the amount, and type, of shielding does reduce the camera background rate, which Figure 9.3 shows is reduced by a factor of ∼5 compared to the camera background without shielding. However, the figure also shows that the introduction of a silica window returns the camera background to almost the same level found with no shielding. This result shows that the majority of gamma background, from the camera, can not be significantly reduced using a shielding geometry with windows. This suggests that alternative methods or possibly a reconsideration of the geometry is required to reduce the gamma background further.

9.4 Conclusion

This chapter described a simulation study of the gamma background, found within a gas mixture of 70% He and 30% CF_4 at atmospheric pressure, from a CMOS camera. The work was conducted as part of the CYGNO project towards the realisation of a CYGNUS prototype TPC, planned for construction at LNGS. The results presented in this chapter show that although the camera background can be reduced using copper shielding, the need for transparent windows causes most of the shielding to be relatively ineffective, as the majority of gammas pass through the silica material used for the windows. This result suggests that means other than, or as well as, shielding are required to reduce the gamma background from the camera. This could involve reducing the camera material as far as practically possible and/or constructing a camera from ultra radio-pure material.

Chapter 10

Conclusion

Chapter 1 described the observational evidence supporting the existence of dark matter, the missing matter component that constitutes ∼84% of the mass in the universe. Some of the theoretically motivated dark matter candidates where also explored, including axions, sterile neutrinos and WIMPs.

Chapter 2 outlined the current methods (indirect, direct and collider) and experimental efforts towards the detection of dark matter. Particular attention was given to direct detection with a gas TPC, for which, it is possible to reconstruct the direction of a recoiling nucleus. The ability to distinguish a recoil direction consistent with the WIMP could potentially provide a discrimination method for a large scale detector sensitive to a neutrino background. It was argued that the negative ion gas, SF_6, is an ideal target for this type of detector, as it enables track reconstruction along the drift direction, target gas fiducialisation and a considerable amount of fluorine for spin dependant (SD) searches.

A key requirement, for pushing the search reach of a detector towards the neutrino floor, is to lower the signal threshold as fas as possible without introducing an intolerable level of background. To that end, Chapter 3 described a study of the gamma rejection at and below 10 keV_{ee}, in 20 Torr SF_6, using a type of Machine Learning (ML) analysis called a Boosted Decision Tree

(BDT). The analysis was performed on parameters derived from simulated electron and nuclear recoils, which included the effects of diffusion and readout resolution. The results of the study suggest that a gamma rejection of $\mathcal{O}(10^{-4})$ is possible, at an energy of 6 keV$_{ee}$ and above, for an averaged 25 cm diffusion and for a readout resolution of 600 μm. The HT effect, introduced in Chapter 2, was looked for using the simulated (sub-10 keV$_{ee}$) recoils, and was found to be present, in 20 Torr SF_6, before diffusion. However, the effect was not present after an averaged 25 cm diffusion. Further work is required to establish the exact relation between the HT effect and diffusion for low energy recoils in SF_6 gas.

The work presented in Chapter 4 explored the potential of ML to increase the detection efficiency of a future large scale detector. This was achieved by applying a type of BDT analysis, called a Random Forest Classifier (RFC), to data obtained using the DRIFT-IId detector. It was found that this analysis improved the detection efficiency of DRIFT-IId (compared to that achieved using the standard analysis), increasing the dark matter cross section reach of the detector by 32%.

Chapter 5 described a Monte Carlo study of the background found within a large scale directional detector, called CYGNUS-1000. This detector was simulated, in GEANT4, as a 1000 m^3 volume of 20 Torr SF_6, located at the Boulby Underground Laboratory. Based on the gamma rejection study described in Chapter 3, a tolerable limit of gamma background was set at $< 10^4$ yr^{-1} keV^{-1}, whilst a limit of < 1 yr^{-1} was set for the neutron background. The gamma rejection study focused on the energy region 1-10 keV and the neutron background energy region of interest was 1-200 keV$_r$. It was found that the neutron and gamma backgrounds originating from the rock cavern could be reduced to within limit with a 85 cm thick water shield and a 30 cm thick copper vessel, respectively. However, further screening of copper is required to establish if the vessel gamma background is within limit and the requirement of a steel or titanium support structure could push the back-

ground levels above limit. A study of the internal TPC background indicated that all components (readouts, amplification devices and field cage resistors) need further purification to fall within the gamma background limit. The MWPC readout with ThGEM amplification device proved to be closest to this goal as well as being within the neutron background limit. Other background sources originating from radon gas and cosmic ray interactions were considered. It was described how the former could be mitigated using a combination of fiducialisation and thin film cathodes, and the latter using a combination of muon tagging techniques and limiting the amount of cosmogenic activation. The SD search reach of CYGNUS-1000 was shown to extend further into the WIMP search parameter space than a Xe based detector without being subject to a neutrino background. The search reach also indicated that a neutrino background would start to become obvious if a sub-6 keV_{ee} threshold could be achieved.

In Chapter 6, the results of Chapter 5 were used to guide the design of a smaller 10 m^3 TPC, called CYGNUS-10, which could be one of many similar detectors that contribute to a total volume on the same scale as CYGNUS-1000. The TPC was simulated as a 13 mm thick cylindrical vessel made of steel, located at Boulby. The vessel geometry and material was chosen to provide the required support against the atmospheric pressures exerted on a vacuum vessel. It was found that a water shield of 50 cm reduced the rock neutron background to $<< 1\ \mathrm{yr}^{-1}$. To shield against the gammas produced in the surrounding rock and vessel material an internal and external copper shield of 5 cm and 10 cm thick, respectively, was required. Based on the results of Chapter 5 the MWPC with ThGEM amplification was chosen as the CYGNUS-10 readout. These were configured in a back-to-back (readout-cathode-readout) arrangement, which produced 70 cm drift regions. An internal acrylic support frame was also simulated along with the background contribution from the field cage resistors. The total gamma background from all of these internal components was found to be around

the 10^4 limit and the contribution to the neutron background from the vessel, shielding and all internal components was found to be $\sim$0.02 yr^{-1}. The search reach of CYGNUS-10 showed that for a threshold of < 6 keV$_{ee}$, the TPC would be sensitive to a WIMP search parameter space that would produce a neutrino background for a Xe based detector. The result also showed that the CYGNUS-10 TPC, by itself, would not be sensitive to a neutrino background, and therefore, multiple such detectors would be required to probe the neutrino floor using a fluorine based target.

The CYGNUS TPC background studies motivated the construction of an MWPC-ThGEM hybrid prototype. The MWPC was constructed as a single 30 cm long wire array with 600 μm pitch. The length was chosen to accommodate the scale up requirements and the pitch, which is the smallest attempted for an MWPC, was chosen to match the readout resolution studied in Chapter 3. The ThGEM used was 10 cm in diameter, as the scaling up of this device was addressed separately in Chapter 8. The 2D reconstruction of alpha tracks, in SF_6 gas, was demonstrated using the prototype and a gain $\mathcal{O}(10^3)$ was shown in CF_4 gas. Future improvements to this readout, in particular to the ThGEM device, would likely allow for a gain measurement in SF_6 and prove this MWPC-ThGEM protoype to be a viable readout option for a future CYGNUS TPC.

Chapter 8 described the design and construction of a large area (40$\times$40 cm^2) ThGEM. Testing of this device was conducted in collaboration with Kobe University, where the tests took place inside a purpose built vacuum vessel. The gain was predicted by a simulation that included the charge up effect of the ThGEM insulating layer and the measured gain was found to be up to 400 times lower than predicted. This results, which is consistent with a previous large area ThGEM study, suggests a reduction in performance when scaling to larger areas. Further work is required to confirm this, however, it could be that the tiling of smaller ThGEMs is required to cover the large readout areas of a CYGNUS TPC.

The gamma background due to a camera based CYGNUS prototype TPC, called CYGNO, was studied in Chapter 9. The gas mixture used in CYGNO comprised of He and CF_4 at a ratio of 70/30 at atmospheric pressure. A radioassay of one of the cameras was conducted using HPGe detectors, located at LNGS. The resulting radioactivities were used to perform a Monte Carlo study of the gamma background rate, due to the camera, found within the CYGNO 1 m^3 target gas volume. To reduce this background a 4 cm thick copper shield was simulated with a 4cm wide and 2 cm thick silica window, behind which, the camera was simulated as a point source. It was found that the need for a silica window caused the shielding to be practically ineffectual, suggesting that other methods, such as constructing cameras from a reduced amount of highly radiopure materials, is required to mitigate the gamma background. As demonstrated in Chapter 3 this is especially important at low energies (sub-10 keV_{ee}) where gamma rejection becomes more challenging.

Bibliography

[1] F. Zwicky, "The Redshift of Extragalactic Nebulae", *Helvetica Physica Acta* **1933**, *6*, 110–127.

[2] M. Schwarzschild, "Mass distribution and mass-luminosity ratio in galaxies", *Astronomical Journal* **1954**, *59*, 273.

[3] R. Fusco-Femiano, J. P. Hughes, "Nonpolytropic model for the Coma Cluster", *The Astrophysical Journal* **1994**, *429*, 545–553.

[4] V. C. Rubin, J. Ford, W. Kent, "Rotation of the Andromeda Nebula from a Spectroscopic Survey of Emission Regions", *The Astrophysical Journal* **1970**, *159*, 379.

[5] V. C. Rubin, "Dark Matter in Spiral Galaxies", *Scientific American* **1983**, *248*, 96–109.

[6] Freese, K., "Review of Observational Evidence for Dark Matter in the Universe and in upcoming searches for Dark Stars", *EAS Publications Series* **2009**, *36*, 113–126.

[7] A. S. Eddington, F. W. Dyson, C. Davidson, "IX. A determination of the deflection of light by the sun's gravitational field, from observations made at the total eclipse of May 29, 1919", **1920**.

[8] D. Clowe et al., "A Direct Empirical Proof of the Existence of Dark Matter", *The Astrophysical Journal* **2006**, *648*, L109–L113.

[9] National Aeronautics and Space Administration, The Bullet Cluster, https://chandra.harvard.edu/graphics/resources/handouts/lithos/bullet_lithos.pdf.

[10] A Coc, "Primordial Nucleosynthesis", *Journal of Physics: Conference Series* **2016**, *665*, 012001.

[11] N Aghanim et al., "Planck 2018 results. VI. Cosmological parameters", *arXiv* **2018**.

[12] B. Gold et al., "Seven Year Wilkinson Microwave Anisotropy Probe (WMAP) Observations: Galactic Foreground Emission", *The Astrophysical Journal Supplement Series* **2011**, *192*, 15.

[13] D. J. Fixsen, "The Temperature of the Cosmic Microwave Background", *The Astrophysical Journal* **2009**, *707*, 916–920.

[14] B. A. Robson in, IntechOpen, **2019**, Chapter Standard Model of Cosmology.

[15] J.-H. Kim et al., "The New Horizon Run Cosmological N-Body Simulations", *The Korean Astronomical Society* **2011**.

[16] J. M. Pendlebury et al., "Revised experimental upper limit on the electric dipole moment of the neutron", *Phys. Rev. D* **2015**, *92*, 092003.

[17] R. D. Peccei, H. R. Quinn, "CP Conservation in the Presence of Pseudoparticles", *Phys. Rev. Lett.* **1977**, *38*, 1440–1443.

[18] S. Weinberg, "A New Light Boson?", *Phys. Rev. Lett.* **1978**, *40*, 223–226.

[19] F. Wilczek, "Problem of Strong P and T Invariance in the Presence of Instantons", *Phys. Rev. Lett.* **1978**, *40*, 279–282.

[20] P. Sikivie, "Experimental Tests of the "Invisible" Axion", *Phys. Rev. Lett.* **1983**, *51*, 1415–1417.

[21] N. Du et al., "Search for Invisible Axion Dark Matter with the Axion Dark Matter Experiment", *Phys. Rev. Lett.* **2018**, *120*, 151301.

[22] The MADMAX collaboration, "A new experimental approach to probe QCD axion dark matter in the mass range above 40 μeV", *arXiv:1901.07401v2* **2019**.

[23] C. Athanassopoulos et al., "Results on ν- $\rightarrow \nu_e$ Neutrino Oscillations from the LSND Experiment", *Phys. Rev. Lett.* **1998**, *81*, 1774–1777.

[24] A. A. Aguilar-Arevalo et al., "Significant Excess of Electronlike Events in the MiniBooNE Short-Baseline Neutrino Experiment", *Phys. Rev. Lett.* **2018**, *121*, 221801.

[25] M. Kamionkowski, "WIMP and Axion Dark Matter", *arXiv:hep-ph/9710467* **1998**.

[26] S. Dimopoulos, H. Georgi, "Softly broken supersymmetry and SU(5)", *Nuclear Physics B* **1981**, *193*, 150 –162.

[27] G. Aad et al., "Observation of a new particle in the search for the Standard Model Higgs boson with the ATLAS detector at the LHC", *Physics Letters B* **2012**, *716*, 1 –29.

[28] G. R. Farrar, P. Fayet, "Phenomenology of the production, decay, and detection of new hadronic states associated with supersymmetry", *Physics Letters B* **1978**, *76*, 575 –579.

[29] J. Reuter, M. Tonini, M. de Vries, "Littlest Higgs with T-parity: status and prospects", *Journal of High Energy Physics* **2014**, *2014*, 53.

[30] T. Kaluza, "On the Unification Problem in Physics", *International Journal of Modern Physics D* **2018**, *27*, 1870001.

[31] O. Klein, "The Atomicity of Electricity as a Quantum Theory Law", *Nature* **1926**, *118*, 516–516.

[32] T. Appelquist, H.-C. Cheng, B. A. Dobrescu, "Bounds on universal extra dimensions", *Phys. Rev. D* **2001**, *64*, 035002.

[33] H.-C. Cheng, K. T. Matchev, M. Schmaltz, "Radiative corrections to Kaluza-Klein masses", *Phys. Rev. D* **2002**, *66*, 036005.

[34] C. Doglioni, D. Tovey, "Searching for Dark Matter with the ATLAS detector", *CERN Accelerating science* **2019**.

[35] G. Busoni et al., "On the validity of the effective field theory for dark matter searches at the LHC", *Physics Letters B* **2014**, *728*, 412 –421.

[36] The Atlas Collaboration, "Atlas Experiment - Public Results", *Atlas Twiki* **2019**.

[37] E. Ozcesmeci, "LHC: pushing computing to the limits", **2019**.

[38] A. Morselli, "Indirect dark-matter searches with gamma-rays: experiments status and future plans from KeV to TeV", *Nuclear and Particle Physics Proceedings* **2017**, *291-293*, "New eyes on the Universe" CRIS 2016 Cosmic Rays International Seminars Proceedings of the Cosmic Rays International Seminars, 20 –24.

[39] M. Danninger, "Review of indirect detection of dark matter with neutrinos", *Journal of Physics: Conference Series* **2017**, *888*, 012039.

[40] M. Cirelli, "Dark matter indirect searches: charged cosmic rays", *Journal of Physics: Conference Series* **2016**, *718*, 022005.

[41] M. Ajello et al., "FERMI-LAT Observations of High Energy γ-Ray Emission Toward the Galactic Centre", *The Astrophysical Journal* **2016**, *819*, 44.

[42] T. Daylan et al., "The Characterization of the Gamma-Ray Signal from the Central Milky Way: A Compelling Case for Annihilating Dark Matter", *arXiv:1402.6703v2* **2015**.

[43] I. Cholis et al., "The PAMELA positron excess from annihilations into a light boson", *Journal of Cosmology and Astroparticle Physics* **2009**, *2009*, 007–007.

[44] R. Agnese et al., "Silicon Detector Dark Matter Results from the Final Exposure of CDMS II", *Phys. Rev. Lett.* **2013**, *111*, 251301.

[45] R. Agnese et al., "Results from the Super Cryogenic Dark Matter Search Experiment at Soudan", *Phys. Rev. Lett.* **2018**, *120*, 061802.

[46] R. Agnese et al., "Projected sensitivity of the SuperCDMS SNOLAB experiment", *Phys. Rev. D* **2017**, *95*, 082002.

[47] CRESST collaboration, "First results on low-mass dark matter from the CRESST-III experiment", *arXiv:1711.07692v1.*

[48] E. Armengaud et al., "Performance of the EDELWEISS-III experiment for direct dark matter searches", *Journal of Instrumentation* **2017**, *12*, P08010–P08010.

[49] C. E. Aalseth et al., "Results from a Search for Light-Mass Dark Matter with a *p*-Type Point Contact Germanium Detector", *Phys. Rev. Lett.* **2011**, *106*, 131301.

[50] C. Aalseth et al., "Maximum Likelihood Signal Extraction Method Applied to 3.4 years of CoGeNT Data", *arXiv:1401.6234v3* **2014**.

[51] A. K. Drukier, K. Freese, D. N. Spergel, "Detecting cold dark-matter candidates", *Phys. Rev. D* **1986**, *33*, 3495–3508.

[52] R. Bernabei et al., "First results from DAMA/LIBRA–phase2", *Nuclear and Particle Physics Proceedings* **2018**, *303-305*, Seventh Workshop on Theory, Phenomenology and Experiments in Flavour Physics. The future of BSM physics FPCapri2018, 74 –79.

[53] G. Adhikari et al., "An experiment to search for dark-matter interactions using sodium iodide detectors", *Nature* **2018**, *564*, 83–86.

[54] G. Adhikari et al., "Search for a Dark Matter-Induced Annual Modulation Signal in NaI(Tl) with the COSINE-100 Experiment", *Phys. Rev. Lett.* **2019**, *123*, 031302.

[55] L. Baudis, "WIMP dark matter direct-detection searches in noble gases", *Physics of the Dark Universe* **2014**, *4*, DARK TAUP2013, 50 –59.

[56] P. Cushman et al., "Snowmass CF1 Summary: WIMP Dark Matter Direct Detection", *arXiv:1310.8327v2* **2013**.

[57] D. S. Akerib et al., "Results from a Search for Dark Matter in the Complete LUX Exposure", *Phys. Rev. Lett.* **2017**, *118*, 021303.

[58] E. Aprile et al., "The XENON1T dark matter experiment", *The European Physical Journal C* **2017**.

[59] X. Cui et al., "Dark Matter Results from 54-Ton-Day Exposure of PandaX-II Experiment", *Phys. Rev. Lett.* **2017**, *119*, 181302.

[60] LZ Collaboration, "LUX-ZEPLIN (LZ) Conceptual Design Report", *arXiv:1509.02910v2* **2015**.

[61] H. Zhang et al., "Dark matter direct search sensitivity of the PandaX-4T experiment", *Science China Physics Mechanics and Astronomy* **2018**.

[62] P. Agnes et al., "First results from the DarkSide-50 dark matter experiment at Laboratori Nazionali del Gran Sasso", *Physics Letters B* **2015**, *743*, 456 –466.

[63] P.-A. Amaudruz et al., "First Results from the DEAP-3600 Dark Matter Search with Argon at SNOLAB", *Phys. Rev. Lett.* **2018**, *121*, 071801.

[64] J. Battat et al., "Measurement of directional range components of nuclear recoil tracks in a fiducialised dark matter detector", *Journal of Instrumentation* **2017**, *12*, P10009–P10009.

[65] J. Battat et al., "First measurement of nuclear recoil head-tail sense in a fiducialised WIMP dark matter detector", *Journal of Instrumentation* **2016**, *11*, P10019–P10019.

[66] B. Morgan, A. M. Green, N. J. C. Spooner, "Directional statistics for realistic weakly interacting massive particle direct detection experiments", *Phys. Rev. D* **2005**, *71*, 103507.

[67] D. Akimov et al., "Observation of coherent elastic neutrino-nucleus scattering", *Science* **2017**, *357*, 1123–1126.

[68] F. Mayet et al., "A review of the discovery reach of directional Dark Matter detection", *Physics Reports* **2016**, *627*, A review of the discovery reach of directional Dark Matter detection, 1 –49.

[69] N. Phan et al., "The novel properties of SF6 for directional dark matter experiments", *Journal of Instrumentation* **2017**, *12*, P02012–P02012.

[70] T. Ohnuki, D. P. Snowden-Ifft, C. Martoff, "Measurement of carbon disulfide anion diffusion in a TPC", *Nuclear Instruments and Methods in Physics Research Section A: Accelerators Spectrometers Detectors and Associated Equipment* **2001**, *463*, 142 –148.

[71] E. Daw et al., "Spin-dependent limits from the DRIFT-IId directional dark matter detector", *Astroparticle Physics* **2012**, *35*, 397 –401.

[72] D. P. Snowden-Ifft, "Discovery of multiple, ionization-created CS2 anions and a new mode of operation for drift chambers", *Review of Scientific Instruments* **2014**, *85*, 013303.

[73] J. Battat et al., "First background-free limit from a directional dark matter experiment: Results from a fully fiducialised DRIFT detector", *Physics of the Dark Universe* **2015**, *9-10*, 1 –7.

[74] A. Ezeribe et al., "Demonstration of radon removal from SF6 using molecular sieves", *Journal of Instrumentation* **2017**, *12*, P09025–P09025.

[75] C. Shalem et al., "Advances in Thick GEM-like gaseous electron multipliers—Part I: atmospheric pressure operation", *Nuclear Instruments and Methods in Physics Research Section A: Accelerators Spectrometers Detectors and Associated Equipment* **2006**, *558*, 475 –489.

[76] J. Battat et al., "Readout technologies for directional WIMP Dark Matter detection", *Physics Reports* **2016**, *662*, Readout technologies for directional WIMP Dark Matter detection, 1 –46.

[77] The Cygnus Collaboration, "Cygnus: Feasibility of a nuclear recoil observatory with directional sensitivity to dark matter and neutrinos", *in preparation*.

[78] A. Ezeribe et al., "Demonstration of ThGEM-Multiwire Hybrid Charge Readout for Directional Dark Matter Searches", *arXiv:1909.13881* **2019**.

[79] A. Ochi et al., "A new design of the gaseous imaging detector: Micro Pixel Chamber", *Nuclear Instruments and Methods in Physics Research Section A: Accelerators Spectrometers Detectors and Associated Equipment* **2001**, *471*, Imaging 2000, 264 –267.

[80] Ikeda, Tomonori et al., "Study of Negative-Ion TPC using μ-PIC for Directional Dark Matter Search", *EPJ Web Conf.* **2018**, *174*, 02006.

[81] K. Nakamura et al., "Direction-sensitive dark matter search with gaseous tracking detector NEWAGE-0.3b'", *Progress of Theoretical and Experimental Physics* **2015**, *2015*, 043F01, DOI 10.1093/ptep/ptv041.

[82] E. Baracchini et al., "Negative Ion Time Projection Chamber operation with SF6 at nearly atmospheric pressure", *Journal of Instrumentation* **2018**, *13*, P04022–P04022.

[83] P. Lewis et al., "Absolute position measurement in a gas time projection chamber via transverse diffusion of drift charge", *Nuclear Instruments and Methods in Physics Research Section A: Accelerators Spectrometers Detectors and Associated Equipment* **2015**, *789*, 81 – 85.

[84] F. J. Iguaz et al., "Micromegas detector developments for Dark Matter directional detection with MIMAC", *Journal of Instrumentation* **2011**, *6*, P07002–P07002.

[85] N. Phan et al., "GEM-based TPC with CCD imaging for directional dark matter detection", *Astroparticle Physics* **2016**, *84*, 82 –96.

[86] C. Deaconu et al., "Track Reconstruction Progress from the DMTPC Directional Dark Matter Experiment", *Physics Procedia* **2015**, *61*, 13th International Conference on Topics in Astroparticle and Underground Physics, TAUP 2013, 39 –44.

[87] S. Ahlen et al., "First dark matter search results from a surface run of the 10-L DMTPC directional dark matter detector", *Physics Letters B* **2011**, *695*, 124 –129.

[88] I Abritta Costa et al., "Performance of Optically Readout GEM-based TPC with a 55Fe source", **2019**.

[89] N D'Ambrosio et al., "Nuclear emulsions as a very high resolution detector for directional dark matter search", *Journal of Instrumentation* **2014**, *9*, C01043–C01043.

[90] F. Aznar et al., "Status of the TREX-DM experiment at the Canfranc Underground Laboratory", *arXiv:1709.10062v1*.

[91] Q. Arnaud et al., "Spherical Proportional Counter: A review of recent developments", *Journal of Physics: Conference Series* **2018**, *1029*, 012006.

[92] NEWS-G collaboration, NEWS-G Website, https://news-g.org/.

[93] Q. Arnaud et al., "First results from the NEWS-G direct dark matter search experiment at the LSM", *Astroparticle Physics* **2018**, *97*, 54 –62.

[94] C. Amole et al., "Dark Matter Search Results from the PICO-2L C_3F_8 Bubble Chamber", *Phys. Rev. Lett.* **2015**, *114*, 231302.

[95] S. Agostinelli et al., "Geant4—a simulation toolkit", *Nuclear Instruments and Methods in Physics Research Section A: Accelerators Spectrometers Detectors and Associated Equipment* **2003**, *506*, 250 –303.

[96] J. F. Ziegler, M. Ziegler, J. Biersack, "SRIM – The stopping and range of ions in matter (2010)", *Nuclear Instruments and Methods in Physics Research Section B: Beam Interactions with Materials and Atoms* **2010**, *268*, 19th International Conference on Ion Beam Analysis, 1818 –1823.

[97] C. Ostrouchov, Y. Zhang, W. J. Weber, "pysrim: Automation, Analysis, and Plotting of SRIM Calculations", *The Journal of Open Source Software* **2018**.

[98] S. Biagi, Degrad - transport of electrons in gas mixtures, http://degrad.web.cern.ch/degrad/.

[99] I Lopes, H Hilmert, W. F. Schmidt, "Ionisation of gaseous and liquid sulphur hexafluoride by ^{60}Co γ-radiation", *Journal of Physics D: Applied Physics* **1986**, *19*, L107–L110.

[100] Guillaudin, O. et al., "Quenching factor measurement in low pressure gas detector for directional dark matter search", *EAS Publications Series* **2012**, *53*, 119–127.

[101] H. Schindler, Garfield++ – simulation of tracking detectors, **2019**, http://garfieldpp.web.cern.ch/garfieldpp/.

[102] H. Schindler, Garfield++ User Guide, http://garfieldpp.web.cern.ch/garfieldpp/documentation/UserGuide.pdf.

[103] A. C. Müller, S. Guido, *Introduction to Machine Learning with Python*, O'Reilly Media Inc. ©2017, **2017**.

[104] G. Alner et al., "The DRIFT-II dark matter detector: Design and commissioning", *Nuclear Instruments and Methods in Physics Research Section A: Accelerators Spectrometers Detectors and Associated Equipment* **2005**, *555*, 173 –183.

[105] J. Battat et al., "Low threshold results and limits from the DRIFT directional dark matter detector", *Astroparticle Physics* **2017**, *91*, 65 –74.

[106] J. Battat et al., "Reducing DRIFT backgrounds with a submicron aluminized-mylar cathode", *Nuclear Instruments and Methods in Physics Research Section A: Accelerators Spectrometers Detectors and Associated Equipment* **2015**, *794*, 33 –46.

[107] R. Catena, P. Ullio, "A novel determination of the local dark matter density", *Journal of Cosmology and Astroparticle Physics* **2010**, *2010*, 004–004.

[108] J. Lewin, P. Smith, "Review of mathematics, numerical factors, and corrections for dark matter experiments based on elastic nuclear recoil", *Astroparticle Physics* **1996**, *6*, 87 –112.

[109] D. Tovey et al., "A new model-independent method for extracting spin-dependent cross section limits from dark matter searches", *Physics Letters B* **2000**, *488*, 17 –26.

[110] J. Bovy, S. Tremaine, "On the Local Dark Matter Density", *The Astrophysical Journal* **2012**, *756*, 89.

[111] J.P.Vallée, "Recent advances in the determination of some Galactic constants in the Milky Way", *Astrophys Space Sci* **2017**.

[112] K. Hattori et al., "Old, Metal-poor Extreme Velocity Stars in the Solar Neighborhood", *The Astrophysical Journal* **2018**, *866*, 121.

[113] F. Mouton, PhD thesis, University of Sheffield, **2017**.

[114] J. Battat et al., "Radon in the DRIFT-II directional dark matter TPC: emanation, detection and mitigation", *Journal of Instrumentation* **2014**, *9*, P11004–P11004.

[115] K. Pushkin, D. Snowden-Ifft, "Measurements of W-value, mobility and gas gain in electronegative gaseous CS2 and CS2 gas mixtures", *Nuclear Instruments and Methods in Physics Research Section A: Accelerators Spectrometers Detectors and Associated Equipment* **2009**, *606*, 569 –577.

[116] G. J. Feldman, R. D. Cousins, "Unified approach to the classical statistical analysis of small signals", *Phys. Rev. D* **1998**, *57*, 3873–3889.

[117] M. Carson et al., "Simulations of neutron background in a time projection chamber relevant to dark matter searches", *Nuclear Instruments and Methods in Physics Research Section A: Accelerators Spectrometers Detectors and Associated Equipment* **2005**, *546*, 509 –522.

[118] J. Brack et al., "Background Assay and Rejection in DRIFT", *Physics Procedia* **2015**, *61*, 13th International Conference on Topics in Astroparticle and Underground Physics, TAUP 2013, 130 –137.

[119] B. Mount et al., "LUX-ZEPLIN (LZ) Technical Design Report", *arXiv:1703.09144v1* **2017**.

[120] V Álvarez et al., "Radiopurity control in the NEXT-100 double beta decay experiment: procedures and initial measurements", *Journal of Instrumentation* **2013**, *8*, T01002–T01002.

[121] A. Hallin., University of Alberta, Private communication.

[122] UKDM Collaboration, Radioactivity test results, https://hepwww.pp.rl.ac.uk/groups/UKDMC/Radioactivity/uk.html.

[123] E Sala et al., "Development of an underground low background instrument for high sensitivity measurements", *Journal of Physics: Conference Series* **2016**, *718*, 062050.

[124] T. Hashimoto et al., "Development of a low-alpha-emitting μ-PIC for NEWAGE direction-sensitive dark-matter search", *AIP Conference Proceedings* **2018**, *1921*, 070001.

[125] K. Miuchi, University of Kobe, Private communication.

[126] W. B. Wilson et al., SOURCES 4C: a code for calculating (alpha,n), spontaneous fission, and delayed neutron sources and spectra, tech. rep., United States, **Jan 2002**, p. 127.

[127] AVCalc LLC ©, Density of Rock Salt, https://www.aqua-calc.com/page/density-table/substance/rock-blank-salt.

[128] P. Smith et al., "Simulation studies of neutron shielding, calibration and veto systems for gaseous dark matter detectors", *Astroparticle Physics* **2005**, *22*, 409 –420.

[129] D. Malczewski, J. Kisiel, J. Dorda, "Gamma background measurements in the Boulby Underground Laboratory", *Journal of Radioanalytical and Nuclear Chemistry* **2013**, *298*, 1483–1489.

[130] M. Garcia-Sciveres et al., "The FE-I4 pixel readout integrated circuit", *Nuclear Instruments and Methods in Physics Research Section A: Accelerators Spectrometers Detectors and Associated Equipment* **2011**.

[131] R. D. Oliveira, European Organization for Nuclear Research, Private communication.

[132] J. F. Castel et al., "Background assessment for the TREX Dark Matter experiment", *arXiv:1812.04519v1* **2018**.

[133] RoHS compliant parts, SM Type Surface Mount Precision Plate Resistors, https://www.jfine.co.jp/eng/e_c/resistors/surface_mount/pdf/e_sm.pdf.

[134] M. P. Lener et al., "The μ-RWELL: A compact, spark protected, single amplification-stage MPGD", *Nuclear Instruments and Methods in Physics Research Section A: Accelerators Spectrometers Detectors and Associated Equipment* **2016**, *824*, Frontier Detectors for Frontier Physics: Proceedings of the 13th Pisa Meeting on Advanced Detectors, 565 –568.

[135] S. Cebrián et al., "Radiopurity of micromegas readout planes", *Astroparticle Physics* **2011**, *34*, 354 –359.

[136] S. Cebrián, "Cosmogenic activation of materials", *International Journal of Modern Physics A* **2017**, *32*, 1743006.

[137] L. Baudis et al., "Cosmogenic activation of xenon and copper", *The European Physical Journal C* **2015**, *75*, 485.

[138] J. Back, Y. Ramachers, "ACTIVIA: Calculation of isotope production cross-sections and yields", *Nuclear Instruments and Methods in Physics Research Section A: Accelerators Spectrometers Detectors and Associated Equipment* **2008**, *586*, 286 –294.

[139] C. Toth, Boulby Underground Laboratory, Private Communication.

[140] Boulby Underground Laboratory, Overview of the Laboratory, https://www.boulby.stfc.ac.uk/Pages/Overview-of-the-Laboratory.aspx.

[141] T. Baroncelli, The University of Melbourne - School of Physics, Private communication.

[142] © 2019 Autodesk Inc., EAGLE PCB Design Software, https://www.autodesk.co.uk/products/eagle/overview.

[143] Quick Circuits Ltd, PCB Manufacturing and Assembly, https://www.quick-circuits.com/.

[144] Cremat, CR-110-R2 charge sensitive preamplifier, application guide, **2018**.

[145] Cremat, CR-200 Gaussian shaping amplifier, application guide, **2017**.

[146] ANSYS Inc., Ansys Mechanical APDL Verification Manual, **2013**.

[147] G. F. Knoll, *Radiation Detection and Measurement*, third, (Ed.: B. Zobrist), John Wiley and Sons Inc, **2000**.

[148] Advanced Measurement Technology Inc., Ortec Model 480 Pulser, **2002**.

[149] G. F. Reinking, L. G. Christophorou, S. R. Hunter, "Studies of total ionization in gases/mixtures of interest to pulsed power applications", *Journal of Applied Physics* **1986**, *60*, 499–508.

[150] J. Burns et al., "Characterisation of large area THGEMs and experimental measurement of the Townsend coefficients for CF4", *Journal of Instrumentation* **2017**, *12*, T10006–T10006.

[151] Cremat, CR-111-R2.1 charge sensitive preamplifier: application guide, tech. rep., **2018**.

[152] Analog Devices, AD8011 Current Feedback Amplifier, data sheet, **2003**.

[153] P. Correia et al., "Simulation of gain stability of THGEM gas-avalanche particle detectors", *Journal of Instrumentation* **2018**, *13*, P01015–P01015.

[154] Elite Material Co. Ltd., Lead-free Halogen-free Material EM-370(5) / EM-37B(5), Technical Data, **2013**.

[155] Hamamatsu, ORCA-Flash4.0 Technical Note, https://www.hamamatsu.com/resources/pdf/sys/SCAS0134E_C13440-20CU_tec.pdf.